Research Report

High-Performance Computing in Hessen

2009

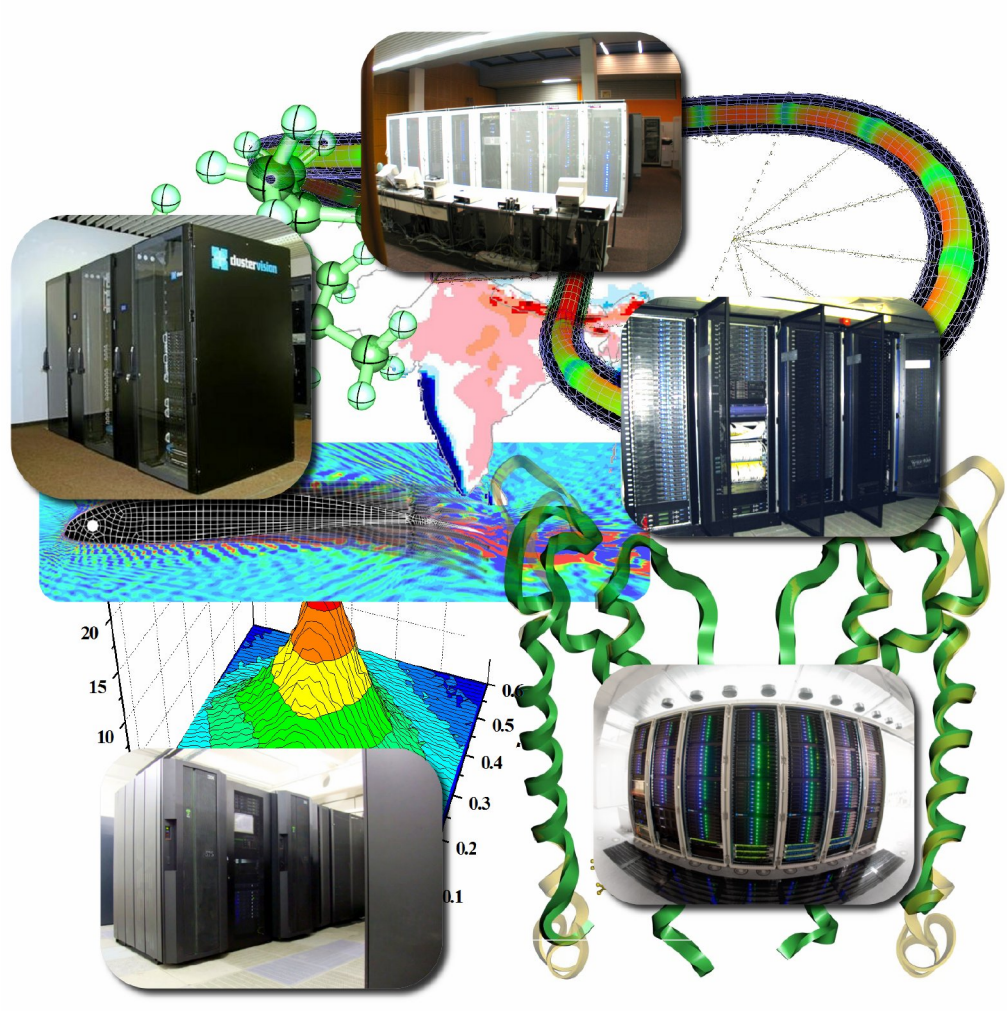

29. März 2010

Inhaltsverzeichnis

1 Vorwort

Die erfolgreiche Durchführung innovativer Forschungsprojekte zur Sicherung des Technologiestandortes Deutschland erfordert in nahezu allen Bereich und speziell bei biologischen, chemischen, mathematischen, physikalischen und ingenieurwissenschaftlichen Fragestellungen neben der experimentellen Untersuchung einen weiterhin steigenden Einsatz computerunterstützter Simulationen. Mittels numerischer Algorithmen können dabei einerseits tiefere wissenschaftliche Erkenntnisse in experimentell schwer zugänglichen Bereichen gewonnen und andererseits Analysen zur gezielten Ausrichtung und folglich zur Reduzierung kostenintensiver Experimente durchgeführt werden. Die dabei stets steigenden Anforderungen führen zu einer wachsenden Komplexität bei den zugrundeliegenden mathematischen Modellen, die nur durch eine Synergie von Soft- und Hardwareentwicklungen bewältigt werden können. Der vorliegende Forschungsbericht liefert in diesem Kontext einen eindrucksvollen Nachweis der existenziellen Relevanz hessischer Hochleistungsrechner bei der wissenschaftlichen Forschungs- und Entwicklungsarbeit an allen beteiligten hessischen Standorten. Erst der kontinuierliche Ausbau der zur Verfügung stehenden Resourcen ermöglich dabei eine anhaltende Wettbewerbsfähigkeit der hessischen Hochschulen im nationalen wie auch internationalen Vergleich.

Die präsentierten Forschungsprojekte zeigen an dieser Stelle die ausgezeichnete Qualität der hierzulande realisierten computerunterstützten Forschung. Ihre internationale Anerkennung wird hierbei sowohl durch die zahlreichen Publikationen in renommierten Zeitschriften als auch durch Beiträge im Rahmen angesehener Fachtagungen belegt. Dabei zeigt sich in beeindruckender Weise die Nutzung der hessischen Hochleistungsrechner bei der notwendigen Grundlagenforschung einerseits und der Umsetzung der hierbei gewonnenen Erkenntnisse innerhalb industrierelevante Anwendungsszenarien andererseits.

Prof. Dr. Andreas Meister
(Vorsitzender des Hessischen Beirats für Hochleistungsrechnen)

2 Einleitung

Die Bedeutung des Wissenschaftlichen Rechnens als eine Schlüsseltechnologie für nahezu alle Bereiche von Wissenschaft und Technik ist heutzutage unumstritten. Trotz der enormen Fortschritte im Bereich der Rechnertechnologie ist hierbei in vielen Anwendungsfällen der Einsatz von Hochleistungsrechnern unerlässlich, nicht zuletzt auch aufgrund der stetig wachsenden Komplexität der Problemstellungen. Das Hochleistungsrechnen trägt entscheidend zur Reduktion von Entwicklungszeiten neuer Methoden und Technologien bei. So können Probleme angegangen werden, die wegen der hohen Anforderungen an die Rechenleistung anderweitig einer numerischen Simulation nicht zugänglich sind.
Der Verfügbarkeit einer adäquaten Hochleistungsrechnerkapazität kommt damit für den Wissenschaftsstandort Hessen eine große Bedeutung zu, da diese die Grundlage für eine national und international konkurrenzfähige Forschung im Bereich des Wissenschaftlichen Rechnens darstellt. Der Erfolg von Sonderforschungsbereichen, Forschergruppen, Graduiertenkollegs und einer Vielzahl unterschiedlicher Einzelprojekte hängt entscheidend davon ab.
Um dem Rechnung zu tragen, wurden nicht nur die beiden großen Hessischen Rechner in Darmstadt und Frankfurt weiter ausgebaut, sondern auch weitere meist schwächer vernetzte Cluster an den Universitäten Gießen, Kassel und Marburg auf- oder ausgebaut.
Durch die Diversifizierung der Leistung soll den stark unterschiedlichen Anforderungen der Nutzer besser Rechnung getragen werden. Problemstellungen mit moderatem Ressourcenbedarf können auf den kleineren System kostengünstig und unbürokratisch abgearbeitet werden, während die Ressourcen der stärker vernetzten großen System für Anwendungen mit entsprechenden Anforderungen geschont werden.
Dem Darmstädter Forschungszentrum CE und dem Frankfurter CSC, die beide assoziierte Mitglieder der Gauss-Allianz sind, kommt die Funktion von Kompetenzzentren im Bereich des Hochleistungsrechners zu. Die notwendige fachübergreifende Kompetenz ist durch die interdisziplinäre Zusammensetzung der beiden Zentren, sowie durch entsprechende Aktivitäten der Mitglieder in Forschung und Lehre gewährleistet. Damit leisten beide Zentren einen Beitrag zu den folgenden Aufgaben:

- Entwicklung bzw. Weiterentwicklung von Anwendungssoftware für Hochleistungsrechner in den verschiedenen Anwendungsbereichen
- Unterstützung von Nutzern bei der Portierung von Anwendungssoftware
- Ausbildung von wissenschaftlichem Nachwuchs im Bereich des Wissenschaftlichen Rechnens
- Technologietransfer in die Industrie im Rahmen von Kooperationsprojekten
- Organisation von regelmäßigen Benutzer-Kolloquien, die den Erfahrungsaustausch zwischen allen Nutzern der jeweiligen Rechner ermöglichen
- Kontaktpflege und Zusammenarbeit mit anderen im Bereich des Hochleistungsrechnens tätigen Arbeitsgruppen im In- und Ausland (z.B. Workshops, Forschungsprojekte)

Die Rechner sind für Nutzer aller hessischen Universitäten zugänglich. Die einzelnen Rechenzeitkontingente richten sich nach den finanziellen Beteiligungen der Hochschulen, Fachbereiche bzw. Fachgebiete.

3 Technik und Organisation

3.1 Der HHLR am Forschungszentrum Computational Engineering (CE) in Darmstadt

3.1.1 Systemaufbau

Seit November 2008 besteht der HHLR aus einem Cluster von 14 Rechenknoten mit jeweils 32 Power6-Prozessoren. Die Prozessoren haben eine Taktfrequenz 4,7 GHz und können vier Floatingpoint Operationen (FLOP) pro Takt verarbeiten. Das gesamte System kam somit auf eine Peakperfomance von 8,5 TFLOP/s. Die Rechenknoten sind mit einem Arbeitsspeicher von 128 GB (einer sogar mit 256 GB) ausgestattet. Auch wenn bei weitem nicht alle Problemstellungen soviel Speicherplatz benötigen, ist es wichtig, dass die zentralen Rechencluster diese Ressourcen vorhalten, da Problemstellungen, die diese Anforderungen haben, auf konvetioneller Hardware nicht lauffähig sind. Durch die 32 in einem System integrierten Prozessoren können auch sehr kommunikationslastige Programme bis zu 32 CPUs nutzen. Alle Knoten des Clusters sind latenzarm mit acht DDR-Infiniband-Lanes vernetzt. Aufgabenstellungen mit moderateren Anforderungen an die Kommunikationsleistung können so auch auf mehrere Knoten verteilt werden.
Das neue System ist von der Systemarchitektur her identisch mit dem Entwicklungscluster (JUMP) des Bundeshöchstleistungsrechners in Jülich. Auch am Höchstleistungsrechner in Garching (RZG MPI/IPP) und am Deutschen Klimarechenzentrum (DKRZ) kommt die gleiche Technik zum Einsatz. Der HHLR ist damit bestens geeignet, als Brücke zwischen den PC-Clustern der Institute und den deutschen Höchstleistungsrechnern zu fungieren.
Im Dezember 2009 wurde das System noch einmal um vier Knoten auf jetzt 18 Maschinen erweitert. Damit besteht der HHLR heute aus 576 eng vernetzten Power6-CPUs und erreicht eine Peakperformance von fast 11 TFLOP/s.

3.1.2 Auslastung des HHLR

Beim Umbau des HHLR Ende 2008 wurden die bisherigen Power5-Rechner durch deutlich leistungsfähigere Power6-Systeme ersetzt. Obwohl sich dabei die Anzahl der CPUs (und damit die verfügbaren CPU-Stunden) etwas verringert haben, steht wegen der gestiegen Leistungsfähigkeit insgesamt mehr Rechenkapazität zur Verfügung. Der in Abbildung 1.2.1 erkennbare Abfall der abgegebenen Rechenzeit zum Jahreswechsel 2008/2009 ist darauf zurückzuführen.
Das Verhältnis von der abgegebenen Rechenzeit zur maximal verfügbaren Rechenzeit des HHLR lag im Jahresmittel bei 90%. Das System ist damit vollständig ausgelastet.
Die Zuweisung der Rechenzeit an die Wissenschaftler der einzelnen Standorte richtet sich nach der Beteiligung der jeweiligen Hochschule an den Investitionskosten. Die TU Darmstadt hat ein Kontingent von 67,5%, der Uni Gießen und Marburg stehen 11,3% bzw. 10,8% zu und die Universitäten in Frankfurt und Kassel haben einen Anspruch auf je 5,2% der Rechenzeit. Wenn ein Standort sein Kontingent nicht ausschöpft, können andere Standorte diese Rechenzeit anteilig nutzen.

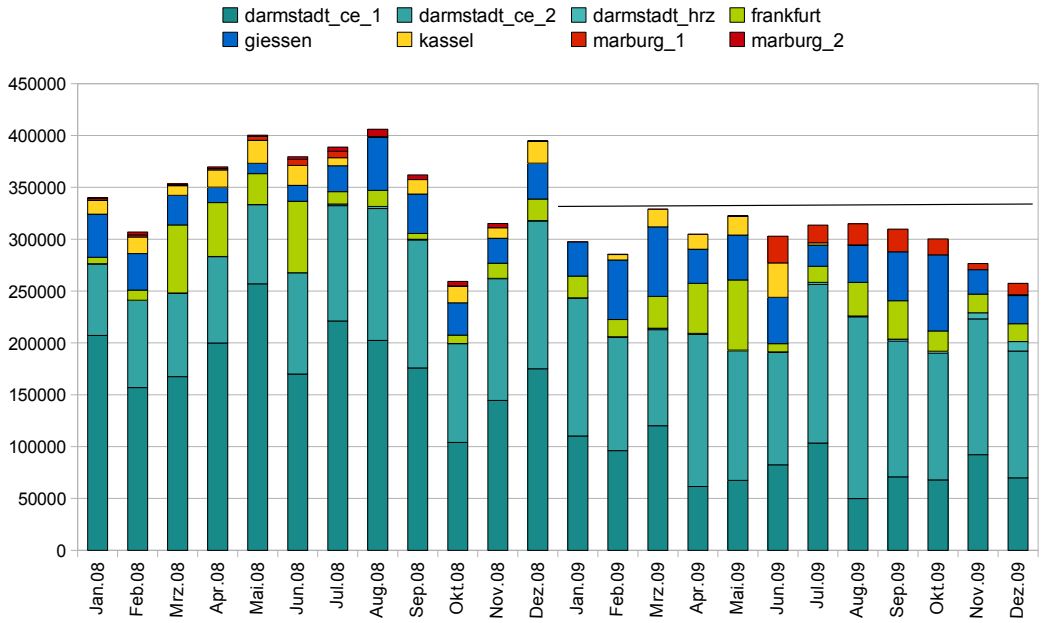

Abbildung 1.2.1: *Verteilung der monatlichen Rechnezeit auf die einzelnen Universitäten*

Die Nutzung des Rechners durch die Universität Marburg ist 2009 wieder gestiegen, sie liegt aber nach wie vor merklich unter ihrem Kontingent. Im Jahresdurchschnitt haben marburger Wissenschaftler knapp 3,3% der insgesamt abgegebenen Rechenzeit genutzt. Auch die Uni Kassel hat mit 2,5% nur die Hälfte ihres Kontingents abgerufen.
Von dieser Zurückhaltung profitieren die anderen Standorte. Die TU Darmstadt nutzte 71% des Rechners, die Uni Frankfurt 9,2% und die Uni Giessen annähern 14%.

3.1.3 Parallelität der Jobs

Betrachtet man die Entwicklung der Jobgößen (Parallelität) (s. Abbildung 1.3.1) so fällt auf, dass sich im Laufe des Jahres 2009 das Maximum der abgegebenen Rechenzeit von 8-fach parallelen zu 32-fach parallelen Jobs verschoben hat. Zu erklären ist diese Verschiebung durch den Umbau des Rechners Ende 2008. Bei diesem Umbau wurde die Knotengrösse von in der Regel 8 CPUs auf 32 CPUs erhöht.
Trotz einer vollständigen Infiniband-Vernetzung werden nach wie vor die meisten Jobs innerhalb eines Knotens gerechnet. Das legt die Vermutung nahe, dass zukünftig noch größere SMP-Systeme oder sehr viel schnellere interne Vernetzungen gebraucht werden, um diese Anwendungen effektiv nutzen zu können.

3.1.4 HPC-Ausbildung an der TU Darmstadt

Mit dem Bachelor- und Master-Studiengang Computational Engineering sowie der Graduiertenschule Computational Engineering wurde an der TU Darmstadt ein durchgängiges konsekutives Konzept zur interdisziplinären Ausbildung im Bereich des High Performance Computing (HPC) etabliert. Der Bachelor-/Master-Studiengang wird vom fachbereichsübergreifenden Studienbereich Computational Engineering organisiert und betreut, der von den Fach- und Studienbereichen Mathematik, Mechanik, Bauingenieurwesen und Geodäsie, Maschinenbau, Elektrotechnik und Informationstechnik, Informatik und dem Forschungszentrum Computational Engineering getragen wird. Den Studierenden werden mathematische, informationswissenschaftliche und ingenieurwissenschaftliche Kenntnisse, mit denen sie physikalische und technische Systeme modellieren und simulieren

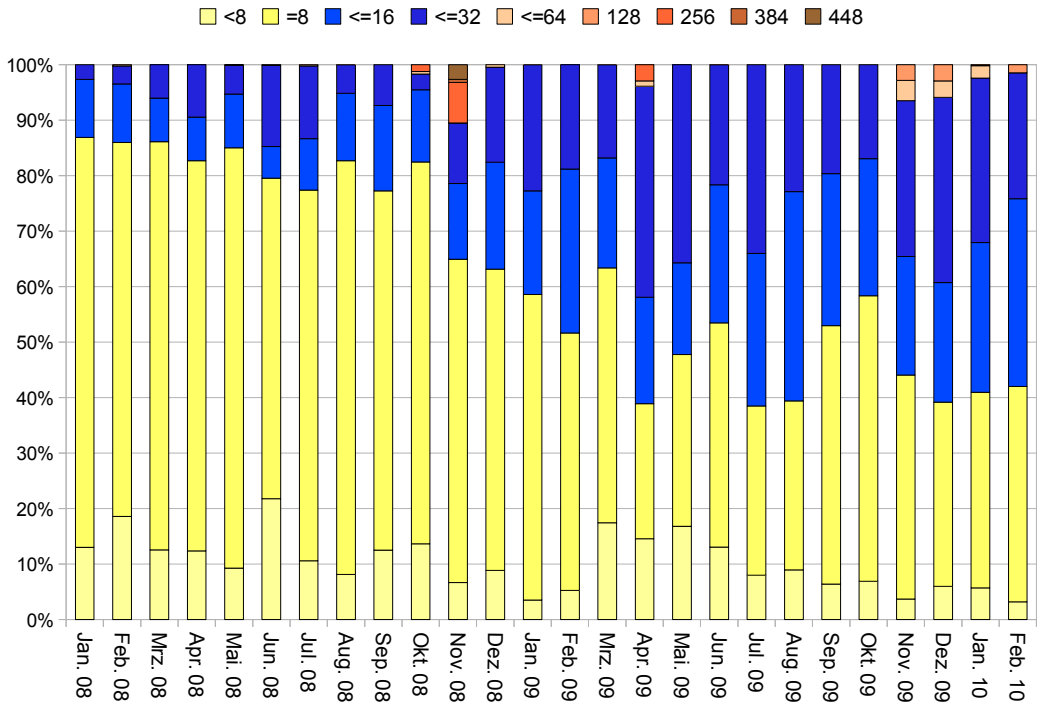

Abbildung 1.3.1: *Verteilung der monatlich abgegebenen Rechenzeit auf die Parallelität der Jobs. Mit dem Umbau des HHLRs auf 32-fach SMPs Ende 2008 hat sich das Maximum von 8-fach parallelen Jos zu 32-fach parallelen Jobs verschoben.*

können, vermittelt. Methoden des HPC sind hierbei ein wesentlicher Bestandteil. Das Ausbildungskonzept wird durch die Graduiertenschule Computational Engineering komplettiert, in welche die Studierenden bereits nach dem ersten Masterjahr eintreten können und diese nach weiteren vier Jahren mit einer Promotion abschließen können. HPC ist ein zentrales Querschnittsthema der Forschungsarbeiten an der Graduiertenschule.

3.1.5 Verweise

1. Weitere Informationen zum HHLR:
   `http://www.hhlr.tu-darmstadt.de`
2. Weitere Informationen zum Forschungszentrum CE:
   `http://www.rc.ce.tu-darmstadt.de/`

3.2 Linux Cluster am Center for Scientific Computing (CSC) der Uni Frankfurt

Das Center for Scientific Computing (CSC) der Goethe-Universität betreibt einen der beiden hessischen Hochleistungsrechner. Das CSC wurde im Jahr 2002 als gemeinsame Initiative von 15 Forschungsgruppen der naturwissenschaftlichen Fachbereiche der Universität Frankfurt ins Leben gerufen. Ausgangspunkt für seine Gründung war die Erkenntnis, dass in den modernen Naturwissenschaften die Bewältigung komplexer numerischer Aufgaben eine zentrale Rolle einnimmt.

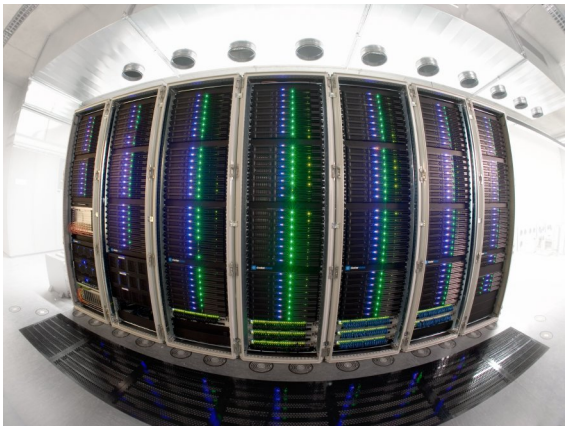

Das CSC bietet daher neben der Bereitstellung einer umfangreichen Rechenkapazität für die Projekte der beteiligten Forschergruppen ein fachübergreifendes Forum auf dem Gebiet Computational Science in Form von interdisziplinären Vorträgen. Darüber hinaus bietet das CSC einen zweijährigen englischsprachigen Masterstudiengang in Computational Science an. Der Studiengang ist in modularer Form konzipiert, so dass alle Studienleistungen in Form von international anerkannten Credit Points gemäß dem European Credit Transfer System bewertet werden. Die durchweg in englischer Sprache gehaltenen Kurse eröffnen auch ausländischen Studierenden eine interdisziplinäre Ausbildung in allen Bereichen der Computer Simulation.

Die Forschungsaktivitäten der am CSC arbeitenden Wissenschaftlern umfassen eine große Zahl von Projekten mit hohem numerischen Aufwand. Die Projekte, die auf dem CSC-Cluster bearbeitet werden, umfassen eine weite Spanne aktueller Themenbereiche. Sie erstrecken sich über so unterschiedliche Gebiete wie die Untersuchung der Strukturen von Proteinen in der Biochemie und die Eigenschaften von Kristallen unter höchstem Druck in der Geophysik. Die Dynamik der Grundbausteine der Materie, der Quarks, und Gluonen, im Urknall und bei Hochenergieexperimenten werden in der theoretischen Physik auf dem CSC simuliert. Wissenschaftler des Frankfurt Institute for Advanced Studies modellieren komplexe atomare Strukturen und untersuchen die Möglichkeiten der Krebstherapie mit Schwerionenstrahlen.

Der Hochleistungsrechner des CSC besteht derzeit aus 2 Linux MPP-Clustern (CSCIII und Erweiterung).

Das Clustersystem CSCIII wurde in 2006 zur Benutzung freigegeben und Anfang 2007 ausgebaut. Es besteht aus 251 Knoten, die jeweils mit 2 DualCore 2GHz Opteron CPUs ausgestattet sind. Jeder Knoten verfügt über 8 GByte Hauptspeicher, zusätzlich sind 44 Knoten auf 16 GByte aufgerüstet worden. 64 der Knoten (und damit 256 Prozessorkerne) sind über Myrinet schnell vernetzt. Ein Raid-System stellt 25 TByte Speicherplatz zur Verfügung.

Der Ende 2009 in Betrieb genommene Ausbau des Clusters umfasst 194 Knoten mit jeweils 2 HexaCore 2,2 Ghz Opteron-Prozessoren, die mit DDR-ConnectX-Infiniband vernetzt sind. Jeder Knoten ist mit 32 GByte Hauptspeicher ausgestattet, 40 Knoten zusätzlich mit 64 GByte. Ein paralleles Dateisystem mit einer Lese- und Schreibrate von mehr als 4 GByte/s steht hier den Benutzern als schnelles globales Scratch-Dateisystem zur Verfügung. Es besteht aus 10 Servern und hat eine Speicherkapazität von 56 TByte. Untergebracht sind die Rechenknoten und Server dieses Clusters in 3 wassergekühlten und 2 luftgekühlten Racks. Die Peak-Rechenleistung des Ausbaus beträgt 20 TFlop/s.

Die Rechenknoten und Server des CSCIII-Systems werden in Kürze in die Erweiterung integriert, so dass aus Benutzersicht die Cluster als einheitliche Rechenumgebung bestehen.

Durch den stetigen Ausbau verfügt das CSC damit über ein MPP-System aus insgesamt 3332 Prozessorkernen mit einer theoretischen Rechenleistung von 24 TFlop/s.

In Kürze steht schon der nächste Ausbau des Clusters an: Zusätzlich werden noch weitere 104 Rechenknoten mit 2 HexaCore 2,2 Ghz Opteron-Prozessoren mit 32 GByte Speicherausbau installiert, ebenso 8 Knoten mit 4 HexaCore 2,2 Ghz Opteron-Prozessoren und 128 GByte Hauptspeicher. Durch weitere 10 Storage-Server wird die Kapazität des parallelen Dateisystems auf 136 Tbyte vergrößert. Die Rechenleistung des Systems wird damit auf 37 TFlop/s erhöht.
Seit 2009 steht allen Mitgliedern des CSC im Rahmen ihrer jeweiligen Rechenkontingente ein kleiner GPGPU-Cluster (Scout) als experimentelles System zur Verfügung. Das System besteht aus 9 Recheneinheiten, wobei jede Einheit aus zwei CPU- und drei GPU- Knoten besteht. Die CPU-Systeme bestehen aus zwei QuadCore Xeon CPUs mit 16 Gbyte Hauptspeicher. Die GPU-Knoten sind Tesla S1070 Systeme von Nvidia. Jeder GPU-Knoten leistet 4 Tflop/s single precision (sp), bzw 345GFlop/s double precision (dp), so dass das Gesamtsystem eine Spitzenleistung von 108 TFlop/s sp, bzw 9.3 Tflop/s dp erreicht. Die Kommunikation innerhalb einer Recheneinheit erfolgt über PCI Express, die Kommunikation zwischen den Recheneinheiten wird ab 2010 durch ein Infiniband-Netzwerk erweitert. Ziel des Scout ist es, allen interessierten Arbeitsgruppen Erfahrungen im Einsatz von GPGPU-Systemen zu ermöglichen.
Den Nutzern wird eine Vielzahl von Softwarepaketen und Compilern zur Verfügung gestellt. Die Datensicherung aller Systeme erfolgt über das Backup-System des Hochschulrechen-zentrums der Universität. Mehr als 500 Wissenschaftler aus über 90 Arbeitsgruppen aus dem Bereich der Naturwissenschaften, Mathematik und Informatik sorgen für eine vollständige Auslastung des Rechners über das ganze Jahr. Etwa ein Viertel der verfügbaren Rechenzeit wird von Gruppen aus Darmstadt, Marburg, Gießen und Kassel verbraucht.
Die Finanzierung der Anlage erfolgte überwiegend durch Beiträge Frankfurter Hochschullehrer und –Institutionen, sowie Zuschüsse des Landes Hessen und des Bundes (im Rahmen des HBFG und Forschungsgroßgeräte-Programms). Über den Verbund der Hessischen Hochleistungsrechner (HHLR) haben Wissenschaftler aller hessischen Hochschulen Zugang zu den Computersystemen des CSC.

3.3 HPC-Cluster der Justus-Liebig-Universität Gießen

Nachdem es an der Universität Gießen mehrere Jahre lang keine eigenen Möglichkeiten für Wissenschaftliches Rechnen gab, hat sich die Situation in 2009 grundlegend verändert. Nach der Bereitstellung von Geldmitteln und einer europaweiten Ausschreibung sowie Zuschlagserteilung in 2008 wurde 2009 ein neues HPC-Cluster installiert und am 25.05.2009 in Betrieb genommen. Die Lieferung der Hardware sowie die Installation und Basiskonfiguration erfolgten durch die Firma Clustervision.

3.3.1 Kennzahlen

- 3 Serverracks
- 2 Kühleinheiten
- 40 Rechenknoten mit je zwei Quad-Core CPUs
- 2 GB Hauptspeicher/Core
- 320 Cores
- 2,94 TFLOPs
- 8 TB Plattenplatz für Home-Verzeichnisse
- 18 TB temporärer Lustre-Speicherplatz
- Gigabit-Ethernet und Infiniband (4x DDR)
- Scientific Linux, C und FORTRAN Compiler
- Queuing-System SUN Grid Engine

3.3.2 Hardware

Die einzelnen Komponenten des Clusters sind in 3 Serverracks im Rechnerraum des HRZ untergebracht. Zwischen diesen Racks sind zur Kühlung des Clusters Luft-/Wasser-Wärmetauschereinheiten (Fabrikat Rittal, LCP plus) angeordnet. Diese werden über einen ebenfalls neu installierten Wasser-/Wasser-Wärmetauscher im Keller des HRZ-Gebäudes versorgt, der wiederum an die Kaltwasserversorgung der Stadtwerke angeschlossen ist. Zur Stromversorgung wurde die bestehende USV-Anlage durch eine zusätzliche zentrale USV-Anlage ergänzt.
Das Cluster besteht aus den Funktionseinheiten: Frontend-Rechner, Rechenknoten, Kommunikationssystem und einem Lustre-Dateisystem.
Die Frontend-Rechner stellen den Login- und Filetransfer-Service sowie das Queuing-System zur Verfügung. Sie sind als HA-Verbund (aktiv/passiv) ausgelegt. Die Hardware besteht aus zwei Supermicro 2HE-Chassis mit H8DMU+-B Motherboard und redundantem Netzteil. In jedem Frontend-Rechner kommen zwei AMD Opteron 2376 Quad-Core-Prozessoren mit 2,3 GHz zum Einsatz. Die sonstigen Daten der Frontend-Rechner sind: 16 GB Hauptspeicher und zwei interne 250 GB Platten (gespiegelt) für das Betriebsstem. Zu der Funktionseinheit Frontend-Rechner gehört weiterhin ein externes RAID-System (DELL Power Vault MD3000 mit 15 1TB 7,2k SATA-Platten). Es wird mit RAID6 plus Hotspare betrieben und stellt ca 12 TB netto als Plattenspeicherplatz zur Verfügung. Dieser wird für die Home-Verzeichnisse der Benutzer (ca. 8 TB) und einen zentralen Ort zur temporären Zwischenspeicherung von Daten (ca. 4 TB) genutzt.
Die Rechenknoten sind 1HE-Twin-Chassis von Supermicro mit je zwei H8DMT-INF+ Motherboards. Je Rechenknoten sind zwei AMD Opteron 2376 Quad-Core-Prozessoren mit einer Taktrate

von 2,3 GHz, 16 GB Hauptspeicher (2 GB pro Core) und zwei 500 GB Platten (gespiegelt) installiert. Die internen Platten dienen als lokaler Scratch-Speicher insbesondere für parallele Prozesse, die lokal auf einem Rechenknoten ablaufen können. Bei den Rechenknoten wurde auf ein redundantes Netzteil verzichtet. Insgesamt sind 20 Twin-Chassis entsprechend 40 Rechenknoten mit je 2 Quad-Core-Prozessoren installiert. Das ergibt zusammen 320 Cores mit einer theoretischen Rechenleistung von 2,94 TFLOPs.
Das Kommunikationssystem besteht aus einem Mangement-, einem Ethernet- und einem Infiniband-Datennetz. Die Verwaltung des Clusters erfolgt über den in jeder Rechnerkomponente installierten IPMI Port. Diese sind über ein 100 MBit-Ethernet Netz miteinander verbunden. Für die Kommunikation der Knoten untereinander und mit den Frontend-Rechnern wird ein 1 GBit-Ethernet Netz bestehend aus drei in einem Stack betriebenen DELL Power Connect 6248 Switches eingesetzt. Ein DDR-Infiniband Netzwerk mit einem bis auf 144 Ports ausbaubaren Flextronics (Mellanox) Switch dient zur schnellen Interprozesskommunikation und für den schnellen Datentransfer mit dem Lustre-Dateisystem.
Das Lustre-Dateisystem besteht aus zwei in Failover-Konfiguration betriebenen Lustre MDS Servern und zwei OSS Fileservern. Die Hardware der MDS Server entspricht dem der Frontend-Rechner, der Hauptspeicher ist allerdings wegen der Funktion als Verzeichnisserver mit 32 GB doppelt so groß ausgelegt. Die Verzeichnisdaten liegen auf einem externen RAID-System (DELL Power Vault MD3000 mit 15 146 GB 15k SAS Platten), das mit RAID10 plus Hotspare betrieben wird. Für den Lustre-Speicherplatz sorgen zwei OSS Server jeweils bestehend aus einem 4 HE Supermicro Chassis mit H8DME-2 Motherboard mit je zwei AMD Operon 2376 Quad-Core-Prozessoren mit einer Taktrate von 2,3 GHz, 8 GB Hauptspeicher und zwei gespiegelten internen 250 GB Platten. Der eigentliche Speicher ist pro OSS Server aus 12 internen 1 TB 7,2k SATA-Platten realisiert, die in RAID6 plus Hotspare Konfiguration betrieben werden. So stehen insgesamt ca. 18 TB netto an Lustre-Speicherplatz zur Verfügung.
In 2009 wurde der weitere Ausbau des Clusters in Auftrag gegeben. Dieser beinhaltet 40 weitere Rechenknoten in 20 Supermicro 1HE-Twin-Chassis mit je zwei D8DMT-IBXF Motherboards. Die Rechenknoten entsprechen den schon installierten Rechenknoten, sind allerdings mit je zwei AMD Opteron 2431 Hexa-Core-Prozessoren mit einer Taktrate von 2,4 GHz und 32 GB Hauptspeicher (2,66 GB pro Core) bestückt. Die Kommunikationsnetze und insbesondere der Infiniband Switch werden entsprechend ausgebaut werden. Zur Unterbringung der neuen Hardware werden ein weiteres Serverrack und zwei weitere Kühleinheiten installiert werden. Durch die neuen Rechenknoten erhöht sich die Anzahl der Cores auf 800 und die theoretische Rechenleistung auf 7,5 TFLOPs.

3.3.3 Software

Das Cluster wird mit der von Clustervision entwickelten Verwaltungssoftware CusterVisionOS betrieben. Auf den einzelnen Knoten läuft Scientific Linux als Betriebssysstem. Zur Programmentwicklung können die Programmiersprachen C und FORTRAN eingesetzt werden. Dazu stehen die Compiler von GNU, Intel und PGI zur Verfügung. Für die Unterstützung zur Optimierung paralleler Prozesse wurde das Tool Alinea Opt installiert. Als Queuing-System wird SUN Grid Engine (SGE) eingesetzt.

3.4 Linux Cluster im IT-Servicezentrum der Universität Kassel

Das Linux Cluster besteht zur Zeit aus 150 Maschinen mit insgesamt 1080 Prozessoren. Jede Maschine hat mindestens 2 AMD-Opteron Prozessoren und 8 GB Hauptspeicher. 62 dieser Systeme sind mit einer Infiniband-Vernetzung ausgestattet. Das Cluster läuft unter dem Betriebssystem CENTOS 5.3 mit PBS-Torque Resource Manager und Maui Cluster Scheduler. 10 Maschinen stehen für interaktive Nutzung zur Verfügung. Der Zugriff auf Plattenspeicher erfolgt über GPFS-Dateisysteme. Von den 1080 Prozessoren wurden 336 Prozessoren aus Mitteln eines Fachgebietes im Fachbereich Naturwissenschaften beschafft und stehen deshalb nur den Mitarbeitern dieses Fachgebietes zur Verfügung. 40 Doppelprozessorsysteme mit je zwei AMD-Sechskernprozessoren und 64 bzw. 128 GB Hauptspeicher wurden gerade erst in Betrieb genommen. Die Geräte wurden nach einen gemeinsamen Großgeräteantrag gemäß Artikel 91b GG von sechs Forschungsgruppen an der Universität beschafft.

Anwendungssoftware: Abaqus-6.5-6 (x86-64), ACML 4.1.0, jrMan, Gausian 03, GROMACS 3.3.3-1, Matlab R2008b, Mathematica 7.0, MD Nastran 2.1 (x86-32), MD Patran 2.1 (x86-32), Meep-0.20.3, MPI: mpich-1.2.7, MPI: LAM/MPI version 7.1.2, MPI: mpich2-1.0.5p4 , MPI: mvapich2-1.0.1, mpb-1.4.2, NWChem 5.1, OpenFOAM-1.5, Pixie-2.2.4, R-2.8.1 (Rmpi mit lme4)

3.4.1 Auslastung

Im zweiten Halbjahr 2009 gab es ca. 60 aktive Nutzer. In diesem Zeitraum wurden 1742961 CPU-Stunden zur Verfügung gestellt, von denen 821245 Stunden abgerufen wurden. Die größten Nutzergruppen kommen aus dem Fachbereichen Physik, Maschinenbau und Elektrotechnik.

3.4.2 SuGI Grid-Cluster

Im Rahmen eines Aufstockungsantrages für das SuGI-Projekt wurde im Dezember 2007 ein zweites Linux Cluster beschafft, das primär für Grid-Computing Anwendungen reserviert ist. Bei diesem Cluster handelt es sich um 21 Doppelprozessorsysteme mit Intel Quad-Core CPU's, 32 GB Hauptspeicher und 10 TB Plattenspeicher. Das Cluster ist seit Januar 2008 im Nutzerbetrieb und soll insbesondere für Grid-Anwendungen in der Chemie genutzt werden. Dazu wurde es als Ressource in mehreren Virtuellen Organisationen des D-Grid angemeldet. Das Cluster läuft unter dem Betriebsystem CENTOS 5 und ist damit kompatibel zum Linuxcluster des HRZ. Für Grid-Anwendungen ist die Middleware Gobus Toolkit auf beiden Linux Clustern installiert. Zudem gibt es für das Grid-Cluster ein UNICORE 5 und ein UNICORE 6 Frontend. Das Cluster ist mit hochschulinternen Nicht-Grid-Anwendungen ebenfalls gut ausgelastet.

3.5 Der Linux-Cluster MaRC an der Philipps-Universität Marburg

3.5.1 Systembeschreibung

Der Linux-Cluster MaRC (**Mar**burger **R**echen**C**luster) besteht aus insgesamt 144 Knoten mit jeweils zwei DualCore AMD Opteron-Prozessoren. Arbeitsgruppen aus verschiedenen Fachbereichen waren maßgeblich an der Finanzierung beteiligt und können MaRC entsprechend nutzen, ebenso Anwender aus anderen hessischen Hochschulen. MaRC wird vom Hochschulrechenzentrum (HRZ) der Philipps-Universität Marburg betrieben.

Abbildung 5.1.1: *MaRC, Ansicht von vorne*

3.5.2 Beschaffung in zwei Ausbaustufen

Die erste Ausbaustufe von MaRC wurde nach längeren Planungen noch im Rahmen eines HBFG-Antrags im Dezember 2005 beschafft und Anfang 2006 in Betrieb genommen.
Eine zweite Ausbaustufe konnte im März 2007 über eine Mischfinanzierung realisiert werden. Neben Restmitteln aus dem HBFG-Antrag wurden dabei weitere Bundesmittel eingesetzt; ein Teil (19) der Knoten sind über das D-Grid-Integrations-Projekt finanziert und daher organisatorisch in das D-Grid integriert.

3.5.3 Hardware

Die insgesamt 144 Knoten von MaRC verteilen sich auf fünf Racks. Sie sind mit 2.0 GHz (1. Ausbaustufe) bzw. 2.4 GHz (2. Ausbaustufe) getaktet. Die 57 neueren Knoten verfügen jeweils über 16 GByte DDR2 Hauptspeicher, die älteren Knoten sind noch mit DDR Hauptspeicher (8 GByte und zum Teil 16 GByte) bestückt. Die innere Vernetzung ist doppelt via GigaBit Ethernet ausgelegt, 24 der neueren Knoten sind zusätzlich über ein InfiniBand-Netzwerk verbunden. Ein Knoten dient als (NFS-)Fileserver und stellt über ein RAID-Subsystem 4 TByte Plattenplatz (brutto) bereit. Seit Mitte 2009 wird zusätzlich über die InfiniBand-Knoten ein verteiltes (GlusterFS-)Filesystem realisiert. Alle Compute-Knoten haben jeweils eine interne 250 GByte SATA-Festplatte.

3.5.4 Nutzung

Das Nutzungsprofil variiert sehr stark in Abhängigkeit von der Benutzergruppe. Während ein Teil der Benutzer ausschließlich fachspezifische Standardprogramme einsetzt, entwickeln und nutzen andere eigene Software; zum Teil ist auch die Organisation paralleler und verteilter Prozesse selbst Gegenstand der Forschung. Durch die Kooperation aller Beteiligten konnten mehrfach Lösungen für besondere Anforderungen gefunden werden, ohne den Produktionsbetrieb signifikant zu beeinträchtigen.

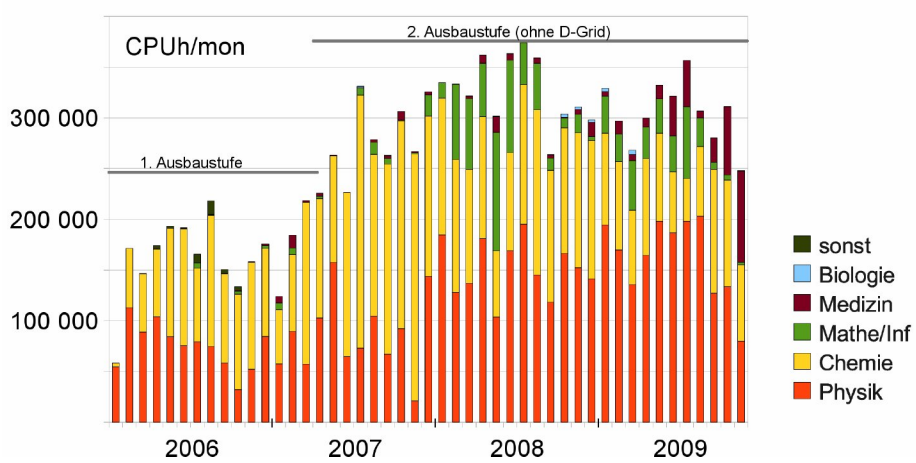

Abbildung 5.4.1: *Nutzung von MaRC durch verschiedene Fachbereiche. Knoten der 2. Ausbaustufe wurden ihrer höheren Taktfrequenz entsprechend mit dem Faktor 1.2 gewichtet.*

Die Nutzung von MaRC durch serielle und parallele Programme hält sich in etwa die Waage. Bei der parallelen Nutzung dominieren Jobs mit 2-8 Prozessen; nur ganz selten werden Jobs mit 64 und mehr Prozessen gestartet. Insbesondere viele serielle Jobs haben einen hohen Hauptspeicherbedarf, so dass manchmal nicht die CPU-Leistung, sondern die Verfügbarkeit von Hauptspeicher die Nutzung des Clusters limitiert; dies ist der Hauptgrund für die niedrigeren Balken in der CPU-Nutzungsstatistik, die in Abb. 5.4.1 dargestellt ist. Die Nutzung des Clusters durch SMP-Jobs ist durch die Architektur der Knoten auf maximal vier Cores bzw. parallele Threads limitiert. Für höhere Anforderungen eignet sich z.B. der HLR in Darmstadt. Durch den Betrieb von MaRC reduzierte sich dort andererseits der Marburger Anteil der HLR-Nutzung, so dass wertvolle Ressourcen gezielter eingesetzt werden konnten.
Die User-Dokumentation von MaRC wird im Sinne eines Gemeinschaftsprojekts in der Form eines Wikis gepflegt.

3.5.5 Verweise

1. MaRC Homepage: `http://www.uni-marburg.de/hrz/infrastruktur/zserv/cluster`
2. User-Dokumentation zu MaRC im Wiki: `http://clust-doc.hrz.uni-marburg.de`

4 Projektberichte

4.1 Chemie

4.1.1 Chemoselective Boron–Carbon Bond Cleavage by Hydroboration of Borirenes

Mehmet A. Celik and G. Frenking
Fachbereich Chemie, Philipps-Universität Marburg

Cyclic boron compounds, such as borirenes (1), are of particular interest with regard to the π-electron acceptor properties. However, very little is known about the reactivity of this class of compounds.[1] In this study, we represent a quantum chemical study on the reaction of 9-BBN (2) across the B-C bond (Path A) and C-C double bond (Path B) of the model compound 1-aminoborirene (3M) where SiMe3 groups are replaced by SiH_3 groups and ethyl groups are replaced by methyl groups. In order to understand the ring strain effect on the reaction mechanisms, we also modeled the addition of 9-BBN to the larger analogous of 3M. To shed light on the reaction mechanisms, we have performed Density Functional Theory calculations (DFT) with the program package Gaussian 03. The geometries have been optimized using the MO5-2X functional[2] with the 6-31G(d) basis set. Improved energies were calculated with a larger basis set at MO5-2X/6-311++G(2d) using MO5-2X/6-31G(d) optimized geometries including zero-point vibrational energy corrections at MO5-2X/6-31G(d).

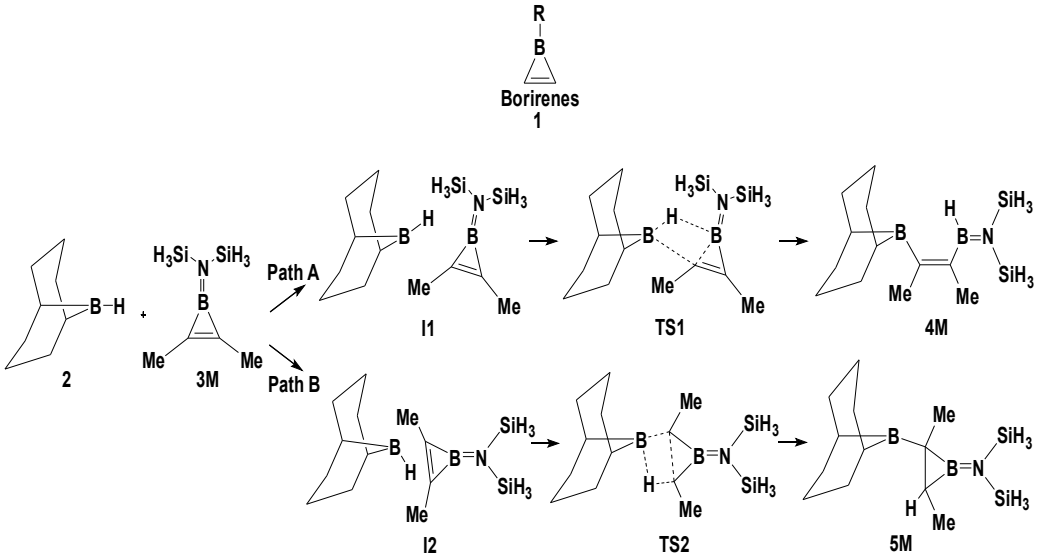

The calculated reaction profile is shown below. The reaction proceeds via the early transition state **TS1** which resembles **I1**. The calculated activation barrier with respect to **I1** is 11.9 kcal/mol. The rather low activation barrier is in agreement with the observation that the reaction proceeds smoothly at 80 °C. DFT calculations suggest that the overall reaction yielding the final product **4M** is very exothermic by 32.0 kcal/mol.
We also considered the reaction course where **9-BBN** reacts with the C=C bond of **3**M. The reaction profile is shown on the left hand side of the Figure below. The latter reaction initially

yields the weakly bonded complex **I2** which is slightly stronger bonded (D_o = -5.9 kcal/mol) than **I1**. However, the further reaction via transition state **TS2** yielding the product molecule **5M** has a higher barrier (14.0 kcal/mol) and is less exothermic (-26.9 kcal/mol) than the reaction of **9-BBN** with the C-B bond. The calculated data agree with the experimental observation that only the latter is observed.

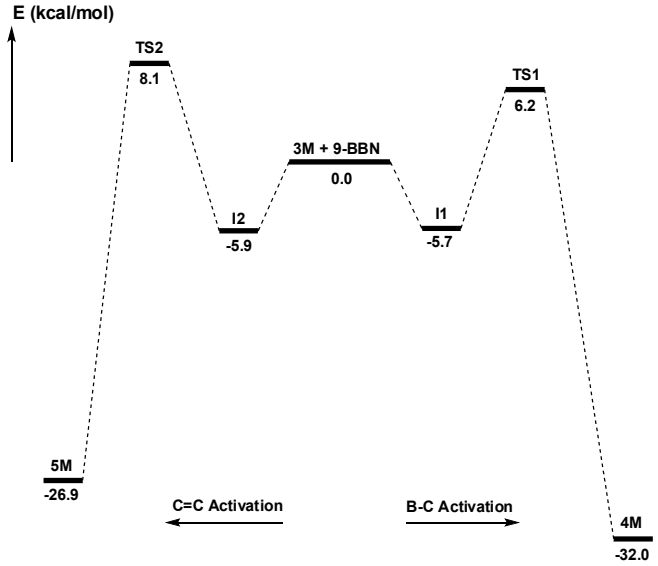

The calculations proved that the addition of **9-BBN** across the B-C bond is both kinetically and thermodynamically favoured. However, in larger analogous of **3M**, addition of **9-BBN** towards the C-C-double bond becomes a competing pathway. Thus, relief of molecular strain is the major thermodynamic driving force for the selective reaction.[1]

References

1. H. Braunschweig, T. Herbst, K. Radacki, G. Frenking, M.A. Celik, *Chem. Eur. J.* 2009, 15, 12099-12106.

2. Y. Zhao, D.G. Truhlar, *Acc. Chem. Res.* 41, 2008, 157–167.

4.1.2 Quantum Chemical Studies on Transition Metal Compounds [M(ZnR)$_n$] (M=Mo, n=12; M=Ru, n=10; M=Rh, n=9; M=Ni, Pd, Pt, n=8) [1]

Moritz von Hopffgarten, Israel Fernández and Gernot Frenking
Fachbereich Chemie, Philipps-Universität Marburg

In a collaborative work with Roland A. Fischer *et al.* we reported the syntheses of the homoleptic transition metal compounds [M(ZnMe)$_n$(ZnCp*)$_m$] (M=Mo, n=9, m=3 (**1**); M=Ru, n=6, m=4 (**2**); M=Ru, n=6, m=3 (**3**); M=Ni, Pd, Pt, n=4, m=4 (**4**, **5**, **6**), Me=CH_3, Cp*=C_5Me_5) and analyses of the nature of the chemical bond in their parent compounds [M(ZnH)$_n$] (M=Mo, n=12 (**1H**); M=Ru, n=10 (**2H**); M=Rh, n=9 (**3H**); M=Ni, Pd, Pt, n=8 (**4H**, **5H**, **6H**)) where all organic moieties were replaced by hydrogen atoms (see Figure 1) [1,2]. The model compounds all exhibit highly symmetric minimum structures of the I_h (**1H**), D_{4d} (**2H**, **H**, **5H**, **6H**) and D_{3h} (**3H**) point groups.

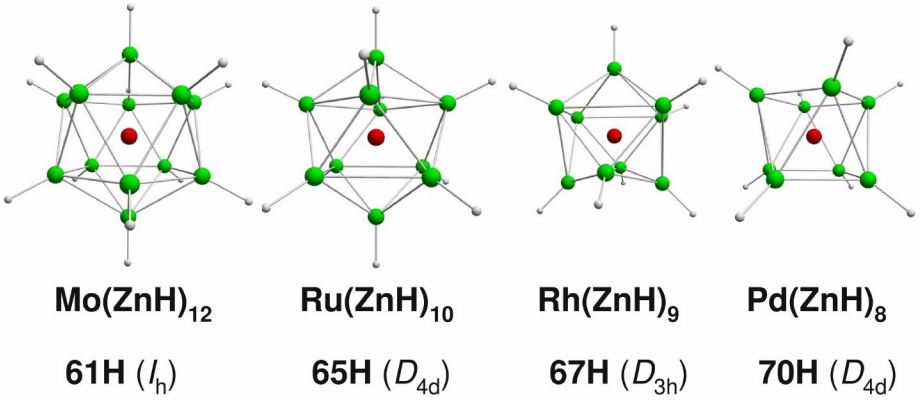

Abbildung 2.1: *Relevant modelcompounds*

For the discussion of the nature of the chemical bond we applied Molecular-Orbital- (MO), Atoms-in-Molecules- (AIM) [3] and the Energy Decomposition Analysis (EDA) that has been developed by Morokuma [4] and Ziegler and Rauk [5]. This energy decomposition analysis decomposes the total interaction energy of two fragments of a molecule into electrostatic interactions, Pauli repulsion and orbital attractions. In symmetric systems the orbital attractions are decomposed into contributions of the irreducible representations of the molecule's point group. As fragments for EDA we chose the central atom interacting with the (ZnH)$_n$ substructure in appropriate electronic states.
MO-analysis of **1H** suggests that the most important orbital interactions should come from the molybdenum's s and d atomic orbitals interacting with a_g and h_g fragment orbitals of the (ZnH)$_{12}$ fragment (see Figure 2).
These findings are supported by the results of the EDA. The EDA shows that the molybdenum in its s^1d^5 ground state interacting with the corresponding $a_g{}^1h_g{}^5$ septet state of the (ZnH)$_{12}$ fragment gives the best description of the molecule in terms of fragment interactions (as implied in Figure 2).
A conclusion of these results is, that chemical bonding in the 18 valence electron compound **1H** may be described as the interaction of a sd^5-hybridised Mo-atom forming six 2-electron-3-centre Zn-Mo-Zn electron sharing bonds pointing at opposing corners of the icosahedron. Twelve valence electrons are engaged in these bonds. The six remaining valence electrons are used for Zn-Zn interactions. With 30 equal Zn-Zn contacts, only 1/10 of a valence electron pair per Zn-Zn contact are present and therefore these interactions should be only weak. As AIM analysis gives only Mo-Zn and Zn-H but no Zn-Zn bond paths it supports this bond picture.
AIM analyses for all other parent compounds **2H**-**6H** also give only M-Zn and Zn-H bond paths and no Zn-Zn bonds. This indicates a similar bonding situation compared to **1H**. EDA results show, that the best description of the compounds **4H**-**6H** in terms of fragment interactions are Ni, Pd and Pt

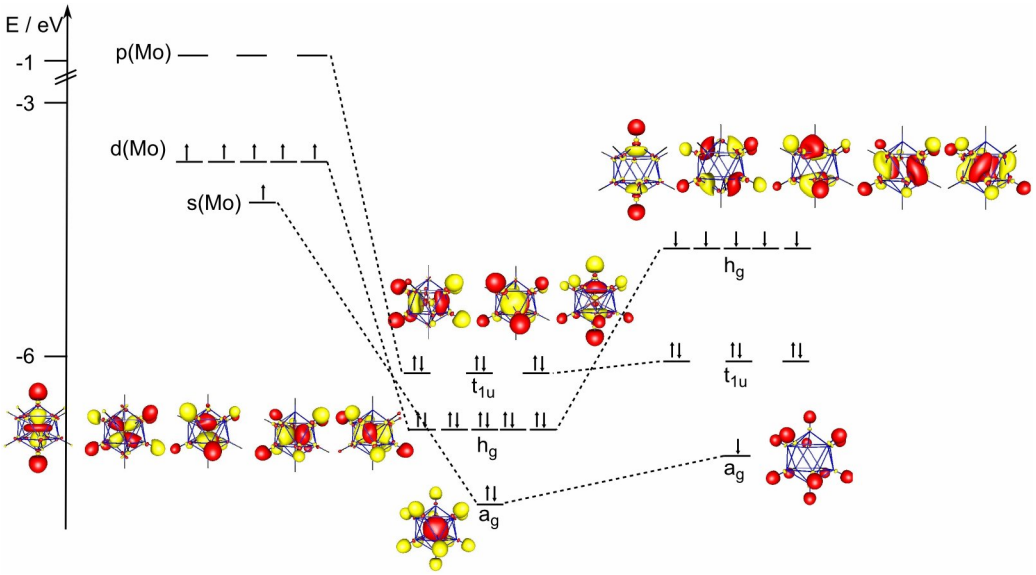

Abbildung 2.2: *MO correlation diagram of 1H*

central atoms in the $ns^0(n\text{-}1)d^{10}$ states forming donor acceptor bonds with the $(ZnH)_8$ fragment in the singlet ground state. Similarresults are obtained for **3H**, according to the EDA this compound should be described by the interaction of a central Rh^- anion in the $[Kr]5s^04d^{10}$ electronic state with the $(ZnH)_9$ fragment via donor-acceptor bonds. The EDA of **2H** results in the description of the bonding interactions as a mixture of electron sharing and donor-acceptor bonds.

References

1. T. Cadenbach, T. Bollermann, C. Gemel, M. Tombul, I. Fernández, M. von Hopffgarten, G. Frenking and R. A. Fischer, *J. Am. Chem. Soc.,* **2009**, *131*, 16063.

2. T. Cadenbach, T. Bollermann, C. Gemel, I. Fernández, M. von Hopffgarten, G. Frenking and R. A. Fischer, *Angew. Chem. Int. Ed.,* **2008**, *47*, 9150.

3. R. F. W. Bader, Atoms in Molecules. A Quantum Theory, Oxford University Press 1990.

4. K. Morokuma, J. Chem. Phys. 55 (1971) 1236.

5. T. Ziegler, A. Rauk, Theor. Chim. Acta 46 (1977) 1.

4.1.3 The Dewar-Chatt-Duncanson Model Reversed – Bonding Analysis of Group-10 Complexes

Catharina Goedecke, Pierre Hillebrecht, Till Uhlemann, Robin Haunschild, and Gernot Frenking
Fachbereich Chemie, Philipps-Universität Marburg

The chemical bonds in donor-acceptor complexes of transition metals with main-group ligands are usually described with the Dewar-Chatt-Duncanson (DCD) model, where the ligand serves as a σ-donor and
π-acceptor while the metal is a σ-acceptor and π-donor (Figure 1a). It is conceivable that electron deficient ligands bind to electron rich (late) transition metals in a reversed fashion where the metal is a σ-donor while the ligand is a σ-acceptor (Figure 1b). This could be possible when a group-13 Lewis acid EX_3 (E = B - Tl) is bonded to a d^{10} metal fragment.

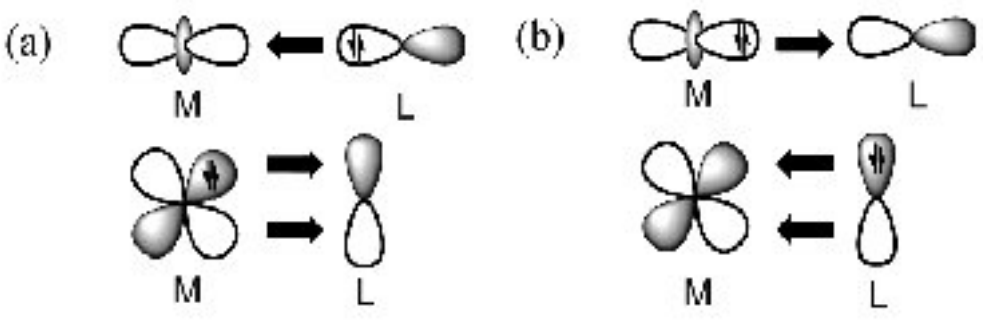

Abbildung 3.1: *Representation of (a) the Dewar-Chatt-Duncanson model and (b) the reversed Dewar-Chatt-Duncanson model.*

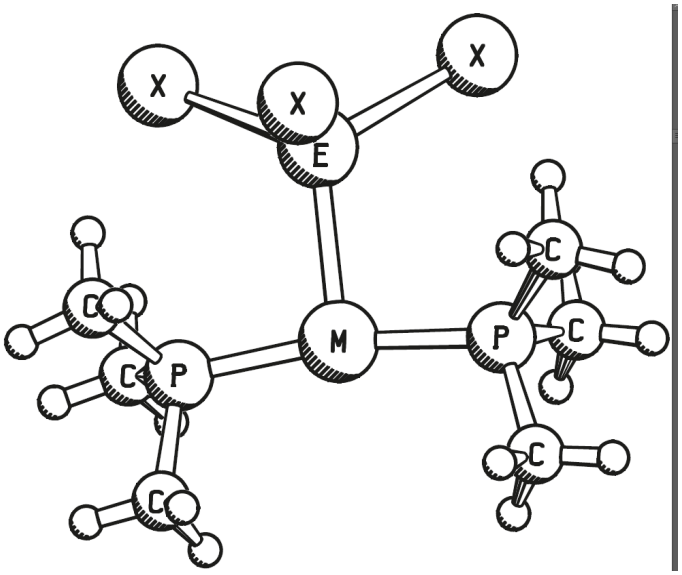

Abbildung 3.2: *Equilibrium structure of a* $[(Me_3P)_2M - EX_3]$ *complex.*

The first neutral donor-acceptor complex with a non-chelating EX_3 ligand of a group-13 element E which was identified by x-ray structure analysis was only reported in 2005 by R.A. Fischer

and coworkers.[1] Later Braunschweig reported the syntheses and x-ray analyses of $[(Cy_3P)_2Pt\text{-}AlCl_3]$[2] and $[(Cy_3P)_2Pt\text{-}GaCl_3]$[3]. A review about the coordination chemistry of aluminum, gallium, and indium with transition metals shows that it is very difficult to prepare neutral complexes [M]-EX_3 which have a non-chelating group-13 ligand EX_3.[4]
Using computer time provided by the HRZ Marburg, the CSC Frankfurt and the HHLR Darmstadt, we reported a charge and energy decomposition analysis of the metal-ligand bonding in the complexes $[(Me_3P)_2M\text{-}EX_3]$ for M = Ni, Pd, Pt; E = B - Tl; X = H, F - I.[5] We also determined equilibrium structures (Figure 2), which are nearly T-shaped with an almost free rotation around the E-M axis. Additionally, bond dissociation energies were calculated, which suggest that further examples of stable complexes with EX_3 ligands could exist. These results should be helpful as a guideline for further synthetic trials.

References

1. T. Steinke, C. Gemel, M. Cokoja, M. Winter, R. A. Fischer, *Dalton Trans.* **2005**, *1*, 55.
2. H. Braunschweig, K. Gruss, K. Radacki, *Angew. Chem.* **2007**, *119* (41), 7929.
3. H. Braunschweig, K. Gruss, K. Radacki, *Inorg. Chem.* **2008**, *47* (19), 8595.
4. R. A. Fischer, J. Weiss, *Angew. Chem. Int. Ed.* **1999**, *38*, 2831.
5. C. Goedecke, P. Hillebrecht, T. Uhlemann, R. Haunschild, G. Frenking, *Can. J. Chem.* **2009**, *87*, 1470.

4.1.4 N-Heterocyclic Carbene Stabilized Digermanium(0)

Susanne Klein, and Gernot Frenking
Fachbereich Chemie, Philipps-Universität Marburg

Although the stabilization of transition metals in the zero oxidation state by very nucleophilic N-heterocyclic carbenes (NHCs) is well documented[1] and the coordination of these ligands to main group elements is well described[2], NHC complexes of p-block elements, formally in the zero oxidation state, were described[3] recently. Robinson et al. synthesized a NHC adduct of Si_2[4] whose description as donor stabilized Si_2 it supported by theoretical calculations[4,5].
In order to shed light on the validity of the bonding description of the synthesized germanium analogue[6] as a **N-heterocyclic carbene stabilized digermanium(0)** quantum chemical calculations were carried out with the program package ADF 2006.01d on MaRC using density functional theory at the BP86/TZ2P level.

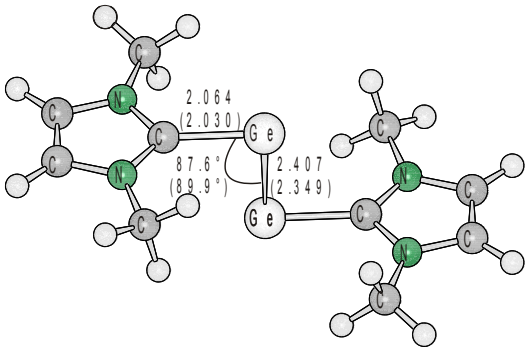

Abbildung 4.1: *Calculated (BP86/TZ2P) structure of the model compound. Bond lengths in Å and angles in degree. Experimental values for the synthesized molecule with aryl substituents at nitrogen instead of methyl groups are given in parentheses.*

The optimized structure of the Ge(0) compound is C_{2h} symmetric with both NHC rings orthogonal to the C-Ge-Ge'-C' plane and a nearly rectangular C-Ge-Ge' bond (figure 1). The preference for the trans-bent geometry can be explained in terms of the orbital interactions between Ge_2 and the NHC ligands. The electronic ground state of Ge_2, schematically shown in Figure 2a, is the $X^3\Sigma_g^-$ state. The electronic reference state for the diamagnetic complex is the $^1\Delta_g$ excited state (Figure 2b) which is only 9.5 kcal/mol higher in energy than the ground state.[8] The orbital occupation of the latter state is perfectly suited for donor-acceptor interactions with two NHC ligands. The vacant π-bonding orbital of the $^1\Delta_g$ state of Ge_2 can serve as acceptor orbital for donation from the minus combination of the carbon lone-pair orbitals of the NHC ligands (b_u symmetry in C_{2h}) while the associated π*-antibonding MO is available as acceptor orbital for electron donation from the plus combination of the NHC donor orbitals (a_g symmetry). The strength of the orbital interactions were analyzed with the EDA[9] (energy decomposition analysis) developed by Morokuma[10] and Ziegler.[11] The total interaction energy ΔE_{int} between ($^1\Delta_g$) Ge_2 and the $(NHC)_2$ ligands using the frozen geometries of the fragments amounts to -100.6 kcal/mol. This gives a bond dissociation energy (BDE) of D_e = 75.6 kcal/mol for both ligands after geometry relaxation yielding two NHC molecules and Ge_2 in its $X^3\Sigma_g^-$ ground state.[12] The average BDE for the (Ge_2)-$(NHC)_2$ donor-acceptor bonds is thus predicted as D_e = 37.8 kcal/mol which is quite high in comparison with other donor-acceptor complexes.[7] The breakdown of the total interaction into its main components shows that the (Ge_2)-$(NHC)_2$ bonds are more electrostatic (ΔE_{elstat} = 59.2%) than covalent (ΔE_{orb} = 40.8%). The orbital interactions which yield (Ge_2)-$(NHC)_2$ covalent bonding come with 46.3%(b_u) and 46.5%(a_g) mainly from the plus and minus combinations of the lone-pairs of the NHC ligands into the vacant in-plane π and π* orbitals of Ge_2. The donation from the occupied π MO of Ge_2 into the $p(\pi)$ orbitals of the carbene carbon atoms (a_u symmetry) provides only 6.2% of ΔE_{orb} and the π donation of the NHC ligands into the out-of-plane π* orbital of Ge_2 (b_g symmetry) is negligibly small. The above EDA results give a comprehensive picture of the nature and the strength of the (Ge_2)-$(NHC)_2$ bonding.

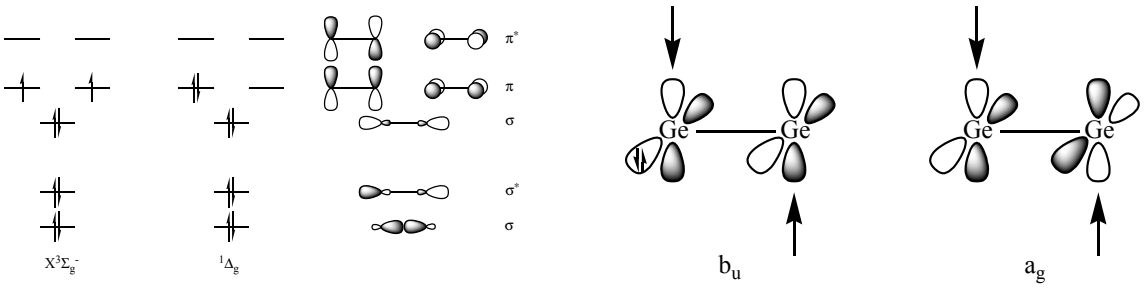

Abbildung 4.2: *Schematic representation of (a) the $X^3\Sigma_g^-$ ground state and (b) the $^1\Delta_g$ excited state of Ge_2. Pictorial description of the electron donation from the carbon σ-lone pair orbitals of the NHC ligands into the vacant orbitals of ($^1\Delta_g$)Ge_2: (c) Donation of the plus combination of the lone-pairs into the in-plane vacant π MO and (d) donation of the minus combination of the lone-pairs into the in-plane vacant π* MO.*

References

1. a) P. de Fremont, N. Marion, S.P. Nolan, *Coord. Chem. Revs.* **2009**, *253*, 862-892; b) F.E. Hahn, M.C. Jahnke, *Angew. Chem.* **2008**, *120*, 3166-3216; *Angew. Chem. Int. Ed.* **2008**, *47*, 3122-3172; c) W.A. Herrmann, *Angew. Chem.* **2002**, *114*, 1342-1363; *Angew. Chem. Int. Ed.* **2002**, *41*, 1290-1309; d) D. Bourissou, O. Guerret, F.P. Gabbaï, G. Bertrand, *Chem. Rev.* **2000**, *100*, 39-91; and references therein.

2. a) N. Kuhn, A. Al-Sheikh, *Coord. Chem. Revs.* **2005**, *249*, 829-857; b) C.J. Carmalt, A.H. Cowley, *Adv. Inorg. Chem.* **2000**, *50*, 1-32; and references therein.

3. Y. Wang, G.H. Robinson, *Chem. Commun.* **2009**, 5201-5213.

4. Y. Wang, Y. Xie, P. Wei, R.B. King, H.F. Schaefer III, P.v.R. Schleyer, G.H. Robinson, *Science* **2008**, *321*, 1069-1071.

5. Z. Liu, *J. Phys. Chem. A* **2009**, *113*, 6410-6414.

6. A. Sidiropoulos, C. Jones, A. Stasch, S. Klein, G. Frenking *Angew. Chem. Int. Ed.* **2009**, *48*, 1.

7. V. Jonas, G. Frenking, M. T. Reetz, *J. Am. Chem. Soc.* **1994**, *116*, 8741.

8. C.C. Arnold, C. Xu, G.R. Burton, D.M. Neumark, *J. Chem. Phys.* **1995**, *102*, 6982-6989.

9. a) F. M. Bickelhaupt, E. J. Baerends, *Rev. Comput. Chem.* **2000**, *15*, 1. b) G. Frenking, K. Wichmann, N. Fröhlich, C. Loschen, M. Lein, J. Frunzke, JV. M. Rayón, *Coord. Chem. Rev.* **2003**, *238-239*, 55. c) M. Lein, G. Frenking, in *Theory and Applications of Computational Chemistry: The First 40 Years*, p. 367, C. E. Dykstra, G. Frenking, K. S. Kim, G.E. Scuseria (Eds), Elsevier, Amsterdam, 2005.

10. K. Morokuma, *J. Chem. Phys.* **1971**, *55*, 1236.

11. a) T. Ziegler, A. Rauk, *Inorg. Chem.* **1979**, *18*, 1755. b) T. Ziegler, A. Rauk, *Inorg. Chem.* **1979**, *18*, 1558.

12. The calculated excitation energy $X^3\Sigma_g^{-1}\Delta_g$ for Ge_2 at BP86/TZ2P is 18.0 kcal/mol which is somewhat higher than the experimental value of 9.5 kcal/mol[8].

4.1.5 Theoretical Study of Divalent Si(0) Compounds

Nozomi Takagi and Gernot Frenking
Fachbereich Chemie, Philipps-Universität Marburg

Successful theoretical research for divalent carbon(0) compounds opened a new area of carbon chemistry [1]. Divalent carbon(0) compounds are considered to have the general formula CL_2 which possess two L→C donor-acceptor bonds and two lone-pair MOs with π and σ symmetry that are localized at carbon atom. Owing to the two lone-pair MOs, divalent carbon(0) compounds have extremely large 2nd proton affinity (PA). It is expected that divalent carbon(0) compounds could be interesting ligands for transition-metal compounds to make new class of complexes.
In the following studies, we answer the question, "Is divalent E(0) chemistry restricted only for carbon compounds?" from a quantum chemical view point.

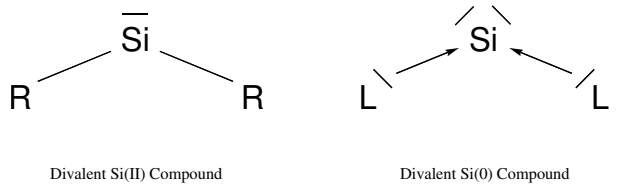

Density functional calculations at the BP86/TZVPP level for the silicon homologues SiL_2 suggest that the molecules **1Si** – **5Si** have strong divalent silicon(0) character, which possess two L→Si donor-acceptor bonds and two lone-pair MOs with π and σ symmetry at silicon atom (Figure 1). This bonding interpretation explains the theoretically predicted large values of the 1st and 2nd PAs (Table 1). There is significant correlation between the 1st PAs and the HOMO (π lone-pair) energies of Si(0) compounds, and the 2nd PAs and the HOMO energies of singly-protonated Si(0) compounds respectively (Figure 2). The calculations predict the first protonation takes place at the energetically higher-lying π lone-pair orbital, whereas it does at the σ-position for the carbon(0) homologues [2].

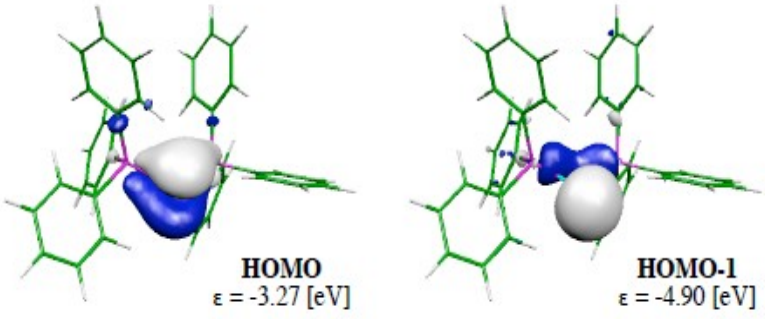

Figure 1. Pictures of the lone-pair orbitals with π ans σ symmetry for the divalent Si(0) compound **1Si**.

From this view point, the recently reported "*trisilaallene*" which has resemble structure to **4Si** is probably better considered as a divalent Si(0) compound rather than an allene compound, owing to the calculated large 1st (257.9 kcal/mol) and 2nd (187.2 kcal/mol) PAs. The theoretical values for the Si-Si distance R1 (2.230Å) and bond angle A1 (135.7°) are very good agreement with the experimental values of 2.177 - 2.188Å and 136.5°. We proposed the name "*silylone*" for the compounds, which distinguish them from the divalent Si(II) compounds *silylene* [2].
We also found that the chemistry of divalent element E(0) is widely applicable not only for carbon and silicon, but also germanium, tin, and lead [3].

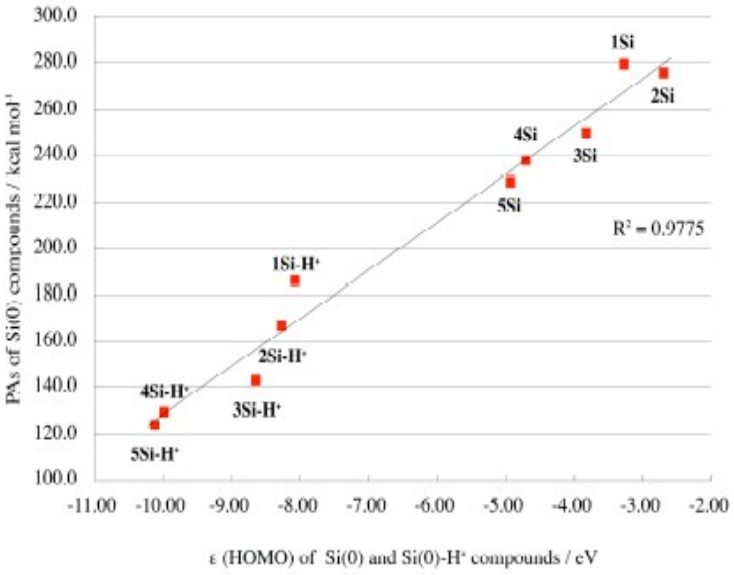

Figure 2. Correlation between the 1st PAs and the HOMO of Si(0) compounds, and the 2nd PAs and HOMO of Si(0)-H^+ compounds.

	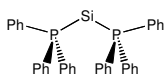 **1Si**	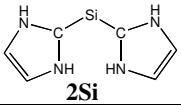 **2Si**	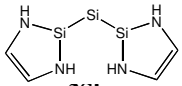 **3Si**	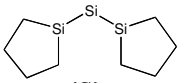 **4Si**	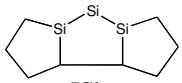 **5Si**
$R1_{Si\text{-}L}$ [Å]	2.266	1.869	2.232	2.241	2.262
$R2_{L\text{-}L}$ [Å]	3.506	2.755	2.675	2.775	2.568
$A1_{L\text{-}Si\text{-}L}$ [°]	101.4	95.0	73.6	76.5	69.2
ε (π) [eV]	-3.27	-2.69	-3.82	-4.70	-4.93
ε (σ) [eV]	-4.90	-4.36	-6.52	-5.90	-5.90
q(Si)	-0.32	0.15	-0.39	-0.15	-0.08
1st PA (298.15K)	279.4	275.9	249.7	237.9	228.8
2nd PA (298.15K)	186.0	166.7	142.9	129.3	123.9

Tabelle 5.1: *Calculated bond lengths and angles, orbital energies of π- and σ-lone-pair orbitals, and NBO partial charges at the central Si atoms for* ***1Si*** *–* ***5Si*** *at BP86/TZVPP level. First and second proton affinities (PAs) at 298.15K are in kcal/mol.*

References

1. R. Tonner, F. Öxler, B. Neumüller, W. Petz, G. Frenking, *Angew. Chem. Int. Ed.* **2006**, *45*, 8038. (b) R. Tonner, G. Frenking, *Angew. Chem. Int. Ed.* **2007**, *46*, 8695.
2. N. Takagi, T. Shimizu, G. Frenking, *Chem. Eur. J.* **2009**, *15*, 3448.
3. (a) N. Takagi, T. Shimizu, G. Frenking, *Chem. Eur. J.* **2009**, *15*, 8593. (b) N. Takagi, G. Frenking, *in preparation.*

4.1.6 Difference in solid-liquid interfacial tension between hydrophobic and hydrophilic solid surfaces by Molecular Dynamics simulations

Frédéric Leroy, Arbeitsgruppe Prof. Dr. Müller-Plathe
Eduard Zintl Institut für Anorganische und Physikalische Chemie, Petersenstr. 20, 64283 Darmstadt
Technische Universität Darmstadt

The knowledge of solid-liquid interfacial tension is of major importance in applications involving wetting properties of a solid surface or adhesion properties of a liquid.[1] Heat transfer through solid-liquid interfaces was also found to depend on thermodynamic interfacial quantities.[2] Therefore, the determination of those quantities has a particular relevance.
When a liquid is partially wetting a solid, a contact angle can be defined.[3] The contact angle θ (see Fig. 6.1) is related to all the surface tensions in the system, namely the liquid-vapor, the solid-vapor and the solid-liquid surface tensions through Young's equation:

$$\cos\theta = \frac{\gamma_{sv} - \gamma_{sl}}{\gamma_{lv}} \qquad (4.1)$$

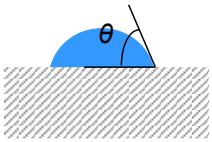

Abbildung 6.1: *Young's equation and contact angle of a liquid droplet on top of a solid surface*

The contact angle is probably the quantity the most employed in order to quantify the affinity of a liquid for a solid surface since it is easily accessible by experimental methods. However, simulation of a liquid droplet from which one can extract the value of a contact angle that can be compared to its macroscopic value requires the use of systems that are large enough. This constraint arises from the fact that a droplet which is too small might have a large tension at its three-phase contact line. This has an influence on the contact angle, and therefore the result obtained in the related condition of line tension might differ from the contact angle value when the line tension plays a less important role. Moreover, employing large systems goes along with intensive calculations when the complexity of the system is increased.
At least, surface tensions determine whether a solid is totally or partially wettable. Therefore their determination is useful even outside the frame of contact angle computation. We have recently compared the contact angle of a liquid droplet on different surfaces having different interaction strength with the liquid. We found that the contact angle variations mainly depended on the variation of the solid-liquid surface tension if the solid had loose interactions with the liquid. The solid-vapor surface tension had a negligible contribution in that situation.[4] It is also expected that solid-vapor surface tension plays a minor role in the determination of the contact angle when the liquid has a low vapor density. We conclude that the knowledge of the variations of the solid-liquid surface tension with respect to an exchange of the nature of the solid surface is a good indicator of how the wetting properties of a liquid will change from one surface to another without reference to the contact angles.
Although intensive work lead to several algorithms useful to compute fluid-fluid surface tensions,[5] the solid-liquid surface tension computation by means of molecular simulations is still an ongoing task. We have recently developed an algorithm that allows one to go further in that challenging issue.[6] Major strengths of our algorithm are its simple implementation in Molecular Dynamics (MD) codes. For instance, it does not depend on the microscopic definition of pressure, which is a major issue in surface tension calculations. Also, it can be applied to systems where the solid layer can be modeled with all its degrees of freedom in contrast to calculations where the solid is modeled with a static external field. Moreover, the algorithm enables calculations where the solid surface has small dimensions.
Up to now the algorithm has mainly been applied to model systems where only van der Waals forces were used. Preliminary results showed its applicability in the frame of the comparison of solid-liquid surface tension calculations of water on smooth and rough graphite surfaces (see Fig. 6.2).

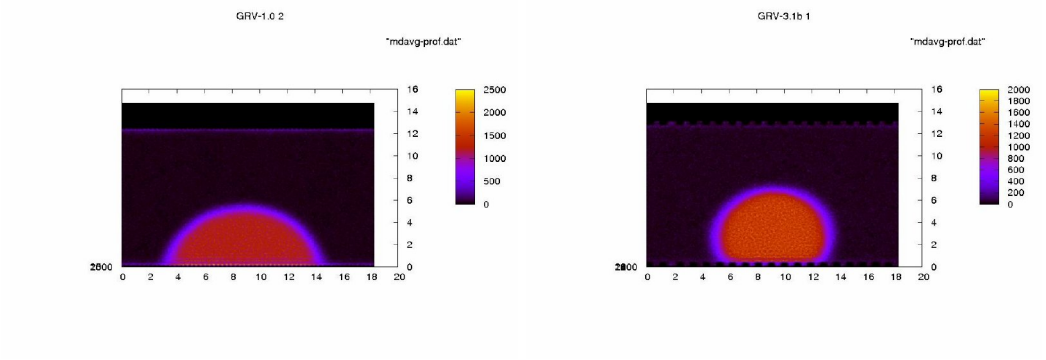

Abbildung 6.2: *Water droplet on a smooth (left) and rough (right) graphite surface*

It is the aim of the present project to systematically apply the algorithm to systems corresponding to other realistic situations. We will use self-assembled monolayers with a broad range of surface chemistries from hydrophobic to hydrophilic in order to sample different characteristics of surface wettability. We will employ classical MD simulations of water on top of a monolayer of crystalline structure based on *n*-eicosane. We will tune the hydrophilic-hydrophibic character of surfaces by replacing the methyl head groups by -CH_3, -OCH_3, -$CONHCH_3$, -CN, -$CONH_2$ and –OH. The difference in solid-liquid surface tension of those systems with respect to a reference system will be obtained. It will yield a quantitative comparison of solid-liquid surface tensions for those systems. There exists no such comparison in the literature.
The study requires intensive calculations. We estimate the total amount of computation time to 5000 CPU hours. The OpenMP version of the YASP MD[7] code which is already installed in the HRZ computer will be used to carry out the computations.

References

1. *Surface and Interfacial Tension. Measurement, Theory, and Applications*, edited by S. Hartland (Marcel Dekker, New York, 2004), Vol. 119.

2. N. Shenogina, R. Godawat, P. Keblinski, and S. Garde, Physical Review Letters **102** (15) (2009).

3. P. G. de Gennes, F. Brochart-Wyart, and D. Quéré, *Capillarity and Wetting Phenomena. Drops, Bubbles, Pearls, Waves.* (Springer, New-York, 2004).

4. F. Leroy and F. Müller-Plathe, to be submitted.

5. G. J. Gloor, G. Jackson, F. J. Blas, and E. de Miguel, Journal of Chemical Physics **123** (13) (2005).

6. F. Leroy, D.J.V.A. dos Santos, and F. Müller-Plathe, Macromolecular Rapid Communications **30** (9-10), 864 (2009).

7. K.B. Tarmyshov, and F. Müller-Plathe, Journal of Chemical Informations and Modeling **45** (6), 1943 (2005).

4.1.7 Band Gap Tuning in Nanodiamonds: First Principle Computational Studies

Andrey A. Fokin and Peter R. Schreiner
Institute of Organic Chemistry, Justus-Liebig University, Heinrich-Buff-Ring 58, 35392 Giessen, Germany

Nanodiamonds are nm-sized single-molecule diamond-like hydrocarbons that close the gap between chemistry, physics, and the material sciences. They represent the long underrated world of sp^3 carbon materials that have complementary properties to the nowadays ubiquitous fullerenes and carbon nanotubes. We present a density functional theory study on changes in band gap effects of nanodiamonds (hydrogen terminated diamond-like molecules, diamondoids) depending on size and shape. Octahedral and tetrahedral nanodiamonds show the same trends in band gap narrowing, and it is the dimension rather than the shape/morphology of the nanodiamonds that alters the band gaps.

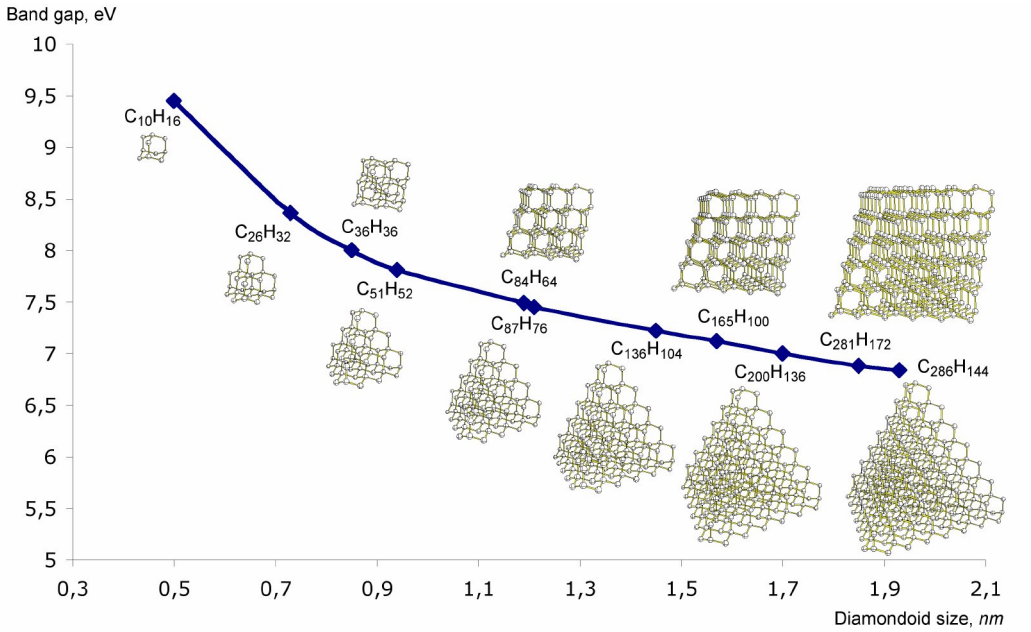

Abbildung 7.1: *The dependence of the band gap of hydrogen-terminated nanodiamonds on particle size (B3LYP/6-31G(d), the surface hydrogens are omitted for clarity).*

Remarkably, the band gap of bis-diadamantyl narrows only slightly relative to that of diamantane (8.8 vs 9.0 eV) despite a doubling of the dimensions of the molecule to 0.8 nm; a band gap of ca 8 eV may have been expected for a diamondoid of that size from the above dependence. We also computed the dimer of tetramantane and found that the band gap in this ca 1.8 nm structure is 8.4 eV, close to that of the parent monomeric hydrocarbon (8.6 eV). These observation allow us to predict that agglomeration of nanodiamond particles, despite a formal increase in size, will show only little quantum confinement effects. This may limit electronic applications of traditional nanodiamond, which consists of conglomerates, whose separation represents a formidable challenge. Thus, clustering of diamondoids apparently does not lead to substantial additive band-gap lowering as shown for the diamondoid dimers; this is also evident from most recent computations on diamondoid crystals.

We also studied the band gap tuning through external (by C–H bond substitution) or internal (by replacing CH or CH_2 moieties) doping is non-additive for the same dopant. We computed the band gaps for a number of preparatively available mono- and disubstituted diamantanes as a model for "external" doping by substitution.

Substitution with alkyl, perfluoroalkyl groups as well as with fluorine increases the band gap in diamantane derivatives mostly due to stabilization of the occupied states (the HOMOs are downshifted by up to 0.03 au). While fluorination of nanodiamond was considered as very promising for several applications, we conclude, however, that the undesired insulating properties of nanodiamond materials will only increase after fluorination of the surface.
A substantial decrease of the band gap of dimantane was achieved through incorporation of amino-, nitro-, and phenyl-functionalities. The substitution effects are not additive since the mono- and dinitroderivatives display similar valies. The most electron-withdrawing group dominates the electronic properties of the substituted diamondoids. With nitro substitution the band gap of dimantane can be reduced to ca. 6 eV. Outstanding semiconductor properties may be expected for the highly polarized betaine structure of the formal bis-apical amino acid derivative of diamantane.
The semiconductor properties of natural bulk diamond are determined by trace amounts of nitrogen (type I) or boron (type II) impurities. Modeling these effects by placing the dopant atom in the center of spherical diamond nanocrystals largely leads to unstable structures. In contrast, substitutional internal doping in diamondoid does give rise to stable molecules. We first computed the band gap for the parent heteroadamantanes with oxygen, nitrogen as well as sulfur as n-, and boron as p-dopants. While the HOMO of n-doped structures mostly describe the n-electrons of the heteroatom, the empty *p*-orbital of boron interacts strongly with the diamondoid LUMOs. Remarkably, interstitial doping dramatically reduces the band gap down to about 7 eV for the sulfur and boron derivatives. Several questions arise: *i*) how does such internal doping influence the band gap for larger diamond particles, *ii*) are these effects additive and do they depend on the position of the dopant, and *iii*) to what extend do conducting and valence bands shrink upon enlarging the particles, *i. e.,* what is the degree of mixing of the carbon and heteroatom orbitals. To answer these questions we fully optimized a number of diamantane and triamantane derivatives at B3PW91/6-31G(d,p). Internal doping of two different CH positions of the cage of diamantane reduces the band gap almost equally relative to the undoped molecule; the substitution of the CH_2 moieties reduces the band gap to a lesser extent. Importantly, double doping virtually provides no additional effect as compared to the incorporation of only one dopant this will make the preparation of such molecules less challenging. In agreement with data for the adamantane derivatives, doping with oxygen is less effective, while sulfur and boron incorporation is more effective than *N*-doping. The most pronounced effect was found for push-pull doping with boron and nitrogen that reduces the band gap of diamantane to that of bulk diamond.
We conclude, that well-defined nanodiamonds display strong quantum confinement effects at particle sizes from 0.5 to at least 2 nm, when their band gaps are reduced to 6.7 eV, which is likely to be still much wider than that of bulk diamond. Octahedral and tetrahedral nanodiamonds show the same trends in band gap narrowing, and it is the dimension rather than the shape/morphology of the nanodiamonds that affects the band gaps. Clustering of diamondoids apparently does not lead to substantial additive band-gap lowering as shown for the diamondoid dimers; this is also evident from most recent computations on diamondoid crystals.
Band gap tuning through external (by C–H bond substitution) or internal (by replacing CH or CH_2 moieties) doping is non-additive for the same dopant. However, push-pull doping, with electron donating and electron withdrawing groups is most effective and reduces the band gap of diamondoids to that of bulk diamond. Further reductions down to 1–2 eV are conceivable with charged external substituents. The combination of increasing the size of the nanodiamond and push-pull doping are likely to make these materials highly valuable for semiconductor applications.

Verweise

1. Fokin, A. A.; Schreiner, P. R. *Mol. Phys.* **2009**, *107*, 8–12, 823–830.

4.1.8 Computational characterization of novel phenylhydroxycarbenes

Dennis Gerbig and Peter R. Schreiner
Intitut für Organische Chemie, 35392 Giessen

This research program combines the preparation, detection, and spectroscopic as well as computational characterization of novel phenylcarbenes of the hydroxycarbene type exhibiting hydrogen tunneling under large barriers at low cryogenic temperatures (down to 10 K). The very low temperatures and the noble gas environment of cryogenic matrices are ideally suited for quantum chemical reaction rate and tunneling studies on single ground-state energy hypersurfaces. The proposed matrix isolation reactions are expected to pave the way for new experiments and, when augmented with sophisticated electronic structure computations (modern **density-functionals**, like the M06 suite, as well as **coupled-cluster techniques**) should shed light on the factors that govern quantum mechanical tunneling under large barriers on timescales of minutes to days.

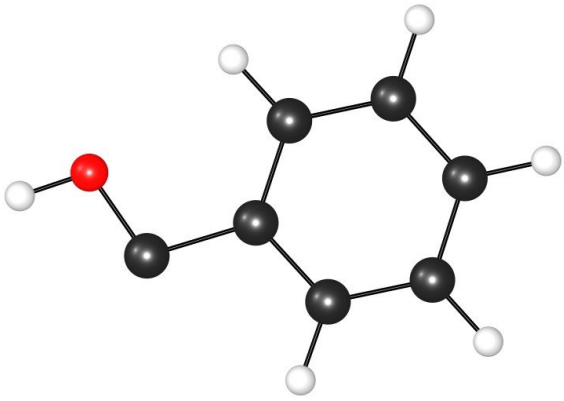

Abbildung 8.1: *Phenylhydroxycarbene, parent of all arylhydroxycarbenes*

Electronic and structural effects will be addressed in order to elucidate the exact quantum tunneling mechanism. Questions the proposed research aims to answer include:

1. how do electronic substituent effects alter the rates of H-tunneling in novel *para*- and *ortho*-phenylhydroxy carbenes;

2. how large a barrier can be afforded for observable H-tunneling; and

3. can hydrogen bonding be used to tune the rate of H-tunneling or even to completely suppress it?

Novel aspects of the proposed research program include:

1. systematic preparation of a series of electronically related substituted, currently yet unknown *para*- and *ortho*-phenylhydroxy carbenes;

2. development of synthetic routes to substituted hydroxycarbenes and their precursor substances;

3. studying the electronic effects on tunneling, utilizing the most advanced levels of quantum chemistry (including **high-level calculations with coupled-cluster theory**);

4. measurement and characterization of vibrational spectra of the obtained carbenes.

Verweise

1. Schreiner, P. R.; Reisenauer, H. P.; Pickard, F. C.; Simmonett, A. C.; Allen, W. D.; Mátyus, E.; Császár, A. G. Capture of hydroxymethylene and its fast disappearance through tunneling, *Nature*, **2008**, *453*, 906-909.

2. Bucher, G. Hydroxycarbene: watching a molecular mole at work, *Angew. Chem. Int. Ed. Engl.* **2008**, *47*, 6957-6958.

3. Bartlett, R. J.; Musial, M. Coupled-cluster theory in quantum chemistry, *Rev. Modern. Phys.* **2007**, *79*, 291-352.

4. Zhao, Y.; Truhlar, D. G. Density functionals with broad applicability in chemistry, *Acc. Chem. Res.* **2008**, *41*, 157-167.

5. Gerbig, D.; Reisenauer, H. P.; Wu, C.-H.; Allen, W. D.; Ley, D.; Schreiner, P. R. Phenylhydroxycarbene, **2009**, manuscript in preparation

4.1.9 Modellierung von Atom-Molekülreaktionen

Jörg Glatthaar
Institut für Organische Chemie, FB08 Biologie und Chemie, Justus-Liebig-Universität Gießen

Im Rahmen einer internationalen Zusammenarbeit mit Prof. Dr. Yuan Pern Lee, National Chiao Tung University, Hsinchu City,Taiwan über Untersuchungen der Reaktion von Silizium- und Germanium-Atomen mit Stickstoffmonoxid N_2O wurden begleitend zu den experimentellen Studien (Matrixisolationsspektroskopische Untersuchungen an der JLU Gießen sowie an der National Chiao Tung University im Rahmen eines visiting assistant professorship vom April 2008 bis April 2009) quantenmechanische Rechnungen unter partieller Nutzung der Rechnereinheit „quad“ am CSC in Frankfurt durchgeführt.

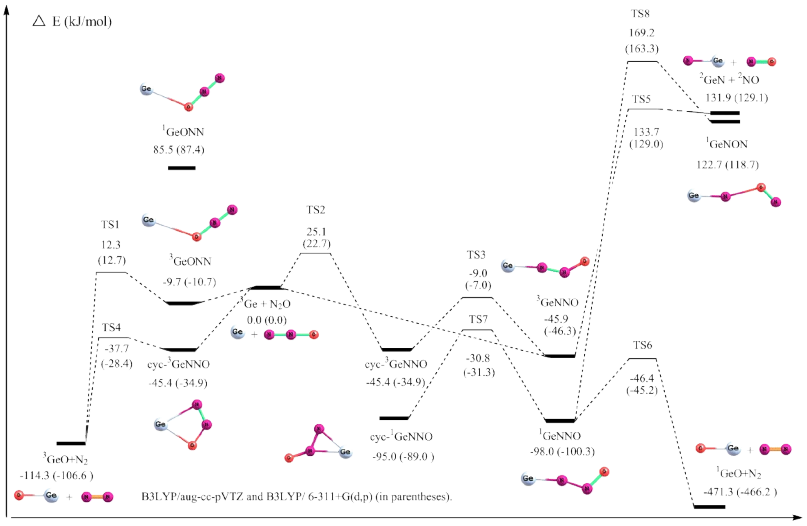

Abbildung 9.1: *Die GeN_2O-Energiehyperfläche*

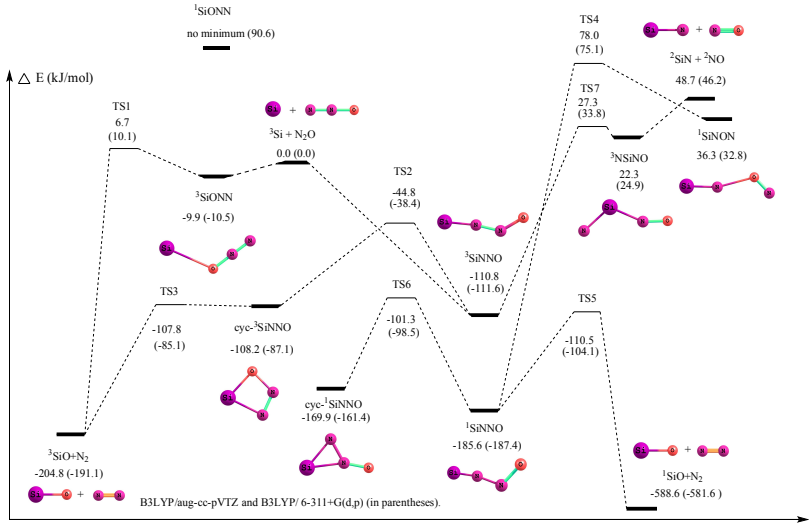

Abbildung 9.2: *Die N_2OSi-Energiehyperfläche*

In der Entwicklung neuer Halbleiter-Elektronik-Bauteile gewinnt die Erzeugung dünner, Stickstoff-dotierter Schichten auf der Basis von Germanium- bzw. Siliziumoxiden an Bedeutung. Bei der Erzeugung dieser Schichten wird vielfach elementares Germanium oder Silizium in Gegenwart von NO oder N_2O[2] zur Reaktion gebracht. Grundlegende Erkenntnisse über die Primär-Reaktionen, die zum Aufbau dieser dotierten Oxid-Schichten führen, sollten experimentell mit Hilfe der Matrixisolationstechnik kombiniert mit quantenchemischen Rechnungen nachgestellt werden.
Erstmals konnten die Energiehyperflächen mit Hilfe von Dichtefunktional-Rechnungen beschrieben werden und die Aussagen über die Stabilität, elektronische Eigenschaften und Reaktivitäten der verschiedenen stabilen Strukturen gewonnen werden.
In der Reaktion zwischen Germanium-Atomen und N_2O wurden neben GeO und N_2 weitere 3 stabile GeN_2O-Isomere identifiziert, ^{1}GeNNO, ^{3}GeONN, sowie das cyc-^{1}GeNNO, eine Verbindung, die einen gespanntes GeNN-Dreiring Strukturmotiv aufweist. In der Reaktion zwischen Silizium-Atomen und N_2O wurden neben SiO und N_2 weitere 2 stabile N_2OSi-Isomere identifiziert, ^{1}SiNNO, sowie das cyc-^{1}SiNNO, eine Verbindung mit einem gespannten SiNN-Dreiring, die über eine photochemisch induzierte Umlagerung von ^{1}SiNNO erzeugt werden konnte.
Die eindeutige Zuordnung der genannten, erstmals nachgewiesenen Verbindungen anhand ihrer IR-Absorptionsmuster gelang mit Hilfe von gezielten Isotopenmarkierungsversuchen mit $^{14}N^{15}NO$, $^{15}N^{14}NO$ sowie dem doppelt markierten $^{15}N^{15}NO$. Außerdem konnten Ge-N bzw. Si-N Bindungen anhand der typischen Germanium- bzw. Silizium-Isotopenaufspaltungsmuster auf der Basis der natürlichen Isotopenzusammensetzung der beiden Elemente identifiziert werden. Dies war nur möglich auf der Basis umfangreicher quantenchemischer Berechnungen der kompletten Aufspaltungsmuster aller möglichen stabilen Isotopomere unter Verwendung sowohl harmonischer als auch anharmonischer Schwingungspotential-funktionen. Während für die Berechnungen der Energien die Methode/Basis-Satz-Kombination B3LYP/aug-cc-pVTZ verwendet werden konnte, lieferte die Kombination B3LYP/6-311+G(d,p) die geringsten Abweichungen bei der Berechnungen der Schwingungspotentiale. In allen Rechnungen wurde das Germanium-Atom mit Hilfe eines Pseudopotentials (Wood-Boring quasi relativistic effective core potential (ECP) MWB28) beschrieben.

Literatur

1. Z.-M. Jiang, J. Glatthaar, Y.-P. Lee. *J. Chem. Phys.* **2009**, *131*, 144504.
2. J. Glatthaar, Z.-M. Jiang, Y.-P. Lee. *J. Chem. Phys.,* Manuskript in Vorbereitung.
3. L. K. Bera, W. K. Choi, C. S. Tan, S. K. Samanta, C. K. Maiti, *IEEE Elec. Dev. Lett.* **2001**, *22*, 387.

4.1.10 Structural Analyses of N-Acetyl-DMAP salts

Volker Lutz and Peter R. Schreiner
Institute of Organic Chemistry, Justus-Liebig University, Heinrich-Buff-Ring 58, 35392 Giessen, Germany

Since the introduction of 4-(dimethylamino)pyridine (DMAP, **1**) as acetylation catalyst for alcohols and amines in the late 1960ies,[1, 2] the mechanisms of these reactions have been debated. Thus, we studied the formation of several N-acetyl-DMAP salts **2a** − **d**, which are considered to be the catalytic active species in DMAP-catalyzed acetylation reactions of alcohols (Scheme 1).

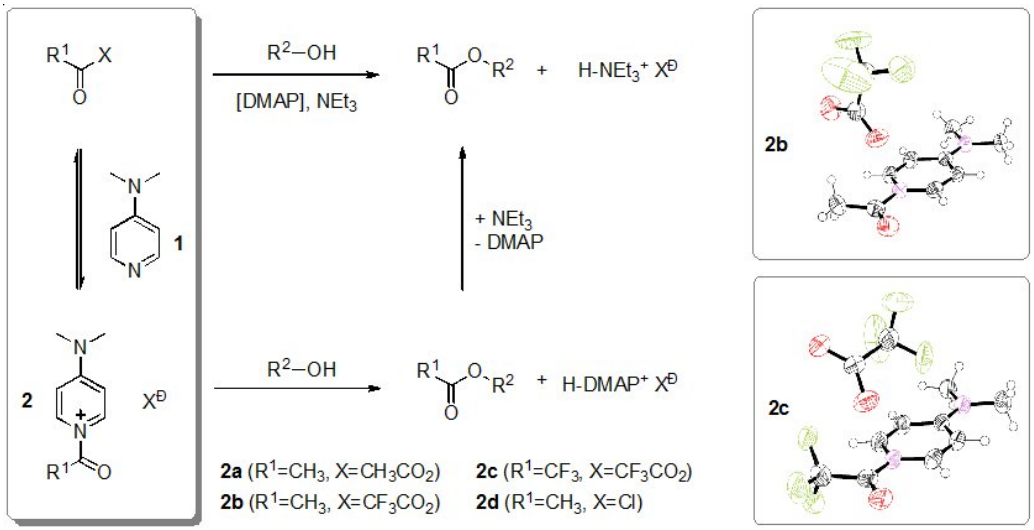

Abbildung 10.1: *Formation of N-acetyl-(4-dimethylamino)pyridinium salts (2) in the mechanism of DMAP catalysis.*

Combined crystal structure analyses, variable temperature matrix IR and NMR spectroscopy as well as computational techniques at the UAHF-PCM-B3LYP/6-311+G(d,p)//B3LYP/6-31G(d) level of theory were utilized to examine the structures and dynamics of salt formation.[3] We see clear evidence for the formation of tight ion pairs that are stabilized by dynamic hydrogen bonding interactions. In contrast to **2b** − **d**, that can be isolated from unpolar solvents, the nucleophilicity of the acetate **2a** only allows a steady-state concentration smaller 1% at room temperature. Therefore, it's nevertheless high catalytic activity must involve additional interactions with alcohols: Expanding the concept of hydrogen bonding, the ability of an anion to guide the alcohol towards the reaction center increases if it acts as an anchor developing hydrogen bonding contacts to the pyridine ring. Thus, we propose bidentate carboxylates such as acetate and trifluoroacetate to be the key stabilization factor in subsequent acetylations.

References

1. a) W. Steglich, G. Hoefle, *Angew. Chem. Int. Ed. Engl.* **1969**, *8*, 981; b) L. M. Litvinenko, A. I. Kirichenko, *Dokl. Akad. Nauk SSSR* **1967**, *176*, 197-100; c) G. Hoefle, W. Steglich, *Synthesis* **1972**, 619-621.
2. a) G. Höfle, W. Steglich, H. Vorbrüggen, *Angew. Chem. Int. Ed.* **1978**, *17*, 569-583; b) E. Guibe-Jampel, G. Le Corre, M. Wakselman, *Tetrahedron Lett.* **1979**, 1157-1160; c) S. J. Xu, I. Held, B. Kempf, H. Mayr, W. Steglich, H. Zipse, *Chem. Eur. J.* **2005**, *11*, 4751-4757.
3. V. Lutz, J. Glatthaar, C. Wuertele, M. Serafin, H. Hausmann, P. R. Schreiner, *Chem. Eur. J.* **2009**, *15*, 8548-8557.

4.1.11 Phosphine und Phosphinoxide

Mareike M. Machuy und Peter R. Schreiner
Institut für Organische Chemie, Justus-Liebig-Universität Gießen

Basierend auf der präparativen Darstellung von Phosphinen und Phosphinoxiden mit Diamantylliganden wurden diese Strukturen in einer homologen Reihe, ausgehend vom jeweiligen Methylphosphin/Methylphosphinoxid bis hin zum Diamantylphosphin/ Diamantylphosphinoxid (Abb. 11.1), um eine Tendenz der sich mit den Liganden veränderenden Bindungslänge zwischen Phosphor und Kohlenstoff festzustellen.

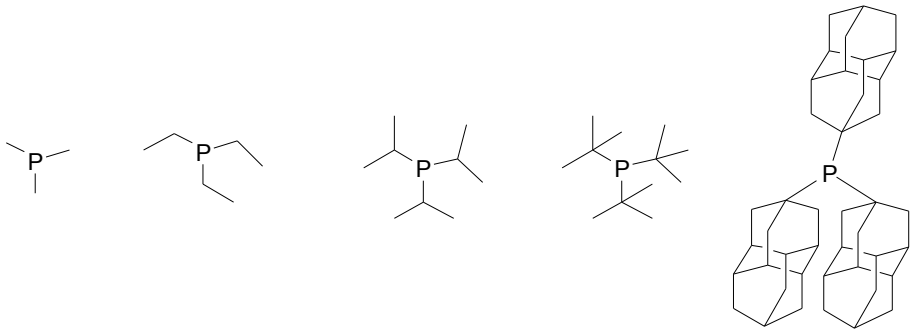

Abbildung 11.1: *Phosphine*

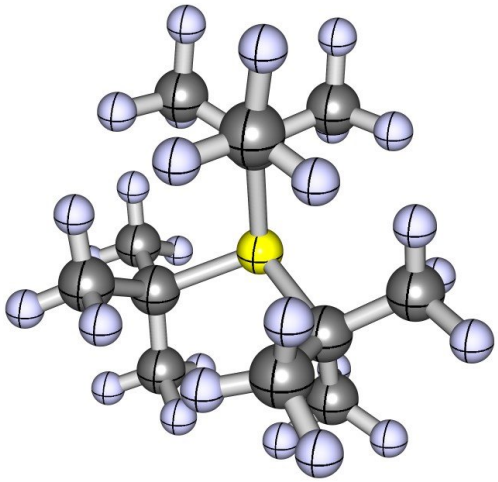

Abbildung 11.2: *Tri-tert-Butylphosphinoxid*

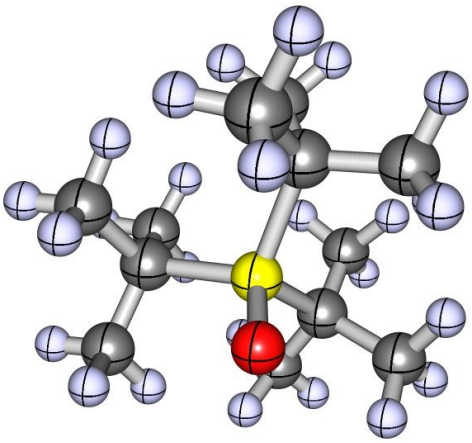

Abbildung 11.3: *Tri-tert-Bulylphosphin*

Ein weiterer Aspekt sind die Toleman-Cone-Angles dieser Verbindungen, die etwas über deren stereoelektronische Eigenschaften als Liganden aussagen. Um evtl. im Folgenden dann auf die Reaktivität der einzelnen Phosphine/Phosphinoxide als Cokatalysatorsysteme schließen zu können. Die Voroptimierung der Geometrie dieser Strukturen wurde anhand empirischer Rechenmethoden (molecular mechanics) durchgeführt. Danach wurde für die Optimierung auf Dichtefunktionaltheorie (DFT)- Methoden (M06-2X) zurückgegriffen;als Basissatz wurde 6-311G(d,p) gewählt.

Verweise

1. A. Fleckenstein, H. Plenio, *Chem. Soc. Rev.*, 2010, DOI: 10.1039/b903646f
2. C. A. Tolman, *Chemical Reviews,* 1977, **77**, 313-348

4.1.12 Investigation of the Addition of C and Si to CH_4 and SiH_4 The Role of Quantum Mechanical Tunneling in the Reaction of C + CH_4 and C + H_2O

Michael L. McKee
Institut für Organische Chemie der Justus-Liebig-Universität Giessen

The reaction profiles for addition of atomic carbon and silicon to methane and silane were investigated at the CCSD(T)/aug-cc-pVTZ level of theory. The results are quite different from a previously published studied[1] but in accord with recent matrix isolation studies. The intrinsic reaction coordinate (IRC) was computed for the reaction of C + CH_4 and C + H_2O. We are investigating the role of quantum mechanical tunneling in the reactions. The IRC has been computed at the M062X/aug-cc-pVTZ level for both reactions (Figure 1) and will be repeated at the more reliable (but more computer intensive) CCSD(T)/aug-cc-pVTZ level. Vibational frequencies will be computer at every point and used to compute the rate of reaction with tunneling effects included.

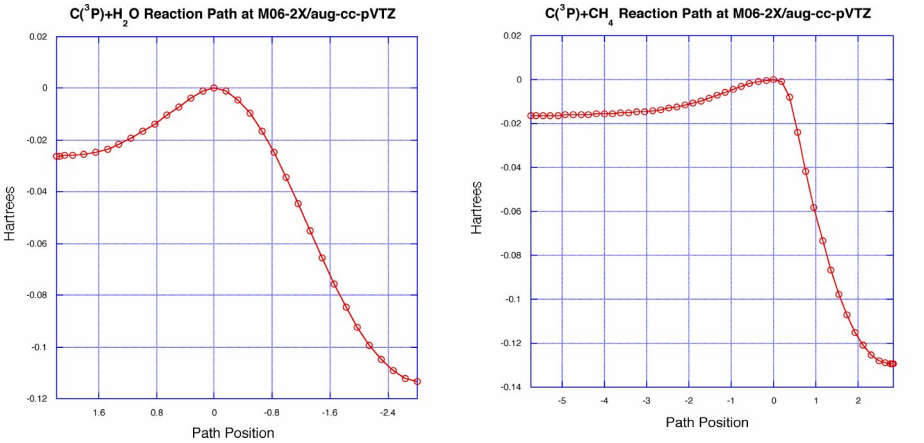

Abbildung 12.1: *Computed IRC for C + CH_4 (right) and C + H_2O (left).*

References

1. "Theoretical Studies of the Insertion Reactions of Atomic Carbon and Silicon into Methane and Silane" S. Sakai, J. Deisz, and M. S. Gordon *J. Phys. Chem.* **1989**, *93,* 1888-1893.

4.1.13 Photochemische Umwandlungen von Molekülen der Formel CH_2OS

Dr. Hans Peter Reisenauer
Institut für Organische Chemie, Justus-Liebig-Universität Gießen

Alle vorstellbaren Mitglieder der Familie der CH_2OS Isomeren, einschließlich beiden bislang bekannten und durch spektroskopische Methoden nachgewiesenen Molküle Sulfin (**1**) [1)] und Monothioameisenäure (**4**) [2)], sind hochreaktiv und daher unter normalen Laborbedingungen nicht fassbar. Unter Hoch-Vakuum-Bedingungen oder isoliert in festen Edelgasen (Matrixisolation) sollten sie jedoch langlebig genug sein, um durch spektroskopische Untersuchungen nachgewiesen werden zu können. Ziel unserer Untersuchungen war der Existenznachweise weiterer CH_2OS Isomeren ,insbesondere des unsubstituierten Oxathiirans (**3**), da Derivate dieser Verbindungsklasse bei der direkten Episulfidierung von Olefinen als reaktive Intermediate diskutiert werden, aber bisher noch nicht nachgewiesen werden konnten.[3)]
Zum Einstieg in die CH_2OS-Energiehyperfläche haben wir Sulfin (**1**) gewählt, das durch die thermische Spaltung seines Dimeren im Hochvakuum erzeugt und bei 10 K in festem Argon isoliert wurde. Anschließend untersuchten wir seine Photochemie bei unterschiedlichen Anregungsenergien. Der zeitliche Verlauf der initierten photochemischen Umwandlungen in andere Isomere wurde durch FTIR- und UV/Vis-Spektroskopie verfolgt.

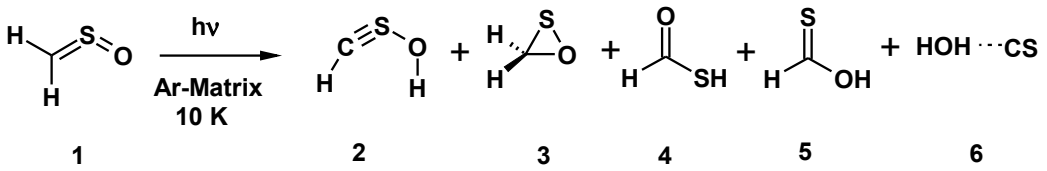

Abbildung 13.1: *Photochemische Umwandlung von Sulfin (1) bei 10 K in festem Argon in andere CH_2 OS Isomere (2 – 6)*

Die aussschließlich auf IR-Spektren beruhende Identifikation der neugebildeten Strukturen setzt eine möglichst genaue Vorhersage der Schwingungsspektren der potentiellen Kandidaten voraus. Wir haben daher alle vorstellbaren Moleküle der Summenformel CH_2OS mit verschiedenen *ab initio*-Methoden, bis hin zu CCSD(T)-Niveau unter Verwendung eines cc-pVTZ-Basissatzes berechnet und mit den experimentellen Daten verglichen.

Wir fanden, dass bei Verwendung von energiereichem Anregungslicht der Wellenlänge 254 nm hauptsächlich H-C≡S-O-H (**2**) gebildet wird.[3)] Für die äußerst ungewöhnliche Struktur dieses Moleküls, das einen sehr kurzen CS-Abstand aufweist und der formal einer Dreifachbindung entspricht, gab es bisher nur wenige Beispiele.
Verwendeten wir anstelle von 254-nm-Licht eine energieärmere Anregungsstrahlung (313 nm), so zeigte sich eine viel komplexere Produktverteilung. **2** wird nur noch in geringem Maße gebildet. Hauptkomponente ist das bisher nicht beschriebene Oxirathiiran (**3**), das allerdings selber photolabil ist und zu den Monothioameisensäuren **4** und **5**, sowie zum einem Komplex zwischen Wasser und CS (**6**) umgelagert wird. Langzeit Bestrahlungen führen schließlich zur vollständigen Spaltung in kleine Bruchstücke wie CO, COS, H_2S und H_2.

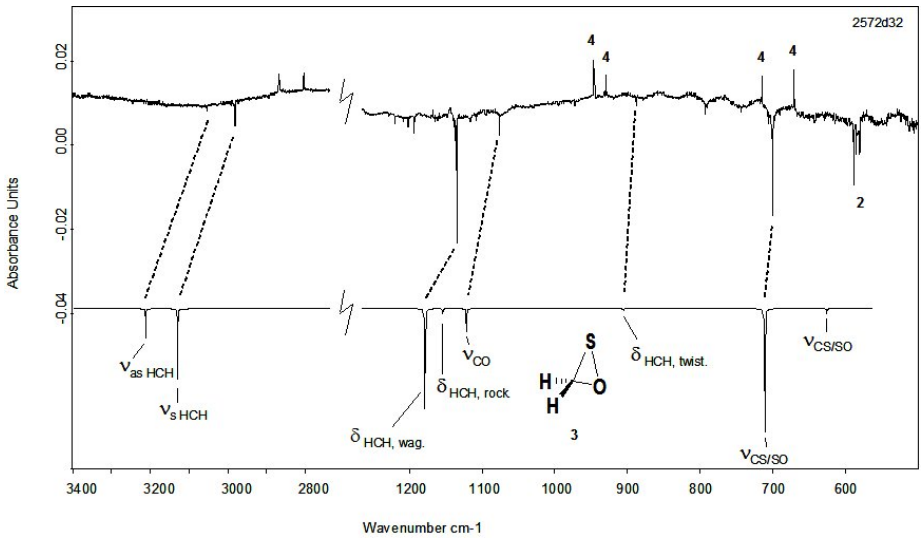

Abbildung 13.2: *Vergleich des berechneten IR-Spektrums (CCSD(T)/cc-pVTZ, unten) von Oxathiiran (**3**) mit dem Experiment (oben). Das experimentelle Spektrum ist das Differenzspektrum der photochemischen Umwandlung von **3**⇒**4** mit Licht der Wellenlängen $\lambda > 360$ nm.*

Verweise

1. E. Block, R. E. Penn, R. J. Olsen, and P. F. Sherwin, *J. Am. Chem. Soc.* **1976**, *98*, 1264; R. E. Penn, and R. J. Olsen, *J. Mol. Spectrosc.* **1976**, *61*, 21; E. Block, E. R. Corey, R. E. Penn, T. L. Renken, P. F. Sherwin, H. Bock, T. Hirabayashi, S. Mohmand, and B. Soluki. *J. Am. Chem. Soc.* **1982**, *104*, 3119–3130.

2. W. H. Hocking, and G. Winnewisser, *Z. Naturforsch. A*, **1976**, *31*, 422–436; 438–453; 95–1001; *ibid*, **1977**, *32*, 1108-1118; H. O. Kalinowski, W. H. Hocking, and B. P. Winnewisser, *J. Chem. Res.*, **1978**, 260–261.

3. W. Adam, B. Fröhling, K. Peters, and S. Weinkötz, *J. Am. Chem. Soc.* **1998**, *120*, 8914–8919; W. Adam, R. M. Bargon, and G. Mloston, *Eur. J. Org. Chem.*, **2003**, 4012–4015.

4. P. R. Schreiner, H. P. Reisenauer, J. Romanski, and G. Mloston, *Angew. Chem. Int. Ed.*, **2009**, *48*, 1–5.

4.1.14 Computational Studies on Asymmetric Hydrogenation of Ketimines with Trichlorosilane

Parham Rooshenas and Peter R. Schreiner
Institute of Organic Chemistry, Justus-Liebig University, Heinrich-Buff-Ring 58, Giessen, Germany

The asymmetric reduction of imines with trichlorosilane (C1) as a hydride donor in conjunction with a chiral organocatalyst represents a direct approach to enantiomerically enriched amines,[1] which are essential as building blocks of natural products or drugs.[2] However, the development of optimized efficient catalysts in the absence of mechanistical details is very difficult.

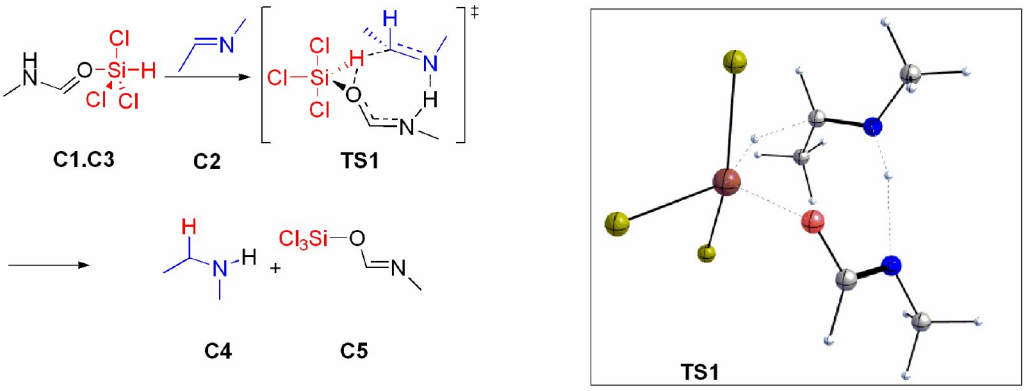

Abbildung 14.1: *Proposed mechanism for the reduction of ketimines with trichlorosilane catalyzed with N-methylformamide (C3) and the optimized geometry of TS1 at B3PW91/cc-pVDZ.*

We utilized computations at B3PW91/cc-pVDZ level of theory to elucidate the mechanism of this reaction. We examined first complex formation between trichlorosilane and model catalysts. We found out that although coordination of the amide group of catalyst to trichlorosilane lowers the barriers for the hydride transfer, this is still too high because of the unfavorable 4c/4e transition structure. Hence we considered another pathway for a reduction with modeled catalysts, which avoids the unsuitable 4c/4e binding situation and emphasizes the role of the secondary amide hydrogen.[3] The coordination of catalyst **C3** to **C1** forms **C1.C3**, which reacts with modeled imine **C2** through transition structure **TS1** (Scheme 1). In the transition structure silicon is pentacoordinated, the oxygen atom of the catalyst takes an equatorial position, as does the hydride. The basic nitrogen attracts the amide proton of **C3**, which increases the nucleophilicity of the oxygen atom. This promotes hydride transfer onto **C2** and results in the formation of the amine **C4** and silylated amide **C5**. The NBO analysis shows also positive charge on the formal proton (+0.455) and a smaller negative charge on the formal hydride (–0.156). Therefore, this reduction can be described as the addition of a formal H^+/H^- pair onto a double bond.[4] The subsequent reaction of **C4** and **C5** regenerates catalyst **C3** and forms silylamine.

We identify a similar reaction pattern for reductions catalyzed with proline derivatives modeled with **C6**. The catalyst forms with **C1** several intermediates (**C1.C6a** to **C1.C6d**). **C1.C6d** reacts with **C2** through **TS2** with a low barrier ($\Delta H_0^{\ddagger} = 2.9$ kcal/mol) to form **C4** and **C7**, which finally give **C6** and the silylamine.

In summary, mechanistic studies by means of DFT computations reveal that the catalyst not only coordinates to trichlorosilane, but also reacts as a proton donor in the crucial transition structure. Indeed, the catalytic reduction of ketimines with trichlorosilane can be described as a formal H^+/H^- transfer to the C=N double bond.[5]

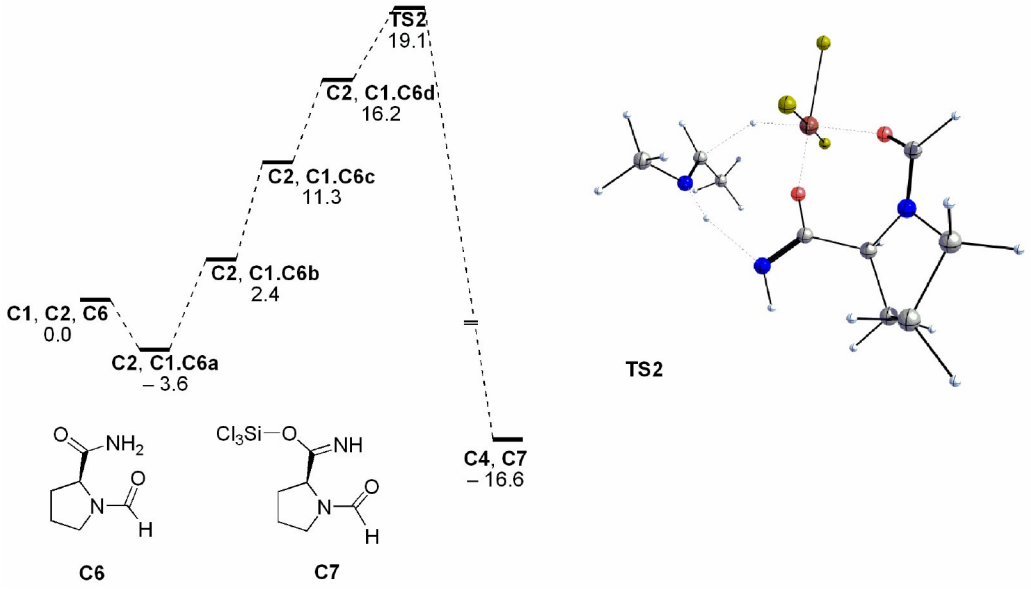

Abbildung 14.2: *The computed energy potential hypersurface for the reduction of C2 with C1 catalyzed with C6 with relative ΔH_0 in kcal mol^{-1} as well as the optimized geometry for TS2 at B3PW91/cc-pVDZ level of theory.*

References

1. Malkov, A. V.; Liddon, A. J. P. S.; Ramírez-López, P.; Bendová, L.; Haigh, D.; Kočovský, P. *Angew. Chem. Int. Ed.* **2006,** *45*, 1432. Wu, P. C.; Wang, Z. Y.; Cheng, M. N.; Zhou, L.; Sun, J. *Tetrahedron* **2008,** *64*, 11304; Wang, C.; Wu, X.; Zhou, L.; Sun, J. *Chem. Eur. J.* **2008,** *14*, 8789; Pei, D.; Zhang, Y.; Wei, S.; Wang, M.; Sun, J. *Adv. Synth. Catal.* **2008,** 350, 787.

2. Kobayashi, S.; Ishitani, H. *Chem. Rev.* **1999,** 99, 1069; Aboul-Enein, H. Y.; Wainer, I. W., The Impact of Stereochemistry on Drug Development and Use; Wiley & Sons Inc.: New York, **1997**.

3. Malkov, A. V.; Stončius, S.; MacDougall, K. N.; Mariani, A.; McGeoch, G. D.; Kočovský, P. *Tetrahedron* **2006,** 62, 264.

4. Spies, P.; Schwendemann, S.; Lange, S.; Kehr, G.; Frohlich, R.; Erker, G. *Angew. Chem. Int. Ed.* **2008,** *47*, 7543.

5. Zhang, Z.; Rooshenas, R.; Hausmann, H.; Schreiner, P. R. *Synthesis* **2009**, 1531.

4.1.15 Molecular Dynamics Simulation of the Kcv Potassium Channel

Stefan M. Kast, Sascha Tayefeh, Michael Kreim, Gerhard Thiel
Eduard-Zintl-Institut für Anorganische und Physikalische Chemie, Institut für Botanik,
Technische Universität Darmstadt

Potassium channels are membrane-bound proteins that enable the cell to selectively exchange potassium ions with the environment. Exploring the relation between amino acid sequence and channel functionality is important for understanding design principles of channel proteins, which will be relevant, e.g., for creating novel biosensors. The Kcv channels from the plant viruses PBCV-1 (Fig. 15.2) and ATCV-1 (Fig. 15.1) represent the smallest functional channels known and therefore serve as ideal model systems for studying structure-functions relationships. Ion conduction characteristics can be tuned by site-directed mutagenesis. However, crystal structures have not been obtained yet. In order to understand mechanistic features on an atomic scale, several molecular dynamics simulation models have been constructed based on the experimentally available KirBac1.1 structure [1-4]. Functional analogues (truncated KirBac1.1) and PBCV-1 Kcv homology models are simulated in a realistic environment (Fig. 15.2) over several tens of nanoseconds in order to extract structural, thermodynamic and dynamical data. Structures were further analyzed by employing a three-dimensional integral equation theory which provides information about ion binding sites. The results lead to a coherent picture of the influence of key amino acids on ion permeation.

Abbildung 15.1: *Superposition of cartoon models of Kcv channels from PBCV-1 (yellow) and ATCV-1 viruses (green).*

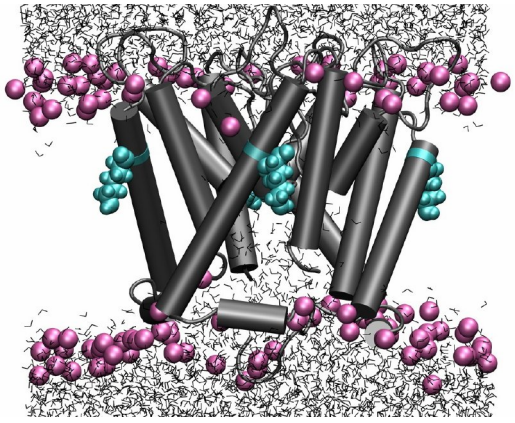

Abbildung 15.2: *Cartoon representation of the PBCV-1 Kcv simulation system, showing the protein, lipid head groups, and solvent molecules.*

References

1. S. Tayefeh, T. Kloss, G. Thiel, B. Hertel, A. Moroni, S. M. Kast, *Biochemistry* **46**, 4826-4839 (2007).

2. S. Tayefeh, T. Kloss, M. Kreim, M. Gebhardt, D. Baumeister, B. Hertel, C. Richter, H. Schwalbe, A. Moroni, G. Thiel, S. M. Kast, *Biophys. J.* **96**, 485-498 (2009).

3. S. Gazzarrini, M. Kang, A. Abenavoli, G. Romani, C. Olivari, D. Gaslini, G. Ferrara, J. L. Van Etten, M. Kreim, S. M. Kast, G. Thiel, A. Moroni, *Biochem. J.* **96**, 420, 295–303 (2009).

4. B. Hertel, S. Tayefeh, T. Kloss, J. Hewing, M. Gebhardt, D. Baumeister, A. Moroni, G. Thiel, S. M. Kast, *Eur. Biophys. J.*, in press (online DOI: 10.1007/s00249-009-0451-z).

4.1.16 Control of the Transmembrane Potential in K^+ Channel Simulations

Stefan M. Kast, Michael Kreim, Gerhard Thiel
Eduard-Zintl-Institut für Anorganische und Physikalische Chemie, Institut für Botanik,
Technische Universität Darmstadt

The transmembrane potential represents the electric voltage difference between the interior (cytosol) and the exterior of a cell. Interior and exterior regions are electric conductors whereas the thin separating region, the cell's plasma membrane, is highly resistive. Due to the different ionic composition of cytosol and exterior solution and due to the presence of ion channels and transporters in the membrane, the resting membrane potential is different from zero and is predominantly controlled by K^+ ions. In electrophysiological experiments the transmembrane potential is varied by electrodes and the current response is measured in order to gain insight into the function of membrane channel and transporter proteins.

A molecular dynamics simulation model of the electric currents across membranes must take into account suitable methods for imposing a given transmembrane potential, i.e. the consequence of the presence of electrodes. Frequently, a linearly varying potential corresponding to a constant electric field and force acting on the atoms is employed which can lead to serious artifacts. Related to the methodology of ref. [1] we have established a physically more realistic model of the membrane potential by creating a slight charge imbalance (different numbers of cations and anions) between cytosol and exterior solution in simulations of the PBCV-1 Kcv potassium channel [2,3] (Fig. 16.1).

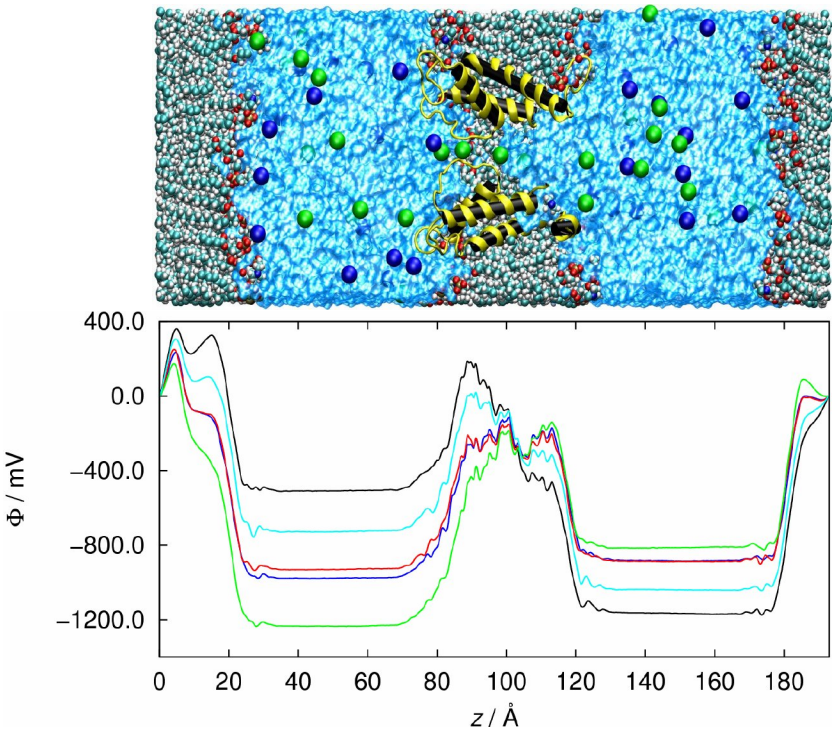

Abbildung 16.1: *Simulation system of the Kcv channel embedded in a lipid membrane, cytosol and exterior bath are separated by a pure lipid membrane (top); transmembrane potentials (bottom).*

In such a double-bilayer system the transmembrane potential follows from inverting Poisson's equation, taking the charge density that is averaged over the trajectory as input.

Extensive molecular dynamics simulations over several tens of nanoseconds revealed a number of key parameters that influence the statistical properties of the resulting potentials and the voltage range as a response to an imposed charge imbalance. Relevant parts of the channel protein that are responsible for a particular potential distribution have been identified. The role of the protein's interior cavity which acts as a concentration buffer has been characterized.

References

1. J. N. Sachs, P. S. Crozier, T. B. Woolf, *J. Chem. Phys.* **121**, 10847-10851 (2004).

2. M. Kreim, Diplomarbeit, Darmstadt 2007.

3. S. Tayefeh, T. Kloss, M. Kreim, M. Gebhardt, D. Baumeister, B. Hertel, C. Richter, H. Schwalbe, A. Moroni, G. Thiel, S. M. Kast, *Biophys. J.* **96**, 485-498 (2009).

4.1.17 Quantum Chemistry in Solution by Combining 3D Integral Equation Theory with a Cluster Embedding Approach

Stefan M. Kast, Thomas Kloss, Jochen Heil
Eduard-Zintl-Institut für Anorganische und Physikalische Chemie,
Technische Universität Darmstadt

Understanding and predicting chemical equilibria and reactivity in solution is a complex problem due to the many degrees of freedom on the atomic scale and due to the difficulty of choosing suitable approximations. In particular, a realistic model has to take into account the mutual response of the electronic structure of the solvated reactants and the solvent structure, which have to be computed self-consistently. Established dielectric continuum solvent models have difficulties to account, e.g., for hydrogen bonding or for heterogeneous environments. A granular, i.e. atomically resolved solvent model is advantageous in such a situation.

To this end, we have developed a hybrid method for the simultaneous solution to the electronic structure problem by quantum chemistry and to the solvent structure by the 3D reference interaction site model (RISM). The electronic structure of the solute is computed self-consistently with the solvent structure by mapping the charge distribution of the solvent onto a set of discrete background point charges that are added to the molecular Hamiltonian, corresponding to an "embedding cluster" (EC-RISM). The EC-RISM procedure yields chemical accuracy in predictions of reaction free energies for several benchmark systems without adjusting empirical parameters [1]. This is supported by a number of methodological developments concerning conceptual and numerical features of 3D-RISM theory [2,3]. A particularly important area of current research is the treatment of acidity (protonation equilibria) in water, characterized by aqueous pK_a values [1], and the prediction of tautomeric equilibria [4].

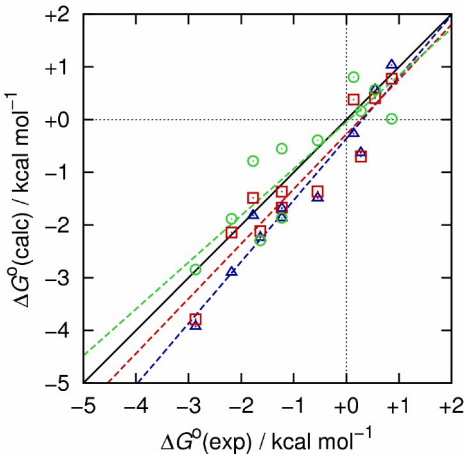

Abbildung 17.1: *Isosurfaces of self-consistent water atom densities around trifluoroacetic acid, red: hydrogen, yellow: oxygen.*

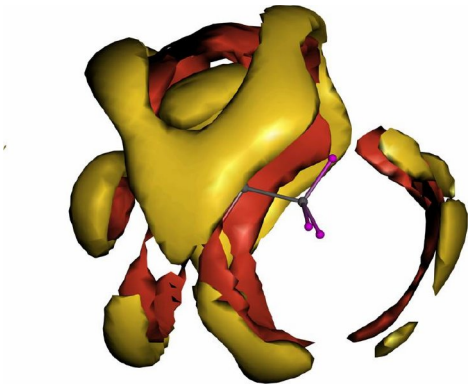

Abbildung 17.2: *Comparison of three different quantum-chemical models for predicting standard reaction free energies of tautomer equilibria in water.*

References

1. T. Kloss, J. Heil, S. M. Kast, *J. Phys. Chem. B* **112**, 4337-4343 (2008).
2. T. Kloss, S. M. Kast, *J. Chem. Phys.* **128**, 134505 (2008).
3. S. M. Kast, T. Kloss, *J. Chem. Phys.*, **129**, 236101 (2008).
4. S. M. Kast, J. Heil, S. Güssregen, K. F. Schmidt, *J. Comp.-Aid. Mol. Des.*, submitted.

4.1.18 Neuartige Hydroxycarbene und deren fundamentale Reaktionen

David Ley
Institut für Organische Chemie, 35392 Giessen

Der neue Hochleistungscluster Skylla wurde hauptsächlich verwendet, um anhand computerchemischer Berechnungen experimentelle Ergebnisse zu stützen. So konnten dank der großen Rechenleistung Erwartungswerte für experimentelle Meßgrößen wie z.B. Aktivierungsenergien und Schwingungsfrequenzen präzise ermittelt und dadurch die experimentelle Arbeit erleichtert werden. Hierfür sowohl Methoden der Dichtefunktionaltheorie in Kombination mit großem Basissatz (B3LYP/6-311++G**), als auch ab initio Methoden auf sehr hohem Niveau (z.B. CCSD(T)/cc-pVTZ) Verwendung.
Es konnten neue Erkenntnisse über die seit längerem vermutete[1] Reaktion von Hydroxycarbenen mit Aldehyden gewonnen werden:

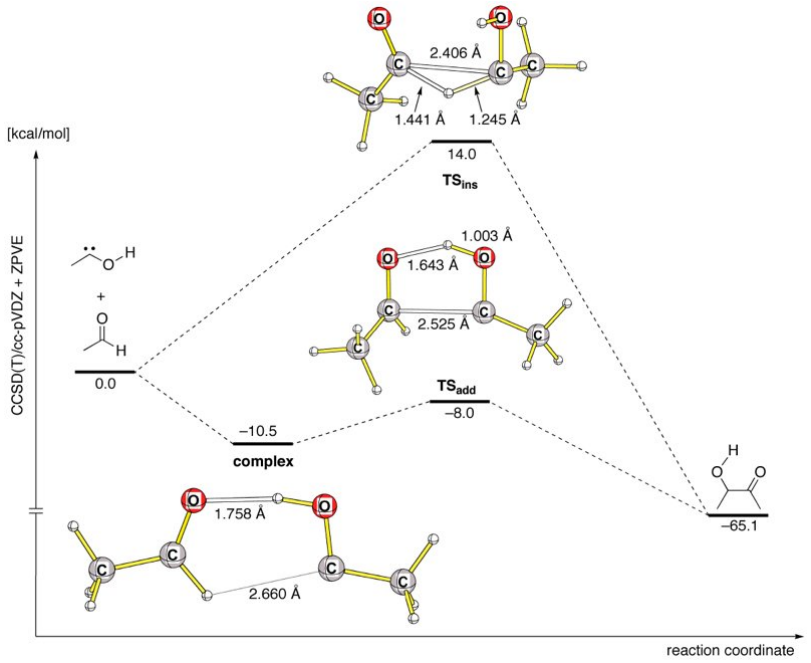

Abbildung 18.1: *Energiehyperfläche der Reaktion von Methylhydroxycarben mit Acetaldehyd.*

Verweise

1. G. Flanagan, S. N. Ahmed, P. B. Shevlin, *J. Am. Chem. Soc.* **1992**, 114, 3892-3896.

4.2 Physik

4.2.1 Phonon Sidebands in the Luminescence Spectrum

Christoph Böttge
Semiconductor Theory Group , Physics Department, Philipps-University of Marburg

The strong interaction between electrons and longitudinal optical phonons in ZnO gives rise to pronounced phonon sidebands in the luminescence spectrum. To develop a consistent microscopic theory of the sideband emission, we have generalized the semiconductor luminescence equations presented in Refs. [1,2] by including phonon-assisted processes. This approach allows us to compute both spontaneous and stimulated emission at the excitonic resonance and its first sideband. With the help of a non-perturbative treatment of the electron-phonon interaction that is based on the so-called polaron picture, we have derived a steady-state luminescence formula for arbitrary-order phonon sidebands. This result can be used to analyze the exceptionally strong phonon-assisted emission observed in recent experiments [3,4].
As a possible practical application of phonon-assisted luminescence in ZnO systems, we propose the construction of a low-threshold laser that is pumped at the excitonic resonance and emits at the first sideband. Here, the active material is placed inside a micro cavity where the cavity mode coincides with the sideband resonance. Because phonon-assisted emission and absorption take place on different sides of the excitonic resonance, we found that no normal-mode splitting occurs for the phonon sideband. Our numerical results confirm that the sideband intensity is strongly enhanced when the reflectivity of the mirrors reaches a critical value.

References

1. Mackillo Kira, Frank Jahnke, Walter Hoyer, and Stephan W. Koch. Quantum theory of spontaneous emission and coherent effects in semiconductor microstructures. Progress in Quantum Electronics, 23(6):189-279, 1999.

2. Mackillo Kira, Frank Jahnke, and Stephan W. Koch. Microscopic Theory of Excitonic Signatures in Semiconductor Photoluminescence. Phys. Rev. Lett., 81(15):3263-3266, 1998.

3. W. Shan, W. Walukiewicz, J.W. Ager III, K.M. Yu, H.B. Yuan, H.P. Xin, G. Cantwell, and J.J. Song. Nature of room-temperature photoluminescence in ZnO. Appl. Phys. Lett., 86:191911, 2005.

4. L. Li, H. Yang, G. Qi, J. Ma, X. Xie, H. Zhao, and F. Gao. Synthesis and photoluminescence of hollow microspheres constructed with ZnO nanorods by H2 bubble templates. Chem. Phys. Lett., 455(1-3):93, 2008.

4.2.2 Modelling of the optical properties of semiconductor gain materials for laser applications

Christina Bückers, Eckhard Kühn, and Stephan W. Koch
Department of Physics and Material Sciences Center, Philipps-University Marburg

For the development and design of semiconductor laser devices a detailed analysis of their optical properties is demanded to characterise and identify the underlying physical processes. Such an analysis is of significant importance to explore the potential of novel material systems and to optimise structural designs with regard to applications. For this purpose, we have developed a numerically complex many-particle theory which includes microscopic interaction effects explicitly. By solving the semiconductor Bloch equations, the semiconductor luminescence equations, and quantum Boltzmann scattering equations several material properties are computed: the absorption, the refractive index, the optical gain, the luminescence and the Auger losses. Thus, main characteristics of a laser system such as lasing wavelength, threshold behaviour or output power can be studied in detail.
Well-established laser materials are (AlGaIn)As compounds which are already used in optically pumped vertical-external-cavity surface-emitting laser (VECSEL) devices. In particular, we analyse the properties of such a laser system operating at a wavelength around 850 nm. The light intensity reflected by the VECSEL structure is given in Fig. 2.1 (left) for various pump powers. The spectra result from transfer matrix calculations where the pre-computed optical response of the active layers is included. With increasing excitation, the reflectance becomes larger than 100% around the central wavelength of 843 nm, i.e. light is amplified in this spectral region. However, the performance of the laser system is not only determined by the gain properties but also by the intrinsic laser losses. These are basically given by radiative and Auger recombination processes and are computed microscopically as well. Finally, from the quantitative knowledge of the absorption, the gain and the laser losses, the pump power necessary to achieve a certain amplification is estimated and an intrinsic limit of the proximity between pump and laser wavelength is concluded (Fig. 2.1, right).
On top of the VECSEL structure is often deposited an antireflection coating in practice. In order to study the influence of such an antireflection coating on the operating properties of a VECSEL we employ an effective rate equation approach including microscopic results for the laser gain and the laser losses. Hence, antireflection-coated and uncoated VECSEL systems can be systematically compared by numerical studies. The simulations show a significantly higher threshold and slower switch-on dynamics for the antireflection-coated devices. Finally, these differences are attributed to a reduced optical confinement of the antireflection-coated devices.

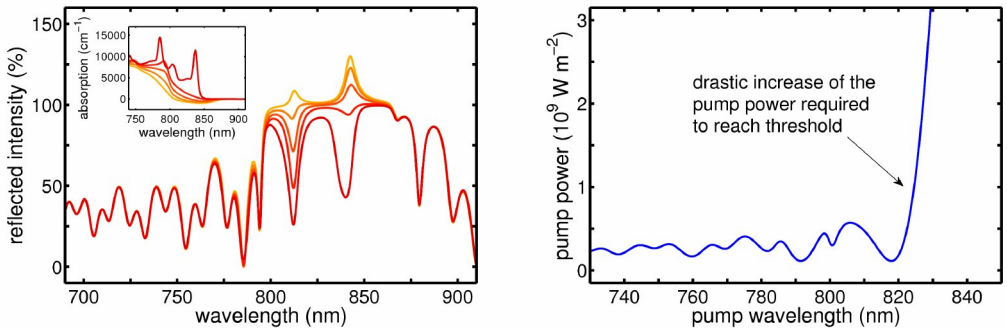

Abbildung 2.1: Left: *Reflectance of the VECSEL structure predicted at a temperature of 300 K for five different pumping levels. The underlying microscopically calculated absorption spectra for the (AlGaIn)As quantum well are displayed in the inset for carriers densities of 0.002, 2, 3, 4 and 5 × 10^{12} cm^{-2} (from top to bottom).* ***Right:*** *Pump power needed to sustain the threshold gain as a function of the pump wavelength. For the evaluation a temperature of 350 K is assumed in the active region.*

Moreover, we combine the microscopic theory with a valence-band anticrossing model in order to simulate the optical properties of dilute bismide Ga(AsBi) structures. This novel material system is particularly interesting for laser applications as its emission wavelength can be tuned over a wide spectral range by modifying the small bismide concentration. Since the band structure parameters of the material are not exactly known at present, we study their influence on the optical gain properties, the luminescence and the laser loss processes systematically. In this manner, characteristic features of the material system are revealed and the potential with regard to applications can be explored.

References

1. C. Bückers, S. Imhof, A. Thränhardt, J. Hader, J. V. Moloney, and S. W. Koch, *Microscopic modeling of quantum well gain media for VECSEL applications*, IEEE Journal of Selected Topics in Quantum Electronics **15**, 984 (2009).

2. E. Kühn, A. Thränhardt, C. Bückers, S. W. Koch, J. Hader, and J. V. Moloney, *Numerical study of the influence of an antireflection coating on the operating properties of vertical-external-cavity surface-emitting lasers*, Journal of Applied Physics **106**, 063105 (2009).

4.2.3 Photon-correlation spectroscopy in strong-coupling semiconductor quantum-dot systems

Lukas Schneebeli, Mackillo Kira, Stephan W. Koch
Department of Physics and Material Sciences Center, Philipps-University, 35032 Marburg, Germany

Strong coupling in semiconductor quantum-dot systems constitutes a very active area of research in the quantum-optics and semiconductor nanostructure communities. While true strong coupling has been realized in atomic cavity QED experiments, it is still missing in solid-state systems. The experimental observation would clearly have potential impact on fast emerging fields like quantum computing, cryptography, etc..
While the observation of the semiclassical vacuum Rabi splitting in semiconductor quantum-dot systems is widely accepted, the observation of the quantum-mechanical Jaynes-Cummings splitting is still a difficult problem due to the dephasing and broadening effects in current samples. Inspired by the fascinating achievements in atomic physics, researchers worldwide are trying to detect the true strong coupling in semiconductor quantum-dot systems.
In Refs. [1-2], we have applied a fully quantized theory to describe the resonance fluorescence from quantum-dot-cavity systems and to study the photon statistics of the fluorescent light. We have shown that the spectrally resolved photon-statistics measurements of the resonance fluorescence from realistic semiconductor quantum-dot systems allow for high contrast identification of the two-photon strong-coupling states.
In Ref. [2], we have developed a reduced model in order to explain the origin of auto- and cross-correlation resonances in the two-photon emission spectrum of the fluorescent light. These resonances are traced back to the two-photon strong-coupling states of Jaynes-Cummings ladder. The accuracy of the reduced model is verified via numerical solution of the resonance fluorescence equations. The formalism also allows us to explain the origin of the squeezed-light emission in optically excited semiconductor systems.

Verweise

1. L. Schneebeli, M. Kira, and S. W. Koch, Characterization of Strong Light-Matter Coupling in Semiconductor Quantum-Dot Microcavities via Photon-Statistics Spectroscopy, Phys. Rev. Lett. 101, 097401 (2008).

2. L. Schneebeli, M. Kira, and S.W. Koch, Microscopic Theory of Squeezed-Light Emission in Strong-Coupling Semiconductor Quantum-Dot Systems, Phys. Rev. A 80, 033843 (2009).

4.2.4 Towards understanding of C_{60}-based nanowire growth with anomalous anisotropy

Ilia A. Solov'yov[1], Junfeng Geng[2], Andrey V. Solov'yov[1] and Brian F. G. Johnson[2]
[1]*Frankfurt Institute for Advanced Studies, Goethe University, Frankfurt am Main, Germany*
[2]*Department of Chemistry, University of Cambridge, Cambridge, United Kingdom*

The growth of one-dimensional (1D) nanocrystals is an important research topic in crystal engineering for nanotechnology because of the properties associated with the low-dimensionality, quantum confinement effect, and potential magnetic and photonic applications.
In a recent study [1], it was demonstrated that exceptionally long fullerene nanowires, with a length-to-width aspect ratio as large as ˜3000-5000, can be grown from 1,2,4-trimethylbenzene solution of C_{60}.
We perform a thorough theoretical analysis, aimed to explain the exceptionally large aspect ratio of C60-based nanowires. By accounting for different interactions in the system we have calculated the structure of the unit cell and determined the role of the fullerene and of the solvent molecules in the crystallization process of the nanowire [2]. The structure of six energetically favorable isomers of the nanowire unit cell is shown in the figure. We have calculated the adhesion energy of C60 molecules to the nanowire surface and demonstrated that it is related to the anisotropy of the crystal.
To get a more in-depth understanding of the nanowire growth mechanism we have also considered the influence of electron polarization on the anisotropy of the C60-based nanowires [3] and studied the possible polymerization reactions in the system, which likely occur between the C60 and the solvent molecules in the nanowire [4,5].

References

1. J. Geng, W. Zhou, P. Skelton, W. Yue, I. Kinloch, A. Windle, and B. Johnson, *J. Am. Chem. Soc.* **130,** 2527 (2008).

2. J. Geng, I.A. Solov'yov, W. Zhou, A.V. Solov'yov, and B.F.G. Johnson,·J. Phys. Chem. C **113**, 6390 (2009).

3. I.A. Solov'yov, J. Geng, A.V. Solov'yov, B.F.G. Johnson, Chem. Phys. Lett. **472**, 166 (2009).

4. J. Geng, I.A Solov'yov, D.G. Reid, P. Skelton, A.E.H. Wheatley, A.V. Solov'yov and B.F.G. Johnson,. [arXiv.org: arXiv:0906.2216v1 physics.chem-ph] (2009)]

5. I.A. Solov'yov, J. Geng, A.V. Solov'yov, and B.F.G. Johnson, AIP Conference Proceedings **1197**, 89 (2009)

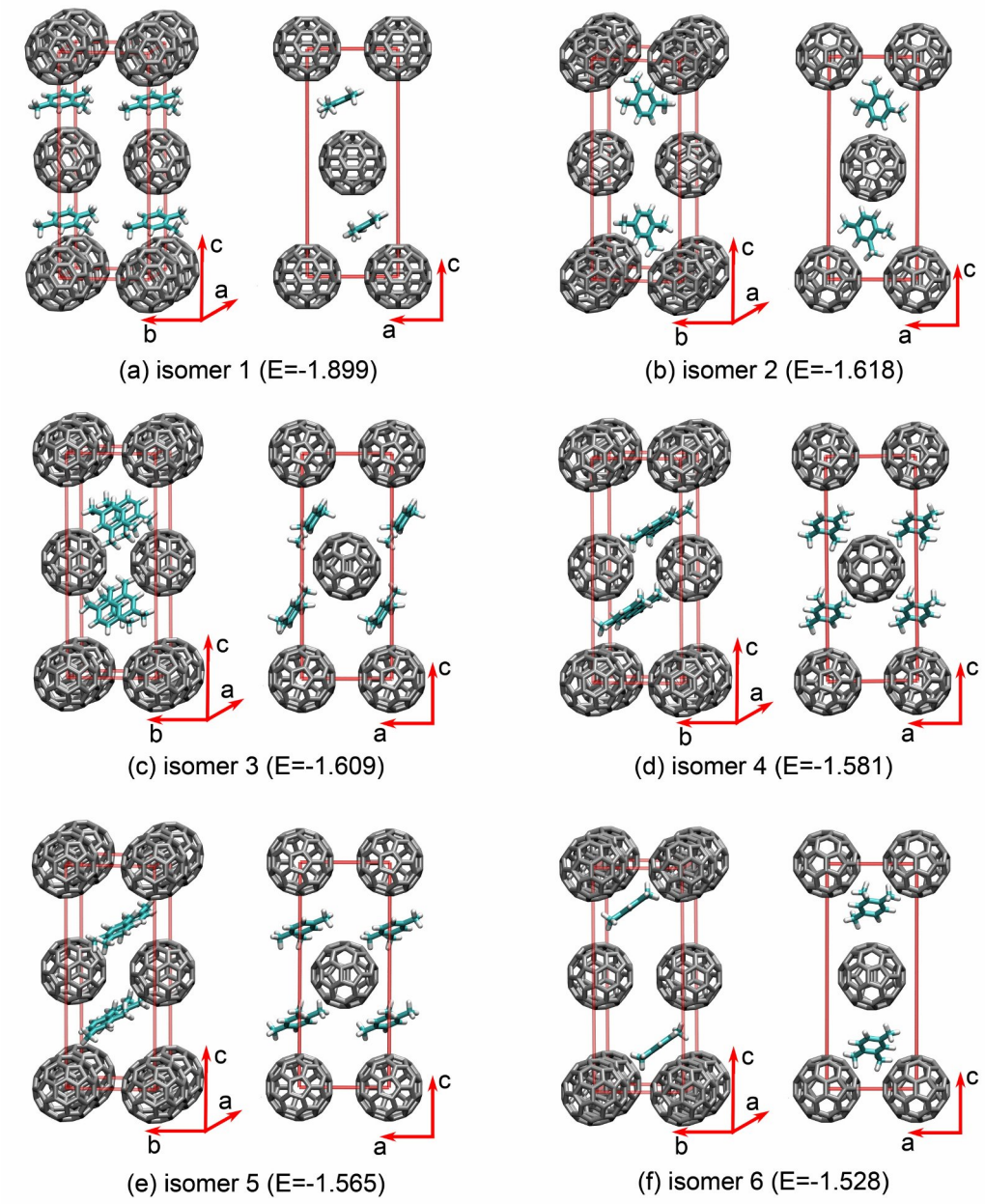

Abbildung 4.1: *Optimized isomeric states in the C_{60}· TMB nanowire unit cell as derived from the calculations. The number in the brackets below each image shows the energy of the structure (in eV). The coordinate frames used in the present work are also indicated.*

4.2.5 Stability of a nanofractal on surface

Veronika V. Dick, Ilia A. Solov'yov, Andrey V. Solov'yov
Frankfurt Institute for Advanced Studies, Ruth-Moufang-Str. 1, 60438 Frankfurt am Main, Germany

The process of the post-growth relaxation and the question of stability of deposited structures is still not well understood [1-4]. The understanding of the post-growth relaxation processes would allow one to controllably influence the self-organization processes of particles on the surface and therefore to obtain patterns with predictable properties.

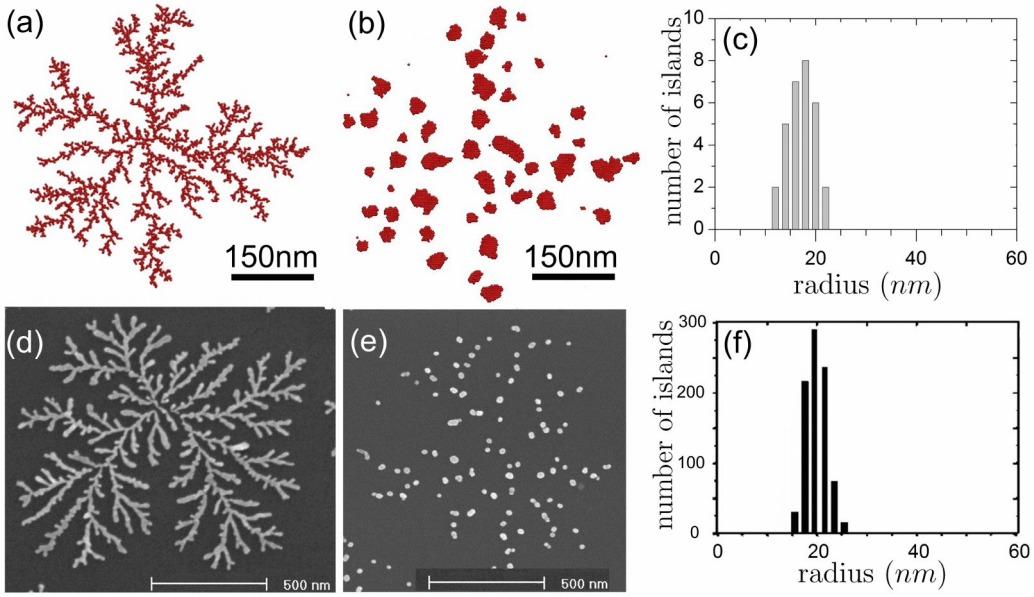

Abbildung 5.1: *Evolution of the fractal structure, calculated with the DLA model with accounting for the internal dynamics of the particles in the fractal (a)-(c) and comparison with the experimental observation of the silver fractal perturbation by adding of oxygen impurities to the silver clusters (d)-(f). (a) fractal structure grown by the DDA method; (b) snapshots of the fractal structure after fragmetation, calculated with the DLA model; (c) size distribution of the islands after fractal fragmentation; (d) structure of the silver cluster fractal grown by cluster deposition technique on the graphite surface from Ref. [1]; (e) results of experimental observation of perturbed silver fractal by adding of oxygen impurity to the silver clusters [1]; (f) size distribution of the silver island on the graphite substrate after pertubation [1]*

Here we present a detailed systematical theoretical analysis of the post-growth processes occurring in a nanofractal on surface. For this study we developed a modified DLA method which describes the internal dynamics of particles in a fractal and accounts for their diffusion and detachment. We demonstrate that these kinetic processes control the final shape of the islands on surface after post-growth relaxation. We consider different scenarios of fractal relaxation and analyze the time evolution of the island's morphology. In Fig. 5.1 we illustrate several scenarios of fractal fragmentation.
We demonstrate that stability of the fractal structure depends strongly on several factors, such as the concentration of impurities and temperature [2-4].

References

1. A. Lando and et al., Phys.Rev.Lett. **97**, 133402 (2006)
2. V.V. Dick, I.A. Solov'yov, A.V. Solov'yov, in preparation (2009)
3. V.V. Dick, I.A. Solov'yov, A.V. Solov'yov, The 4th International Symposium Atomic Cluster Collisions: structure and dynamics from the nuclear to the biological scale, ISACC 2009, Ann Arbor, USA, July 14-18, (2009), Book of abstracts, p. 34.
4. V.V. Dick, I.A. Solov'yov, A.V. Solov'yov, AIP Conference Proceedings **1197**, 76 (2009)

4.2.6 Phase transitions in fullerenes

Adilah Hussein, Alexander Yakubovich, Andrey Solov'yov and Walter Greiner
Frankfurt Institute for Advanced Studies, Goethe University, Frankfurt am Main, Germany

The phase transition of fullerenes C_{60} and C_{240} by was investigated by conducting constant-temperature molecular dynamics simulations. We have simulated the self assembly process of the C_{60} from a gaseous phase in the vicinity of the phase transition temperature at which the two phases coexist. Here, the fullerene system is seen to continuously oscillate between two phases: the solid-like cage and the gas-like state of dimers and short chains. These oscillations correspond to consecutive fragmentation and assembly of the fullerene cage. We have also investigated the temperature-dependent heat capacity of the fullerenes, whose prominent peaks are signatures of the finite system analogue of first-order phase transitions. Our simulations were conducted for 500 ns using a developed topologically constrained forcefield and were then supplemented by statistical mechanics analysis to take into account pressure and entropy corrections. These corrections lead to a phase transition temperature of 3800-4200 K, for the pressure range of 10-100 kPa, in good agreement with available experimental values.

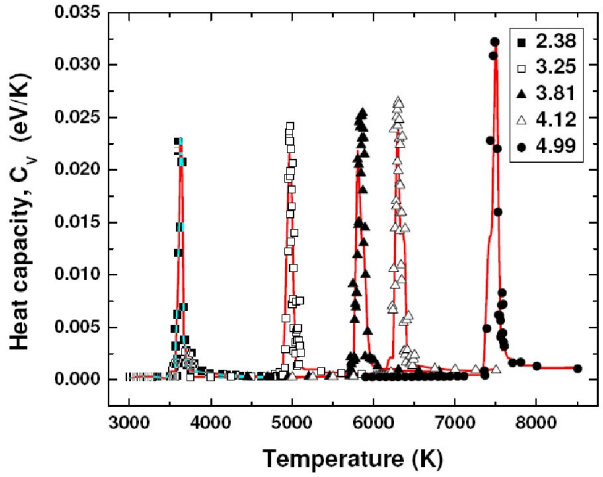

Abbildung 6.1: *C_{60} heat capacity plots obtained for different energies of the single bonds in the system. The temperature at the maximum of each heat capacity curve is denoted the phase transition temperature, T_{PT}: 3500 K (2.38 eV), 4950 K (3.25 eV), 5855 K (3.81 eV), 6450 K (4.12 eV), 7450 K (4.99 eV). The scatter plots are calculated using the fluctuations of the total energy while the thick solid lines were differentiated from the cubic B-spline interpolation of the total energy on temperature dependence.*

References

1. A Hussien, A Yakubovich, A Solov'yov and W Greiner, Submitted to Eur. Phys. J. D (2009); http://arxiv.org/abs/0807.4435v1 (2008)

2. A. Hussien, A.V. Yakubovich, and A.V. Solov'yov, AIP Conference Proceedings **1197**, 152 (2009)

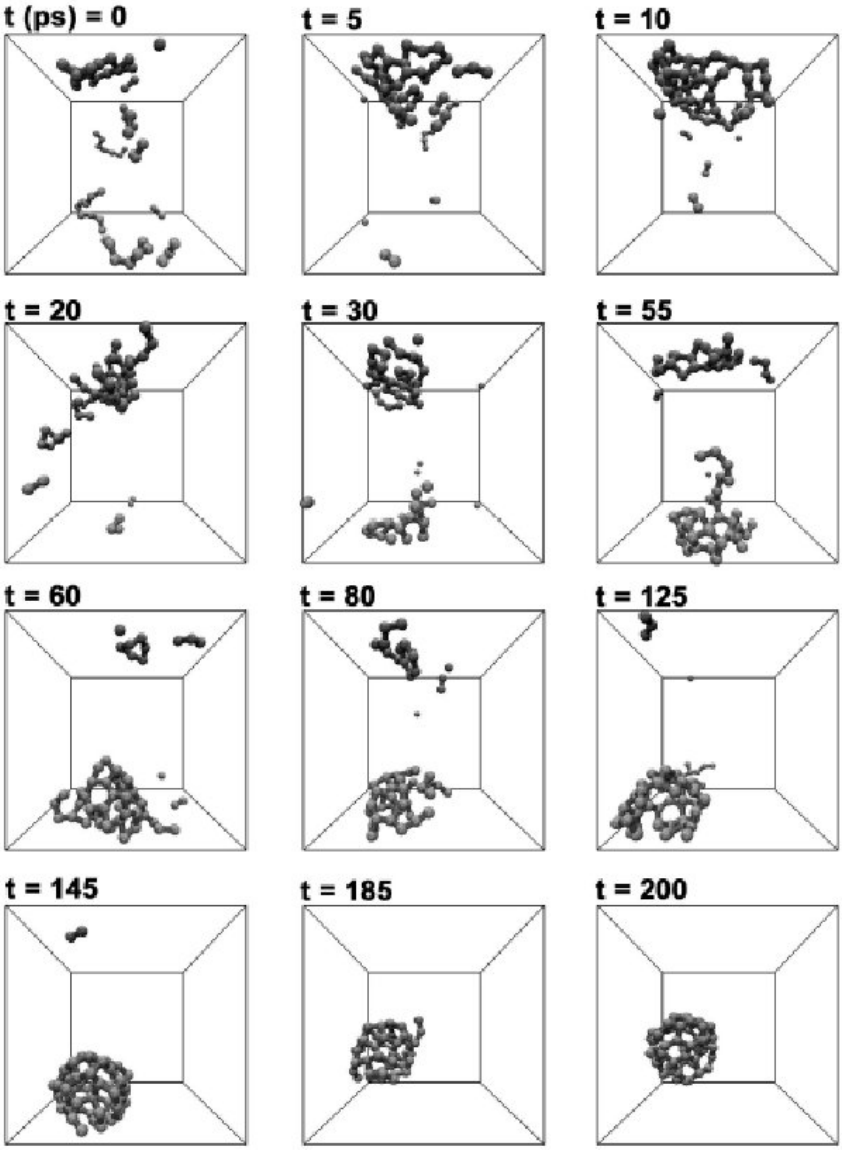

Abbildung 6.2: *Snapshots of the re-assembly process (gas-like phase to solid-like phase) from the coexistence behavior of C_{60} in the phase transition region at $T = 5855$ K. All times are in ps and denote the interval from the first snapshot.*

4.2.7 Phase transitions in proteins

Alexander Yakubovich, Andrey Solov'yov and Walter Greiner
Frankfurt Institute for Advanced Studies, Goethe University, Frankfurt am Main, Germany

Proteins are biological polymers consisting of elementary structural units, amino acids. Being synthesized at ribosome the protein is exposed to the cell interior where it folds into its unique three dimensional structure. The process of forming of protein's three dimensional structure is called the process of protein folding. The correct folding of protein is of crucial importance for the protein's proper functioning.

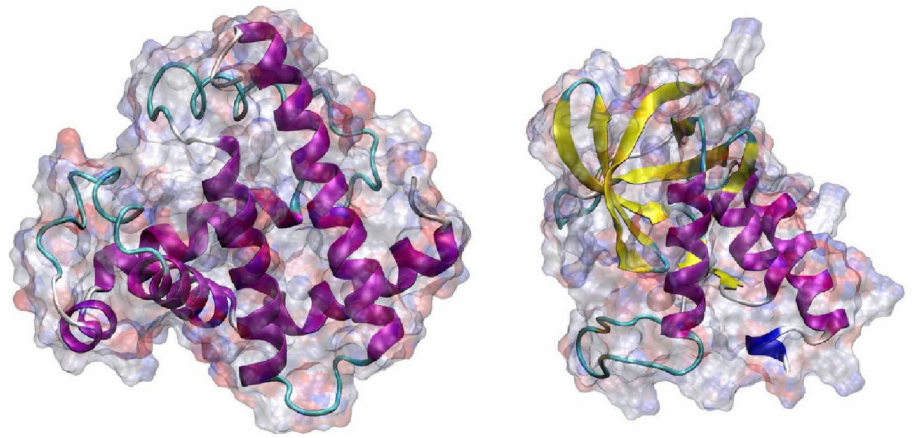

Abbildung 7.1: *The structure of horse heart metmyoglobin (right, PDB ID 1YMB) and the structure of staphylococcal nuclease (left, PDB ID 1EYD).*

We have developed a novel statistical mechanics model for the description of folding-unfolding processes in small globular proteins obeying simple two-stage-like folding kinetics. The introduced statistical mechanics model is based on the construction of the partition function of a protein in water environment. The partition function of a system is constructed as a sum over all statistically relevant conformational states of a protein, while the partition function of each state is a product of partition functions of a protein in a given conformational state, partition function of water molecules and a partition function of water molecules that are affected by the interaction with the protein.
We performed the comparison of the results of the statistical mechanics model with experimentally measured data of the heat capacity on temperature dependencies for two globular proteins, namely staphylococcal nuclease and metmyoglobin. These experiments were performed for different values of pH of the solvent which resulted in various profiles of heat capacity dependence under different values of pH of the medium.
The introduced statistical mechanics model is capable to reproduce within a single framework various peculiarities of 20 the heat capacity profile, such as the temperatures of cold and hot denaturation of the protein, the corresponding maximum values of the heat capacities, the temperature rangeof the cold and hot denaturation transitions, the di®erence between heat capacities of the folded and unfolded states of the protein.

References

1. A.V. Yakubovich, A.V. Solov'yov, W. Greiner, *International Journal of Quantum Chemistry,* **110**, 257 (2009)
2. A.V. Yakubovich, A.V. Solov'yov, W. Greiner, AIP Conference Proceedings **1197**, 186 (2009)
3. Y. Griko, P. Privalov, J. Aturtevant, and S. Venyaminov, Proc. Natl. Acad. Sci. USA **85**, 3343 (1988)
4. P. Privalov, Journal of Chemical Thermodynamics, **29**, 447 (1997)

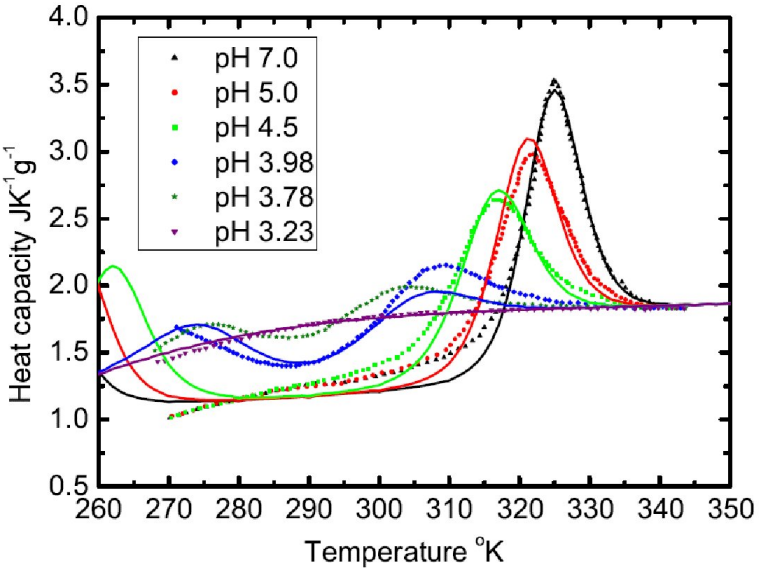

Abbildung 7.2: *The dependencies of the heat capacity on temperature of staphylococcal nuclease (PDB ID 1EYD) at different values of pH. By solid lines are shown the results of theoretical model. By symbols are shown the experimental measurements from Ref.[3].*

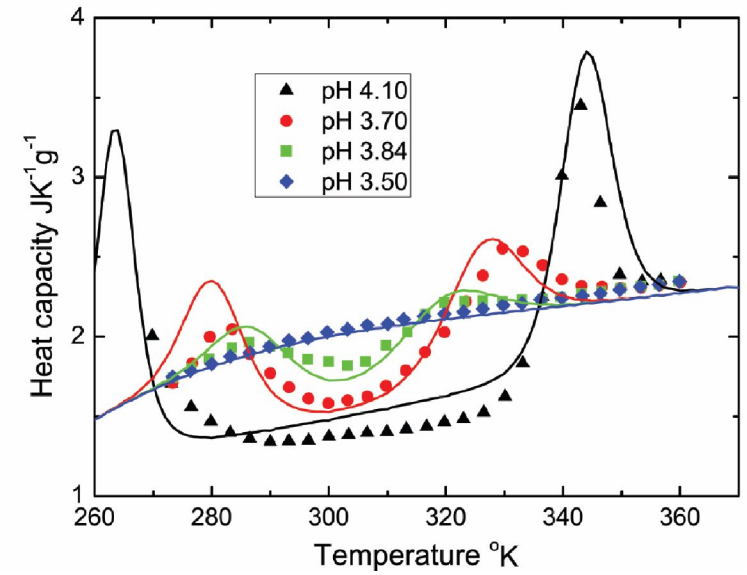

Abbildung 7.3: *The dependencies of the heat capacity on temperature of horse heart metmyoglobin (PDB ID 1YMB) at different values of pH. By solid lines are shown the results of theoretical model. The experimental measurements from Ref. [4] are shown by symbols.*

4.2.8 Impurity effect on the melting of nickel clusters as seen via molecular dynamics simulations

Andrey Lyalin, Adilah Hussien, Andrey V. Solov'yov and Walter Greiner
Frankfurt Institute for Advanced Studies, Goethe University, Frankfurt am Main, Germany

Doping of Ni147 with a carbon impurity lowers its melting temperature by 30 K due to excessive stress on the cluster lattice. The distortion of the cluster lattice results in the change of the cluster's energetics as well as its entropy. The magnitude of the change induced is dependent upon the parameters of the interaction between the nickel atoms and the carbon impurity. We have demonstrated that an induced contraction of the icosahedral cluster's lattice in the vicinity of the impurity results in an increase of the melting temperature of the cluster; whereas additional strain in the lattice results in the reduction of the melting temperature. Therefore, the melting temperature of atomic clusters can be ffectively tuned by the addition of an impurity of a particular type.
Doping by a C or C2 impurity changes the melting temperature of the cluster, consequently this means that doping affects the mobility of the atoms in the Ni cluster. This effect has to be taken into consideration in particular applications with metal clusters when the entire process depends on the thermodynamic state of the cluster. An example of such experiment is the process of the catalytically activated growth of carbon nanotubes. The kinetics of the carbon nanotube growth depends upon diffusion of carbon atoms through the metal catalyst. Presence of the impurities can considerably change the flux, thereby affecting the growth rate of the carbon nanotube. The additional change in the thermodynamic state of the catalytic particle in the nanotube growth process might also depend on the strength of the interaction of the particle with a substrate.

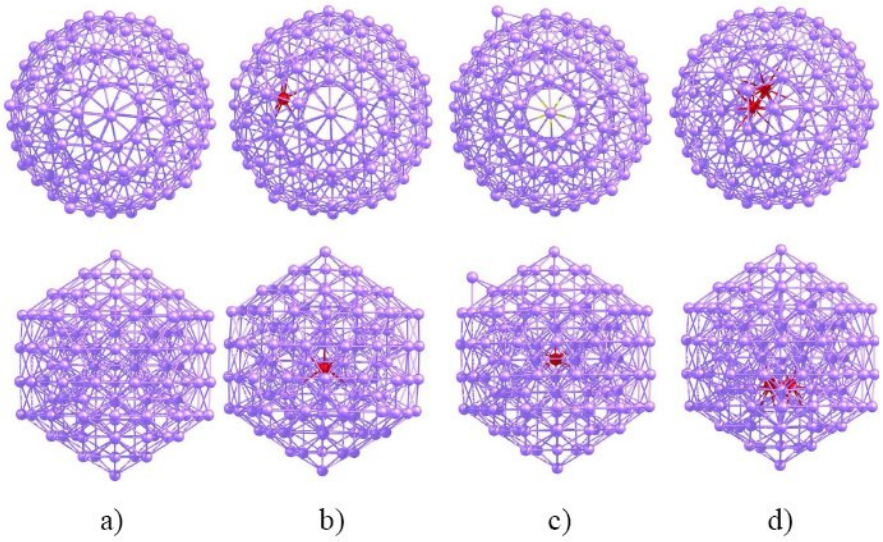

Abbildung 8.1: *(a) Optimized structure of a pure Ni147 cluster; (b) the isomer state structure of the C-doped Ni147 cluster; (c) the ground state structure of the C-doped Ni147 cluster; (d) the optimized structure of the C2-doped Ni147 cluster.*

In the present work [1], we have considered a single C and C2 impurity in the cluster of Ni147. It is interesting to study how several C impurities will influence the thermodynamic properties of the host cluster. In particular, it is important to find the optimum conditions (concentration of C atoms, temperature, thermodynamic state of the particle, etc.) when the C atoms begin aggregating into ordered carbon structures, such as nanotubes. This study requires careful investigation of the reliable many-body potentials for C-C interactions in the host metal cluster. The influence of impurities on properties of finite systems is a general effect. While our results were obtained for free

clusters, many interesting problems can be found when one considers the influence of impurities on the phase transitions and stability of clusters deposited on a substrate. Thus, recently it has been experimentally shown that the oxidation of silver clusters deposited on a HOPG surface changes the stability and morphology of cluster formations. Clusters on substrates have important technological applications and the understanding of how these clusters stabilize on the surface are of profound interest.

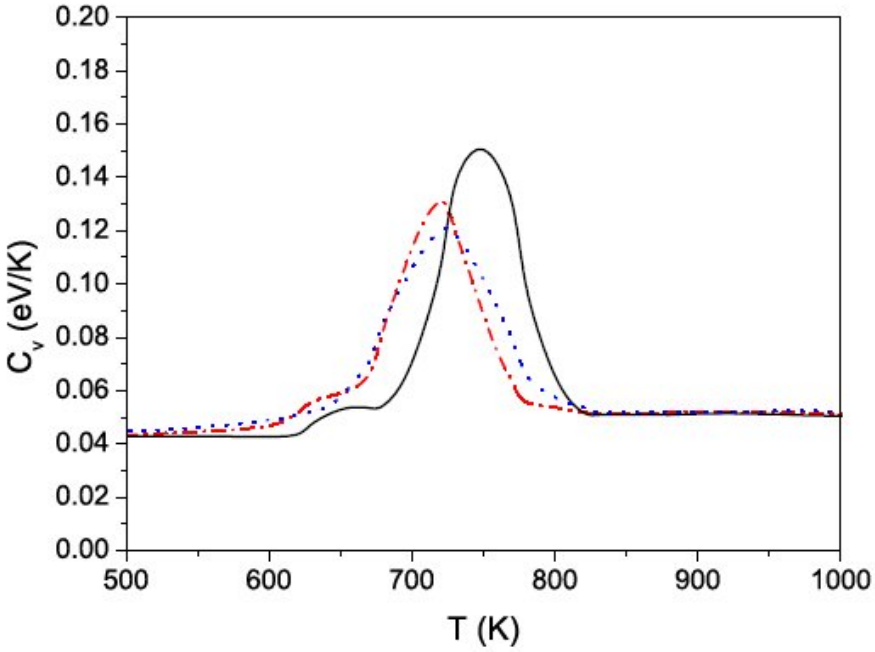

Abbildung 8.2: *Heat capacity for the pure Ni147 cluster (solid line), the C-doped Ni147 cluster (dashed-dotted line) and the C-doped Ni147 cluster (dotted line) as a function of T.Temperatures Tm = 750 K, 720 K and 725 K corresponds to the melting temperatures of the pure, the C-doped Ni147 and the C2-doped Ni147 cluster, respectively.*

References

1. A.G. Lyalin, A. Hussien, A.V. Solov'yov, W. Greiner, Physical Review B **79**, p.165403 (2009)

4.2.9 Defects in epitaxial graphene layers: Density functional theory studies

Michael Bachmann, Christian Heiliger
I. Physikalisches Institut, Justus-Liebig-Universität, Gießen

Recent experimental observations of bilayer graphene using scanning tunneling microscopy (STM) show scattering patterns with a 6-fold symmetry [1,2]. These cannot be explained by substitutional defects which cause scattering patterns with 3-fold symmetry. We perform *ab initio* calculations of defects in bilayer graphene that can explain the 6-fold symmetry of the measured scattering patterns. They do not occur in single layer graphene. They occur if a defect in one layer induces changes in the electronic structure of the other layer. For all calculations we employ the ABINIT package [3].
To obtain a scattering pattern with a 6-fold symmetry, we replace a carbon atom in the second layer of bilayer graphene with a silicon atom. Subsequently, we perform a structural relaxation and observe a shift of the silicon atom to a position between the layers. This causes a 6-fold symmetry scattering pattern in the first layer. In a second step we perform a full relaxation of the whole structure. Due to this full structural relaxation the size of the 6-fold scattering pattern is increasing and is in good agreement with the scattering pattern that is observed in the experiments [1,2]. In Figure 9.1 we show the calculated structures.

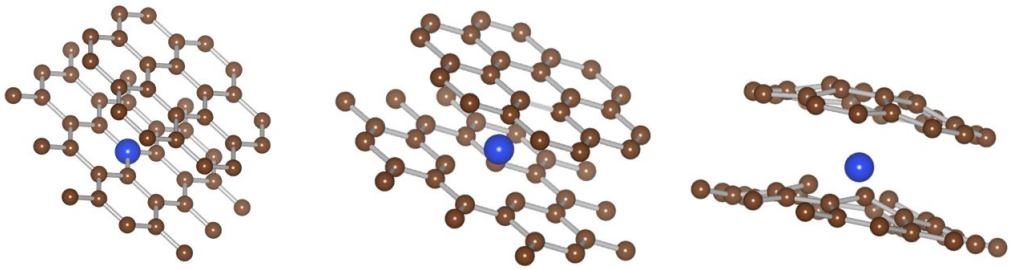

Abbildung 9.1: ***Left:*** *Bilayer graphene with one carbon atom replaced by a silicon atom.* ***Middle:*** *Bilayer graphene with one relaxed silicon atom.* ***Right:*** *Full relaxed structure of bilayer graphene with one silicon defect in between the layers.*

References

1. G.M. Rutter, J.N. Crain, N.P. Guisinger, T. Li, N.P. First, J.A. Stroscio, Science 317, 219 (2007)

2. N.P. Guisinger, G.M. Rutter, J.N. Crain, C. Heiliger, N.P. First, J.A. Stroscio, J. Vac. Sci. Technol. 26, 932 (2008)

3. `http://www.abinit.org`

4.2.10 *Ab initio* calculations of ZnMgO lattice parameters

Markus Heinemann, Marcel Giar, Christian Heiliger
I. Physikalisches Institut, Justus-Liebig-Universität, Gießen

ZnO with a band gap of about 3.4 eV is a wide band gap semiconductor that may be used for opto-electronic devices such as light emitting diodes with an operational range from blue to ultraviolet. For that purpose band gap modulations are usually achieved by substituting bivalent metals (i.e. Mg) for Zinc. Recent experimental works have successfully investigated the influence of increasing Mg content x on $Zn_{1-x}Mg_xO$ thin films grown by pulsed laser deposition (PLD) [1] or plasma assisted molecular beam epitaxy (PAMBE) [2] and found wurtzite $Zn_{1-x}Mg_xO$ alloys to be stable within a range from x=*0* to x≈0.4.

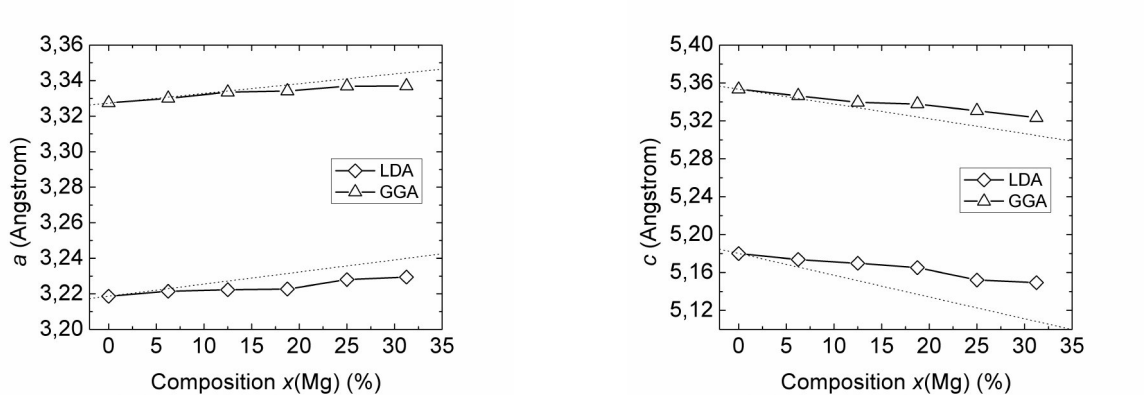

Abbildung 10.1: *Computed LDA (◇) and GGA (Δ) equilibrium lattice parameters a (left) and c (right) for wurtzite $Zn_{1-x}Mg_xO$ as function of Mg concentration. [3]*

In this work we use a density functional theory (DFT) method to calculate the structural properties of wurtzite type $Zn_{1-x}Mg_xO$ alloys in the range $0 \leq x \leq 0.32$. We use the projector augmented wave method (PAW) implemented in the ABINIT programme package. For the exchange correlation functional we choose the local density approximation (LDA) as well as the generalized gradient approximation (GGA). The calculations are carried out in a 2x2x2 supercell where in a first step the atomic positions are relaxed and subsequently a geometrical optimization is carried out in which the cell parameters are changed until the equilibrium lattice parameters are reached.
The obtained equilibrium lattice parameters a and c are shown in figure 10.1. The lattice parameter a increases slowly with x whereas c decreases. In LDA as well as GGA calculations both parameters, a and c, show a deviation from Vegard's law which predicts a linear behavior. The volume per unit cell stays constant. LDA and GGA results seem to give a lower and upper boundary for the actual structural parameters.

References

1. A. Ohtomo and A. Tsukazaki, *Semicond. Sci. Technol.* **20**, S1-S12 (2005)
2. T. A. Wassner, B. Laumer, S. Maier, A. Laufer, B. K. Meyer, M. Stutzmann and M. Eickhoff, *J. Appl. Phys.*, **105,** 023505 (2009)
3. M. Heinemann, M. Giar and C. Heiliger, *MRS Symposium Proceedings* **1201**, submitted (2009)

4.2.11 Metallization of the $\sqrt{3}\times\sqrt{3}$ 4-mercaptopyridine SAM on Au(111)

John A. Keith, Timo Jacob, Burkhard Fricke
Institut für Elektrochemie, Universität Ulm, D-89075 Ulm
Fachbereich Physik, Universität Kassel, 34130 Kassel

The development of high performance molecular electronics and nanotech applications requires deep understanding of atomic level structural, electronic, and magnetic properties of electrode/molecular interfaces. To clarify the initial stages of interface formation during self-assembled monolayer (SAM) metallization, we used first principles density functional theory (DFT) calculations to study Pd diffusion on top of 4-mercaptopyridine (4MP)-SAMs on Au(111) with a $\sqrt{3}\times\sqrt{3}$ surface structure. After distinguishing potential energy surfaces (PESs) for singlet and triplet spin configurations for Pd on the SAM, we find adatom diffusion is not possible over the clean 4MP-SAM surface. Pre-adsorption of Pd, however, facilitates Pd diffusion that appears to explain multiple reports on experimentally observed island and monolayer formation on top of SAMs. Vertical diffusion processes were also investigated, and the highly packed SAM appears to prevent Pd permeation through the SAM to the substrate.

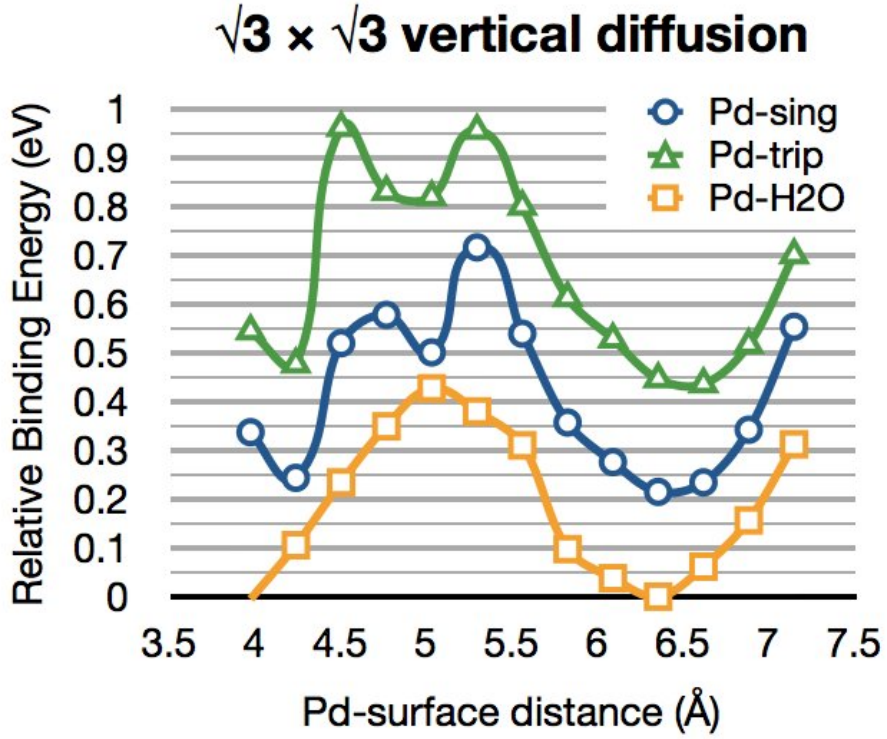

Abbildung 11.1: *Vertical diffusions for a Pd atom in its singlet state, triplet state, and in the presence of an explicit water molecule.*

All periodic density functional theory (DFT) calculations were performed with SeqQuest,[1] which is based on localized basis sets represented by linear combinations of contracted Gaussian functions (at the "double-zeta plus polarization"-level). We employed the PBE-GGA[2] exchange–correlation functional in tandem with standard (nonlocal) norm-conserving pseudopotentials. [3,4] Integrations in reciprocal space were performed with a converged Brillouin zone sampling of 8×8 k-points per $\sqrt{3}\times\sqrt{3}$ unit cell. Our studies represented the Au(111) surface as a three-layer slab, where the lowest two layers were fixed to the calculated bulk structure, while the top-most Au-layer, the 4MP-SAM molecules, and the adsorbed Pd atoms were allowed to freely optimize their geometry (up to < 0.1

eV/Å). Pd adsorption with different coverages was studied on both $\sqrt{3}\times\sqrt{3}$ and $2\sqrt{3}\times\sqrt{3}$ surface unit cells. The latter model involved 44 atoms and eliminated periodic constraints on the SAM. The $\sqrt{3}\times\sqrt{3}$ unit cell has a surface coverage of 1/3. In reality, a combination of different SAM structures are expected to be present on an Au(111) surface, however the $7\times\sqrt{3}$ adlayer[5] and the $\sqrt{3}\times\sqrt{3}$ structures represent the lower and higher limits in the high coverage SAM structures. We find that vertical diffusion of a Pd atom through the SAM is always unfavorable at high coverages such as the $\sqrt{3}\times\sqrt{3}$ structure (Fig. 11.1).
Potential energy surfaces (PES) were also calculated to describe the horizontal diffusion of atoms above a SAM. As was found previously,[5] single atoms must overcome a large barrier for diffusion across the top of the SAM. The presence of pre-adsorbed atoms on the surface, however, cause sizable changes in the structure of the SAM and the binding energy of subsequent metal atoms, and in the magnetic properties of the SAM (Fig. 11.2).

References

1. Verdozzi, C.; Schultz, P. A.; Wu, R.; Edwards, A. H.; Kioussis, N. *Phys. Rev. B* **2002**, *66*, 125408.

2. Perdew, J. P.; Burke, K.; Ernzerhof, M. *Phys. Rev. Lett.* **1996**, *77*, 3865-3868.

3. Hamann, D. R. *Phys. Rev. B* **1989**, *40*, 2980-2987.

4. Louie, S. G.; Froyen, S.; Cohen, M. L. *Phys. Rev. B* **1982**, *26*, 1738-1742. Keith, J.A.; Jacob, T. *Submitted to Nanoletters*

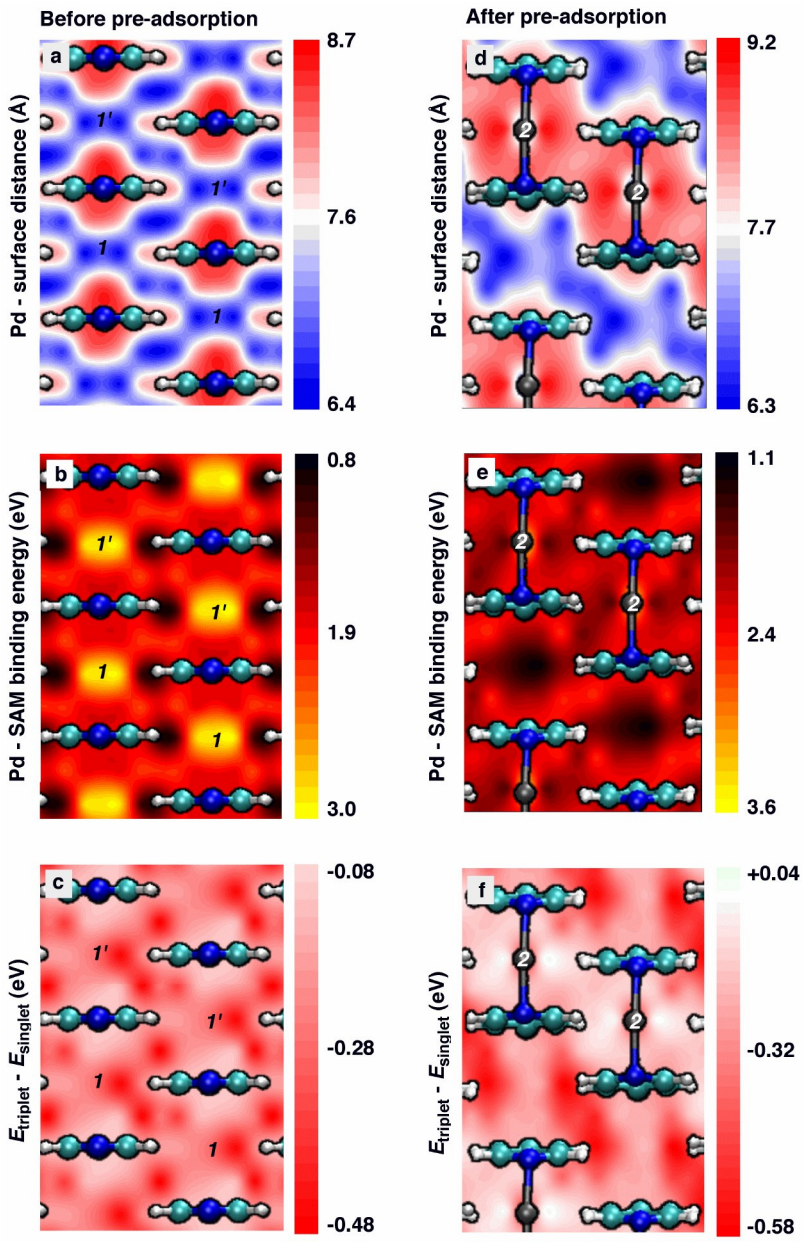

Abbildung 11.2: *Potential energy surfaces for atomic Pd diffusing across the clean $2\sqrt{3}\times\sqrt{3}$ 4MP-SAM (left) and across the $2\sqrt{3}\times\sqrt{3}$ 4MP-SAM with pre-adsorbed Pd atoms (right). The different figures show the Pd–surface height profiles [(a) and (d)], the Pd–SAM binding energy profiles [(b) and (e)], and the difference between triplet and singlet energies [(c) and (f)]. Positive values denote preference to triplet spin states.*

4.2.12 Numerical simulations of the magnetic properties of nanoscale alloys

J. Mokkath, M. Saubanère and G M. Pastor
Institut für Physik, Universität Kassel, 34140 Kassel, Germany

Strong electron-correlation phenomena and in particular magnetism are probably the most interesting and challenging topics in nanostructured materials research. Current activities range from fundamental investigations all over to materials-science studies geared to technological applications such as memory devices and high-density storage media. Recent experimental studies on atom-by-atom engineered structures have revealed a number of amazing effects such as the enhancement of orbital magnetism and magnetic anisotropy, long-range adatom ordering, magnetization reversal and spin-reorientation transitions, as well as non-collinear spin arrangements, quantum confinement and self-alignment of magnetic moments in nanowires. Consequently, the interest in theoretical developments and large-scale realistic numerical simulations on these systems has been growing steadily. In the following we present examples of investigations on novel magnetic nanoscale materials, which were performed at the Hessen's high-performance computing facilities and which were supported in part by the Deutsche Forschungsgemeinschaft.[1–4]

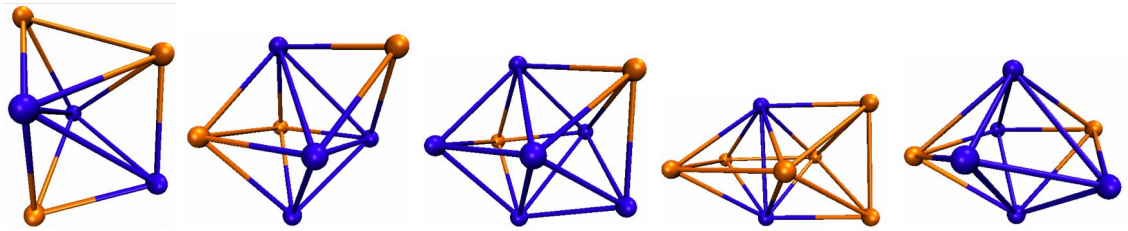

Abbildung 12.1: *Representative structures of small FeRh clusters*

Magnetism, structure and chemical order in small FeRh clusters

The theoretical study of binary-metal clusters is hindered by the diversity of geometrical conformations, ordered and disorder arrangements, as well as segregation tendencies, which pose serious challenges to both first-principles and model approaches. The interplay between cluster structure, chemical order and magnetism in FeRh clusters has been investigated by performing a comprehensive set of electronic calculations.[1] The structural, electronic and magnetic properties of small Fe_mRh_n clusters were determined in the framework of a generalized gradient approximation to density-functional theory. The optimized cluster structures are compact with a clear tendency to maximize the number of nearest-neighbor FeRh pairs (see Figure 12.1). For very small sizes the low-lying isomers present a different topology than the optimal structure, while for larger clusters the lowest-energy isomerizations imply mainly changes in the chemical order. The correlation between structure, chemical order, and magnetic behavior has been analyzed as a function of size and composition. All optimized clusters show ferromagnetic-like order. However, antiferromagnetic-like spin arrangements are found in some low-lying isomers. The average magnetic moment per atom μ_N increases approximately linearly with Fe content. A remarkable enhancement of the local Fe moments is observed as result of Rh doping. This is a consequence of the increase in the number of Fe d holes, due to FeRh charge transfer, combined with the extremely reduced local coordination. The Rh local moments, which are important already in the pure clusters, are not significantly enhanced by Fe doping. However, the overall stability of magnetism —as measured by the total energy gain upon spin polarization at T = 0— increases when Rh is replaced by Fe. Finally, the composition dependence of the electronic structure has been quantified. Further studies on 2nm CoRh alloy particles may be found in Ref. 2.

Local moment formation and screening of magnetic impurities in one-dimensional wires

The local moment formation in one-dimensional (1D) systems has been investigated in Ref. 3. The electronic and magnetic properties of Co and Ni impurities in finite Cu wires have been determined as a function of experimentally relevant parameters such as wire length, impurity-host distance, impurity position within the wire, and total spin polarization Sz. This includes ab initio results for the interatomic equilibrium distances, relative stability of different total spin configurations, local magnetic moments, electronic density of states, and induced magnetic moments in the 1D metal including their coupling with the impurity. The calculations show that the optimal total spin polarization is one above the minimal value. In fact, for chains having an even number of Cu atoms, the ground-state total spin is Sz = 1 for Ni doped wires and Sz = 3/2 for Co doped wires. Both Co and Ni impurities preserve their magnetic degree of freedom and develop large local magnetic moments in all low-lying spin configurations (Sz $\leq$ 5/2). These almost completely saturated impurity moments are largely dominated by the d-electron contributions. In the ground state the magnetic coupling between the impurity and the induced moments at the host atoms is ferromagnetic like (see). Thus, the local exchange energy dominates over hybridization and spin-fluctuation effects, at least in the framework of the present approximation to DFT. The local density of electronic states (LDOS) at the impurity is found to have essentially d character in the whole valence-band range. Large exchange splittings, consistent with saturated d moments, and a full minority-spin polarization of the LDOS at the Fermi energy are observed. The overall behavior is found to be very robust. Only marginal dependences on bond-length and impurity position are observed.

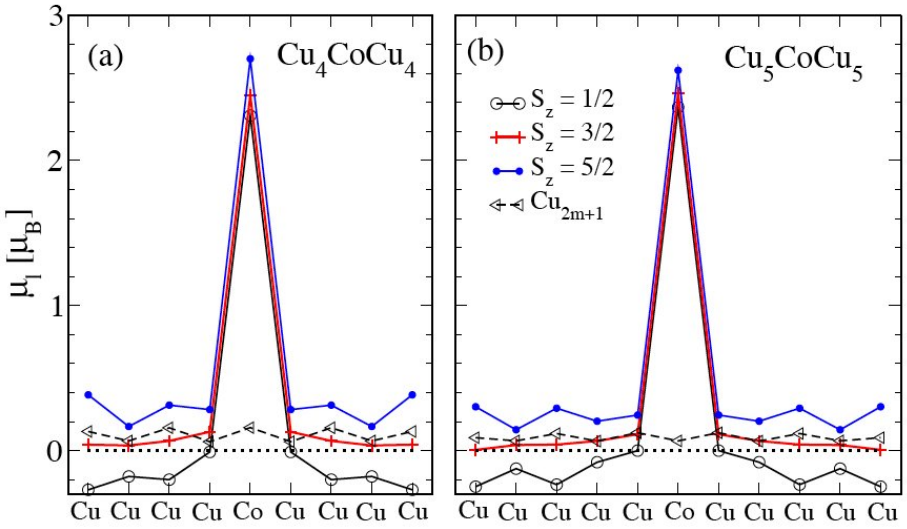

Abbildung 12.2: *Magnetization profiles of Ni and Co impurities in Cu wires.*

References

1. J. Mokkath and G. M. Pastor, submitted to Phys. Rev. B. (2010).
2. M. Muñoz-Navia, J. Dorantes-Davila, D. Zitoun, C. Amiens, N. Jaouen, A. Rogalev, M. Respaud and G.M. Pastor, Appl. Phys. Lett. **95**, 233107 (2009).
3. M. Saubanère, J. L. Ricardo-Chavez and G. M. Pastor, Phys. Rev. B. (2010).
4. S. M. Valvidares, J. Dorantes-Davila, H. Isern, S. Ferrer and G. M. Pastor, Phys. Rev. B **81** (2010), in press.

4.2.13 Dileptons and charm as probes of the strongly interacting quark-gluon plasma within parton-hadron-string-dynamics (PHSD) transport.

O. Linnyk[a], E. L. Bratkovskaya[a], W. Cassing[b]
[a]Institut für Theoretische Physik, JWG Universität Frankfurt am Main;
[b]Institut für Theoretische Physik, JL Universität Gießen.

Our ultimate goal is understanding the dynamical properties of the partonic phase with quarks, antiquarks and gluons as dynamical degrees of freedom (strongly-interacting QGP) and the phase transition to an interacting hadronic system that is colorless and confined. During 2009 we focused on studying how the QGP phase transition influences the charm and dilepton production. The charm quark degrees of freedom are of particular importance since they are expected to be dominantly produced in the early (QGP) state of the heavy ion collisions. The dileptons are particularly well suited for an investigation of the violent phases of a high-energy heavy-ion collision, because they can leave the reaction volume essentially undistorted by final-state interactions. The study of dileptons produced in relativistic heavy-ion collisions allows addressing the issue of chiral symmetry restoration and in-medium effects on hadrons, too. As 'research tools' we are using effective field theory based on the high temperature QCD and the microscopic Parton-Hadron-String-Dynamics (PHSD) transport approach.

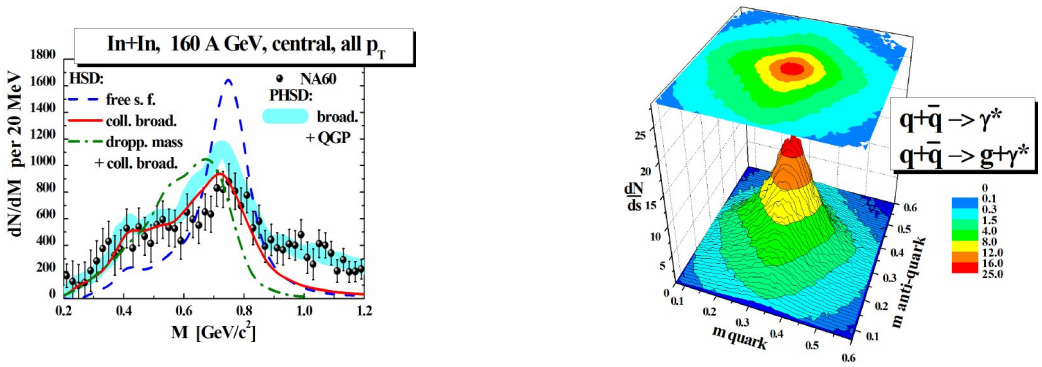

Abbildung 13.1: Left: *Quark masses in sQGP.* ***Right:*** *Spectra of dileptons at SPS energy.*

At RHIC and LHC energies the radiation from QGP is expected to constitute a large contribution to the dilepton spectrum. On the other hand, at lower energies one probes the physics of the nuclear matter at extremely high baryonic densities as will be produced at the future experimental facility FAIR. The FAIR facility will allow the study of charm hadron production closer to the threshold for charm production in pp reactions so that in-medium effects might have a strong influence on the open and hidden charm production. The dilepton production at FAIR energies will reflect the properties of hadrons in the dense nuclear medium.

References

1. O. Linnyk, E. L. Bratkovskaya, W. Cassing, J. Phys. G36, 064059 (2009),
   Charmed hadron signals of partonic medium

2. E. L. Bratkovskaya, W. Cassing, O. Linnyk, Phys. Lett. B 670, 428 (2009),
   Low mass dilepton production at ultrarelativistic energies

3. O. Linnyk, E. L. Bratkovskaya, W. Cassing, Nucl. Phys. A 830, 491 (2009),
   Dileptons from the strongly-interacting Quark-Gluon Plasma within the Parton-Hadron-String-Dynamics (PHSD) approach

4.2.14 Exotische hadronische Materie und Atomkerne

Prof. Dr. Stefan Schramm, Dr. Verônica Dexheimer, Jan Steinheimer, T. Schürhoff
Center for Scientific Computing, Frankfurt Institute for Advanced Studies und Institut für Theoretische Physik der Johann Wolfgang Goethe-Universität, Max-von-Laue-Straße 1, D-60438 Frankfurt am Main

Die Arbeitsgruppe ``Hadronische Materie'' beschäftigt sich seit einer Reihe von Jahren mit der Untersuchung von selbstkonsistenten hadronischen Modellen zur Beschreibung stark wechselwirkender Materie unter extremen äuß eren Bedingungen von Dichte, Temperatur und Isospin.

Ein Schwerpunkt ist die Untersuchung der Isospinabhängigkeit der starken Wechselwirkung, die relativ wenig verstanden ist. Diese Abhängigkeit wird besonders in extremen hadronischen Zuständen sehr wichtig, wenn etwa die Zahl der Neutronen

erheblich höher ist als die Protonzahl. Ein System mit nahezu maximaler Isospinasymmetrie ist der Neutronenstern. Ein anderer Bereich ist die Physik exotischer neutronenreicher Kerne.

Wie es sich in ursprünglichen detaillierten Studien gezeigt hat [1-3], kann man mit einem auf chiraler und Flavor-SU(3)-Symmetrie basierenden Modell eine quantitativ sehr gute Beschreibung von Kernmaterie im Grundzustand als auch von wesentlichen Eigenschaften von Atomkernen über ein groß es Gebiet von Proton- und Neutronzahlen erreichen. Weitere Rechnungen zeigen weiterhin gute Beschreibungen hochangeregter hadronischer Materie [4] sowie der Struktur von Neutronensternen [5]. Das erlaubt insbesonders die Untersuchung der Isospinabhängigkeit der Kernkraft, wie sie speziell in sehr neutronenreichen Umgebungen wichtig ist. Dazu gehört zum einen Neutronensternmaterie als auch die Eigenschaften exotischer Kerne in der Nähe der Stabilitätsgrenze bezüglich Neutronemission („neutron drip line“). Die Kenntnis des Verlaufs dieser Grenze ist auch für das Verständnis der stellaren Nukleosynthese entscheidend. Sowohl die Struktur der Isospinkräfte als auch Deformationseffekte haben entscheidenden Einfluss auf diesen Bereich exotischer Kerne. Eine systematische Untersuchung der Stabilitätsgrenze, ihre Isospinabhängigkeit als auch deren Korrelation mit Neutronensterneigenschaften ist eine wichtige, weitgehend unerledigte Aufgabe, die erheblichen numerischen Aufwand erfordert [6]. Auf experimenteller Seite besteht ein großes Interesse an der Physik exotischer Kerne, die eines der zentralen Forschungsgebiete der neuen FAIR-Beschleunigeranlage an der GSI, Darmstadt, darstellt.

Hier wird zurzeit der Einfluss von Hyperonen auf die Stabilität neutronenreicher Kerne studiert.

Mit demselben Modellansatz lassen sich hochangeregte Zustände beschreiben, die in ultrarelativistischen Schwerionenstößen erzeugt werden. Die in dem Modell erzeugte Zustandsgleichung der Materie bei gegebener Temperatur und chemischen Potential wird dazu in numerisch sehr anspruchsvolle relativistische molekulardynamische und dreidimesnionale hydrodynamische Simulationen integriert [7], womit Nichtgleichgewichts-studien der heißen und dichten hadronischen Materie möglich sind. Damit lässt sich die Phasenstruktur des Übergangs von einem Quark-Gluon-Plasma-Zustand zu der kalten hadronischen Materie beschreiben, was das zentrale Thema der Schwerionen-Forschungen an den Beschleunigern am RHIC, USA, an der GSI in Darmstadt und am CERN in Genf, darstellt.

In neuen Untersuchungen konnten wir hadronische und Quarkfreiheitsgrade in einem vereinheitlichten Modell beschreiben [8,9,10], wobei wir erstmals sowohl eine realistische Beschreibung von Atomkernen als auch die korrekten asymptotischen Freiheitsgrade bei hohen Temperaturen und Dichten in einer Rechnung integrieren konnten. Diese Resultate wurden von uns in numerischen hydrodynamischen Simulationen von ultrarelativistischen Schwerionen eingesetzt. Die isentropische Expansion des heißen und verdichteten Systems ist in der Figur, abhängig von der Strahlenergie dargestellt. Man sieht, wie das System bei der Expansion den Phasenübergang von Quark-Gluon-Plasma zu hadronischer Materie durchläuft [8].

Isentropen in ultralrelativistischen Schwerionenstößen bei unterschiedlichen Strahlenergien aufgetragen gegen Temperatur und chemischem Potential. Ein möglicher kritischer Endpunkt einer Linie von Phasenübergängen erster Ordnung ist dargestellt. Strahlenergien jenseits von 160 GeV/A (SPS) können diesen Bereich direkt treffen [8].

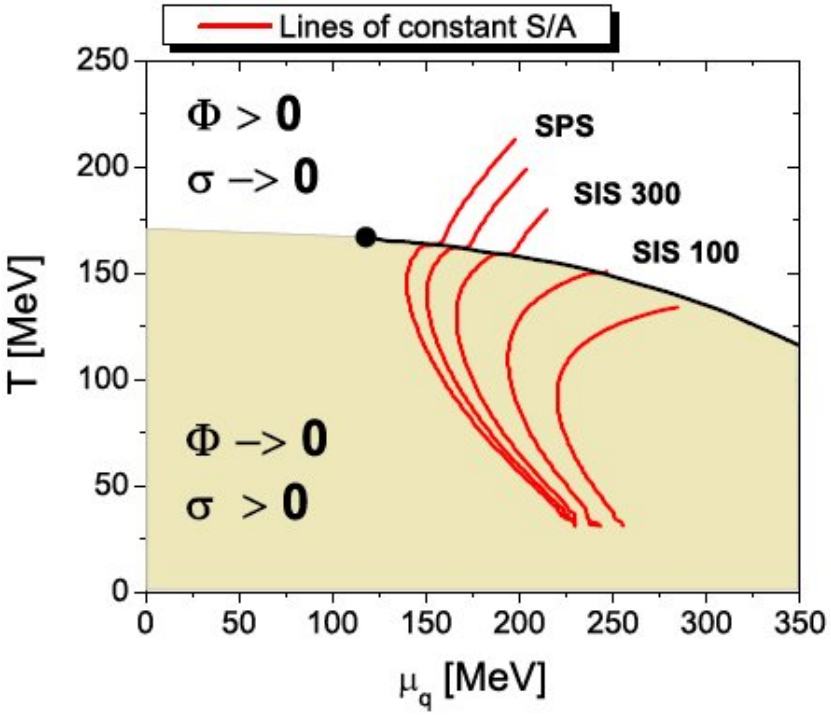

Verweise

1. S. Schramm, Phys. Rev. C **66**, 064310 (2002).
2. S. Schramm, Phys. Lett. B**560**, 164 (2003).
3. h. Beckmann, P. Papazoglou, D. Zschiesche, S. Schramm, H. Stöcker, and W. Greiner, Phys. Rev. C **65**, 024301 (2002)
4. D. Zschiesche, S. Schramm, H. Stöcker and W. Greiner, Phys. Rev. C **65** (2002) 064902.
5. V. Dexheimer and S. Schramm, Astrophys. Journal, 683, 943 (2008).
6. Khin-Nyan Linn, Doktorarbeit, Universität Frankfurt, 2008.
7. J. Steinheimer, M. Bleicher, H. Petersen, S. Schramm, H. Stöcker, D. Zschiesche, Phys. Rev. C **77**, 034901 (2008).
8. J. Steinheimer, V. Dexheimer, H. Petersen, M. Bleicher, S. Schramm, H. Stöcker, submitted to Phys. Rev. C, arxiv:hep-ph/0905.3099
9. J. Steinheimer, S. Schramm, H. Stöcker, submitted to Phys.Rev.C, arxiv:hep-ph/0909.4421
10. V. Dexheimer und S. Schramm, submitted to Phys. Rev. C, arxiv:astr-ph/0901.1748

4.2.15 Strongly interacting Fermi systems in 1/N expansion: From cold atoms to color superconductivity

Hiroaki Abuki and Tomás Brauner
Institut für Theoretische Physik, Goethe-Universität, Frankfurt am Main

We investigate the $1/N$ expansion proposed recently as a strategy to include quantum fluctuation effects in the nonrelativistic, attractive Fermi gas at and near unitarity. We extend the previous results by calculating the next-to-leading order correction to the critical temperature along the whole BCS–BEC crossover. We demonstrate explicitly that the extrapolation from the mean-field approximation, based on the $1/N$ expansion, provides a useful approximation scheme only on the BCS side of the crossover. We then apply the technique to the study of strongly interacting relativistic many-fermion systems. Having in mind the application to color superconductivity in cold dense quark matter, we develop, within a simple model, a formalism suitable to compare the effects of order parameter fluctuations in phases with different pairing patterns. Our main conclusion is that the relative correction to the critical temperature is to a good accuracy proportional to the mean-field ratio of the critical temperature and the chemical potential. As a consequence, it is significant even rather deep in the BCS regime, where phenomenologically interesting values of the quark–quark coupling are expected. Figure 15.1, adapted from [1], shows that the effect of pairing fluctuations is in a sense similar to that of a finite strange quark mass. The size of the fluctuation corrections is small in the far BCS regime and increases as the density drops, eventually becoming as large as tens per cent. Details of computations may be found in [2].

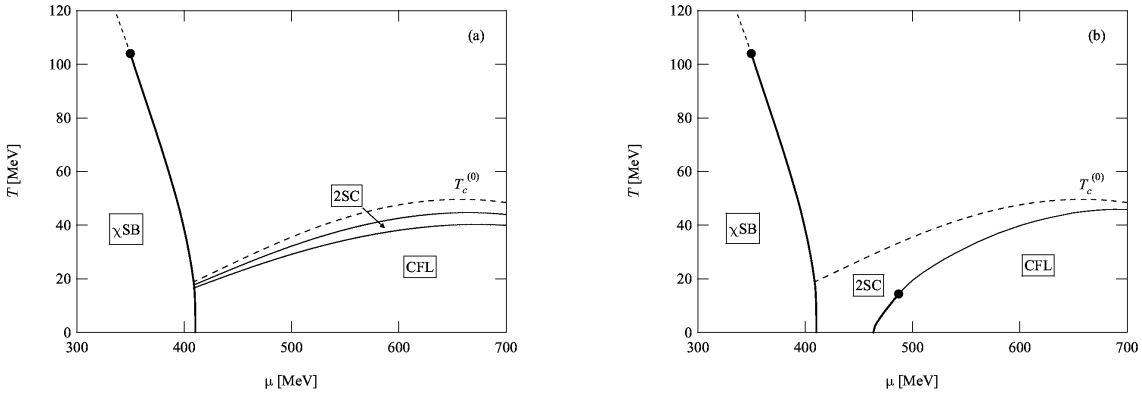

Abbildung 15.1: *Left panel: Phase diagram at vanishing strange quark mass M_s but* with *fluctuation effects. Right panel: The same phase diagram for $M_s = 200$ MeV* without *fluctuation effects. $T_c^{(0)}$ is the critical temperature at the leading order in $1/N$.*

References

1. H. Abuki and T. Kunihiro, "Extensive study of phase diagram for charge neutral homogeneous quark matter affected by dynamical chiral condensation: Unified picture for thermal unpairing transitions from weak to strong coupling," Nucl. Phys. A **768**, 118 (2006).

2. H. Abuki and T. Brauner, "Strongly interacting Fermi systems in $1/N$ expansion: From cold atoms to color superconductivity," Phys. Rev. D **78**, 125010 (2008).

4.2.16 Design Studies on a High Current Storage Ring

M. Droba, N. Joshi, O. Meusel, K. Schulte, U. Ratzinger
Institut für Angewandte Physik, Goethe Universität, Frankfurt am Main

A high current storage ring [1] for multi- Ampere proton and ion beams with eneries in the 100 AkeV to 1 AMeV range was designed. The *Figure-8* (see Abb. 16.1) configuration with a main longitudinal magnetic field component (in 5-7 T range) provides quite a homogenous focusing channel with additional compensation of various drifts in curved sectors. The folded magnetic flux structure was discretized on a numerical mesh to describe charged particle motion in such a geometry.

[!h]

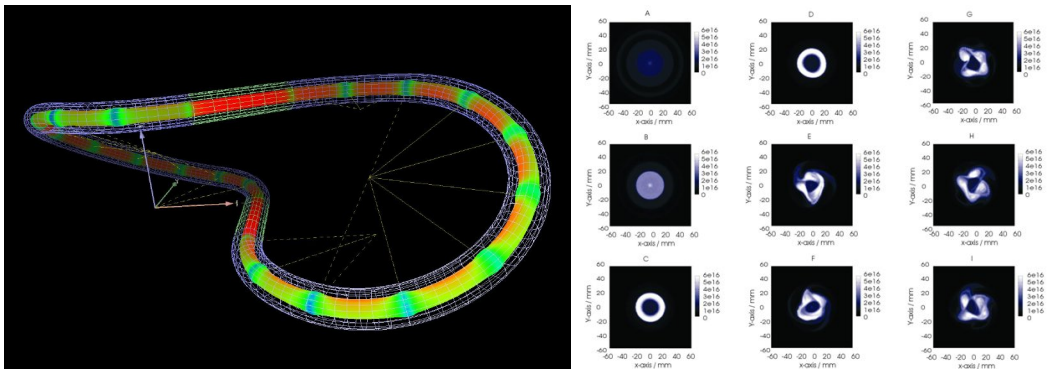

Abbildung 16.1: *An example of Figure-8 geometry with a color coded magnetic field strength on a flux surface (left), evolution of diocotron instability (right)*

The PIC (Particle-in-Cell) method is used to divide the charge density on the grid points, distributed on typically 10 processors. The electric potential is solved numerically by an iterative method (BiCGSTAB - BiConjugate Gradient Stabilized Method), where the potentials stored on nodes asymptotically converge to the global solution. Particle motion is solved by the guiding center technique with fields interpolated from mesh points. The whole simulation is running on 20-30 processors of the CSC Opteron Cluster for several days. Results showed stable orbits for the beam motion in clockwise and anticlockwise directions. Especially, the beam colliding zones are of great interest and will be studied in the future in detail.
Parallel simulation studies on the so called *diocotron* instabillity were done. Multi species (ions and electrons) code in cylindrical geometry was written using the same techniques for field calculation as mentioned above. Due to the crossed ExB fields in a hollow density profile charged particle distributions tend to generate drift waves which destroy the confinement. Typically the time evolution of this instabilities is in a range of 10ns - 1μs depending on the charge density and magnetic fields. The controlling and damping of the instability is crucial for the storage ring and for the Gabor plasma lens device[2], for which a constant electron density distribution is essential. All numerical studies are important for designing and optimisation of the proposed storage ring and investigation of collective phenomena in the confinement zones.

Verweise

1. Droba, M., et. al., “Design Studies on a Novel Stellarator Type High Current Ion Storage Ring”, EPAC06, Edinburgh, UK, Jun 2006, pp.297.

2. Schulte, K., et. al., “A Space Charge Lens for Focusing Uranium Beams”, GSI Scientific Report 2008.

4.2.17 Ratio Fluctuations in Nucleus-Nucleus Collisions from Microscopic Transport Approach

V.P.Konchakovski, E.L.Bratkovskaya
Institut für Theoretische Physik, JWG Universität Frankfurt, Germany

Event-by-event fluctuations qof the kaon to pion number ratio in nucleus-nucleus collisions aqre studied within the statistical hadron-resonance gas model q(SM) for different statistical ensembles and in the Hadron-String-Dynamics (HSD) transport approach [1]. Substantial differences in the HSD and SM results are found for the fluctuations and correlations of the kaon and pion numbers.

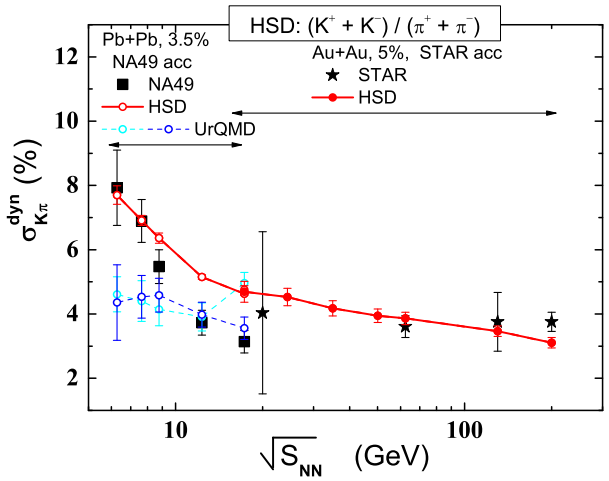

Abbildung 17.1: *The HSD results for the $\sigma_{dyn}^{K/\pi}$ excitation function in comparison to the experimental data measured by the NA49 Collaboration at SPS and STAR Collaboration at RHIC*

It has been found that the HSD model can qualitatively reproduce the measured excitation function for the K/π ratio fluctuations in central Au+Au (or Pb+Pb) collisions from low SPS up to top RHIC energies (Fig. 17.1). Accounting for the experimental acceptance as well as the centrality selection has a relatively small influence on σ_{dyn} and does not change the shape of the σ_{dyn} excitation function.
Thus, the HSD hadron-string model - which does not have a QGP phase transition and not explicitly includes the quark and gluon degrees of freedom - can reproduce qualitatively the experimental excitation function. In particular, it gives the rise of σ_{dyn} with lowering the bombarding energy. This fact brings to the conclusion that the observable σ_{dyn} might dominantly signal of nonequilibrium string dynamics rather than a phase transition of hadronic to partonic matter or to the QCD critical point. These predictions impose a challenge for future experiments.

References

1. M. I. Gorenstein, M. Hauer, V. P. Konchakovski and E. L. Bratkovskaya, Phys. Rev. C **79** (2009) 024907.

4.2.18 Microscopic description of the phase transition from hadronic to partonic matter and dynamics of hadronization

E. L. Bratkovskaya[a], *W. Cassing*[b]
a Institut für Theoretische Physik, Universität Frankfurt, Germany
b Institute für Theoretische Physik, Universität Giessen, Germany

The nature of confinement and the dynamics of the phase transition from hadronic to partonic mattre is an outstanding question of todays physics. The dynamics of partons, hadrons and strings in relativistic nucleus-nucleus collisions is analyzed within the novel Parton-Hadron-String Dynamics (PHSD) transport approach, which is based on a dynamical quasiparticle model for partons (DQPM) matched to reproduce recent lattice-QCD results - including the partonic equation of state - in thermodynamic equilibrium. Scalar- and vector-interaction densities are extracted from the DQPM as well as effective scalar- and vector-mean fields for the partons. The transition from partonic to hadronic degrees of freedom is described by covariant transition rates for the fusion of quark-antiquark pairs or three quarks (antiquarks), respectively, obeying flavor current-conservation, color neutrality as well as energy-momentum conservation. Since the dynamical quarks and antiquarks become very massive close to the phase transition, the formed resonant 'pre-hadronic' color-dipole states ($q\bar{q}$ or qqq) are of high invariant mass, too, and sequentially decay to the groundstate meson and baryon octets increasing the total entropy.

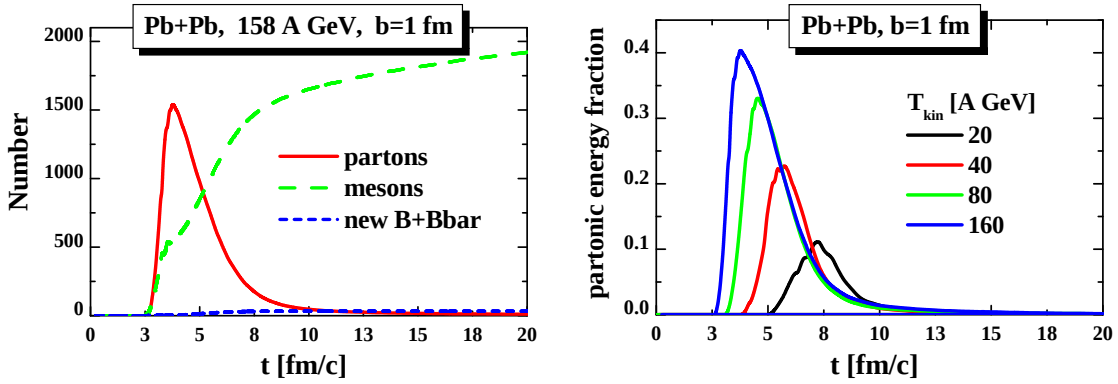

Abbildung 18.1: *L.h.s.: The number of produced partons (solid red line), mesons (long dashed green line) and newly produced baryon + antibaryons (blue dashed line) as a function of time for Pb+Pb at 158 A·GeV (for b=1fm). R.h.s.: The partonic energy fraction as a function of time for impact parameter b = 1 fm for Pb+Pb at 160, 80, 40 and 20 A·GeV.*

The PHSD approach is applied to nucleus-nucleus collisions from 20 to 160 A·GeV in order to explore the space-time regions of 'partonic matter'. We find that even central collisions at the top-SPS energy of 158 A· GeV show a large fraction of non-partonic, i.e. hadronic or string-like matter, which can be viewed as a hadronic corona. Studying in detail Pb+Pb reactions from 40 to 158 A·GeV - we observe that the partonic phase has a very low impact on rapidity distributions of hadrons but a sizeable influence on the transverse mass distribution of final kaons due to the repulsive partonic mean fields. Furthermore, we find a significant effect on the production of multi-strange antibaryons due to a slightly enhanced $s\bar{s}$ pair production in the partonic phase from massive time-like gluon decay and a larger formation of antibaryons in the hadronization process.

References

1. W. Cassing and E.L. Bratkovskaya, *'Parton-Hadron-String Dynamics: an off-shell transport approach for relativistic energies'*, **Nucl. Phys. A831** (2009) 215.

2. W. Cassing and E.L. Bratkovskaya, *'Parton transport and hadronization from the dynamical quasiparticle point of view'*, **Phys. Rev. C 78** (2008) 034919.

3. W. Cassing, E.L. Bratkovskaya, Y.-.Z. Xing, *'Parton dynamics and hadronization from the sQGP'*, **Prog. Part. Nucl. Phys. 62** (2009) 359-364.

4.2.19 Orbital-dependent exchange-correlation energy functionals

E. Engel, R. N. Schmid
Center for Scientific Computing, J.W.Goethe-Universität Frankfurt am Main

The success of density functional theory is based on the quality of the present standard approximation for the exchange-correlation (xc) energy functional, the generalized gradient approximation (GGA). However, just as the older local density approximation (LDA), the GGA fails for important classes of materials, as for instance highly correlated solids. A systematic improvement over the GGA is offered by xc-functionals which depend on the Kohn-Sham (KS) orbitals, rather than just on the density. In this formalism, the exchange energy can be treated exactly (EXX), which solves the long-standing self-interaction problem in the LDA and GGA. As a consequence, one e.g. obtains a Rydberg series of unoccupied states for neutral atoms, implying the existence of negative atomic ions. Applications to solids point at an improved description of the band gaps of semiconductors.
Recently, however, this general perception of improvement by the EXX approach has been questioned by the first full-potential linearized-augmented-plane-wave (LAPW) calculations with the EXX [1]. In many cases, including such elementary solids as diamond, the LAPW band gaps turned out to be much larger (or much smaller) than the EXX values published earlier, which were mostly based on pseudopotential (PP) calculations. The discrepancy between PP and LAPW data was attributed to the missing core-valence interaction in the PP approach.

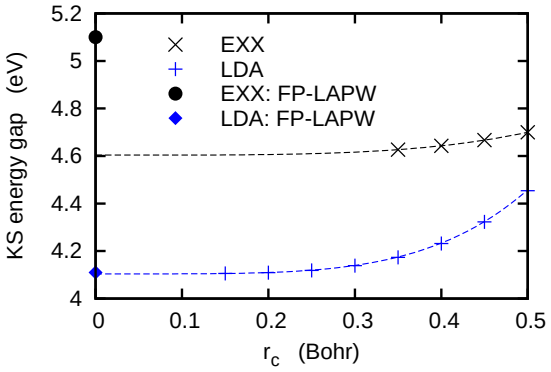

Abbildung 19.1: *Fundamental KS band gap of diamond versus AE cut-off radius r_c: LDA versus EXX-only results. Also shown are 2-parameter fits to the data at $r_c = 0.35\,Bohr$ and $0.45\,Bohr$, using $E_g(r_c) = E_g(0) + \alpha r_c^4$, and the corresponding LAPW gaps.*

In the present project [2] the role of the core-valence interaction in EXX calculations was investigated by comparison of PP with all-electron (AE) results for diamond and lithium. The same full-potential framework is applied in the case of both approaches, checking carefully the convergence of all results. The AE calculations are performed with a non-zero cut-off radius r_c for the $1s$-orbital (in order to allow the consistent use of plane-wave basis sets) and then extrapolated to $r_c = 0$ (compare Fig.19.1). It was found that the AE band structures of both prototype solids are well reproduced by the PP scheme. The PP and AE band gaps differ by less than 0.1 eV, in obvious contrast to the data of [1]. This result gives further credence to the use of pseudopotentials in combination with the EXX.
In a second project [3] the importance of a proper cancellation of the self-interaction by the EXX was investigated for the antiferromagnetic (type II) phases of the transition metal monoxides MnO, FeO, CoO and NiO. In contrast to the LDA and GGA (see e.g. [4]), the EXX (combined with LDA correlation) correctly yields insulating ground states for all four compounds (see Fig.19.2 for the band structure and density of states of FeO). The values for the band gaps and magnetic moments obtained with the EXX method are in good agreement with the experimental data. State-dependent potentials, as used in the LDA+U or SIC-LDA methods, are thus not required for obtaining a gap for these highly correlated systems.
EXX calculations for solids are still extremely challenging, due to the high computational demands resulting from the solution of the integral equation which determines the corresponding EXX potential (as is obvious from the discrepancies between [1] and [2]). This is true in particular for

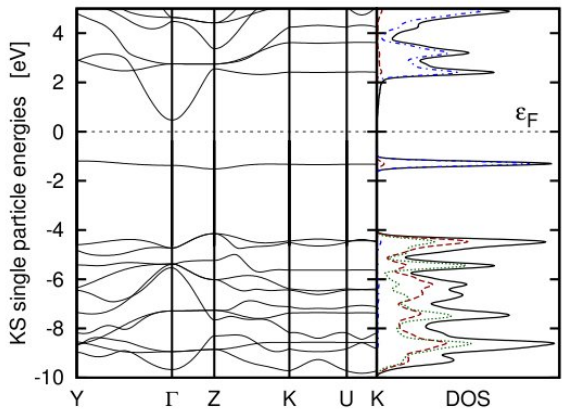

Abbildung 19.2: *Band structure of FeO (AF II) obtained by PP calculation with EXX in combination with LDA correlation. Also shown are the total (solid, black line) and partial densities of states (DOS): O2p – dashed, red line; Fe3d at sites with majority spin ↑ – dotted, green line; Fe3d at sites with majority spin ↓ – dash-dotted, blue line.*

full-potential calculations without any approximation for the Green's function, which determines the response of the system (the response enters into the integral equation). EXX calculations for solids therefore require substantial computing resources, which, for the present project, have been provided by the HPC cluster of the CSC at Goethe University Frankfurt.

References:

1. S. Sharma, J. K. Dewhurst, and C. Ambrosch-Draxl, Phys. Rev. Lett. **95**, 136402 (2005).
2. E. Engel, Phys. Rev. B, **80** 161205(R) (2009).
3. E. Engel and R. N. Schmid, Phys. Rev. Lett. **103**, 036404 (2009).
4. P. Dufek, P. Blaha, and K. Schwarz, Phys. Rev. B **50**, 7279 (1994).

4.2.20 Ultrakalte Atome in optischen Gittern & Nanostrukturen

Walter Hofstetter, Reza M. Bakhtiari, Antonio Privitera, Irakli Titvinidze, Liang He, Yongqiang Li, Denis Semmler, Julia Wernsdorfer, Ulf Bissbort, David Roosen
Frankfurt

Der Fokus der Forschung unserer Arbeitsgruppe liegt auf zwei Bereichen der theoretischen Physik der kondensierten Materie: (i) Quantenphasen ultrakalter Atome in optischen Gittern und (ii) elektronischer Transport in Nanostrukturen.

Ultrakalte Atome in optischen Gittern

Ultrakalte Atome in optischen Gittern erlauben eine direkte experimentelle Realisierung von stark korrelierten Quanten-Vielteilchensystemen. Diese Systeme kennzeichnen sich durch ihre Reinheit und die Kontrollierbarkeit der eingehenden physikalischen Parameter aus. Hierdurch lassen sich fundamentale Modelle der theoretischen Festkörperphysik simulieren sowie neuartige Quantensysteme realisieren, die fundamental neue Physik aufweisen. Im Nachfolgenden werden unsere Forschungsgebiete kurz aufgeführt.

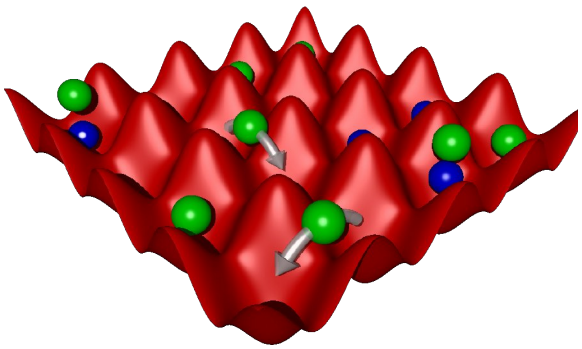

Abbildung 20.1: *Optisches Gitter mit ultrakalten Atomen.*

In neuen Experimenten werden **Mischungen verschiedener bosonischer Atome** (z.B. ^{87}Rb und ^{41}K) in einem optischem Gitter untersucht [1]. Ein hochinteressantes Phänomen ist der auftretende **Quantenmagnetismus**. Um diesen zu beschreiben, haben wir analog zur erfolgreichen fermionischen Methode die **bosonische dynamische Molekularfeldtheorie** entwickelt [2]. Mit dieser konnten wir zweikomponentige Systeme und deren vielfältiges Phasendiagramm charakterisieren. Kürzlich haben wir die Methode um Ortsauflösung erweitert, womit wir den Einfluss optischen Falle untersuchen und somit eine hohe Vergleichbarkeit mit experimentellen Resultaten erreichen können. Neueste Ergebnisse zeigen das Auftreten verschiedener Spinordnungen, wie z.B. XY-Ferromagnet and XY-Superfluid. Im Kontext zweikomponentiger bosonischer Mischungen interessiert uns zudem eine realistische Beschreibung von Nichtgleichgewichtseffekten in aktuellen Experimenten [3], wobei mit Hilfe der dynamischen Gutzwiller-Theorie [4] die Dynamik in einem solchen System beim "Anschalten" des optischen Gitters untersucht wird. Wir konnten zeigen [5], dass die Adiabatizität bei diesen Prozessen verletzt wird. Darüberhinaus konnten die bisher nur experimentell beobachteten Oszilationen [6] der Visibilität des Kondensats theoretisch reproduziert und erklärt werden.

Des Weiteren studieren wir **resonante Suprafluidität** ultrakalter Fermionen, indem wir eine Mischung aus Fermionen und bosonischen Feshbach-Molekülen betrachten [7]. Dieses System wird durch das Bose-Fermi-Hubbard Modell beschrieben, welches sowohl die ortsabhängige Wechselwirkung der Fermionen untereinander, der Bosonen untereinander, als auch die Wechselwirkung zwischen Fermionen und Bosonen berücksichtigt. Zusätzlich zu diesen Wechselwirkungen enthält das betrachtete Modell auch einen Feshbach-Term, mittels welchem zwei Fermionen in ein molekulares Boson umgewandelt werden und umgekehrt. Da diese verschiedenen Wechselwirkungen jeweils anziehend oder abstoßend sein können, ergibt sich ein reichhaltiges Phasendiagramm. Je nach Wahl der Parameter erhält man eine suprafluide Phase, Antiferromagnetismus, Ladungsdichtewellen, Mott-Isolatoren, metallische Phasen oder auch Phasenseparation.

Von großem aktuellen Interesse sind auch Mischungen aus **Fermionen mit drei verschiedenen "Farbladungen"** (Hyperfeinzuständen) [8,9,10] in optischen Gittern. Befinden sich alle drei Fermionen an ein und demselben Gitterplatz, so kann erreicht werden, dass sie sich gegenseitig

abstoßen, was einem effektiven Verbot dieser Besetzung gleich kommt [11]. Erhöht man die Wechselwirkung zweier Fermionen an einem Gitterplatz, so beobachtet man für ein System ohne diese 3-Teilchen-Abstoßung einen Quanten-Phasenübergang von einer Farb-Supraflüssigkeit zu einer trionischen Phase [12,13], welche zusätzlich eine Ladungsdichtewelle aufweist. Berücksichtigt man allerdings die 3-Teilchen-Abstoßung, so ändert sich das Phasendiagramm qualitativ: die Phasengrenze verschwindet und man findet immer eine Farb-suprafluide Phase. Im Gegensatz zur trionischen Phase für den Fall ohne Abstoßung, kann man nun eine Tendenz zur "Phasenseparation" beobachten: das System bildet spontan Domänen aus, in denen sich ausschließlich Cooper-Paare zweier der drei Fermionen-"Flavors" aufhalten.

Weiterhin studieren wir **Fermionen in inhomogenem Umfeld**, wie z. B. einem optischen Potential. Um die auftretenden inhomogenen Quantenzustände beschreiben zu können, benötigen wir theoretische Methoden, welche ohne Translationsinvarianz, also ohne den Impuls als Quantenzahl, auskommen. Hierzu haben wir eine verallgemeinerte Version der dynamischen Molekularfeldtheorie (DMFT) entwickelt, welche eine positionsabhängige Selbstenergie zulässt [14]. Diese Ortsraum-DMFT erlaubt es uns beispielsweise Mischungen verschiedener Fermionen zu untersuchen und dort den Effekt der Wechselwirkungsstärke auf die Ausdehnung der atomaren Wolke, welche sich in Experimenten einfach messen lässt, zu berechnen. Für mehrkomponentige Systeme, deren Teilchenzahl nicht ausgeglichen ist, finden wir außerdem "gekippten" Antiferromagnetismus.

Unordnung in optischen Gittern verändert das quantenmechanische Verhalten der Atome drastisch. In Systemen ultrakalter, wechselwirkender Bosonen kann eine beliebig schwache Hinzugabe von Unordnung beispielsweise zu Anderson-Lokalisierung führen. In Anwesenheit von Unordnung und Wechselwirkung zwischen den Bosonen tritt neben den bisher gut erforschten Mott Isolator- und kondensierten Phasen eine neue exotische Bose-Glas Phase auf. Eine Beschreibung dieser Phase bei $T = 0$ mittels der in unserer Arbeitsgruppe entwickelten stochastischen Molekularfeldnäherung [15,16] dient als Ausgangspunkt zur weiteren Analyse komplexer Systeme. Insbesondere werden Effekte bei endlichen Temperaturen berücksichtigt und ultrakalte Atome in dreidimensionalen Gittern mit anisotroper Unordnung betrachtet, was von unmittelbarem Interesse für aktuelle Experimente ist [17]. Darüberhinaus verwenden wir Erweiterungen der fermionischen dynamischen Molekularfeldtheorie, die die Analyse ungeordneter stark korrelierter Systeme ermöglichen. Einerseits kann das Phänomen der Anderson-Lokalisierung über die typische Medium-Theorie [18,19] beschrieben werden, womit wir kürzlich einen neuartigen unordnungsinduzierten Antiferromagneten für Spin-1/2-Fermionen nachweisen konnten [20]. Lokalisierungseffekte können rigoroser mit Hilfe der statistischen dynamische Molekularfeldtheorie [21] beschrieben werden. Diese Methode haben wir kürzlich implementiert und stark korrelierte Fermionen in binär ungeordneten Gittern studiert. In dieser Arbeit konnten wir die komplexe Lokalisierungsphysik von diskret ungeordneten Systemen auflösen und einen Mott-Isolator Quantenphasenübergang bei nicht ganzzahliger Füllung nachweisen [22]. Momentan verallgemeinern wir die Methode zu endlichen Temperaturen und experimentell realistischer Speckle-Unordnung. Durch die somit erreichte Nähe zu zukünftigen experimentellen Realisierungen sind neue Einsichten in das bislang kaum verstandene Zusammenspiel von Wechselwirkung und Unordnung möglich, das von fundamentalen Interesse in der theoretischen Festkörperphysik ist.

Im Laufe des letzten Jahres sind erste Messungen spektroskopischer Größen mittels der zwei-Photonen **Bragg-Spektroskopie** an kalten Bosonen in optischen Gittern durchgeführt worden. Diese ermöglichen Energie- und Impulsaufgelöste Einblicke in diese Systeme über die gesamte Bandbreite einstellbarer Wechselwirkungsstärken, die weit über etablierte Methoden wie die zeitabhängige Gross-Pitaevskii Theorie hinausgehen. Die nicht-perturbative zeitabhängige bosonische Gutzwiller Methode wurde für diese Systeme weiterentwickelt und ermöglicht eine Simulation realistisch großer, sowie inhomogener kondensierter Systeme für beliebige Wechselwirkungsstärken. Während im Grenzfall schwacher Wechselwirkung die Gross-Pitaevskii Theorie mit der zugehörigen akustischen Mode reproduziert wird, beobachtet man für starke Wechselwirkung eine zusätzlich "Amplitudenmode", die auch bei kleinen Impulsüberträgen eine endliche Energielücke beibehält,

allerdings bisher experimentell nicht nachgewiesen worden ist.

Nanostrukturen

In unserer Arbeitsgruppe wird neben den obigen Themen die Physik von **Quanten-Störstellen-Modellen** untersucht. Wir sind hierbei insbesondere an Phänomenen interessiert, welche bei sehr tiefen Temperaturen in diesen Systemen auftreten. Bei Temperaturen in der Nähe des absoluten Nullpunktes reicht eine störungstheoretische Beschreibung der Systeme oftmals nicht mehr aus. Dies macht es notwendig, nicht-perturbative numerische Verfahren, wie z. B. die Numerische Renormierungsgruppe (NRG) [12], zu benutzen. Unser Ziel ist es, mit Erweiterungen dieser Methode auch Nicht-Gleichgewichtsphänomene zu studieren.

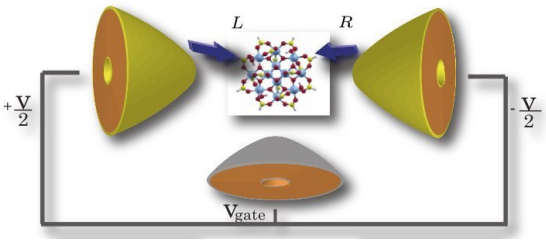

Abbildung 20.2: *Molekularer Magnet an metallischen Leitern.*

Motiviert durch Experimente, bei denen es erstmals möglich war, isolierte molekulare Magneten an metallische Leiter zu koppeln und Stromtransport durch sie zu messen [13], untersuchen wir den zeitabhängigen Kondo-Effekt in molekularen Magneten [14] sowie die Beeinflussung des Stromtransport durch Vibrationsanregungen des Moleküls.

Des weiteren interessiert uns der Effekt bosonischer Anregungen auf die Dynamik gekoppelter Spins. Ein einfaches Modell, welches zur Beschreibung von Bits in Quantencomputern bis hin zum Elektronentransport in Biomolekülen vielfältige Anwendungen hat, besteht aus zwei gekoppelten Spins, die an ein gemeinsames "Bad" bosonischer Teilchen koppeln. Wir untersuchen das Zusammenspiel aus direkter Kopplung der beiden Spins durch eine Dipol-Wechselwirkung, Dekohärenz der einzelnen Spins durch bosonische Anregungen des Systems und einer indirekten Wechselwirkung der beiden Spins, die durch das gemeinsames Spektrum bosonischer Teilchen induziert wird.

Verweise

1. I. Bloch, Physics World **17**, 25-29 (2004).
2. A. Hubener. M. Snoek and W. Hofstetter, Phys. Rev. B **80**, 245109 (2009).
3. J. Catani, L. D. Sarlo, G. Barontini, F. Minardi and M. Inguscio, Phys. Rev. A **77** (2008).
4. M. Snoek and W. Hofstetter, Phys. Rev. A **76**, 051603 (2007).
5. J. Wernsdorfer, M. Snoek, and W. Hofstetter, preprint arXiv:0911.0697.
6. T. Gericke, F. Gerbier, A. Widera, S. Fölling, O. Mandel and I. Bloch, Journal of Modern Optics **54**, 735 (2007).
7. I. Titvinidze, M. Snoek and W. Hofstetter, Phys. Rev. Lett. **100**, 100401 (2008); Phys. Rev. B **79**, 144506 (2009).
8. T. Ottenstein, T. Lompe, M. Kohnen, A.N. Wenz and S. Jochim, Phys. Rev. Lett. **101**, 203202 (2008).
9. J.H. Huckans, J.R. Williams, E.L. Hazlett, R.W. Stites and K.M. O'Hara, Phys. Rev. Lett. **102**, 165302 (2009).
10. C. Honerkamp and W. Hofstetter, Phys. Rev. B **70**, 094521 (2004), Phys. Rev. Lett. **92**, 170403 (2004).
11. A. Kantian, M. Dalmonte, S. Diehl, W. Hofstetter, P. Zoller and A.J. Daley, Phys. Rev. Lett. **103**, 240401 (2009).
12. A. Rapp, W. Hofstetter and G. Zarand, Phys. Rev. B **77**, 144520 (2008).

13. A. Rapp, G. Zarand, C. Honerkamp and W. Hofstetter, Phys. Rev. Lett. **98**, 160405 (2007).

14. M. Snoek, I. Titvinidze, C. Töke, K. Byczuk and W. Hofstetter, NJP **8**, 093008 (2008).

15. U. Bissbort and W. Hofstetter, Europhys. Lett. **86**, 50007 (2009).

16. U. Bissbort, R. Thomale and W. Hofstetter, preprint arXiv:0911.0923.

17. M. White, M. Pasienski, D. McKay, S.Q. Zhou, D. Ceperley and B. DeMarco, Phys. Rev. Lett. **102**, 055301 (2009).

18. V. Dobrosavljević, A.A. Pastor and B.K. Nikolić, Europhys. Lett. **62**, 76 (2003).

19. K. Byczuk, W. Hofstetter and D. Vollhardt, Phys. Rev. Lett. **94**, 056404 (2005).

20. K. Byczuk, W. Hofstetter and D. Vollhardt, Phys. Rev. Lett. **102**, 146403 (2009).

21. V. Dobrosavljević and G. Kotliar, Phys. Rev. Lett. **78**, 3943 (1997).

22. D. Semmler, K. Byczuk and W. Hofstetter, preprint arXiv:0911.0934.

23. H. Heersche et al., Phys. Rev. Lett. **96**, 206801 (2006).

24. K.G. Wilson, Rev. Mod. Phys. **47**, 773 (1975).

4.2.21 Pion induced coherent strangeness production

Stefan Bender
Institut für Theoretsiche Physik, Universität Gießen

We investigated pion induced coherent strangeness production on light (^{12}C) and medium-heavy (^{40}Ca, ^{51}V, ^{89}Y) nuclei with a covariant model. This model was based on a Lagrangian approach, where resonance excitation and decay is the driving mechanism behind the elementary process. The aim of this work was to apply this model, which was already successfully applied to strangeness production on nuclei in proton [1, 2] and photon [3] induced reactions, to pion-nucleus reactions.

The first discovery of a hypernucleus, that is, a nucleus where one of the nucleons is replaced by a particle containing a strange quark (in our case this is a Λ), goes back to the observation of cosmic rays in emulsion chambers in 1952. A historical review of the physics of strange particles can be found, for example, in [4]. Later experiments with hypernuclei were performed at CERN and at the Brookhaven National Laboratory (BNL). Other experiments were performed in Japan at KEK and even more are planned for the future [5], for example at MAMI-C and PANDA-GSI [6].

Furthermore, hypernulcei can be produced in secondary reactions in heavy-ion collisions [7, 8, 9]. In these processes, particles from the fireball from the primary interaction reach the—up to then—spectator core and produce strange particles, by the same process that we consider in this thesis. This process, induced by heavy-ion reactions, is subject to active research, theoretically for example within the semiclassical transport model approaches [10, 11], as well as experimentally by the HypHI collaboration [12].

An extensive review on the production and decay of hypernuclei by Bandō et al. can be found in [13], where also different production mechanisms are discussed. The theoretical approaches to the experimental data deal with the production [14] or the polarisation of hypernuclei [15, 16] in (π^+, K^+) reactions. The experiments were mostly done in Japan at the KEK facility [17, 18, 19, 20, 21]. A recent review on the available spectroscopic data using the various reactions can be found in [22].

Since the Λ is not subject to Pauli blocking with respect to the other nucleons, it provides an excellent probe for the interplay of single-particle and many-body degrees of freedom in nuclei. They are, therefore, a suitable choice when it comes to verify our models of these bound states and for doing spectroscopy. It is a field of ongoing active research as can be seen by the variety of experiments in this area, some of them are listed above and still more are planned.

The theoretical description, however, gets rather involved since one is dealing with interacting many-body systems and approximations are necessary when dealing with them. Most of the theoretical models used so far to describe the (π^+, K^+) reaction employ a non-relativistic distorted wave impulse approximation (DWIA) framework [23] (see also Ref. [13] for a comprehensive review of these models) without resolving the production vertex. In these calculations, the Λ bound states are generated by solving the Schrödinger equation with Woods–Saxon or harmonic oscillator potentials. However, for processes involving momentum transfers of typically 300 MeV/c or more, a non-relativistic treatment of the corresponding wave functions may not be adequate as in this region the lower component of the Dirac spinor is no longer negligible in comparison to its upper component (see, e.g., Ref. [24]).

In our work, we studied the $\mathrm{A}(\pi^+, K^+)_\Lambda\mathrm{A}$ reaction within a fully covariant model by retaining the field theoretical structure of the interaction vertices and by treating the baryons as Dirac particles. In this model, the kaon production proceeds via the collision of the projectile pion with one of the target nucleons. This excites intermediate baryon resonance states (N^*) which decay into a kaon and a Λ hyperon. The hyperon is captured in the respective nuclear orbit while the kaon rescatters onto its mass shell. A similar picture has been used to describe the $\mathrm{A}(p, K^+)_\Lambda\mathrm{B}$ and $\mathrm{A}(\gamma, K^+)_\Lambda\mathrm{B}$ reactions in Refs. [1, 2, 3]. In our model, the intermediate resonance states included are $N^*(1650)[\frac{1}{2}^-]$, $N^*(1710)[\frac{1}{2}^+]$, and $N^*(1720)[\frac{3}{2}^+]$ which have dominant branching ratios for the decay to the $K^+\Lambda$ channel [25, 26]. Terms corresponding to the interference among various resonance excitations are included in the total reaction amplitude.

We find that excitations of $N^*(1650)$, and $N^*(1710)$ resonant states dominate the cross sections for the (π^+, K^+) reaction for beam energies below 2 GeV. Our model describes well the shapes of the experimental angular distributions for the two states which corresponds to the prominent peaks in the ${}^{12}_{\Lambda}$C spectrum. The total cross sections show a substantial dependence on the beam energy with a distinct peak around 1 GeV for reactions on both ^{12}C and ^{40}Ca targets. The differential cross sections peak near zero degrees for both light mass as well as heavier targets. Thus, measurements at forward angles and at beam energies around 1 GeV are expected to have high yields.
The characteristic bump structures reflecting the Λ major shell orbits as seen in the spectra of the ${}^{51}_{\Lambda}$V and ${}^{89}_{\Lambda}$Y hypernuclei were reproduced reasonably well by our model. However, for a quantitative description of the spectra, more realistic calculations with configuration mixed Λ particle, neutron hole states are required. Mixing of the different parity states within a given particle-hole configuration may also be needed.

Literaturverzeichnis

[1] R. Shyam, H. Lenske and U. Mosel, Phys. Rev. C **69** (2004) 065205 [arXiv:nucl-th/0308085].

[2] R. Shyam, H. Lenske and U. Mosel, Nucl. Phys. A **764** (2006) 313 [arXiv:nucl-th/0505043].

[3] R. Shyam, H. Lenske and U. Mosel, Phys. Rev. C **77** (2008) 052201 [arXiv:0710.4888 [nucl-th]].

[4] A. K. Wroblewski, Acta Phys. Polon. B **35** (2004) 901.

[5] A. Zenoni and P. Gianotti, Europhys. News **33** (2002) 157.

[6] J. Pochodzalla, Nucl. Phys. A **754** (2005) 430.

[7] H. Bando, M. Sano, M. Wakai and J. Zofka, Nucl. Phys. A **501** (1989) 900.

[8] M. Wakai, H. Bando and M. Sano, Phys. Rev. C **38** (1988) 748.

[9] M. Wakai, Nucl. Phys. A **547** (1992) 89C.

[10] T. Gaitanos, H. Lenske and U. Mosel, Phys. Lett. B **663** (2008) 197 [arXiv:0712.3292 [nucl-th]].

[11] T. Gaitanos, H. Lenske and U. Mosel, arXiv:0904.2106 [nucl-th].

[12] S. BIANCHIN *et al.*, arXiv:0812.4148 [nucl-ex].

[13] H. Bando, T. Motoba and J. Zofka, Int. J. Mod. Phys. A **5** (1990) 4021.

[14] T. Motoba, H. Bando, R. Wunsch and J. Zofka, Phys. Rev. C **38** (1988) 1322.

[15] H. Bando, T. Motoba, M. Sotona and J. Zofka, Phys. Rev. C **39** (1989) 587.

[16] K. Itonaga, T. Motoba, O. Richter and M. Sotona, Phys. Rev. C **49** (1994) 1045.

[17] P. H. Pile *et al.*, Phys. Rev. Lett. **66** (1991) 2585.

[18] S. Ajimura *et al.*, Nucl. Phys. A **585** (1995) 173C.

[19] M. May *et al.*, Phys. Rev. Lett. **78** (1997) 4343.

[20] T. Hasegawa *et al.*, Phys. Rev. C **53** (1996) 1210.

[21] H. Hotchi *et al.*, Phys. Rev. C **64** (2001) 044302.

[22] O. Hashimoto and H. Tamura, Prog. Part. Nucl. Phys. **57** (2006) 564.

[23] C. B. Dover, L. Ludeking and G. E. Walker, Phys. Rev. C **22** (1980) 2073.

[24] R. Shyam, W. Cassing and U. Mosel, Nucl. Phys. A **586** (1995) 557.

[25] R. Shyam, Phys. Rev. C **60** (1999) 055213 [arXiv:nucl-th/9901038].

[26] C. Amsler *et al.* [Particle Data Group], Phys. Lett. B **667** (2008) 1.

4.2.22 Parton-Hadron-String Dynamics

W. Cassing, Elena L. Bratkovskaya
Institute for Theoretical Physics, University of Gießen, Germany and Institute for Theoretical Physics, JWG University of Frankfurt, Germany

The 'Big Bang' scenario implies that in the first micro-seconds of the universe the entire state has emerged from a partonic system of quarks, antiquarks and gluons – a quark-gluon plasma (QGP) – to color neutral hadronic matter consisting of interacting hadronic states (and resonances) in which the partonic degrees of freedom are confined. The nature of confinement and the dynamics of this phase transition has motivated a large community for several decades and is still an outstanding question of todays physics. Early concepts of the QGP were guided by the idea of a weakly interacting system of partons which might be described by perturbative QCD (pQCD). However, experimental observations at the Relativistic Heavy Ion Collider (RHIC) indicated that the new medium created in ultrarelativistic Au+Au collisions is interacting more strongly than hadronic matter and consequently this concept had to be severely questioned. Moreover, in line with theoretical studies the medium showed phenomena of an almost perfect liquid of partons as extracted from the strong radial expansion and the scaling of elliptic flow $v_2(p_T)$ of mesons and baryons with the number of constituent quarks and antiquarks.

A consistent dynamical approach - valid also for strongly interacting systems - can be formulated on the basis of Kadanoff-Baym (KB) equations [1,2] or off-shell transport equations in phase-space representation, respectively. In the KB theory the field quanta are described in terms of dressed propagators with complex selfenergies. Whereas the real part of the selfenergies can be related to mean-field potentials (of Lorentz scalar, vector or tensor type), the imaginary parts provide information about the lifetime and/or reaction rates of time-like 'particles'. Once the proper (complex) selfenergies of the degrees of freedom are known the time evolution of the system is fully governed by off-shell transport equations. The Parton-Hadron-String Dynamics (PHSD) approach is based on these off-shell transport equations with partonic selfenergies from the dynamical quasiparticle model (DQPM) matched to reproduce recent lattice-QCD results in thermodynamic equilibrium. Scalar- and vector-interaction densities are extracted from the DQPM as well as effective scalar- and vector-mean fields for the partons. The transition from partonic to hadronic degrees of freedom is described by covariant transition rates for the fusion of quark-antiquark pairs or three quarks (antiquarks), respectively, obeying flavor current-conservation, color neutrality as well as energy-momentum conservation [3]. Since the dynamical quarks and antiquarks become very massive close to the phase transition, the formed resonant 'pre-hadronic' color-dipole states ($q\bar{q}$ or qqq) are of high invariant mass, too, and sequentially decay to the groundstate meson and baryon octets increasing the total entropy. The dynamics of interacting hadrons, furthermore, is described by the conventional HSD approach [4].

The PHSD approach has been applied to nucleus-nucleus collisions from 20 to 160 A·GeV in order to explore the space-time regions of 'partonic matter' [5]. We find that even central collisions at the top-SPS energy of 158 A· GeV show a large fraction of non-partonic, i.e. hadronic or string-like matter, which can be viewed as a hadronic corona. This finding implies that neither hadronic nor only partonic 'models' can be employed to extract physical conclusions in comparing model results with data. On the other hand - studying in detail Pb+Pb reactions from 40 to 158 A·GeV - we observe that the partonic phase has a very low impact on rapidity distributions of hadrons but a sizeable influence on the transverse mass distribution of final kaons due to the repulsive partonic mean fields (cf. Fig. 22.1). Furthermore, we find a significant effect on the production of multi-strange antibaryons due to a slightly enhanced $s\bar{s}$ pair production in the partonic phase from massive time-like gluon decay and a larger formation of antibaryons in the hadronization process.

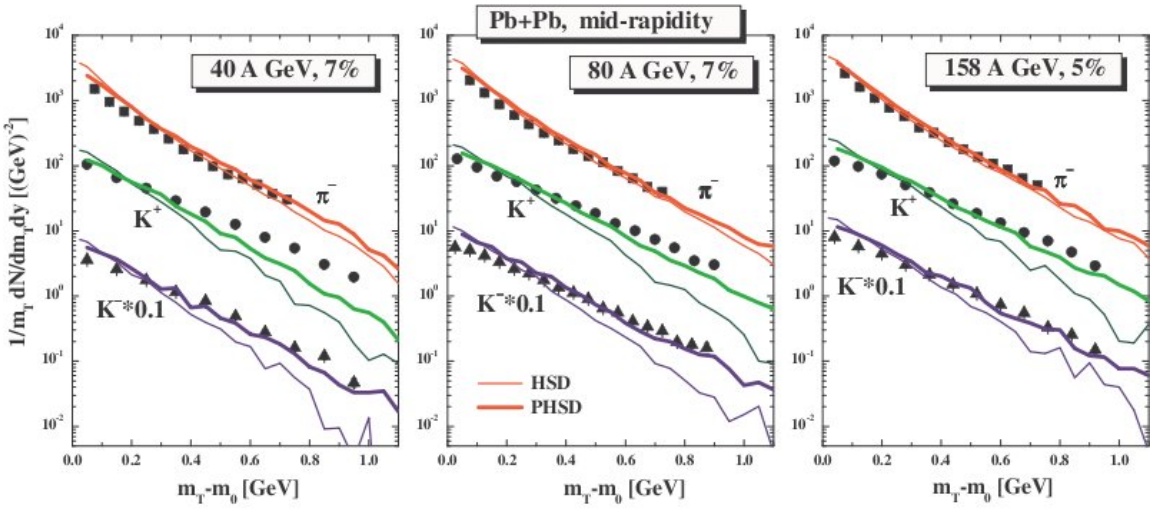

Abbildung 22.1: *The π^-, K^+ and K^- transverse mass spectra for central Pb+Pb collisions at 40, 80 and 158 A·GeV from PHSD (thick solid lines) in comparison to the distributions from HSD (thin solid lines) and the experimental data from the NA49 Collaboration.*

Verweise

1. L. P. Kadanoff, G. Baym, *Quantum Statistical Mechanics*, Benjamin, 1962.
2. S. Juchem, W. Cassing and C. Greiner, Phys. Rev. D 69 (2004) 025006; Nucl. Phys. A 743 (2004) 92.
3. W. Cassing and E. L. Bratkovskaya, Phys. Rev. C 78 (2008) 034919.
4. W. Cassing and E. L. Bratkovskaya, Phys. Rep. 308 (1999) 65.
5. W. Cassing and E. L. Bratkovskaya, Nucl. Phys. A 834 (2009) 215.

4.2.23 Effects from transverse momentum and mass distributions of partons in the Drell-Yan process at $\overline{\mathrm{P}}$ANDA energies

Fabian Eichstädt
Institut für Theoretische Physik I, Gießen

The research project covers the effects of intrinsic quark distributions of transverse momentum and mass on the unpolarised production of Drell-Yan (DY) pairs in the energy regime relevant for the $\overline{\mathrm{P}}$ANDA experiment at FAIR. As laid out in the $\overline{\mathrm{P}}$ANDA physics book [1] unpolarised cross sections will be among the first to be measured, since single and especially double polarised experiments will be possible only later in the project. Therefore the project described here is of high relevance already for the "day one" experiments of $\overline{\mathrm{P}}$ANDA.
The standard collinear perturbative QCD leading-order description already shows some shortcomings at high center-of-mass (c.m.) energies [2]: A K-factor is needed to account for the absolute size of the cross section and the transverse momentum (p_T) spectrum of the DY pair is inaccessible. A next-to-leading-order calculation can improve on the K-factor part, but shows divergent behavior in the p_T spectrum for $p_T \to 0$. At $\overline{\mathrm{P}}$ANDA the limits of the standard collinear perturbative QCD description will be revealed even further, since measurements will be taken at comparatively low hadron c.m. energies of $\sqrt{s} \approx 5.5$ GeV and in an invariant mass range of $1.5\ \mathrm{GeV} < M < 2.5\ \mathrm{GeV}$. At such low energies and thus large ratios of $\tau = M^2/s$ non-perturbative (higher-twist) effects are expected to play an important role.
To account for the shortcomings of the standard description and for the above mentioned higher-twist effects at $\overline{\mathrm{P}}$ANDA energies a QCD inspired phenomenological parton model is studied. It includes leading-order [3] and next-to-leading order production processes. In addition the full kinematics of these processes is taken into account (non-collinear approach) and the soft interactions are modeled by phenomenological quark transverse momentum and mass distributions. Fixing these distributions at available data the aim of the research project is to make predictions for the unpolarised DY production at $\overline{\mathrm{P}}$ANDA.

Verweise

1. M. F. M. Lutz et al. (PANDA), **arXiv: 0809.2262** [hep-ex].
2. S. Gavin et al., Int. J. Mod. Phys. **A10**, 2961 (1995).
3. F. Eichstädt et al., Phys. Rev. D in press, **arXiv:0909.4159** [hep-ph].

4.2.24 Simulationsrechnungen zur Photoproduktion von ω-Mesonen

Stefan Friedrich
Gießen

Die Eigenschaften von Vektormesonen in Kernmaterie sind Gegenstand der aktuellen Forschung zur Frage der Wiederherstellung der chiralen Symmetrie im nuklearen Medium. Erste Hinweise zu In-Medium Modifikationen des ω-Mesons wurden in [1] veröffentlicht. Hierbei wird die Photoproduktion von ω-Mesonen an Kernen via $\gamma A \rightarrow \omega X$ untersucht. Durch Messung der ω-Ausbeute an verschiedenen Kernen [2] konnte im Vergleich zu Transportrechnungen [3] eine Verbreiterung des ω-Mesons in Kernmaterie nachgewiesen werden. Die in [1] publizierten Resultate erwiesen sich jedoch sensitiv auf die Behandlung des Untergrundes [4].
Rechnungen mithilfe eines semiklassischen BUU-Modells [5], entwickelt vom Gießener Institut für Theoretische Physik, sollen Aufschluss darüber geben, wie der Untergrund zu behandeln ist. Diese GiBUU-Simulationen versuchen, die wichtigsten Untergrundbeiträge des Kanals $\omega \rightarrow \pi^0\gamma$ zu modellieren, um eine unabhängige Bestimmung des Untergrundes zu ermöglichen. Abbildung 24.1 zeigt das Ergebnis mehrerer Rechnungen für die einzelnen Untergrundkanäle. In schwarz sind experimentelle Daten zum Vergleich eingefügt.
Von weiterem Interesse sind Simulationsrechnungen zur Anregungsfunktion des ω unter verschie-

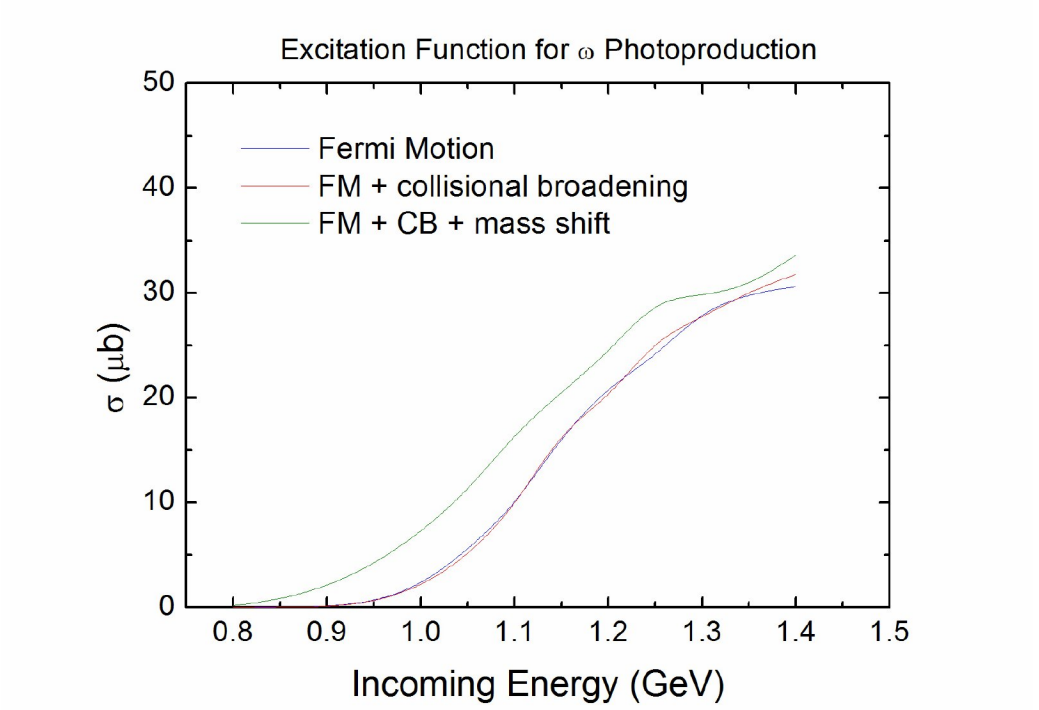

Abbildung 24.1: *Simuliertes Spektrum der invarianten Masse von 3γ Ereignissen*

denen Szenarien wie Massenverschiebung und Verbreiterung. In Abbildung 24.2 sind die Ergebnisse der Simulationen für drei unterschiedliche Szenarien aufgezeigt. Außerdem können die Rechnungen zeigen, wie der Anteil der In-Medium Zerfälle mittels geeigneter Datenselektion erhöht werden kann. Seit Juni 2009 führe ich auf dem HP-Cluster des HRZ der Universität Gießen GiBUU-Simulationen durch. Die Anmeldeformalitäten sowie der Benutzerservice sind sehr unkompliziert bzw. vorbildlich.

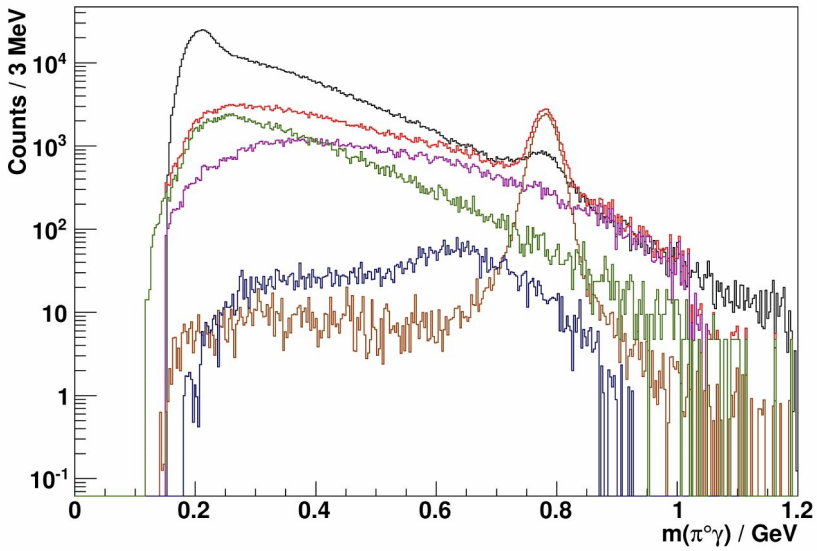

Abbildung 24.2: *Simulationen der Anregungsfunktion des ω-Mesons*

Verweise

1. Trnka et al., *Phys. Rev. Lett.* **94**, 192303 (2005)
2. Kotulla et al., *Phys. Rev. Lett.* **100**, 192302 (2008)
3. Mühlich, Mosel, *Nucl. Phys. A* **773**, 156 (2006)
4. Kaskulov et al., *Eur. Phys. Jour. A* **31**, 245 (2007)
5. `http://gibuu.physik.uni-giessen.de`

4.2.25 Superscaling in lepton-nucleus scattering

Ivan Lappo-Danilevski
Institut für theoretische Physik 1, JLU Giessen

Scaling is a general phenomenon occurring in various areas of physics that deal with probes weakly interacting with many-body systems in which a single constituent of the target absorbs the entire energy and momentum transfer (first pointed out by West in his seminal paper [1]). In brief, scaling is the reduction of the target response to a simple function of one kinematical variable (scaling of first kind) independent of the special form of the target (scaling of second kind, together with the first called superscaling). The validity of the concepts of scaling and superscaling applied to inclusive quasi-elastic electron scattering at intermediate energies has been investigated in depth. In addition the approach has been extended to neutrino-nucleus scattering (investigated by Amaro in 2005 [2]). Whereas for charged-current (CC) weak interactions some comparison to data is expected to be available in the near future (maybe from MiniBooNE or later from MINERνA), the neutral-current (NC) case is very difficult to assess experimentally since it is not possible to reconstruct the incoming/outgoing lepton kinematics.
The general approach in the case of lepton-nucleus scattering can be summarized as follows:

1. At first one has to model the **interaction**. This is usually done in impulse approximation, i.e. under the assumption that only one virtual photon is exchanged during the process and no other processes are involved.

2. On the other hand, the incoming and outgoing **lepton**s also have to be modelled. Plane-wave functions are often applied, letting the leptons propagate freely.

3. To describe the **nucleus**, one usually makes the ansatz of an ensemble of non-interacting fermions (which can form a Fermi gas).

4. After the **separation** of the trivial kinematical factors from the cross sections, evaluated using the approximations, 1-3 one looks at the remaining response functions.

5. Usually, they can be shown to depend strongly on one combination of kinematical variables (**the scaling variable**) and only weakly on other combinations. Those other dependencies are neglected.

6. After this approximation one can once again divide out trivial factors and is left with one universal function depending on only one variable which incorporates all of the nontrivial nucleus response (**the experimental scaling function**).

7. Further, one **analyses** whether scaling of first and second kind are fulfilled, i.e., if the scaling function takes on the same values for different kinematical regimes and nuclear targets.

Evidently any of the approximations listed above can be replaced by a more accurate model, eventually leading to better agreement with experimental data. Thus a variety of different scaling models can be found in literature.
Superscaling is an active field of research, especially since with growing interest in neutrino physics, extrapolating the concepts of (e, e')- to (ν_l, l^-)-scattering offers a way to predict the cross sections in the region of the QE peak in an almost model-independent way. A major point of interest is the non-scaling of the transverse response. It has been found that scale-breaking in the resonance region can be drastically reduced using yet another kind of scaling variable Ψ'_*, incorporating the higher mass m_* of the knocked-out resonance. A similar approach can be applied to the DIS region, integrating over different invariant masses W.
For the case of neutrinos one assumes that the same scaling function will underlie the scattering process, since the same nucleon distributions are expected. In practice one takes the data on longitudinal responses to extract a universal scaling function, which is then multiplied by the appropriate

factors (evidently the single-nucleon cross sections are more involved than those for the electron) to predict both transversal and longitudinal results and thus the entire cross section.
On the other hand, superscaling can be a powerful tool to test these less phenomenological models, aiming to describe wide ranges of q and A, since superscaling is an observable feature of nature. Thus we were glad to find that the GiBUU model, a semi-classical transport model developed at the Giessen institute of theoretical physics, exhibits this behavior. Various runs of the GiBUU simulation have been undertaken by me to examine superscaling in the electron nucleus elementary reaction. Most of them have focused on a context most likely to favor scaling (no in-medium width of nucleons and no processes other than the quasi-elastic), but more realistic scenarios have also been studied.

Verweise

1. *West, G. B.*, 1975, Physics Reports 18 263-323
2. *Amaro, J. E. and Barbaro, M. B. and Caballero, J. A. and Donnelly, T. W. and Molinari, A. and Sick, I.*, 2005, Physical Review C 71 15501

4.2.26 Korrelationen in exotischer Kernmaterie

Patrick Konrad, Horst Lenske
Gießen

Wir untersuchen den Einfluß von kurzreichweitigen Korrelationen in neutronenreicher Kernmaterie und Kernmaterie mit Strangeness im β-Gleichgewicht. Hierzu berechnen wir die dynamischen Selbstenergien, die durch kurzreichweitige Korrelationen entstehen, und untersuchen deren Einfluß auf die die Spektralfunktion der Protonen, Neutronen und Λ-Hyperonen. In unserem Modell nutzen wir die Beziehungen zwischen den Spektralfunktionen und Stoßintegralen aus, um die Spektralfunktionen und die 2p1h und 1p2h Selbstenergien selbstkonsistent zu berechnen. Die Ergebnisse werden eingesetzt in numerisch aufwändigen Rechnungen für Neutronensterne und transporttheoretischen Simulationen für die Produktion von Hyperkernen in hochrelativistischen Schwerionenreaktionen. Besonders rechenintensive ist dabei die selbstkonsistente Berechnung der Selbstenergien aus den Stoßintegralen. Hierbei wird für alle Energien und Impulse und für jede Teilchensorte ein 6-dimensionales Integrale gelöst. Die gewonnen Ergebnisse dienen dann als Ausgangspunkt für die erneute Berechnung der Spektralfuntionen und Selbstenergien. Die Rechnung wird bis zu Selbstkonsistenz der Ergebnisse iteriert. In den Transportrechnungen werden die gleichen oder ähnlichen Wechselwirkungen benutzt, wobei große gekoppelte Systeme von partiellen Differentialgleichungen numerisch berechnet werden müssen.

Verweise

1. Patrick Konrad PhD thesis (October 2009): `http://www.uni-giessen.de/cms/fbz/fb07/fachgebiete/physik/einrichtungen/theorie/theorie1/`

4.2.27 Neutrino-nucleus interactions in a coupled-channel hadronic transport model

Tina Leitner
Gießen

Present-day neutrino oscillation experiments use nuclear targets to increase the neutrino cross section. This causes a major difficulty: particles produced in neutrino interactions can reinteract before leaving the nucleus and can be absorbed, change their kinematics or even charge before being detected. Nuclear reinteractions limit our ability to identify the reaction channel and they change the topology of the measured hadronic final state. Consequently, the detected rates on nuclei are changed significantly compared to the ones on free nucleons. This has important consequences for oscillation measurements: ν_μ disappearance experiments for example search for a distortion in the neutrino flux in the detector positioned far away from the source. By comparing the un-oscillated with the oscillated flux, one gains information about the oscillation probability and with that about mixing angles and mass squared differences. However, the neutrino energy cannot be measured directly but has to be reconstructed from the final-state particles that are detected, thus, a good understanding of the nuclear effects is essential. Appearance experiments, for instance, search for a specific neutrino flavor in a neutrino beam of different flavor. The flavor of the neutrino can only be determined from the charged lepton it produces in the interaction. π^0 production events in neutral current reactions are a source of background in ν_e appearance searches in a ν_μ beam because they might be misidentified as charge current (ν_e, e^-) interactions.

The intention of our work has been to develop a model that provides a combined description of neutrino-nucleus scattering from the quasielastic to the resonance region, i.e., which is applicable for neutrino energies from a few hundred MeV to about 2 GeV. Our approach is based on two pillars, both equally important: a good description of the neutrino-nucleon reaction and a realistic treatment of in-medium effects and final-state interactions (FSI).

In the energy regime from 0.5 to 2 GeV, the neutrino-nucleon reaction is dominated by three contributions: quasielastic (QE) scattering, resonance excitation and non-resonant pion production. They are described with a relativistic formalism in terms of form factors. For the nucleon vector form factors we apply the latest BBBA-2007 analysis accounting for new electron scattering data; the $N-\Delta$ and $N-N^*$ vector form factors are based on the recent MAID analysis for the helicity amplitudes. The axial form factor of the nucleon and the Δ resonance as well as the non-vector background contribution are constrained by neutrino-nucleon scattering data, and the resonance axial couplings are obtained applying the PCAC theorem [1].

In the nuclear medium, the neutrino-nucleon cross sections are modified. We use a local Thomas-Fermi approximation for the phase space density of the bound nucleons which is based on realistic nuclear densities. The nucleons are exposed to a mean-field potential which depends on density and momentum. We also take Pauli blocking and in-medium spectral functions of the outgoing hadrons into account. The imaginary part of the self energies entering the spectral functions are calculated in a consistent way employing the low-density approximation, the real part of the self energies is obtained from dispersion relations [1].

After the initial neutrino-nucleon interaction, the produced particles propagate out of the nucleus. During propagation they undergo FSI which are simulated with the coupled-channel semi-classical GiBUU transport model. It models the full space-time evolution of the phase space densities of all relevant particle species during a nuclear reaction within a consistent treatment of the initial vertex and the final-state processes. This space-time evolution is determined by the BUU equations, which describe the propagation of the particles in their mean-field potentials and also the collisions between them. Nucleons and resonances acquire medium-modified spectral functions and are propagated off-shell. The collision term accounts for changes (gain and loss) in the phase-space density due to elastic and inelastic collisions between the particles, and also due to particle decays into other hadrons. The BUU equations for all particle species are thus coupled through the collision term and also through the potentials. Such a coupled-channel treatment is required to account for side feeding into different channels. The comparison with experimental data for pion, photon and electron induced

reactions shows that the treatment of initial and final-state interactions is under good control and leads to reliable predictions. Furthermore, it allows to make estimates for the expected accuracy in neutrino-induced reactions [2].
We have studied the influence of nuclear effects on inclusive scattering, pion-production mechanisms and nucleon knockout [1,3,4]. Neutrino-induced pion production off nuclei is strongly influenced by in-medium corrections and, especially, final-state interactions. They lead to large absorption mainly in the Δ region. In the kinematical region under investigation, the pions originate mainly from the initial Δ excitation; QE scattering followed by π production in NN collisions contributes only weakly. Furthermore, we have found an enhancement of the subdominant channel through side-feeding caused by charge-exchange scattering from the dominant channel. Nucleon knockout reactions are also strongly modified by final-state interactions. High energy nucleons rescatter in the nucleus, which leads to a decrease of the flux at higher energies, but also to secondary knocked-out nucleons with low kinetic energies. Side feeding is important also for nucleon knockout: in the elementary charged-current (CC) quasielastic reaction, the final state contains only protons, but no neutrons, however, we have found that, as a consequence of the final-state interactions, a large fraction of neutrons is knocked out. In addition, we have illustrated that initial resonance excitation gives a significant contribution to nucleon knockout.
We have applied our model to questions relevant for neutrino oscillation experiments, in particular to the question of energy reconstruction. The oscillation probability depends directly on the neutrino energy which has to be reconstructed from the final-state particles. Most experiments use the CCQE reaction for the reconstruction, thus, a correct identification of CCQE events is important. However, a significant part of CC1π^+ events is detected as CCQE-like which is caused by the pion absorption in the nucleus. Their influence on the neutrino energy reconstruction and on the CCQE cross section which is the signal channel in oscillation experiments is significant, it shifts the reconstructed energy to smaller values.
Finally, we have compared our results to recent data measured at MiniBooNE and K2K [5,6,7]. While the agreement to the K2K data is satisfying, our calculations underestimate the MiniBooNE data significantly. However, these data are "corrected/extracted" using specific Monte Carlo event generators with specific assumptions on the initial neutrino nucleon cross section and the nuclear model. To solve this problem, more data also from other experiments are needed. These data should be as model-independent as possible to perform meaningful comparisons with theoretical calculations.
To extract the oscillation parameters from the measured particle yields, the experimental analyses have to rely on models for the neutrino-nucleus interaction. Thus, the theoretical understanding of nuclear effects is essential for the interpretation of the data and represents both a challenge and an opportunity. Only with precise and well-tested models it is possible to minimize the systematic uncertainties in neutrino fluxes, backgrounds and detector responses.

Verweise

1. T. Leitner, O. Buss, L. Alvarez-Ruso and U. Mosel, Phys. Rev. **C79**, 034601 (2009).
2. T. Leitner, O. Buss and U. Mosel, Acta Phys. Pol. **B40**, 2571 (2009).
3. T. Leitner, L. Alvarez-Ruso and U. Mosel, Phys. Rev. **C73**, 065502 (2006).
4. T. Leitner, L. Alvarez-Ruso and U. Mosel, Phys. Rev. **C74**, 065502 (2006).
5. T. Leitner, O. Buss, U. Mosel and L. Alvarez-Ruso, Phys. Rev. **C79**, 038501 (2009).
6. T. Leitner, O. Buss, U. Mosel and L. Alvarez-Ruso, AIP Conf. Proc. **1189**, 207 (2009).
7. L. Alvarez-Ruso, O. Buss, T. Leitner and U. Mosel, AIP Conf. Proc. **1189**, 151 (2009).

4.2.28 Thermodynamics of the quark-gluon plasma

Stefano Mattiello
Institute for Theoretical Physics, University of Gießen, Germany

The aim of the project is to get a deeper understanding of the phase structure of quantum chromodynamics (QCD) and, in particular, of the properties of the quark-gluon plasma. Lattice Monte Carlo simulations have revealed several exciting results over the past decade [1]. At finite densities, modeling of QCD has added substantially to our understanding of its rich phase structure [2]. In the last years heavy-ion collision experiments focus on the investigation of the quark-gluon plasma (QGP). Early concepts of the QGP were guided by the assumption of a weakly interacting systems of partons because the entropy density s and the energy density ε calculated from lattice QCD were close to the Stefan Boltzmann (SB) limit for a relativistic noninteracting system, i.e. about $\approx 10-15\%$ lower. However, recent observations at the Relativistic Heavy Ion Collider (RHIC) indicated that the QGP created in ultrarelativistic Au + Au collision was interacting more strongly than hadronic matter [3]. Due to these experimental facts the $10-15\%$ deviation from the SB limit became more important and has been reinterpreted. In this context the interaction between the partons in the deconfined phase plays a crucial role to understand the properties of the QGP. For its investigation a generalized classic virial expansion has been developed [4] to calculate the corrections to a single-particle partition function starting from an interaction potential. While hadronic matter is described by a generalized resonance-gas model, we fix the interaction in the QGP phase by lattice calculations for the heavy quark free energy. We adopt a phenomenological model which includes non-perturbative effects from dimension two gluon condensates that describe the free energy of quenched QCD very well at vanishing chemical potential. Explicit expressions for the partition function and the pressure in the deconfined phase are derived. Our results for $\mu_q = 0$ and $N_\mathrm{f} = 3$ for pressure, entropy density, speed of sound and interaction measure at nonzero temperature compare well with three-flavor QCD lattice calculations with almost physical masses from Ref. [1]. We find that a coupling parameter $\tilde{g} = 1.30$ provides a good agreement for all quantities. Furthermore, we have extended this approach to finite densities introducing an explicit μ-dependence of the interaction (via the Debye mass following perturbation theory). This allows to calculate the thermodynamic quantities of interest such as pressure and quark-number density etc. also at finite μ_q; the results again compare well with lattice calculations scaled from $N_\mathrm{f} = 2$ to $N_\mathrm{f} = 3$ with minimal deviations at the critical temperature T_c.

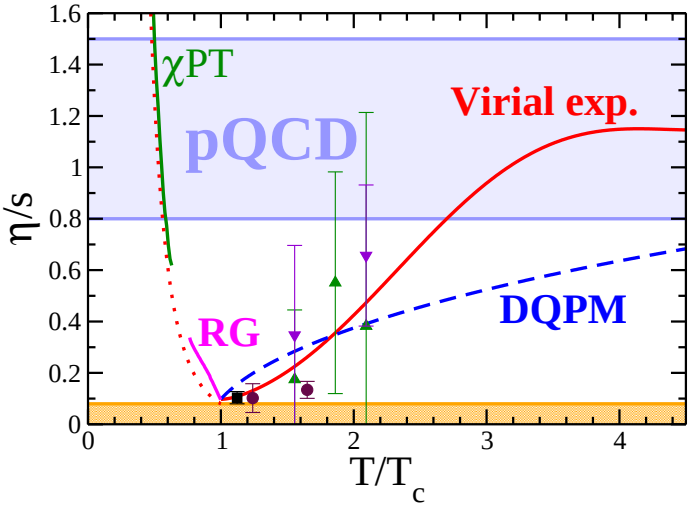

Abbildung 28.1: *The viscosity/entropy density ratio η/s as a function of the temperature expressed in units of the critical temperature T_c for $T/T_\mathrm{c} < 1$ and $T/T_\mathrm{c} > 1$. The triangles and the full dots show the lattice results. The square is the experimental point. The different lines denoted by* χPT, RG, DQPM *and* Virial exp. *stand for the results from chiral perturbation theory, the hadron resonance gas, the dynamical quasiparticle model and the virial expansion approach, respectively.*

Furthermore, we calculate the shear viscosity η in the QGP within relativistic kinetic theory, with particular interest in the ratio of η to the entropy density s, i.e. η/s [5]. We directly extract from the potential the effective coupling α_V for the determination of η. Our numerical results give a

ratio $\eta/s = 0.097$ at the critical temperature T_c, which is very close to the theoretical bound of $1/(4\pi)$. Furthermore, for temperatures $T \leq 1.8T_c$ the ratio η/s is in the range of the present experimental estimates $0.1 - 0.3$ at RHIC. When combing our results for η/s in the deconfined phase with those from chiral perturbation theory or the resonance gas model in the confined phase we observe a minimum of η/s close to the critical temperature T_c. These results are shown in Fig. 28.1 Additionally, we have investigated the structure of the phase diagram also in the region inaccessible to lattice calculations, i.e. $\mu_q \geq T$. We have calculated the isobaric line, which agrees remarkably well with the cross over transition evaluated by lattice calculations with the reweighting method. The direct knowledge of the partition function allows to calculate the equation of state of the quark gluon plasma which also reproduces very well the predictions of the lattice calculations. The QGP is a strongly correlated system and also at $T = 2T_c$ there is a remarkable deviation of the EoS of the QGP from the Stefan Boltzmann limit which is a clear signal of surviving correlations in the deconfined phase.

Verweise

1. M. Cheng *et al.*, Phys. Rev. D **77**, 014511 (2008).
2. W. Cassing, Nucl. Phys. A **795**, 70 (2007).
3. K. Adcox *et al.*, Phys. Rev. Lett. **89**, 212301 (2002).
4. S. Mattiello and W. Cassing, J. Phys. G **36**, 125003 (2009).
5. S. Mattiello and W. Cassing, hep-ph/0911.4647.

4.2.29 In-Medium Properties of Vector Mesons

Janus Weil
Institut für Theoretische Physik, JLU Giessen

While the vacuum properties (masses, decay widths, etc) of most hadrons are known to reasonable accuracy today, it is a much-debated question how these properties change in nuclear matter, i.e. how they are influenced by a surrounding hadronic medium. In particular for the light vector mesons [$\rho(770)$, $\omega(782)$ and $\phi(1020)$] there have been various theoretical predictions regarding their in-medium properties.

One of the expected in-medium effects is an additional term contributing to the meson width, due to inleastic collisions with the hadronic medium. This enhanced width means that the spectral function in medium becomes much broader than in the vacuum, which is usually referred to as 'collisional broadening'. It's rather clear that this effect must occur, the question is how strong it is, and whether it can be observed experimentally. A second class of predictions claim that the vector meson masses will be shifted in the medium [1]. These changes of the peak mass can be attributed to the partial restoration of chiral symmetry in the medium and have been studied via QCD sum rules [2]. This effect has been claimed to be seen experimentally, but it is highly controversial. It has also been found that QCD sum rules put cetain restrictions on the interplay of collisional broadening and mass shift [3].

The supreme tool for studying in-medium properties of vector mesons are dileptons. All neutral vector mesons have a decay mode into e^+e^-, and if such a decay happens inside nuclear matter, the emanating lepton pair can carry the in-medium information outside to the detector. By measuring the invariant mass of the lepton pair, the in-medium mass of the meson can be reconstructed. In this way it is possible to get a handle on the in-medium properties of the vector mesons. The particular advantage of dileptons is of course that they only interact electromagnetically, and are undisturbed by the strong nuclear force. However, they are quite rare: The branching ratios of the dilepton channels are on the order of 10^{-5}. The more prominent hadronic decay channels suffer from the drawback that the decay products are affected by final-state interaction with the hadronic medium.

Although dilepton production has first been studied in heavy-ion collisions and a large amount of research is still being done in this area, we concentrate on elementary nuclear reactions in our work, especially on photon- and proton-induced reactions. These elementary collisions have a number of advantages, in particular they involve a more sharply defined density and are simply much cleaner. While a heavy-ion collision involves various phases of temperature and density, the nucleus stays basically in its ground state in elementary collisions at low energies. Therefore it is easier to interpret the resulting spectra, to disentangle the various contributing channels and to separate the in-medium signal from background sources. Of course one can reach much higher densities in heavy-ion collisions, but the predicted effects should be large enough to be observed already at normal nuclear density.

Experimentally, dilepton spectra from elementary nuclear reactions are being studied e.g. with the CLAS detector at JLAB, where Bremsstrahlung photons in the energy range of about 1-3 GeV are shot on nuclei [4,5], or by the E325 experiment at the Japanese KEK facility, where 12 GeV protons are used as projectile [6,7,8,9]. Also the HADES detector at GSI is measuring dilepton spectra from nucleus-nucleus and proton-nucleus reactions. On the side of the hadronic decays, most notably $\omega \to \pi^0\gamma$ is being investigated by the CB/TAPS group in photon-induced reactions at the ELSA accelerator [10,11].

For the numerical simulation of these processes we use the GiBUU transport model [12], which provides a unified framework for various types of elementary reactions on nuclei as well as heavy-ion collisions. This model takes care of the correct transport-theoretical description of the hadronic degrees of freedom in nuclear reactions and all the subtleties this may involve, including the propagation, collisions and decays of particles in a nuclear environment. For the investigation of in-medium properties of vector mesons, the most crucial parts of the transport model are:

1. The production mechanisms of vector mesons on nuclei, e.g. $\gamma N \to VX$ or $NN \to VX$.

2. The description of the VN interaction, which is responsible for absorption and collisional broadening.

3. A proper off-shell treatment in the propagation of vector mesons and the handling of density-dependent spectral functions.

4. A correct description of the background processes (Dalitz decays, Bremsstrahlung, etc).

The GiBUU model has a strong history in the study of mesonic in-medium properties [13,14,15,16]. We build our work upon these earlier results and will continue to improve the treatment of vector mesons in the nuclear medium.

Verweise

1. G. E. Brown and M. Rho, Phys. Rev. Lett. 66, 2720 (1991).

2. T. Hatsuda and S. H. Lee, Phys. Rev. C46, 34 (1992).

3. S. Leupold, W. Peters and U. Mosel, Nucl. Phys. A628, 311 (1998), [nucl-th/9708016].

4. R. Nasseripour et al., Phys. Rev. Lett. 99, 262302 (2007), [0707.2324].

5. M. H. Wood et al., Phys. Rev. C78, 015201 (2008), [0803.0492].

6. K. Ozawa et al., Phys. Rev. Lett. 86, 5019 (2001), [nucl-ex/0011013].

7. M. Naruki et al., Phys. Rev. Lett. 96, 092301 (2006), [nucl-ex/0504016].

8. R. Muto et al., Phys. Rev. Lett. 98, 042501 (2007), [nucl-ex/0511019].

9. F. Sakuma et al., Phys. Rev. Lett. 98, 152302 (2007), [nucl-ex/0606029].

10. D. Trnka et al., Phys. Rev. Lett. 94, 192303 (2005), [nucl-ex/0504010].

11. M. Kotulla et al., Phys. Rev. Lett. 100, 192302 (2008), [0802.0989].

12. http://gibuu.physik.uni-giessen.de

13. M. Effenberger, E. L. Bratkovskaya and U. Mosel, Phys. Rev. C60, 044614 (1999), [nucl-th/9903026].

14. M. Effenberger, E. L. Bratkovskaya, W. Cassing and U. Mosel, Phys. Rev. C60, 027601 (1999), [nucl-th/9901039].

15. P. Muehlich, T. Falter and U. Mosel, Eur. Phys. J. A20, 499 (2004), [nucl-th/0310067].

16. P. Muehlich and U. Mosel, Nucl. Phys. A773, 156 (2006), [nucl-th/0602054].

4.2.30 R-Matrix-Rechnungen zur Photoionisation atomarer Ionen

Stefan Schippers
Institut für Atom- und Molekülphysik, Justus-Liebig-Universität Gießen

Die Photoionisation atomarer Ionen ist ein Prozess, der das Ladungsgleichgewicht in Plasmen entscheidend bestimmt. Das Institut für Atom- und Molekülphysik führt im Rahmen einer internationalen Kollaboration (Deutschland, USA, Mexiko, Nordirland) seit einem Jahrzehnt Messungen von Photoionisationsquerschnitten atomarer Ionen an der Synchrotronstrahlungsquelle ALS in Berkeley, Kalifornien durch. Die gemessenen Querschnitte sind von Bedeutung vor allem für die astrophysikalische Interpretation von astronomischen Beobachtungen an kosmischen Plasmen, wie z.B. die Sonnenkorona, Supernovaüberreste, das interstellare Medium und aktive Galaxienkerne.

Die von der Astrophysik zur Modellierung dieser Objekte herangezogenen atomphysikalischen Daten sind überwiegend theoretischer Provenienz. Eine Überprüfung der theoretischen Rechnungen durch experimentelle Messungen ist daher unabdingbar für eine Einschätzung der Qualität der Rechnungen und der gezielten Weiterentwicklung der theoretischen Methoden. Abbildung 30.1 gibt ein Beispiel für das Zusammenspiel zwischen Experiment und Theorie [1]. Gezeigt ist der Wirkungsquerschnitt für die Photoionisation von dreifach geladenen Kohlenstoffionen als Funktion der Photonenenergie. Bei bestimmten Energien weist dieser Resonanzstrukturen auf, die durch Photodoppelanregung mit nachfolgender Autoionisation zu Stande kommen. Die exakte theoretische Beschreibung der Resonanzparameter, d.h. von Resonanzlage, -form und -stärke, ist auf Grund des Vielteilchencharakters des Problems eine besondere Herausforderung.

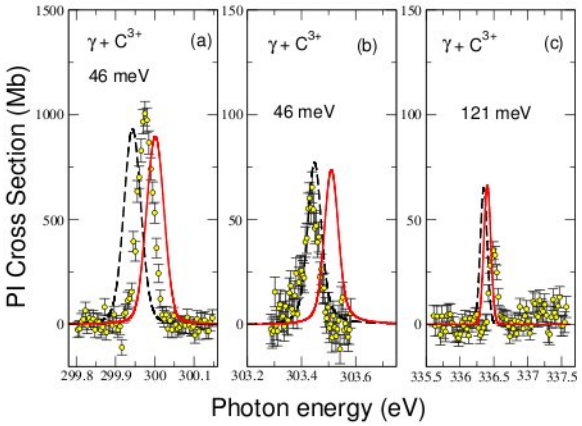

Abbildung 30.1: *Vergleich zwischen gemessenen und berechneten Wirkungsquerschnitten für die K-Schalen-Photoionisation von C^{3+}-Ionen [2].*

Unsere Kollaboration verwendet für die theoretische Berechnung atomarer Photoionisationsquerschnitte (Abb. 30.1) die in Belfast entwickelten R-Matrix-Programme [2]. Diese wurden vor kurzem auf dem neuen Gießener HPC-Cluster installiert, und erste Testläufe wurden absolviert. In naher Zukunft soll vor allem die Interpretation der an der ALS gemessenen experimentellen Daten durch begleitende R-Matrix-Rechnungen unterstützt werden.

Verweise

1. A. Müller, S. Schippers, R. A. Phaneuf, et al., J. Phys. B **42**, 235602 (2009).
2. K. A. Berrington, W. Eissner und P. H. Norrington, Comput.Phys. Commun. **92** 290 (1995). `http://amdpp.phys.strath.ac.uk/APAP`

4.2.31 Simulation of the FRANZ bunchcompressor

D. Noll, L.P. Chau, R. Tiede, M. Droba, U. Ratzinger
Institut für Angewandte Physik, Goethe Universität, Frankfurt am Main

The Frankfurt Neutron Source at the Stern-Gerlach-Zentrum (FRANZ) currently under construction at IAP (University of Frankfurt) is designed to produce short neutron pulses at high intensity and repetition rates using the $^7Li(p,n)^7Be$ reaction [1]. To achieve a bunch length of one nanosecond, a bunch compressor of the Mobley type [2] using four dipole magnets and two rebunchers has been developed (figure 31.1).
To obtain the best beam quality possible, beam dynamic simulations of every part of the bunch compressor have to be made. For the simulation of individual components a finite-difference particle-in-cell code supporting open boundaries has been developed and successfully tested. This code was used to simulate the merging of the nine bunches in the final section of the bunch compressor, where high space charge forces come into play. The results are important to calculate the final focus of the proton beam on the target and the resulting neutron production.

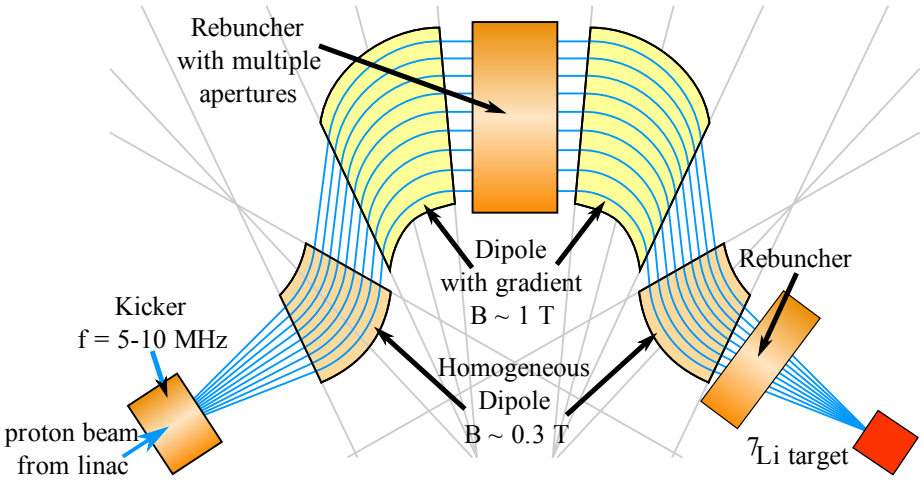

Abbildung 31.1: *Layout of the FRANZ bunchcompressor*

To estimate the beam dynamics of the whole bunch compressor and the preceding linear accelerator, the LORASR code developed in our group was used [3]. Due to the high number of parameters (17 total) manual optimization is difficult at best. For this reason particle swarm optimization, an derivative-free, stochastic direct search algorithm, was used. This was done on the CSC Quad Cluster, using 10 to 25 cpus for several days. Current results look very promising. The same optimization technique was also used to find the best layout for the kicker at the start of the compressor using the aforementioned PIC-code. In the future we intend to include those simulations of the individual components in these optimization runs.

Verweise

1. L.P. Chau, O. Meusel, U. Ratzinger, A. Schempp, K. Volk, M. Heil - The Frankfurt Neutron Source At The Stern-Gerlach-Zentrum (FRANZ), Proceedings of EPAC 06

2. R.C. Mobley - “Proposed Method for Producing Short Intense Monoenergetic Ion Pulses“, Phys. Rev.88(2), 360-361 (1951)

3. R. Tiede, G. Clemente, H. Podlech, U. Ratzinger, A. Sauer, S. Minaev - LORASR Code Development, Proceedings of EPAC 06

4.2.32 About the origin of the mass of the nucleon in a linear sigma model

Susanna Gallas, Francesco Giacosa, Dirk H. Rischke
Institut für Theoretische Physik, J.W. Goethe Universität Frankfurt

Understanding the mass of the nucleon is one of the most important issues in modern physics. Neglecting the small contribution of the explicit symmetry breaking, in the classical linear sigma model the mass of the nucleon is generated exclusively through spontaneous breaking of the chiral symmetry, leading to the appearance of a chiral condensate $\phi \sim f_\pi$, where $f_\pi = 92.4$ MeV is the pion decay constant [1]. The chiral condensate ϕ can be directly related to the fundamental quark condensate $\langle \bar{q}q \rangle$ as $\phi \simeq \Lambda_{QCD}^{-2} \langle \bar{q}q \rangle$, where Λ_{QCD} is the QCD Yang-Mills scale.
However, not only the quark condensate, but also other condensates, such as the gluon and the tetraquark ones, can contribute to the mass of the nucleon m_N and it is not yet settled which is their quantitative role [2]. A possibility to study this problem in the context of a linear sigma model goes via the so called mirror assignment, which was first discussed in Ref. [3] and extensively analyzed in Refs. [4, 5]. In this assignment, the nucleon N and its chiral partner N^* form a doublet of the chiral group. Then it is possible to introduce a chirally invariant mass term parametrized by m_0. This leads to non-vanishing masses of the nucleon and its chiral partner in the chirally restored phase where $\phi \to 0$, instead they acquire the same mass $m_0 \neq 0$. We show this in Fig. 32.1.
A study of the parameters using the decays $N^* \to N\pi$ and $a_1 \to \pi\gamma$ results in a value of 460 MeV for m_0 which denotes the contribution to the mass of the nucleon *not* stemming from the quark condensate [6].
The viability of our model is tested by studying the decay $N^* \to N\eta$ and pion-nucleon scattering at tree level. This can provide useful information to clarify the origin of the nucleon mass and its behavior in the chirally restored phase.

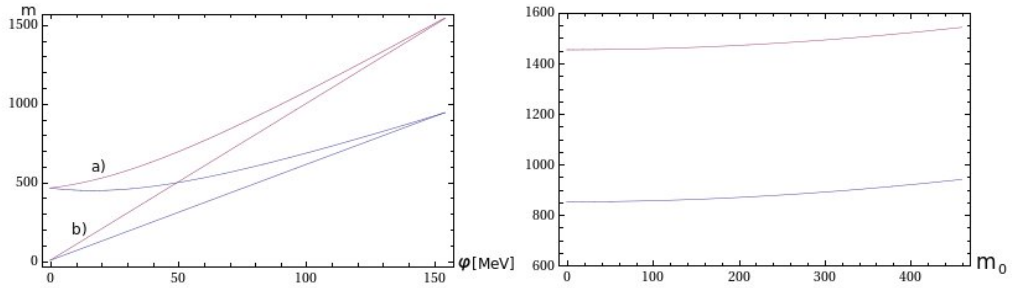

Abbildung 32.1: *Left panel: The masses of the nucleon (blue line) and its chiral partner (purple line) as a function of the quark condensate at fixed $m_0 = 460$ MeV. a) When varying ϕ from 0 to the physical value the nucleon mass goes from $m_0 = 460$ MeV to 939 MeV, thus showing that in limit $\phi \to 0$ the mass does not vanish. b) If we turn off m_0, the masses are exclusively generated by chiral symmetry breaking, thus vanishing for $\phi \to 0$. Right panel: The chiral condensate ϕ is kept fixed to its physical value but the parameter m_0 is left free. The baryon masses are plotted as function of m_0.*

Literaturverzeichnis

[1] R. D. Pisarski, arXiv:hep-ph/9503330.

[2] T. D. Cohen, R. J. Furnstahl, D. K. Griegel and X. m. Jin, Prog. Part. Nucl. Phys. **35** (1995) 221.

[3] B.W. Lee, "Chiral Dynamics", Gordon and Breach, New York, 1972

[4] C. DeTar and T. Kunihiro, Phys. Rev. D **39** (1989) 2805.

[5] D. Jido, M. Oka, and A. Hosaka, Prog. Theor. Phys. **106** (2001) 873. D. Jido, Y. Nemoto, M. Oka and A. Hosaka, Nucl. Phys. A **671** (2000) 471.

[6] S. Gallas, F. Giacosa and D. H. Rischke, arXiv:0907.5084 [hep-ph]. submitted to Phys. Rev. D.

4.3 Ingenieurwissenschaften

4.3.1 Geometrische Struktur kleinskaliger Turbulenz

Dipl.-Ing. Fettah Aldudak, Prof. Dr.-Ing. Martin Oberlack
Fachgebiet für Strömungsdynamik, Darmstadt

Bei der Turbulenz handelt es sich um ein weit verbreitetes Naturphänomen, das heute noch in vielfacher Hinsicht unverstanden ist. Ihr ausgeprägt chaotischer und dreidimensionaler Charakter tragen zu einem großen Teil hierzu bei.
Turbulenz tritt in vielen Bereichen der Natur und Technik auf, in der Geo- und Astrophysik, in der Meteorologie sowie der Aerodynamik, aber auch in technischen Apparaten und Maschinen sowie teilweise in biologischen Systemen. Bislang beschränken sich die Berechnungsmethoden für die Vorhersage turbulenter Strömungen immer noch größtenteils auf halbempirische Schließungsannahmen und Modelle für sogenannte integrale Größen. Diese sind z.B. das integrale Zeit- und Längenmaß und repräsentieren die großen Strukturen in einem turbulenten Strömungsfeld. Sie werden durch Differentialgleichungen für die turbulente kinetische Energie k únd die Dissipation ε ausgedrückt. Für kleinere Längen- und Zeitskalen bleibt das Verständnis bruchstückhaft. Die einzige durch Experimente und Theorie weitgehend abgesicherte Aussage für kleinere Längenmaße beruht auf einer Dimensionsanalyse von Strukturfunktionen nach Kolmogorov, die besagt, dass die Differenz der Geschwindigkeitsfluktuationen zwischen zwei Punkten im Strömungsfeld proportional zur 1/3-Potenz des Abstandes zwischen den Punkten sein muss. Die heute verbreitet verwendeten Simulationstechniken lösen, wie im Falle von Large-Eddy-Simulationen, bestenfalls die großen Strukturen numerisch auf, müssen jedoch bei der Betrachtung der kleinen Skalen Gebrauch von Modellen machen, die das Schließungsproblem der Turbulenz somit lediglich zu kleineren Skalen verschieben. Direkte Numerische Simulationen sind die einzige Methode, die turbulente Strukturen bis zu Kolmogorov-Skalen numerisch auflösen können, stellen aber aufgrund ihrer Beschränktheit auf sehr einfache Geometrien und niedrige Strömungsgeschwindigkeiten keine Alternative für anwendungsnahe technische Probleme.
Um die Kolmogorov'schen Skalierungen in die Formulierung von Turbulenzmodellierung einfließen zu lassen, sollte das Augenmerk auf die geometrische Eigenschaft des turbulenten Feldes gerichtet werden. Die Frage nach einer Klassifizierung des turbulenten Skalenspektrums ist hier von besonderer Bedeutung. Um dies zu ermöglichen, bedarf es allerdings einer Methode, die das gesamte turbulente Feld in Gebiete vergleichbarer geometrischer Strukturen aufteilt und Rückschlüsse auf ihre Eigenschaften erlaubt. Bisher war es nicht gelungen, die Geometrie der Turbulenz vollständig durch Objekte endlicher Größe darzustellen und damit das innerhalb der Kaskade veränderliche Längenmaß quantitativ zu erfassen.
Geometrische Strukturen in der Turbulenz können sinnvollerweise nur mit statistischen Methoden beschrieben werden, wobei die beschreibenden Parameter Längen sein werden. In diesem Sinne wird im Rahmen dieses Projektes die Theorie der sogenannten Dissipationselemente behandelt, die auf Wang & Peters [1] zurückgeht. Das Ziel dieser Theorie ist es, das gesamte Strömungsfeld in kleine Einheiten zu zerlegen und aus diesen statistische Informationen der Strömung zu rekonstruieren. Sie können mit der Methode der Gradienten-Trajektorien bestimmt werden. Gradienten-Trajektorien starten von jeder Gitterzelle im Feld in Richtung steigender und fallender Gradienten, bis sie jeweils einen Maximum- bzw. ein Minimum-Punkt erreichen. Das Feld kann hierbei eine beliebige skalare Größe sein wie die Geschindigkeit, ihre Fluktuation oder die Dissipation. Alle Punkte im physikalischen Raum, deren Trajektorie an den zwei selben Extrempunkten endet, werden zu einem Element zusammengefasst, das als „Dissipationselement" bezeichnet wird. Da durch jeden Punkt im Raum genau eine Trajektorie verläuft, kann somit der Raum eindeutig eingeteilt werden. Alle Extrempunkte des Skalarfeldes stellen Endpunkte eines Elementes dar, und somit variiert der Skalar monoton innerhalb des Elements. Die Geometrie eines Dissipationselementes lässt sich zunächst durch den linearen Abstand zwischen den jeweiligen Minimum- und Maximum-Punkten parametrisieren.
An dieser Stelle wird nicht nur die so definierten Elemente mit Hilfe von drei-dimensionalen DNS-Daten betrachtet, sondern auch eine Theorie zur Beschreibung der statistischen Eigenschaften dieser

Elemente anhand der Verteilung des Längenmaßes entwickelt werden.
Ein besonderer Schwerpunkt bei diesem Projekt ist die Betrachtung wandgebundener Strömung, was im Zusammenhang mit Dissipationselementen erstmalig behandelt wird. Die hierfür verwendete Strömungskonfiguration ist die einer in vertikaler Richtung von Wänden begrenzten Kanalgeometrie. Hierbei wird die von [1] entwickelte Gleichung für die Verteilungsfunktionen der aus den Dissipationselementen gewonnenen Längenmaße um eine Abhängigkeit von wandnormaler Richtung ergänzt. Die einzelnen Terme dieser Gleichung sollen, gestützt auf DNS-Daten, überprüft und gegebenenfalls modifiziert werden. Ein weiteres Ziel ist es, ausgehend von dieser Gleichung eine physikalische Begründung der Gleichung für die Dissipation ε in Zwei-Gleichungs-Modellen für turbulente Strömungen zu liefern. Die Abbildung 1.1 zeigt zwei Beispiele für Dissipationselemente. Die Farbkodierung zeigt den Wert des passiven Skalars an, wobei blau dem Minimum und rot dem Maximum entspricht.

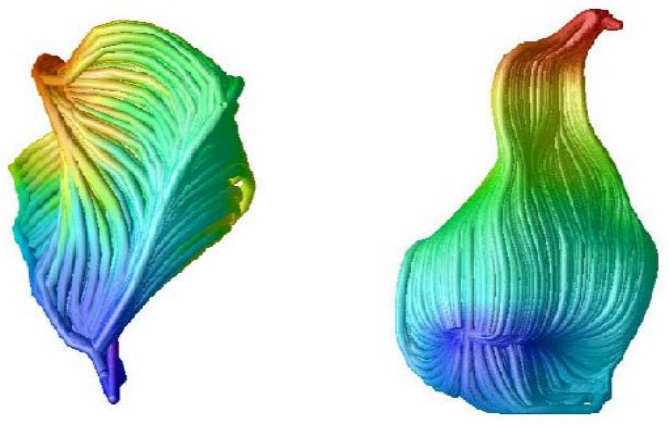

Abbildung 1.1: *Schematische Darstellung von Dissipationselementen.*

In diesem Rahmen wurden erste Ergebnisse in der Veröffentlichung [2] vorgestellt. Es konnte gezeigt werden, dass für den betrachteten Bereich die Verteilung der Wahrscheinlichkeitsdichte für die normierte Länge der Dissipationselemente weder von der Wahl des Skalars noch der der Reynoldszahl abhängt. Hingegen konnte eine Abhängigkeit von der wandnormalen Richtung beobachtet werden. Die Arbeit geht im nächsten Schritt auf die wandnormale Verteilung der Extremalpunkte und der mittleren Elementlänge ein. Auch hier war eine ausgeprägte Abhängigkeit beider Parameter vom Wandabstand zu vermerken. Geplant ist zudem die Betrachtung und Auswertung der kondizierten Statistiken entlang der Gradiententrajektorien.

Verweise

1. N. Peters, L. Wang, "Dissipation element analysis of scalar fields in turbulence," C. R. Mech. 334, 433506 (2006).

2. F. Aldudak, M. Oberlack, "Dissipation element analysis of scalar fields in wallbounded turbulent flow," Proceedings of EUROMECH Colloquium 512: Small Scale Turbulence and Related Gradient Statistics, Torino, Italy (2009).

4.3.2 DFG-Graduiertenkolleg 1344: „Instationäre Systemmodellierung von Flugtriebwerken“ A4: „Vermischungsvorgänge in der Turbine“

Stavros Pyliouras, Heinz-Peter Schiffer
Fachgebiet für Gasturbinen, Luft- und Raumfahrtantriebe,
TechnischeUniversität Darmstadt

Eine Möglichkeit, die stetig steigenden Anforderungen an Wirtschaftlichkeit von Fluggasturbinen zu erfüllen, ist, den isentropen Wirkungsgrad der Teilkomponenten zu verbessern. Sekundäre, d.h. ungewollt auftretende, Verlustmechanismen tragen zu einem erheblichen Teil zu den Verlusten einer Turbinenstufe bei. Diesen bekannten Verlustmechanismen wird heute schon bei der Auslegung der Turbinenkomponente Rechnung getragen. Da die Optimierung des Kompentenwirkungsgrades durch Forschung und Entwicklung stetig vorangetrieben wird, lohnt es sich, immer komplexere Strömungsdetails zu untersuchen und zu optimieren. An diesem Punkt knüpft die vorliegende Arbeit an. Sie erweitert die Betrachtung der Hochdruckturbinenstufe um die detailliertere Berücksichtigung der Brennkammeraustrittsströmung und zieht damit die komponentenübergreifende Interaktion mit der Brennkammer in Betracht (siehe Abbildung 2.1).

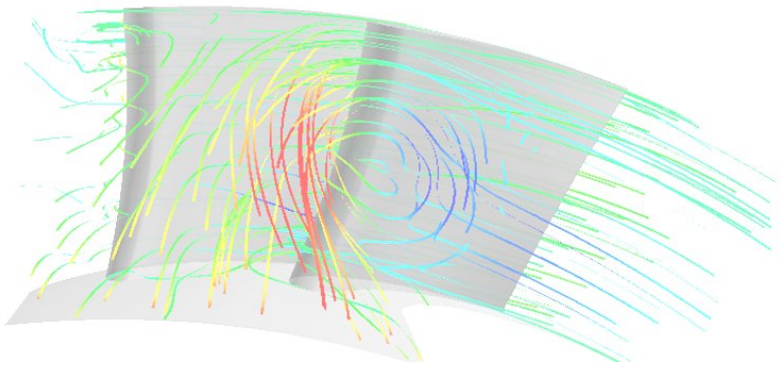

Abbildung 2.1: *Verdrallte Brennkammeraustrittsströmung mit anschließender Statorbeschaufelung*

In mittel- bis langfristiger Zukunft, zur Erfüllung der etappenweise sich verschärfenden NOx Emissionsvorschriften, werden Brennkammerkonzepte realisiert werden, die eine mager-vorgemischte Verbrennung umsetzen. Dazu muss mehr als die Hälfte des Gesamtmassenstroms des Kerntriebwerks durch den Drallerzeuger der Brennkammer geleitet werden, was zu einer stark verdrallten Anströmung der ersten Hochdruckturbinenstufe führen wird. Da die erste Turbinenstufe meist auf Basis umfangsgemittelter, radialer Eintrittsprofile von Totaldruck, -temperatur und Strömungswinkeln ausgelegt wird und bislang umgesetzte Brennkammerkonzepte zu einer vergleichsweise moderat verdrallten Eintrittsströmung führen, sind durch die Berücksichtigung der stark verdrallten Austrittsströmung der Mager-Brennkammer Einflüsse auf die Turbinenstufenaerodynamik bzw. -wirkungsgrad zu erwarten.
Ziel dieses Projekts ist es, den qualitativen und quantitativen Einfluss der verdrallten Brennkammeraustrittsströmung einer Mager-Brennkammer auf die Aerodynamik der nachfolgenden Hochdruckturbinenstufe zu untersuchen. Da sich der Fokus der Arbeit auf die Vorgänge in der Turbine richtet, allerdings die Rückwirkung der Turbine auf die Brennkammerströmung bei dieser Art der Herangehensweise nicht berücksichtigt ist, muss diese Arbeit als Untersuchung der unidirektionalen Brennkammer-Turbine Interaktion angesehen werden. Diese Untersuchungen werden rein numerisch mit dem 3D Strömungslöser Hydra von Rolls-Royce Deutschland (Abk.: RRD) ausgeführt. Die Software wird kostenfrei von RRD zur Verfügung gestellt, allerdings ohne Zugriff auf die numerischen Parameter des Lösers. Genau wie der Löser wurde auch die zu untersuchende Geometrie mit dem Projektpartner RRD abgesprochen. Dabei wurde auf den Technologieträger der Magerverbrennung im Hause RRD zurückgegriffen. Das mit Hilfe von Bundesmitteln entwickelte Kerntriebwerk E3E

Core 3/2 beinhaltet den Hochdruckkompressor, die Brennkammer und die Hochdruckturbine. Den Untersuchungen an der realen Triebwerksgeometrie folgen Untersuchungen an einer Prüfstandsgeometrie, die ebenfalls gemeinsam mit RRD ausgewählt wurde. Dabei handelt es sich ebenfalls um eine RRD Geometrie, die im Rahmen des Teilprojekts B5 („Experimentelle Untersuchungen von Vermischungsvorgängen in einer 1,5-stufigen Turbine“) des Kollegs entwickelt wurde und im Laufe des Jahres 2010 am Fachgebiet GLR in Betrieb genommen werden wird. Damit können die Erkenntnisse aus den Berechnungen an der realen Triebwerksgeometrie den Erkenntnissen aus dem 1,5-stufigen Turbinenprüfstand gegenübergestellt werden. Anhand dieser Gegenüberstellung kann anschließend eine Aussage darüber gemacht werden, ob Erkenntnisse aus Prüfstandsergebnissen übertragbar auf die Bedingungen des realen Triebwerks sind.
Alle numerischen Rechnungen werden zeitaufgelöst durchgeführt, um hochaufgelöste Informationen zur Interaktion des Brennkammerdralls mit den in der Hochdruckstufe auftretenden Sekundärströmungen zu gewinnen, wie z.B. Hufeinsenwirbel, Filmkühlung, Passagenwirbel, Rotorspaltströmung und Sperrlufteinblasung. Des Weiteren wird der Einfluss des veränderten Eintrittsprofils auf die Wärmebelastung der Oberflächen untersucht, z.B. der Schaufeloberfläche, den Endwänden und insbesondere dem Bereich des Rotorspitzenspaltes.
Damit trägt die Aufgabenstellung dem übergeordneten Thema der „Instationären Systemmodellierung von Flugtriebwerken“ Rechnung. Im vorliegenden Projekt wird die komplette erste Hochdruckturbinenstufe zeitabhängig und ganzheitlich modelliert und analysiert. Dieses Projekt kann am Fachgebiet Gasturbinen, Luft- und Raumfahrtantriebe als Pionierarbeit zur Brennkammer-Turbine Interaktion angesehen werden. Die Arbeit wird ebenso einen Beitrag im Rahmen der Einrichtung des „Rolls-Royce University Technology Center: Combustor and Turbine Aerothermal Interaction“ leisten und den Status der Technische Universität Darmstadt als bevorzugten universitären Kooperationspartner von Rolls-Royce Deutschland und Rolls-Royce plc. (RR plc.) auf diesem Gebiet zugute komme.

Verweise

1. M. Kegalj, N. Winter, H.-P. Schiffer, S. Pyliouras, and J. Taege. Through Flow Modelling of a Modern Turbine Stator Cooling System. ISAIF paper ISAIF8-0052, 2007.

2. S. Pyliouras, M. Kegalj, C. Starke, and H.-P. Schiffer. Consequences of Unsteady Wake Interaction in Multi-Stage Turbines. ISABE paper 2009-1261, 2009.

3. E. V. Klapdor, S. Pyliouras, R. L. G. M. Eggels, and J. Janicka. Methodology for Simulating Combustor Turbine Interaction (abstract accepted). ASME paper GT2010-22933, 2010.

4. Mehr Informationen unter: `http://www.glr.tu-darmstadt.de/`

4.3.3 Wall Normal Rotating Channel Flow: Direct Numerical Simulation, Modeling and Lie Group Analysis

A. Mehdizadeh, M.Oberlack
Chair of fluid dynamics, Technische Universität Darmstadt

Rotating channel flows are of great importance in many engineering applications. In these flows the structure of turbulence and mechanism of momentum transport are highly affected by additional body forces, namely, Coriolis and centrifugal forces. Turbulent channel flows with the spanwise and the streamwise rotation have been extensively studied by many authors see, [1], [2] and [3].
However, the turbulent channel flows with the wall-normal rotation have been rarely and only for weak rotation rates investigated [4]. Since there is no possible experimental approach to the investigation of these flows, the direct numerical simulation (DNS) is the only available method to precisely examine their behaviors. Since a rather complicated analytical solution for the laminar case for arbitrary rotation rate is known we can compare the behavior of the flow in laminar and turbulent state. The flow geometry can be seen in Figure 3.1.

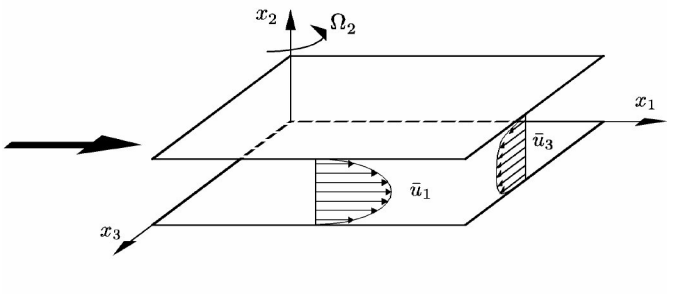

Abbildung 3.1: *wall-normal rotating channel flow*

The project entirely could be summarized in the following tasks:

1. Provide a reference data base using direct numerical simulation (DNS) for different Reynolds numbers for wide ranges of rotation rates and analyze the results. (see [6])

2. Use the DNS data to study the ability of turbulence models to predict the flow under consideration. (see [7])

3. Use Lie group analysis to find symmetries of the equations of the motion and to derive new scaling laws.

The DNS code which we are using is based on standard spectral method with Fourier decomposition in the streamwise and spanwise directions as well as Chebyshev decomposition in the wall normal direction. The original version of the code was developed at KTH in Stockholm. For more detail see [5].
The code is parallelized by OpenMp. The OpenMp application programming interface (API) supports multi-platform shared memory multiprocessing programming. All calculations have been conducted at Hessian High Performance Computer (HHLR).

References

1. Johanson J.P., Halleen R.M., Lezius D.K. Effects of the spanwise rotation on the structure of two-dimensional fully developed turbulent channel flow. J.Fluid Mech., vol. 56, pp. 533-557, 1972

2. Grundestam O., Wallin S., V.Johansson A. Direct numerical simulation of rotating turbulent channel flow. J.Fluid Mech., vol. 598, pp. 177-199, 2008

3. Oberlack M., Cabot W., Pettersson Reif B.A., Weller T. “Group analysis, DNS and modeling of a turbulent channel flow with streamwise rotation.” J.Fluid Mech., vol. 562, pp. 383-403, 2006

4. Li B.-Y., Liu N.-S., Lu X.-Y . “Direct numerical simulation of wall-normal rotating channel flow with heat transfer.” International journal of heat and mass transfer. vol.49, pp. 1162-1175, 2006

5. Lundbladh A., Henningson D., Johansson A. Aeronautical Research Institute of Sweden, Bromma. “An efficient spectral integration method for the solution of the Navier-Stokes equation.” 1992

6. Mehdizadeh A, Oberlack Martin
A study of turbulent Poiseuille-Ekman flow at different rotation rates using DNS
In proceeding of the 12th EUROMECH European turbulence conference, Marburg, Germany, pp. 393-397, 2009

7. Mehdizadeh A., Oberlack M., Hosseinzadeh A DNS and modeling of turbulent channel flow with wall-normal roation. In proceeding of the Sixth International Symposium on Turbulence Shear Flow Phenomena, Seoul, Korea pp. 557-562, 2009

4.3.4 FSI-basierte Optimierung von Profilstrukturen

Nima Aghajari, Michael Schäfer
Fachgebiet Numerische Berechnungsverfahren im Maschinenbau,
Technische Universität Darmstadt

Bei vielen technischen Anwendungen treten zwischen Festkörpern und umströmenden Fluiden Wechselwirkungen auf, welche einen erheblichen Einfluss auf den gewünschten Prozessablauf haben können. Solche Vorgänge sind als Fluid-Struktur-Interaktion (FSI) bekannt und sind seit einigen Jahren Gegenstand intensiver Forschung [1]. Besonders im Fokus der Untersuchungen stehen dabei Wechselwirkungen, die beim Umströmen von Profilstrukturen auftreten, da diese oftmals die Grundlage komplexer Hochleistungsbauteile wie z.B. Turbinenschaufeln, Rotorblättern oder Flugzeugtragflächen darstellen.

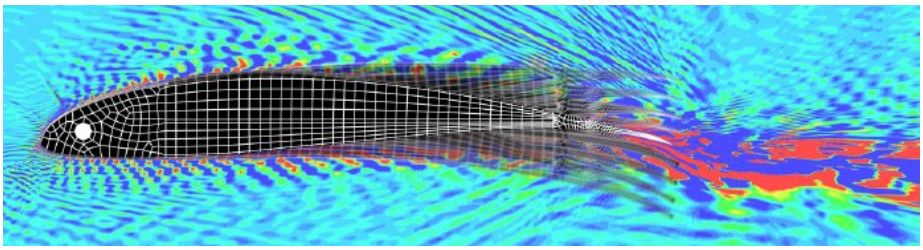

Abbildung 4.1: *Momentaufnahme der FSI bei einer Profilumströmung; Konturdarstellung der Wirbelviskosität*

In diesem Zusammenhang treten Auswirkungen der FSI meist als unerwünschte Begleiterscheinung auf, die den sicheren Betrieb einer Anlage gefährden. Dies kann so weit führen, dass infolge von strömungsseitig hervorgerufenen Schwingungen das komplette Bauteil zerstört wird. Ein bekanntes Beispiel hierfür ist die Tacoma-Narrows-Brücke, die 1940 in Folge von starkem Wind in eine selbstangeregte torsionale Schwingung versetzt wurde und daraufhin eingestürzt ist [2].
Da die komplexen Vorgänge, die bei einer FSI ablaufen stark von der jeweils betrachteten Problemkonfiguration abhängen, sind für zuverlässige Aussagen über das Verhalten eines Systems experimentelle Versuchsaufbauten unerlässlich. Diese sind jedoch mit einem enormen Kostenaufwand verbunden, weshalb zu Entwicklungszwecken vermehrt auf die numerischen Simulation als Hilfsmittel zurückgegriffen wird.
So können ausgehend von validierten Berechnungsergebnissen kostengünstig Parameterstudien durchgeführt werden, um den Einfluss bestimmter Designgrößen auf das Systemverhalten zu bestimmen. Ferner besteht die Möglichkeit, durch die Anwendung geeigneter Optimierungsalgorithmen ideale Ausgangskonfigurationen für ein Profil (z.B. Geometrie oder Steifigkeit) bei einen bestimmten Betriebszustand vorherzusagen.
Eine besondere Herausforderung bei der Simulation einer FSI bei technischen Anwendungen stellt die Berechnung der turbulenten Strömung dar. Um die auftretenden Phänomene korrekt zu erfassen, wird für die Berechnung der instationären Strömungsgrößen eine hohe Genauigkeit gefordert, wobei der Zeitaufwand der Simulation einen noch vertretbaren Rahmen einhalten muss. Einen Kompromiss dieser beiden gegensätzlichen Anforderungen stellt die Large-Eddy-Simulation (LES) dar, welche im Rahmen dieses Projektes Anwendung findet. Um eine höchstmögliche Effizienz zu erreichen, erfolgen zudem sämtliche Berechnungen auf blockstrukturierten Gittern unter Verwendung von Multigrid-Algorithmen parallel auf dem Hessischen Hochleistungsrechner (HHLR).

Verweise

1. Dowell, E. H. and Hall, K. C., Modeling of Fluid-Structure Interaction, *Annual Review of Fluid Mechanics* **33**, S. 445-490, 2001

2. Billah, K. Y. and Scanlan, R. H., Resonance, Tacoma Narrows Bridge Failure, and Undergraduate Physics Textbooks, *American Journal of Physics* **59** (2), S. 118–124, 1991

4.3.5 Parallel Non-Linear Finite Elements for Micropolar Continua

Steffen Bauer, Michael Schäfer
Fachgebiet Numerische Berechnungsverfahren im Maschinenbau,
Technische Universität Darmstadt

The classical continuum theory is based on the hypothesis of continuously distributed mass densities in material bodies, irrespective of their spatial dimensions and their inherent discrete molecular structure. This assumption holds for the majority of practical applications in the field of engineering sciences, since the structures of interest can be considered as large in relation to their sub-microscopic assembly. However, there exist various experimental works describing interesting phenom-ena that might be of growing relevance due to a sustaining trend towards miniaturization in many fields of industry, e.g. [1]. In brief, the those experiments imply that noteworthy length scale (non-locality) effects arise whenever the lateral dimensions of specimens become comparable with the material's intrinsic length scales. These effects can not be modeled by classical continuum theories. As is known, the theory of micropolar solids offers a phenomenological approach for the introduction of length scales into the governing equations. Nevertheless, analytical solutions are available for elementary cases only, and therefore casting the model's theoretical framework into a numerical scheme such as the Finite Element Method (FEM) is inevitable for solving real life engineering problems exhibiting complex geometries and loads.

Non-linear FEM applications, suitable for spatial micropolar configurations undergoing large deformations as proposed in [2], entail drastically increased computational effort in comparison to conventional formulations. Non-symmetric and indefinite global tangent stiffness arrays, a sophisticated numerical treatment of additionally appearing microrotational degrees of freedom and a large set of history variables are main features that challenge an effective computation. Optimization and adaption of algorithms, both on the element and on the solver level, may increase the size of manageable configurations on serial computers. However, this approach is limited and a treatment of micropolar structures with practical relevance and according mesh sizes on serial machines is unlikely to become possible. Therefore, parallel Finite Elements and the access to a sufficient amount of high-performance computing resources on the HHLR play a pivotal role for our studies. Initial analysis with a parallelized build of the FE code FEAP, basing on the parallel data structure suite PETSc and the graph partitioner METIS, show promising results in regard to accuracy, speed-up and scale-up. Current issues of our studies concern the implementation and application of direct solvers. Furthermore, the construction of Krylov subspace preconditioners that allow to iteratively solving the indefinite non-symmetric system matrices efficiently will be important to assure the scalability of the micropolar implementation.

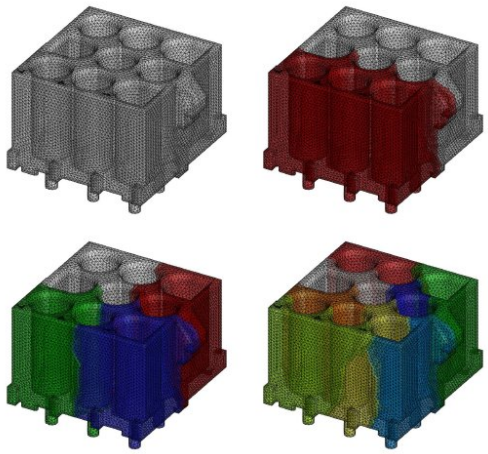

Abbildung 5.1: *Complex problem domain discretized with micropolar tetrahedral elements; exemplary partition in 1, 2, 4 and 8 domains.*

References

1. S. Bauer et al., Three-dimensional finite elements for large displacement micropolar elasticity, Comput. Methods Appl. Mech. Engrg. (2009), 26 pages, revision being processed : D-09-00153

2. S. Bauer and M. Schäfer, Numerical aspects of finite rotation parameterization for non-linear micropolar Finite Element analysis, Eur. J. Mech. A Solids (2009), 16 pages , in review: D-09-00218

4.3.6 Grobstruktursimulation der Strömung über periodische Hügel bei hohen Reynolds-Zahlen

Christine Baur, Michael Schäfer
Fachgebiet Numerische Berechnungsverfahren im Maschinenbau,
Technische Universität Darmstadt

Nach wie vor ist es ein schwieriges Problem komplexe turbulente Strömungen mit hinreichender Genauigkeit zu simulieren. Ein vielversprechender Ansatz ist die Methode der Grobstruktursimulation (LES), bei der nur die kleinen turbulenten Skalen modelliert und die großen direkt gelöst werden. Die LES ist als Mittelweg zwischen direkter Simulation und statistischen Modellen zu verstehen. Allerdings nimmt die Grobstruktursimulation immer noch sehr hohe Rechenzeiten und sehr viel Speicherplatz in Anspruch [2]. Aufgrund dessen lassen sich solche Problemstellungen derzeit nur auf parallelen Hochleistungsrechnern wie dem HHLR innerhalb akzeptabler Rechenzeiten simulieren.
Im Rahmen dieses Projekts wird zur LES mit dem dynamischen Smagorinsky Modell der auf der Finite-Volumen-Methode basierte Strömungslöser FASTEST verwendet [1], der auf einer randangepassten, dreidimensionalen, block-strukturierten räumlichen Diskretisierung basiert. In Abbildung 6.1 ist die Geometrie und die instationäre Geschwindigkeitsverteilung in x-Richtung für einen Zeitschritt des bekannten Testfalls *„Strömung über zweidimensionale periodische Hügel“* zu sehen. Hierbei handelt es sich um einen Ausschnitt aus einem periodischen Kanal, der durch Hügel an der unteren Wand eingegrenzt wird. Die Herausforderung an diesem Testfall ist die betrachtete hohe Reynolds-Zahl Re=37000, welche eine extrem hohe Auflösung in Wandnähe erfordert. Ausführliche Untersuchungen zu niedrigeren Reynolds-Zahlen existieren bereits [2]. Die instationären Größen werden zeitlich gemittelt und mit den bestehenden experimentellen Daten [3] an unterschiedlichen Schnitten der Geometrie verglichen.

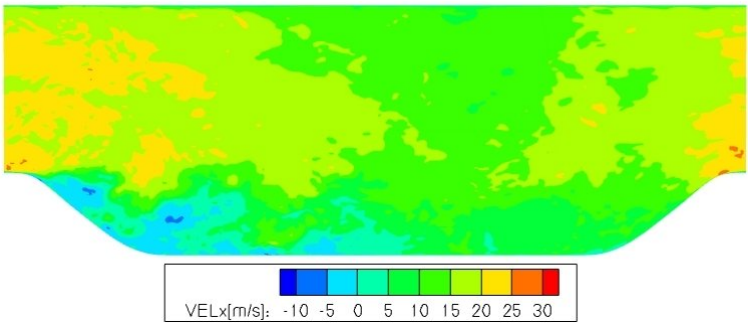

Abbildung 6.1: *Strömung über periodische Hügel: Geschwindigkeit in x-Richtung*

Das Berechnungsgitter besteht aus circa 13 Millionen Kontrollvolumina und die Berechnung wird auf 32 Prozessoren durchgeführt.

Literatur

1. D. C. Sternel. FASTEST-Manual, Fachgebiet Numerische Berechnungsverfahren im Maschinenbau, Technische Universität Darmstadt, 2005.

2. M. Kornhaas, D.C. Sternel, M. Schäfer. Influence of time step size and convergence criteria on large eddy simulations with implicit time discretization. In J. Meyers, B.J. Guerts, and P. Sagaut (eds.), Quality and Reliability of Large-Eddy Simulations, pages 119-130, Springer, Berlin, 2008.

3. C. Rapp. Experimentelle Studie der turbulenten Strömung über periodische Hügel, Dissertation, Technische Universität München, 2008.

4.3.7 Parallel Computation of Fluid Structure Interaction in Labyrinth Seals of Jet Engines

Yu Du, Michael Schäfer
Fachgebiet Numerische Berechnungsverfahren im Maschinenbau, Technische Universität Darmstadt

Labyrinth seals are widely used in gas turbine engines to control internal leakage, thereby increase engine performance and decrease operating costs. To provide sealing across a stationary/rotating interface, labyrinth seals have to be non-contacting to avoid excessive heat production. However, their sealing capacities are limited by the need to maintain a clearance between the seal and the rotating surface. Hence improving sealing performances is equivalent to minimizing leakages while preventing any forms of contact in seals, where the interaction between the leakage flow and the seal structure plays a dominant role. Such problems are known as Fluid Structure Interaction (FSI) problems. Therefore, FSI needs to be employed in numerical simulations to accurately represent the coupled physics in labyrinth seals.

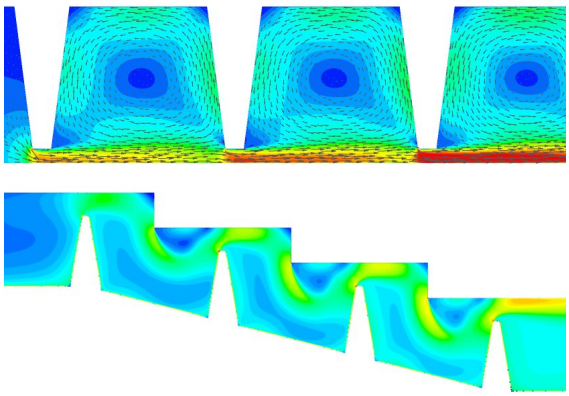

Abbildung 7.1: *Various labyrinth seals*

FSI is an important branch of multi–physics analysis, and is applied when the physics is more complex than a single field analysis can simulate. FSI has attracted many researchers and has become a major focus in the field of computational engineering over the past years.
This project is focused on the numerical simulation of two-way mechanical and thermal FSI in labyrinth seals (Fig. 7.1). Fluid force induced vibration, heat transfer across the fluid-solid surface, as well as rotationally induced inertial effects are investigated using FSI [1-2]. The fluid solver ANSYS® CFX® and the structural solver ANSYS® Mechanical^{TM} are coupled implicitly without any third-party interface (Fig. 7.2). The simulations run in parallel on the HHLR.
Understanding the interaction between the fluid and the structure is essential for the design of labyrinth seals. By employing fully coupled FSI into the numerical simulations, the FSI effects in labyrinth seals are determined directly without any simplifications or empirical assumptions, which cannot be achieved by single field approaches. Thereby the complex coupled physics is numerically investigated with a greater accuracy as well as a greater flexibility.

Literature

1. Y. Du and M. Schäfer. *Fluid structure interaction in non-contacting gas seals*, in: Computational Methods for Coupled Problems in Science and Engineering III, Ischia, Italy, 2009.

2. Y. Du and M. Schäfer. *Fluid structure interaction in non-contacting gas seals*, in: First International Workshop on Computational Engineering, Herrsching, Germany, 2009.

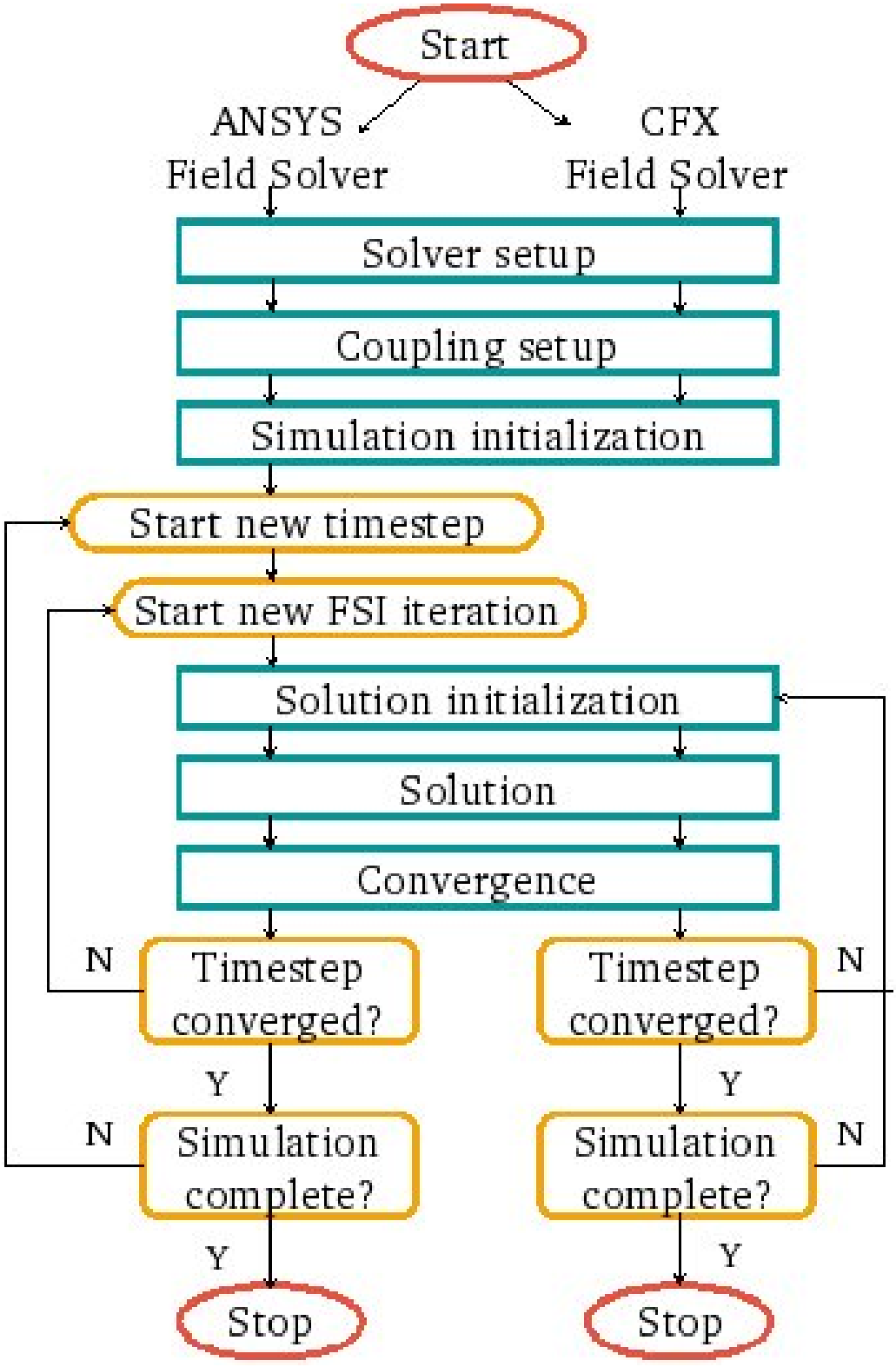

Abbildung 7.2: *FSI approach in ANSYS*

4.3.8 Grobstruktursimulation turbulenter Strömungen

Frank Flitz, Michael Schäfer
Fachgebiet Numerische Berechnungsverfahren im Maschinenbau, Technische Universität Darmstadt

Die Akustik turbulenter Strömungen spielt in der Industrie eine wichtige Rolle, so z. B. in der Umströmung von Fahrzeugen. Zur Simulation der Schallabstrahlung werden aus der Strömungssimulation die akustischen Quellterme ermittelt. Da diese Quellterme dafür zeitlich aufgelöst vorliegen müssen, eignen sich zur Strömungssimulation nur die Direkte Numerische Simulation (DNS) und die Grobstruktursimulation (Large Eddy Simulation, LES). Die wesentlich weniger rechenintensive Simulation der Reynoldsgemittelten Navier-Stokes Gleichungen (Reynolds-Averaged-Navier-Stokes, RANS) ist dafür nicht geeignet.

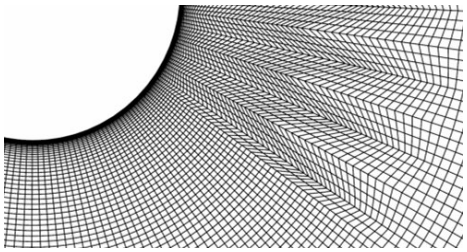

Abbildung 8.1: *Gezielt verzerrtes Gitter*

Eine Simulation mittels der sehr rechenintensiven DNS ist bisher nur auf einfachen Geometrien bei geringen Reynoldszahlen möglich. Der Fokus in der Simulation turbulenter Strömungen auf komplexen Geometrien in der Zukunft liegt daher auf der LES. Die Diskretisierungsordnung der bei der LES eingesetzten Standarddiskretisierung CDS verringert sich aber auf verzerrten Gittern, wie sie bei komplexen Geometrien auftreten, von zwei auf eins. Daher wird hier der Einfluss des alternativen Diskretisierungsschemas MuLi [1] untersucht, welches auf verzerrten Gittern keinen Ordnungsverlust aufweist. Zwei Punkte sind bei den Untersuchungen von besonderem Interesse:

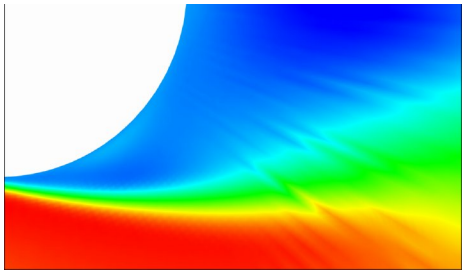

Abbildung 8.2: *Die Diskretisierung mittels CDS liefert kein „glattes“ Ergebnis*

Zum Einen ist zu untersuchen ob die Diskretisierung mit MuLi zu einer genaueren Abbildung der Realität führt. Dies lässt sich bei einer turbulenten Strömung nicht anhand einer Momentaufnahme der Strömungsgrößen beurteilen. Vielmehr müssen diese dafür über einen großen Zeitraum gemittelt werden um auskonvergierte Mittelwerte der Strömungsgrößen zu erhalten.
Zum Anderen ist die „Glattheit“ der Strömungsgrößen von Interesse. Ist diese nicht gewährleistet, entstehen dadurch künstliche akustische Quellen, welche die Simulation der Schallabstrahlung negativ beeinflussen. Die Diskretisierung mittels CDS neigt unter bestimmten Umständen zu nicht glatten Ergebnissen. Daher ist ein weiterer Schwerpunkt der Untersuchungen das Potential zur Erhöhung der Glattheit durch die Diskretisierung mit MuLi.

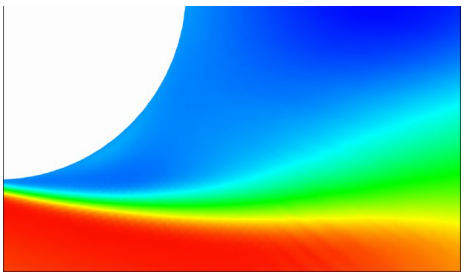

Abbildung 8.3: *"Glatteres" Ergebnis durch die Diskretisierung mittels MuLi*

Zur Untersuchung der Unterschiede zwischen den Diskretisierungen wird in einem turbulenten Strömungsbereich gezielt eine Gitterverzerrung eingebracht (s. Abbildungen).
Durch den ständigen Zugewinn an Rechenleistung wird es in Zukunft möglich sein die turbulente Strömung auf komplexen Geometrien instationär zu berechnen. Die Benutzung des HHLR erlaubt es die zukünftigen Herausforderungen bereits heute anzugehen.

Literatur

1. T. Lehnhäuser, M. Schäfer “Improved linear interpolation practice for finite-volume schemes on complex grids”, Int. Journal of Numerical Methods in Fluids, Vol. 83/No. 7, 625-645 (2002)

4.3.9 Aeroacoustics of turbulent flows at low Mach number

Michael Kornhaas, Michael Schäfer
Fachgebiet Numerische Berechnungsverfahren im Maschinenbau, Technische Universität Darmstadt

A major part of the noise generation in urban environments is caused by turbulent flows, e.g. the noise of driving cars, fans, etc. Even though the prediction and reduction of noise is of great importance and an important issue during the design process, the physical mechanisms of noise generation in turbulent flows are still not fully understood for many applications. Computational fluid dynamics (CFD), especially time resolved methods like the Direct Numerical Simulation (DNS) and the Large Eddy Simulation (LES) can be a powerful tool for a better understanding of flow physics and the mechanisms of aerodynamic noise generation. This is not only because of their capability of predicting fluctuating quantities that can be used as source terms for aero-acoustic simulations, but also because of their higher accuracy compared to the numerically cheaper Reynolds Averaged Navier-Stokes (RANS) simulations.

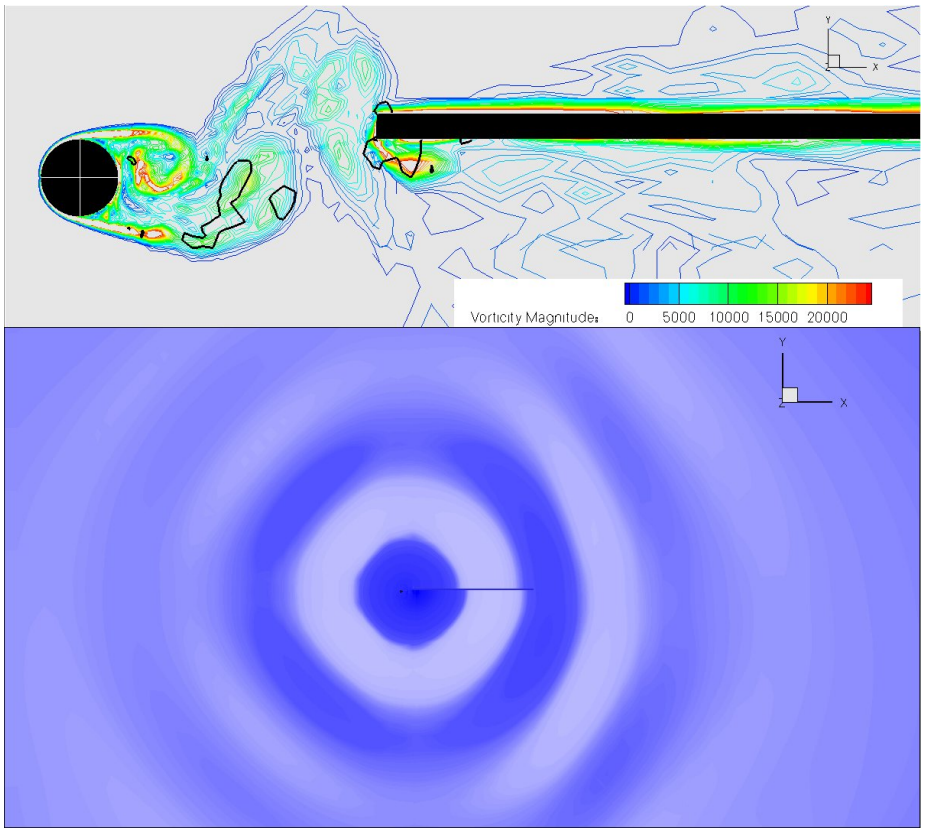

Abbildung 9.1: *Turbulent structures around a cylinder plate configuration (top) and corresponding acoustic field (bottom).*

However, only recently sufficient computational power has become available to perform such computations for configurations of practical interest. In this project a numerical method for the simulation of aerodynamic noise caused by flows at low Mach numbers within and/or around complex geometries is developed. To account for sound propagation the in-house finite volume flow solver FASTEST [1] is extended by a high resolution finite volume scheme that solves the linearized Euler equations (LEE) on boundary fitted, block structured hexahedral meshes. Aeroacoustic sources are obtained from the unsteady calculated flow field following the basic ideas of Hardin's and Pope's acoustic/viscous splitting technique [2].

In order to speed up the coupled simulation and to account for the very different length scales of small turbulence structures and the long-wave acoustics, the acoustic field is computed on the hierarchically coarsened CFD grid. Further, different time scales are employed so that multiple acoustic time steps can be performed within one CFD time step.
Figure 9.1 shows the turbulent structures and the corresponding acoustic field for the flow around a cylinder plate configuration as example for a coupled aeroacoustic computation. The results were obtained on a 4 million control volume grid and were computed with 16 CPUs on the HHLR.

References

1. FASTEST Manual, *Chair of Numerical Methods in Mechanical Engineering, Technische Universität Darmstadt.* , Germany (2005)

2. J.C. Hardin and D.S. Pope, An Acoustic/Viscous Splitting Technique for Computational Aeroacoustics, *Theoret. Comp. Fluid Dynamics* , **6**, pp. 323-340 (1994)

4.3.10 Flow optimization using parallel solved sensitivity equations

Julian Michaelis, Michael Schäfer
Institute of Numerical Methods in Mechanical Engineering, Technische Universität Darmstadt

Numerical flow simulation is a well-established field in modern mechanical engineering. The numerical algorithms support the practical experiment by providing cost-efficient and risk-free methodologies for flow engineers. Because of the continuous increasing CPU power and the development of more sophisticated algorithms a new research field got into the spotlight of interest. The automated flow optimization process is an ongoing topic in today's research.
The task herein is providing algorithms which are able to deal with arbitrary objective functionals depending on predefined design parameters (e.g. geometry deformation, wall temperature, inlet velocity) and state variables (e.g. velocity, pressure and temperature distribution). The algorithms have to be fast and robust enough to find an optimal solution within a short period of time, even for umpteen different control parameters. An example for such a challenging optimization problem is the redesign of a technical component within an engine with the objective to minimize the pressure loss within the component, while assuring an acceptable fluid temperature distribution.

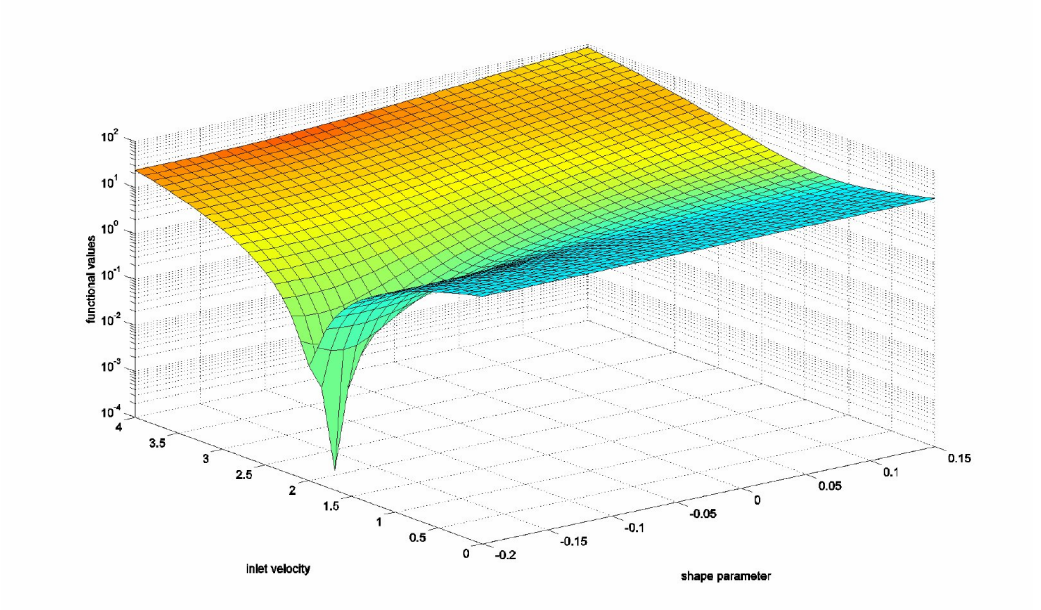

Abbildung 10.1: *Logarithmic representation of an exemplary objective functional*

The derivative based methods are one approach for these optimization problems. Therein it is necessary to compute the gradient of the objective functional. An efficient way to get this gradient is to solve the continuous sensitivity equations arising from differentiating the Navier-Stokes equations with respect to each design parameter. Solving these equations provides knowledge about the influence of the different control parameters and this allows calculating the functionals gradient. Assuming the optimization problem has N independent design parameters, this approach will lead to N different sensitivity equations that need to be solved.
In current research an intense focus is on accelerating the solving procedure of the sensitivity equations. Besides the implementation of a multigrid algorithm working on these equations the next step is to implement a fully parallelized solving method to speed up the optimization process. The anticipated gain bases upon the simultaneous calculation of the flow sensitivities. All these speed-up strategies will enable to solve highly complex optimization problems taking innumerous control variables into account, like the problem described above.

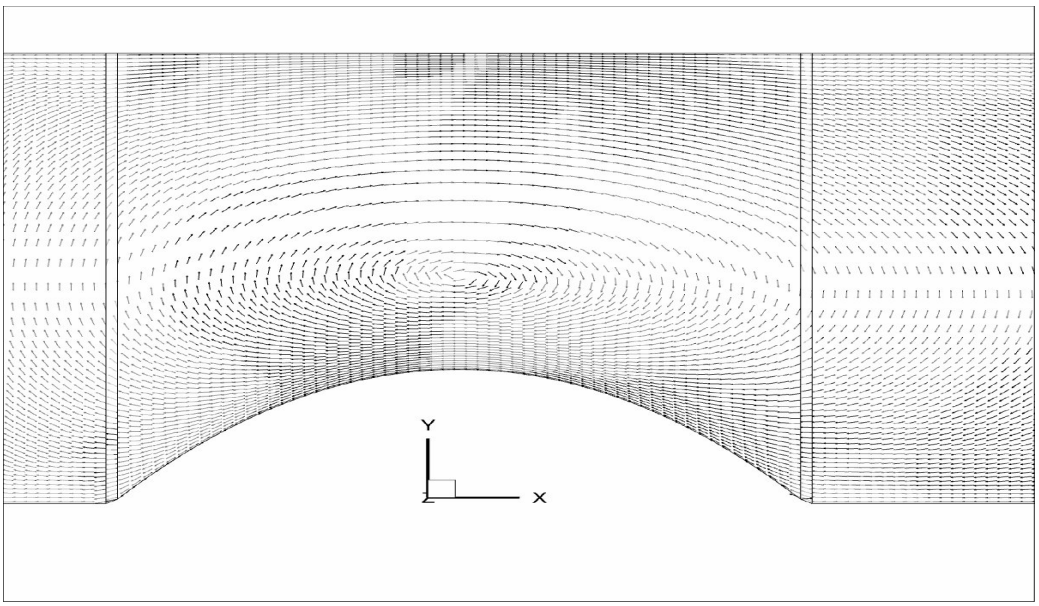

Abbildung 10.2: *Vectorial sensitivity plot of shape influence on the flow field.*

References

1. Siegmann, J., Becker, G., Michaelis, J., Schäfer, M., A general sensitivity based shape optimization approach for arbitrary surfaces. Proceedings of the 8th World Congress on Structural and Multidisciplinary Optimization Rodrigues, H.C. et al. (eds.), Lisbon (2009)

4.3.11 Multigrid Methods applied to Fluid-Structure Interaction

Stephen Sachs, Dörte Sternel, Michael Schäfer
Fachgebiet Numerische Berechnungsverfahren im Maschinenbau,
Technische Universität Darmstadt

This work focuses on the acceleration of the combined simulation of fluid surrounded structures or structure enclosed fluids. In numerous numerical simulations [FB02?]ow cannot be described correctly without any knowledge of the behavior of the passed structure and vice versa. Provoked by the huge rise of computing power in the last years, the possibilities of solving both [FB02?]uid and structure problems have achieved a level of accuracy, such that a simulation of the counterpart by mere predetermined boundary conditions is not adequate any more. Fluid-Structure Interaction (FSI) dissolves this problem by solving both the fluid and the structure problem simultaneously.
Every numerical simulation of a physical process which can be described by a partial differential equation results in a large system of linear equations. In terms of computing time solving these systems is one of the most challenging tasks in numerical simulation. In the case of FSI problems there are even two such systems to solve.
As the direct evaluation of such a system would be inefficient, a great number of sophisticated indirect or iterative solvers for these kinds of problems have been developed. One method to improve the convergence speed of iterative solvers is the Multigrid Method. As low-frequency errors are reduced substantially faster on coarser grids than on fine ones and coarse grid iterations are per se faster, Multigrid has a noticeable influence on computing time.

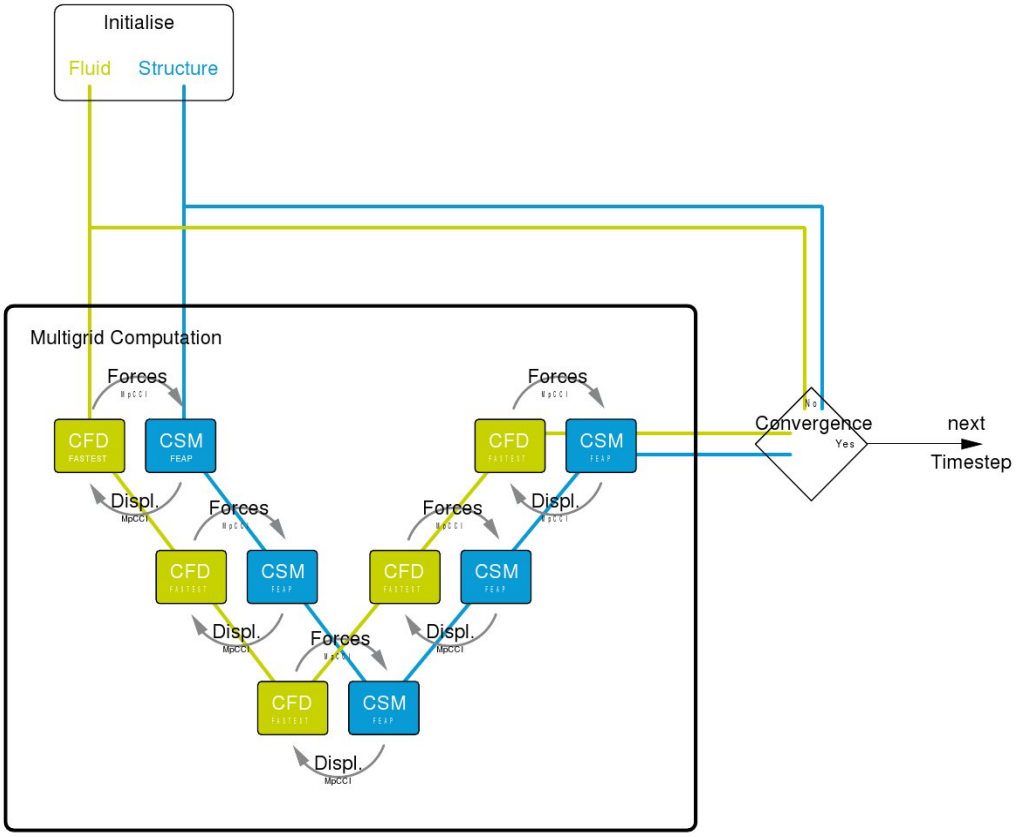

There are two main approaches to FSI problems with well known advantages and drawbacks. On the one hand the numerically robust monolithic approach with its comparably low flexibility and on the other hand the highly adaptable but numerically challenging partitioned approach. A symbiosis of these two approaches is the implicit partitioned approach. Built from the partitioned approach

it inherits its flexibility but gains more stability by several implicit coupling steps within a time step. In addition to the implicit partitioned approach we introduce the global Multigrid, which is even closer to a monolithic approach while preserving the flexibility of two independent codes. The fluid and the structure problem are both solved via the Multigrid Method and run in simultaneous V-cycles. Coupling is applied at every grid level and restriction and prolongation are performed in accord. By this interactive manner of computation, the error that arises from the coupling itself is directly affected in the Multigrid computation. In other words, a great part of it is eliminated during coarse grid iterations.
Another great advantage of the geometric Multigrid Method is its comparably easy application to domain decomposition. Thus the computations can be parallelized and efficiently calculated on multiple processors of the HHLR.

4.3.12 Numerical flow control and optimization

Johannes Siegmann, Michael Schäfer
Fachgebiet Numerische Berechnungsverfahren im Maschinenbau
Technische Universität Darmstadt

Computational fluid dynamics (CFD) is a major subject in various engineering applications, e.g. aerodynamics in aeronautical and automotive engineering which has led to the development of sophisticated CFD codes. With those and increasing computational power a new topic became increasingly interesting besides the pure flow simulation: numerical flow optimization. Not only the behavior of a flow field is of interest anymore but how to affect this flow to reach given aims. These objectives can be miscellaneous, one can think of aerodynamic improvements via the cooling of a engine block to the design improvement of a combustion chamber.
The work presented shows the implementation and validation of a sensitivity based shape optimization method for arbitrary surfaces. The governing state equations as well as the resulting sensitivity equations are solved with our in-house code FASTEST. This solver applies a fully conservative finite-volume approach to solve the incompressible Navier-Stokes equations on a non-staggered, block structured and cell centered grid. A highly efficient computation can be obtained due to the close relationship of solving sensitivities and flow governing equations.
Common methods for the resolution of minimization problems can be divided into strategies with and without derivative determination of the cost functional. In the first case the cost functional is approximated via a polynomial ansatz which can then be differentiated at low cost. In opposite, the second case is based on the gradient evaluation of the real cost functional. Hence there are several ways to calculate the differential. Examples are the finite difference method, the solution of the adjoint equation or the evaluation of sensitivities. The resulting gradient is transferred to the optimization algorithm, which allows the determination of the cost functionals minimum.
The sensitivities are calculated with a differentiate-then-discretize approach, i.e. the sensitivity equations are obtained via differentiation of the non-discretized partial differential equations followed by discretization. The resulting PDE-system is then solved with the finite-volume approach described above. Particular attention to the boundary conditions is required, i.e. they have to be differentiated as well. Thus, for the optimization with shape parameters the derivative of the flow at the boundary as well as the derivative of the boundary describing functional has to be calculated. In our case the surfaces are described with NURBS surfaces, i.e. we need their derivative with respect to the shape parameters.
The calculation of the flow parameters and the according sensitivities are characterized by a high computational effort. In order to achieve acceptable computation times it is inevitable to parallelize the given procedure. On the side of the flow calculation this work is already done and works fine on the HHLR. For the calculation of the sensitivities it is either possible to parallelize the sequential calculation of the sensitivities or to distribute the different equation systems for the varying parameters to several processors.

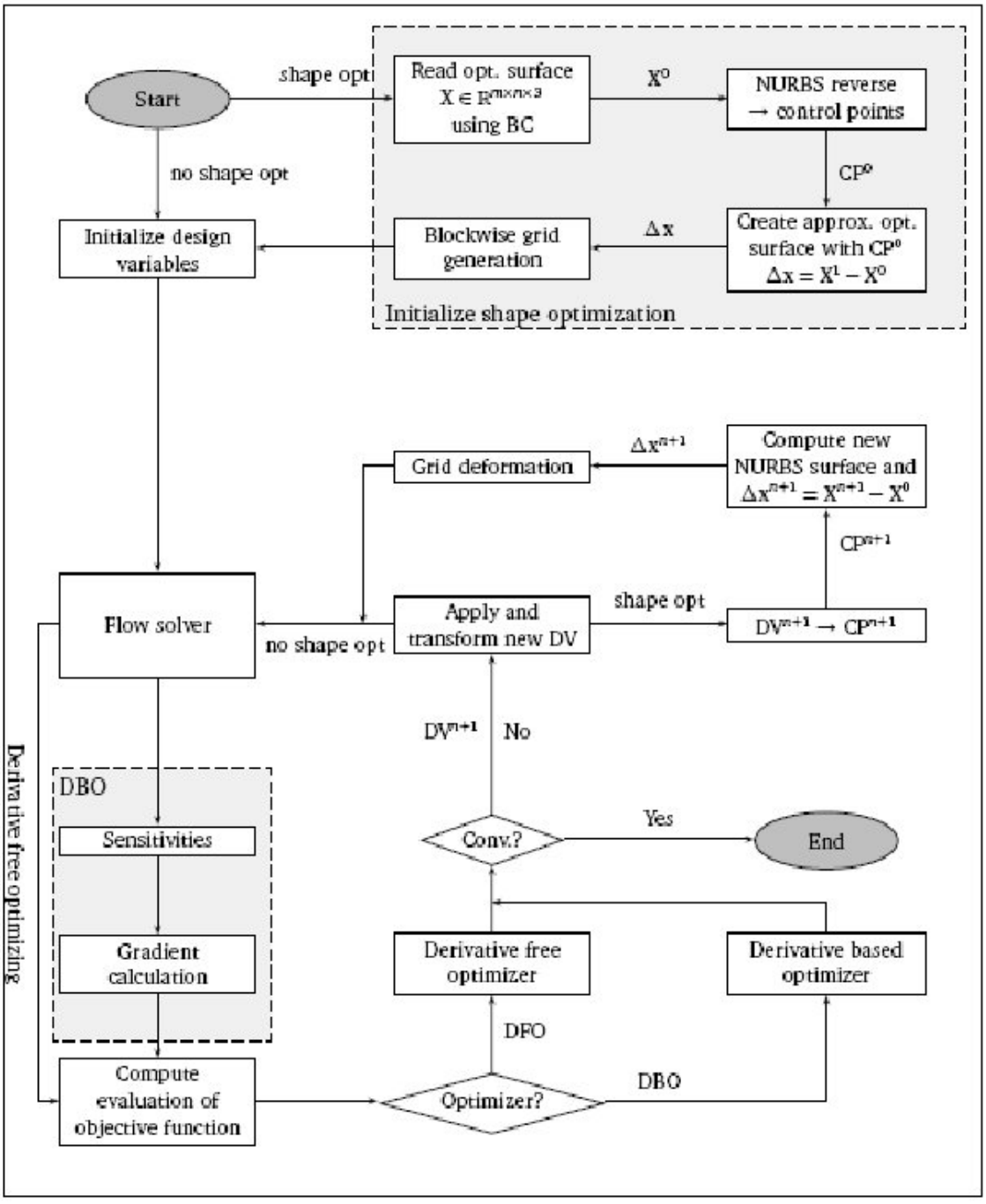

Abbildung 12.1: *Description of the algorithm*

4.3.13 Simulation turbulenter Fluid-Struktur-Interaktion

Dörte C. Sternel, Plamen Pironkov, Michael Schäfer
Fachgebiet Numerische Berechnungsverfahren im Maschinenbau,
Technische Universität Darmstadt

Fluid Struktur Interaktion (FSI) ist ein Phänomen das sowohl in vielen alltäglichen Bereichen auftritt, wie z.B. bei Bäumen im Wind, oder in vielen technischen Anwendungen, wie z.B. bei Windrädern oder in Gasturbinen. Kennzeichnend für dieses Phänomen ist, dass die Strömung Kräfte auf die Struktur aufbringt und diese dadurch verformt wird. Durch die Verformung der Struktur ändert sich die Berandung des Strömungsgebietes und dadurch das Strömungsfeld und damit wiederum die Kräfte die auf die Struktur wirken.

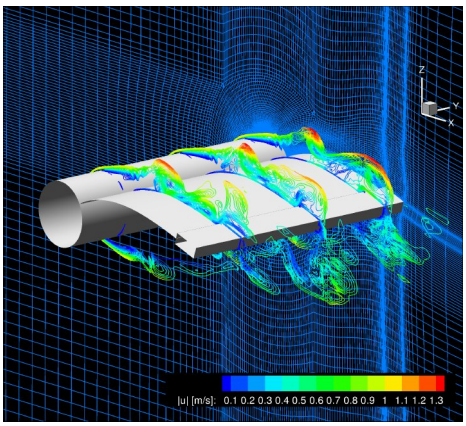

Das für dieses Projekt weiterentwickelte und verwendete Verfahren zur Simulationen der FSI basiert auf einem partitionierten Ansatz [1]. Das Strömungsfeld und die auf die Struktur wirkenden Kräfte werden hierbei mit dem Finite Volumen Löser FASTEST berechnet, diese Kräfte werden dann mittels des Interfaces MpCCI an den Strukturlöser FEAP übergeben in dem die daraus resultierende Verformung berechnet wird und diese dann wiederum über MpCCI an FASTEST gegeben werden. Hier wird das Strömungsgebiet und das Diskretisierungsgitter an die Verformung angepasst und das veränderte Strömungsfeld berechnet. Die Anpassung des Gitters erfordert eine besondere Aufmerksamkeit, da insbesondere bei turbulenten Strömungen die Gitterqualität einen entscheidenden Einfluss auf die Lösung hat, so darf sich Beispielsweise die Dicke der wandnächsten Kontrollvolumen nicht wesentlich ändern oder bestimmte Winkel dürfen nicht zu klein werden. Da zeitaufgelöste turbulente Strömungen nur mit sehr rechenintensiven Verfahren, wie z.B. der Grobstruktursimulation (Large Eddy Simulation, LES), lösen lassen müssen alle verwendeten Komponenten effektiv parallelisiert sein [5]. Die Abbildung zeigt eine Momentaufnahme des Strömungsfeldes um eine bewegte Struktur dargestellt, abgebildet sind Isolinien der Wirbelstärke und das Gitter für den Strömungslöser in einer Ebene. Der Testfall basiert auf einer vermessenen Konfiguration [6]. Die Berechnung wurde mit ungefähr 10 Millionen Kontrollvolumen auf dem Hessischen Hochleistungsrechner durchgeführt.

Verweise

1. D.C. Sternel, M. Schäfer, M. Heck and S. Yigit. Efficency and accuracy of fluid-structure interaction simulations using an implicit partitioned approach. Computational Mechanics, 43:103-113, 2008.

2. D.C. Sternel, P.Pironkov, M. Kornhaas and M. Schäfer. Fluid-Structure Interaction in Turbulent Flow. In Computational Methods for Coupled Problems in Science and Engineering III, Ischia, Italy, June 2009, CIMNE.

4.3.14 Evolutionary Optimization Methods for flow Shape Optimization

Hongtao Sun, Michael Schäfer
Fachgebiet Numerische Berechnungsverfahren im Maschinenbau,
Technische Universität Darmstadt

Evolutionary algorithms (EAs) have been receiving increasing interest in solving CFD-based shape optimization problems because of their derivative-free property and the capability of dealing with global and multi-objective optimization problems. An essential challenge for the application is the huge time consumption since EAs usually require a large number of function evaluations, which is especially true when the optimization problem has a high-dimensional design space, and the flow analysis may be computationally expensive. This work proposes an efficient optimization methodology for solving flow shape optimization problems is proposed, which is based on EA for its attractive properties and meanwhile improves optimization efficiency of EA by adopting the following approaches:

- Combine a deterministic optimization method with EA to accelerate the local convergence.
- Parallelize the function evaluations in EA to reduce the computational time.
- Construct approximation models to substitute the exact function evaluations to reduce the computational cost.
- Employ a promising control procedure during the evolutionary optimization to improve the approximation accuracy.

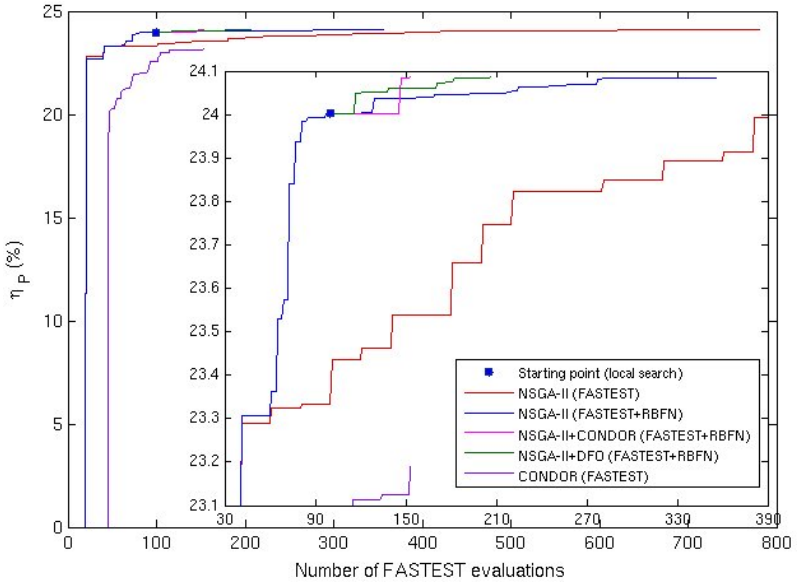

Abbildung 14.1: *Convergence efficiency of different optimization schemes for a pipe shape optimization case*

The proposed optimization methodology consists of two separate parts: the global search using a modified parallel NSGA-II and the local search using deterministic method such as the derivative-free trust-region method CONDOR and DFO. The approximation models based on radial basis function network (RBFN) will be constructed and are incorporated into the global part.
A complete optimization framework is developed for solving flow shape optimization problems. The optimizer manages and controls the whole optimization process. The shape variation and flow

simulation are intergrated for the evaluation of objective functions and the construction of the database. The flow simulation is performed using the flow solver FASTEST. FFD is selected for the shape variation because it directly modifies the computational grids required by the flow solver and provides a flexible deformation through the movement of only a small number of points. It is especially advantage since the number of design variables is an important factor that determines directly the optimization cost and also influence the accuracy of the approximation model. The proposed optimization methodology is applied to several analytical and numerical test cases, where a significant reduction of the computational cost is achieved without sacrificing the optimization performance.

Literature

1. K. Deb, Multi-Objective Optimization using Evolutionary Algorithms. Wiley, 1 edition,2001

4.3.15 Modelling of solidification of binary fluids with non-linear viscosity models

Tomasz Wacławczyk, Michael Schäfer, Dörte Sternel
Fachgebiet Numerische Berechnungsverfahren im Maschinenbau,
Technische Universität Darmstadt

During solidification of binary fluids, e.g. metal alloys, for a certain range of temperatures and compositions a mushy zone is created. The influence of the mushy zone morphology on the flow field can be modeled by two approaches: porous media model, where the Carman-Kozeny relation couples local porosity of the medium with the local liquid fraction, or direct modification of the local fluid viscosity relatively to the local solid fraction. These two physical models are valid in different regions of the mushy layer: the region of stationary, columnar crystals where the solid velocity is zero and the region of the equiaxed crystals where the velocity of solid is assumed to be equal to the velocity of the melt. The difficulties in the modeling of the mushy zone by a one-field model arise during the transition from the mixture velocity (for fluid and solid) to the interstitial velocity in the porous zone. In the case of the second approach, an assumption about the continuous change of the material properties across the solid, the mushy layer and the liquid is used. A common approach employs a lever rule to approximate density and viscosity in the mushy zone together with a linear dependence of the solid fraction on temperature inherited from the linearised phase change diagram. The linear dependence of solid and liquid viscosities based on the lever rule is not appropriate since the solid viscosity can not be defined. During our work, based on the experimental evidence we postulated an alternative non-linear dependence of the viscosity on the solid fraction and the shear velocity, see Fig. 15.2 for results of the performed simulations. The viscosity values used for partial validation of the model were obtained during measurements in a cylindrical rheometer, see Fig. 15.1 for comparison of the simulations with experimental data.

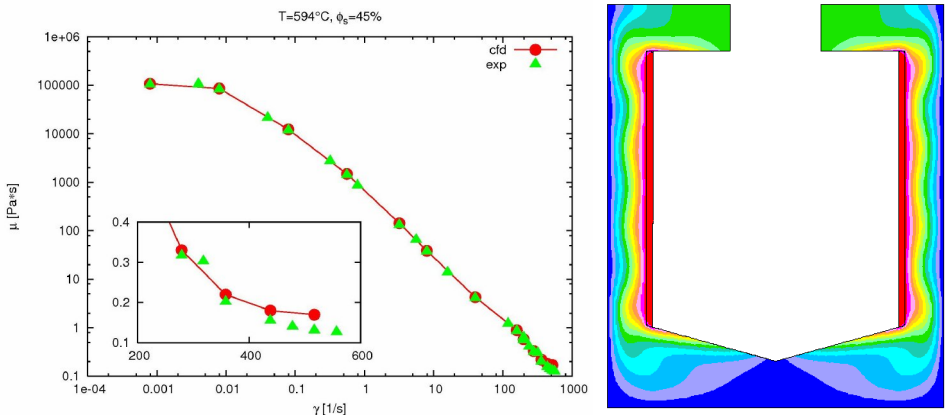

Abbildung 15.1: *Comparison of experimental data and numerical simulations in the case of constant viscosity assumption during flow in cylindrical rheometer (left), the velocity field (right) for single simulation point*

References

1. T. Wacławczyk, D. Sternel, M. Schäfer, Modeling of solidification of binary fluids with non-linear viscosity models, Proceedings of Computational Methods in Multiphase Flows V, New-Forest, UK

2. M. Le Bars, M. G. Worster, Solidification of a binary alloy: Finite-element, single-domain simulation and new benchmark solutions, *J. Comp. Phys.,* Vol. 216, pp. 247-253, 2006

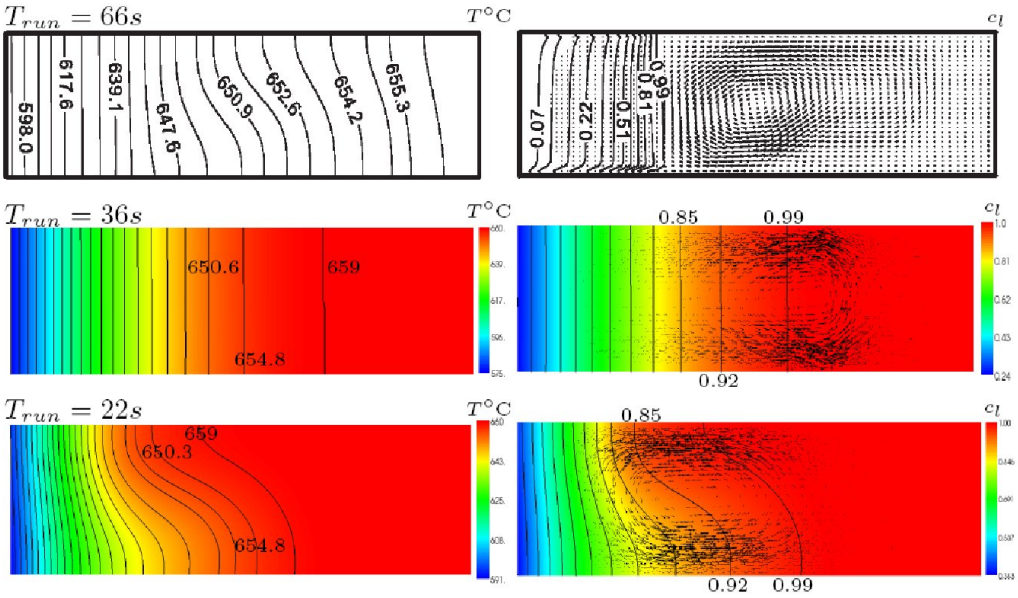

Abbildung 15.2: *Comparison of the isotherms (left)) and liquid volume fractions (right) with simulations data from literature (top) in the case of solidification in rectangular cavity with and without nonlinear viscosity model*

4.3.16 Simulation and Control of Drop Size Distributions in Stirred Liquid/Liquid Systems

Astrid Walle, Michael Schäfer
Institute of Numerical Methods in Mechanical Engineering,
Technische Universität Darmstadt

Mixing is a very important process in various applications, especially in oil and gas, chemical and food industries, therefore it is of major importance to get a deep insight into the flow properties in a stirrer. In particular the most common mixing process, when one liquid disperses into another by building drops, is of special interest. The attributes of these drops affect the technical process, e.g. chemical reactions. That's why it is desirable to control the drop size distribution (DSD).

Experimental investigations are very costly and time-consuming, so the advantages of computational fluid dynamics (CFD) should be utilized also for the field of mixing processes. CFD is the standard tool for predicting turbulent flows and showed already good results for stirred tanks [1][2]. The numerical simulations during the investigation of the drop size distributions are done with our in-house flow solver FASTEST-3D [3], which is based on a fully conservative finite volume method for the solution of the incompressible Navier-Stokes equations on a non-staggered, cell-centered, block-structured, boundary-fitted grid.

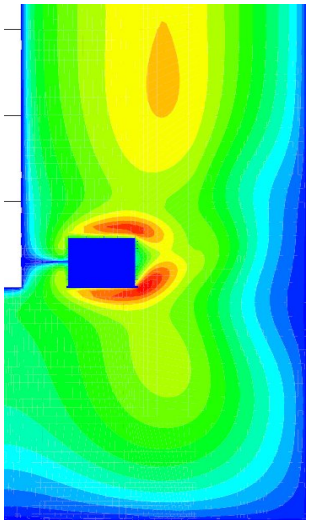

Abbildung 16.1: *Turbulent kinetic energy (Rushton turbine at Re=1000)*

Within the framework of this project several population balance equations (PBE), which calculate the transient drop size distributions, are implemented into the flow solver. This is done by applying the direct quadrature method of moments (DQMOM) to the integro-differential PBE, which is dependent on time, space and internal coordinates, e.g. the drop-diameter. When using DQMOM, this internal coordinate is "integrated out" and the moments of the PBE only depend on time and space. Additionally to the Navier-Stokes equations for the flow, there are scalar transport equations to solve for every control volume and every time step.

The flow in the stirrer is turbulent and because of that very complex with small scales, a fine grid resolution is necessary which requires efficient computer codes to solve these problems. The high number of grid cells and the additional equations lead to a high necessity of memory and CPU-time. Thus the investigation derives high benefit by executing the computations on parallel high-performance computers. In addition to solving the flow and population balance properties, an active control is applied to this coupled system, via an interface between the flow solver FASTEST-3D with the integrated PBE and the software Matlab (to use the vast set of methods implemented in the Matlab Control Toolbox). To achieve acceptable computing times and to be able to perform on high-performance computers, like the HHLR, an efficient parallelization of the complete coupled system is a major ambition.

References

1. Z. Harth, Automated Numerical Shape Optimization of 3-dimensional Flow Geometry Configuratiuons, Dissertation, Technische Universität Darmstadt, 2008
2. R. Sieber, Numerische Simulation technischer Strömungen mit Fluid-Struktur-Kopplung, Dissertation, Technische Universität Darmstadt, 2002
3. FASTEST, User Manual, Institute of Numerical Methods in Mechanical Engineering, Technische Universität Darmstadt, 2006

4.3.17 Elastohydrodynamische Mehrkörpersimulationstechnik

Prof. Knoll
Institut für Maschinenelemente und Konstruktionstechnik, Universität Kassel

Der Schwerpunkt der Forschungsarbeiten des IMK liegt in der Entwicklung von Simulationstechniken für strukturdynamisch/elastohydrodynamisch gekoppelte Systeme (Mehrkörpersysteme) mit den Zielstellungen zeit- und kostenintensive Prüfstands- oder Feldversuche zu vermeiden und Rechenzeit zu optimieren. Dabei stehen die Strukturdynamik und die tribologisch/mechanische Bauteilbeanspruchungsanalyse im Vordergrund der Arbeiten.

Die Beanspruchungsanalyse unter motorischen Lastkollektiven erfordert transiente Berechnungsalgorithmen, wobei aus Sicht der mechanisch/physikalischen Modellierung als maßgebliche Einflussgrößen neben der Steifigkeit und der Masse der Komponenten auch deren Wechselwirkung unter den einwirkenden äußeren Randbedingungen bzw. Belastungskollektive zu berücksichtigen sind. Die Erhöhung der Aussagesicherheit von Simulationstechniken für gekoppelte Tribosysteme erfordert die Berücksichtigung realer konstruktiver Gestaltung der Bauteile, deren Materialeigenschaften, sowie deren Lastübertragungsmechanismen, die sich aufgrund der stark nichtlinearen Schmierfilmreaktionen einstellen (Erhöhung der Modellierungstiefe). Die hierzu notwendigen physikalischen Modelle beschreiben die elasto-hydrodynamischen Schmierfilmreaktionen einschließlich der auftretenden Festkörpertraganteile auf Basis einer erweiterten hydrodynamischen Schmierungstheorie für raue Oberflächen. Neben den Schmierstoffgesetzen werden hierbei auch belastungs-, thermisch- und montagebedingte Formabweichungen der Funktionsflächen sowie deren mikrostrukturelle Eigenschaften berücksichtigt.

Grundlage einer transienten Berechnung der Kinematik und Kinetik von Mehrkörpersystemen ist die Formulierung der Newtonschen Bewegungsgleichungen. Hierzu wird eine spezielle Form der Bewegungsgleichung verwendet, die den allgemeinen Bewegungszustand aufteilt in Starrköperbewegungsanteile und in kinematische Anteile, die sich aus der lokalen Deformationsbeschleunigung der elastischen Körper ergeben.

Intensive Entwicklungsarbeit wird derzeit im Bereich motorischer Tribosysteme geleistet, da die Komponenten moderner Verbrennungsmotoren durch neue Technologien, wie Spitzendrucksteigerung, Downsizing, Stop and Go immer höhere spezifische Belastungen aufweisen. Zunehmend müssen hierbei auch partielle Mischreibungskontakte beherrscht werden. Viele tribologisch belastete Bauteile eines Motors laufen in weiten Bereichen des Arbeitsspiels im Mischreibungskontakt, d.h. ein beträchtlicher Teil der Belastung wird durch den Festkörperkontakt übertragen. Im Mischreibungskontakt steigt neben der Normalbeanspruchung zunehmend auch die Tangentialbeanspruchung an, da neben der dissipativen Energieumsetzung im Schmierfilm durch Scher- und Verdrängungsströmung auch die thermisch umgesetzte Energie infolge Festkörperreibung zunimmt. Aus diesem Zustand heraus können sich kritische Zustände entwickeln, in deren Folge der Schmierfilm lokal versagt, so dass verstärkt Verschleißzustände auftreten, die bei entsprechender Fressneigung der Tribosysteme zum Totalausfall führen können.

Ein Schlüssel zum vertieften Verständnis der in Tribokontakten ablaufenden Prozesse und deren Relevanz auf die Verschleißgefährdung liegt in der Entwicklung und Anwendung von Simulationstechniken, welche auch die bestimmenden Parameter der Mischreibung berücksichtigen.

Ein möglicher Weg ist die Verwendung von tribologischen Kennwerten zur Beschreibung der mikrohydrodynamischen und kontaktmechanischen Vorgänge im tribologischen Kontakt und Einbindung in die elastohydrodynamische Bauteilsimulationstechnik, siehe Abbildung 17.1.

Die vorgenannten komplexen Berechnungsverfahren lassen sich nicht effizient mit Institutsbordmitteln bestreiten. Ein Linux-Cluster schafft erst die Voraussetzung, die derzeitigen simulationstechnischen Möglichkeiten der Softwaretools in einer Modellbildungsstufe mit der höchsten Abbildungsgenauigkeit auch konsequent auszuschöpfen. Darüber hinaus sind dann Berechnungen möglich, die über die Berechnung eines Betriebspunktes weit hinaus gehen. Höhere Rechnerkapazitäten lassen die Berechnung unter Berücksichtigung einer Vielzahl an Einflussparametern für das gesamte Motorenkennfeld zu.

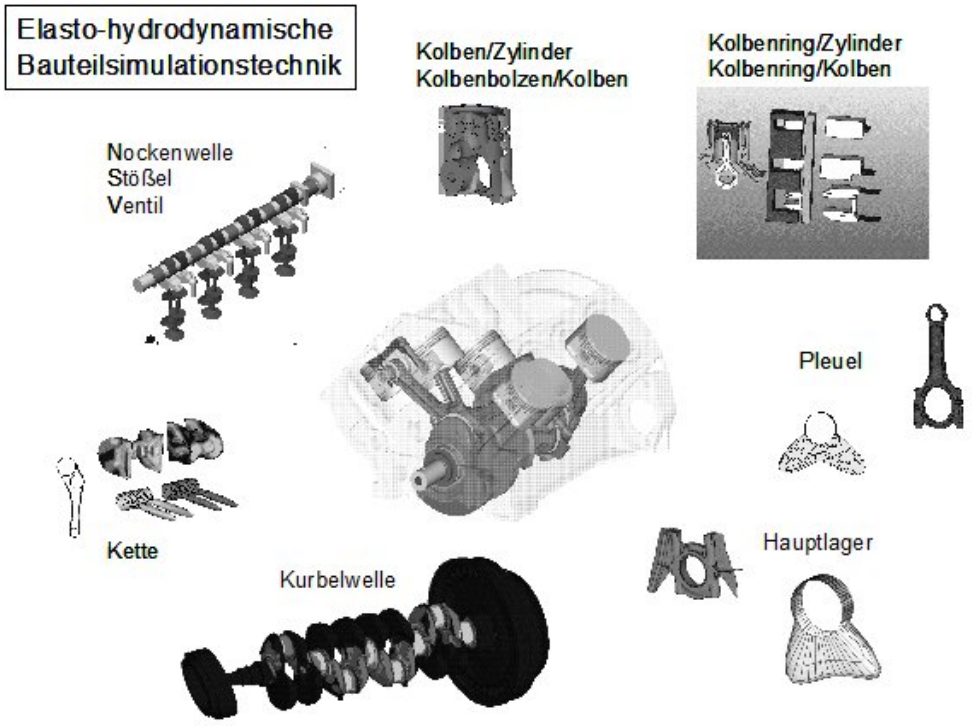

Abbildung 17.1: *Kassel-Knoll Bauteil-Simulationstechnik, EHD*

Literatur

1. Knoll G., Peeken H.J., Lechtape-Grüter R.: Computer Aided Simulation of Piston and Piston Ring Dynamik. Proceedings of the 16th Annual Fall Technical Conference of the international Engine Division, ASME, ICE Vol. 22. Lafayette Indiana October 2-6, 1994.

2. Knoll, G., R. Lechtape-Grüter. FVV-Forschungsvorhaben „Kolbenringdynamik“. AiF-Nr. 7269, 8488.

3. Knoll, G. FVV-Forschungsvorhaben Kolben-Zylinder-Dynamik, AIF-Nr. 8894, 1992-96.

4. Lang, J.: Kolben-Zylinder-Dynamik / Finite Elemente Bewegungssimulation unter Berücksichtigung strukturdynamischer und elastohydrodynamischer Wechselwirkung, Universität Kassel, Dissertation, 1997

5. Lechtape-Grüter, R.: Kolbenringdynamik / Dreidimensionale Finite Elemente Bewegungssimulation unter Berücksichtigung hydrodynamischer und gasdynamischer Wechselwirkungen, Universität Kassel, Dissertation, 1995

6. Schönen, R.: StrukturdynamischeMehrkörpersimulation des Verbrennungsmotors mit elastohydrodynamischer Grundlagerkopplung, Universität Kassel, Dissertation, 2003

4.4 Mathematik & Informatik

4.4.1 Adaptive numerical wavelet frame methods for elliptic and parabolic operator equations and inverse problems

Stephan Dahlke, Thorsten Raasch, Manuel Werner
AG Numerik und Optimierung, Fachbereich Mathematik und Informatik,
Philipps–Universität Marburg

Many real-world phenomena are modelled by partial differential or integral equations. Prominent examples are elliptic equations on domains $\Omega \subset \mathbb{R}^n$. Even in relatively low dimensions, the discretization of the equations usually leads to systems involving millions of unknowns. In such a situation, for the efficient numerical computation of a highly accurate approximate solution, suitable updating strategies, i.e. *adaptive schemes*, are often indispensable. In recent years, adaptive methods based on wavelets have been brought into focus. It is known that wavelets are predestined to resolve well local phenomena, such as singularities, while smooth data can be coded with very few coefficients.

In different research projects, we have developed, implemented and tested new adaptive wavelet algorithms for the solution of well-posed elliptic and parabolic operator equations. Moreover, another field of our current research is the adaptive solution of inverse (ill-posed) problems.

The starting point of our numerical methods is the construction of a proper wavelet collection spanning the solution space. In order not to be forced to cope with the often complicated construction of a wavelet Riesz basis on a general domain, we have focused on the weaker concept of wavelet frames. Indeed, using an overlapping decomposition of the domain Ω into subdomains, each of them being a sufficiently smooth parametric image of the unit cube, and by lifting reference wavelet Riesz bases on the cube to each of the subdomains, a proper wavelet frame can be constructed, see [2, 3, 5]. Based on this approach, in [6] a new type of *parallel* adaptive wavelet frame methods has been introduced. These schemes have been successfully tested on the *MARC Linux Cluster* placed at the Marburg University Computing Center. In particular, it has turned out that these new wavelet algorithms potentially generate significantly sparser approximations than comparable standard finite element methods, cf. Figs. 1.1–1.3. In addition, a parallel implementation of the methods from [6] has been developed and tested on *MARC*. Here, to each of the subdomains of the overlapping covering of Ω, as mentioned above, one processor is assigned. The original problem on the whole Ω is treated by an iterated solution of local auxiliary problems on all of the, say n, subdomains. In one iterative step, each processor thus has to solve one auxiliary problem. Our numerical tests have revealed that, for a fixed domain decomposition, the transition from one to n processors may lead to a reduction of the computing time by a factor n, see Fig. 1.5.

Another focus was the efficient numerical treatment of parameter identification problems. Special emphasis was layed on inverse heat conduction problems [1]. In that project, recent results on the regularization of ill posed problems by iterated soft shrinkage are combined with adaptive wavelet algorithms for the forward problem. The algorithms have been applied to an inverse parabolic problem that stems from the industrial process of melting iron in a steel furnace. All the numerical experiments have been performed on *MARC*.

We have also been concerned with the development of adaptive wavelet methods for partial differential equations of parabolic type, see [4]. By using the Rothe method, the equation is interpreted as an ordinary differential equation in a suitable function space, and well-established time step size control algorithms can be applied. For stability reasons, one has to use an implicit scheme, so that in each time step an additional elliptic problem has to be solved. All the expensive calculations have been performed on *MARC*.

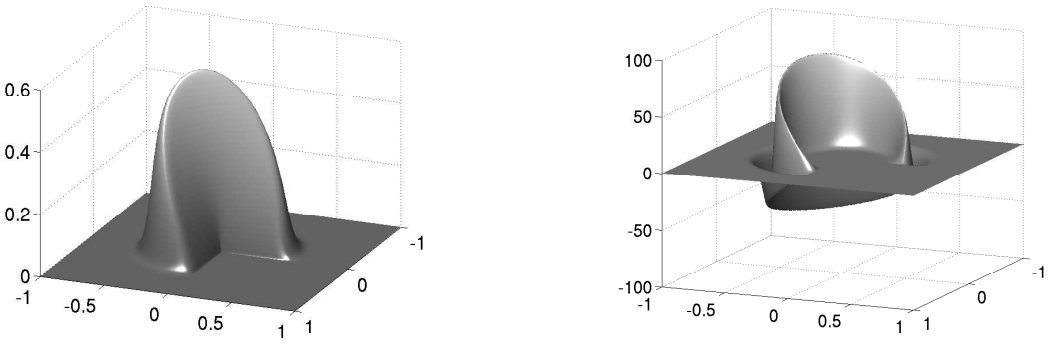

Abbildung 1.1: *Exact solution (left) and right-hand side of a two-dimensional Poisson equation in the L-shaped domain* $\Omega = [(-1,1) \times (-1,0)] \cup [(-1,0) \times (-1,1)]$.

$\Omega_0 = (-1,1) \times (-1,0)$ $\Omega_1 = (-1,0) \times (-1,1)$

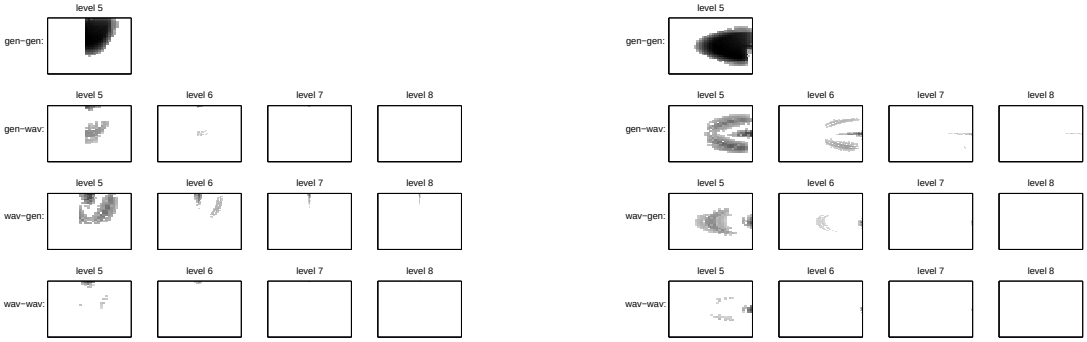

Abbildung 1.2: *Distribution of wavelet coefficients of the approximation of the solution of the Poisson equation (cf. Fig. 1.1 left) produced by an adaptive wavelet frame Schwarz domain decomposition method on the two different subdomains of an overlapping covering of* $\Omega = \Omega_0 \cup \Omega_1$ *for piecewise cubic spline wavelets.*

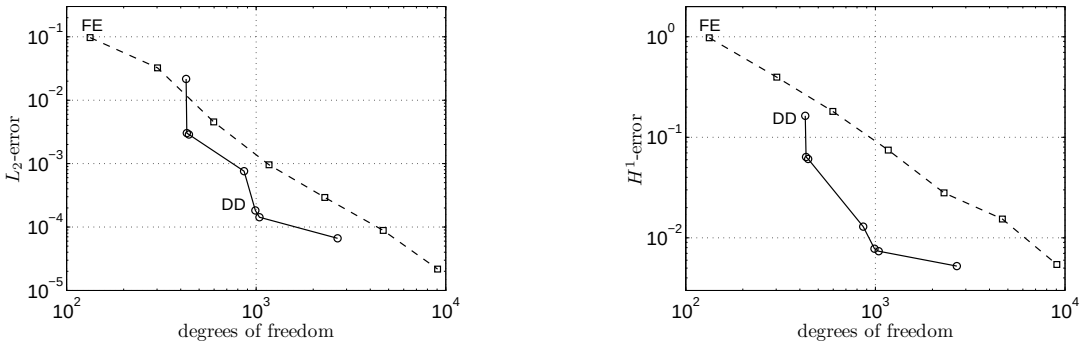

Abbildung 1.3: *Comparison of an adaptive wavelet frame Schwarz domain decomposition method (solid line) with a standard adaptive finite element solver from the deal.II software library (dashed line) for the Poisson equation on an L-shaped domain with piecewise cubic elements and spline wavelets. Left: Degrees of freedom vs.* L_2*-error. Right: Degrees of freedom vs.* H^1*-error.*

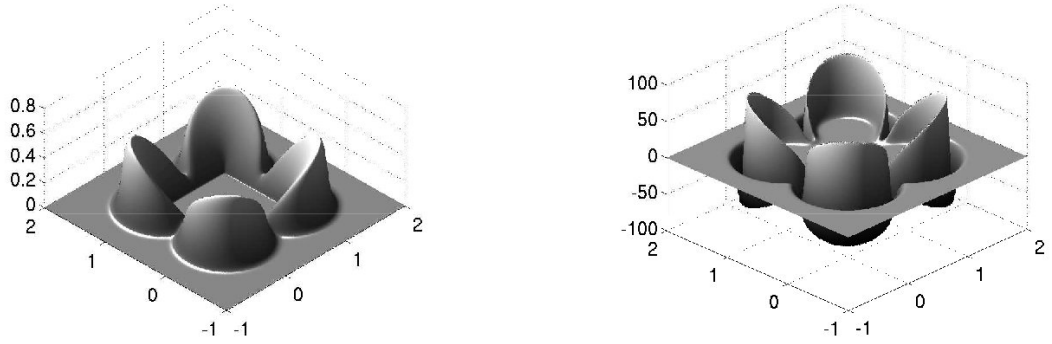

Abbildung 1.4: *Exact solution (left) and right-hand side (right) for the Poisson equation in the ring-domain* $\Omega = (-1,2)^2 \setminus [0,1]^2$.

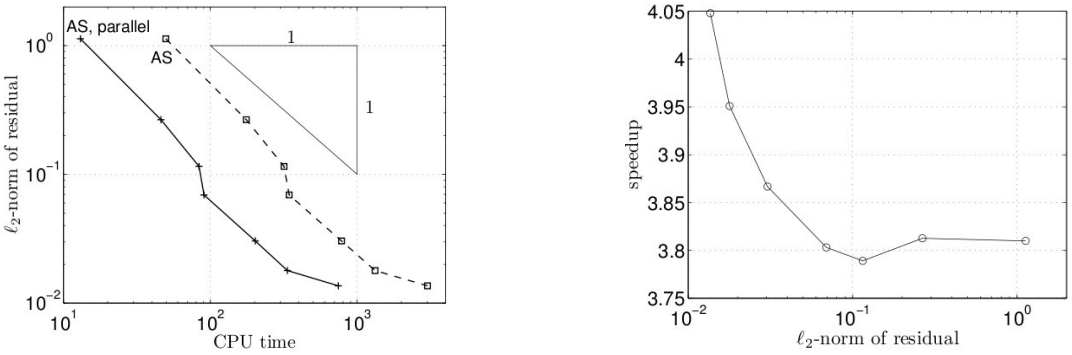

Abbildung 1.5: *Left:* ℓ_2*-norms of the discrete residuals within an adaptive wavelet frame Schwarz domain decomposition method for the Poisson equation in a ring-shaped domain with exact solution and right-hand side as depicted in Fig. 1.4. Solid line: parallel solution of local problems, dashed line: sequential solution of local problems. Right: Ratios between CPU times of parallel and sequential code. For the parallel computation* 4 *processors have been used.*

References

1. T. Bonesky, S. Dahlke, P. Maass, and T. Raasch, *Adaptive wavelet methods and sparsity reconstruction for inverse heat conduction problems*, to appear in J. Inverse Ill-Posed Probl., 2009.

2. S. Dahlke, M. Fornasier, and T. Raasch, *Adaptive frame methods for elliptic operator equations*, Adv. Comput. Math. **27**(1), 27–63, 2007.

3. S. Dahlke, M. Fornasier, T. Raasch, R. Stevenson, and M. Werner, *Adaptive frame methods for elliptic operator equations: The steepest descent approach*, IMA J. Numer. Anal, **27**(4), 717–740, 2007.

4. T. Raasch, *Adaptive Wavelet and Frame Schemes for Elliptic and Parabolic Equations*, Dissertation, Philipps-Universität Marburg, 2007.

5. R. Stevenson, *Adaptive solution of operator equations using wavelet frames*, SIAM J. Numer. Anal. **41**(3), 1074–1100, 2003.

6. M. Werner, *Adaptive Wavelet Frame Domain Decomposition Methods for Elliptic Operator Equations*, Dissertation, Philipps-Universität Marburg, 2009.

4.4.2 Parallel peer methods for initial value problems

Bernhard Schmitt
AG Numerik und Optimierung, Fachbereich Mathematik und Informatik,
Philipps–Universität Marburg

In this project new standard methods for the parallel solution of large, ordinary initial value problems $y'(t) = f(t, y(t))$, $y(t_0) = y_0$ are developed and optimized. By design the class of two-step peer methods allows an easy parallelization across the method. This structure has the advantage that users have to provide only a non-parallel implementation of the function call of the right-hand side $f(t, u)$ as with classical non-parallel integration methods like one-step or multistep methods. The peer method manages the parallel implementation for a moderate number of processors (up to 8). Further parallelization within the function call f is possible, of course.

Parallel peer methods were proposed first for stiff initial value problems as implicit methods. Recently also explicit methods for non-stiff problems were discussed. Computations on the cluster *MARC* in Marburg were used for the optimization with realistic problems like reaction-diffusion problems with small diffusion constants and some large multibody problems. Figure 2.1 shows a benchmark for a multibody problem where two explicit parallel peer methods are compared with a non-parallel reference method (DOPRI5) for a set of different tolerances. On one processor DOPRI5 (black crosses) is still faster than the 4-stage peer method (red circles). With 4 processors, however, it is outperformed by the peer methods (magenta circles and blue boxes). The parallel speed-up is nearly optimal in this problem.

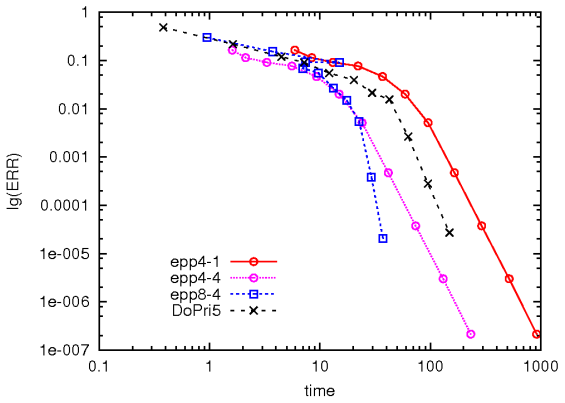

Abbildung 2.1: *Parallel efficiency*

References

1. B.A. Schmitt, R. Weiner, S. Jebens, *Parameter optimization for explicit parallel peer two-step methods.* Appl. Numer. Math. 59 (2009), 769-782.

2. B.A. Schmitt, R. Weiner, *Parallel start for explicit parallel two-step peer methods.* To appear in Numer. Algorithms, DOI:10.1007/s11075-009-9267-2.

4.4.3 Grid Workflow Modeling and Execution

Tim Dörnemann, Ernst Juhnke, and Bernd Freisleben
Philipps-Universität Marburg, Fachbereich Mathematik und Informatik

The Business Process Execution Language for Web Services (BPEL4WS or WS-BPEL) is the *de facto* standard for service composition in business applications, but there is no commonly agreed equivalent standard for scientific applications. Several workflow languages for particular scientific domains have been proposed, without being generally applicable and providing adequate tool support. Barker et al. suggest that scientists should "stick to standards" (BPEL) and "not implement another workflow language". In recent years, BPEL has gained interest in the scientific community, since it is – in contrast to the majority of DAG-based (direct acyclic graph based) workflow languages – a turing-complete general-purpose workflow modeling language that offers excellent industrial-strength tool support and seamlessly integrates with service-oriented architectures. It supports "Programming in the Large" which means that applications may be composed of existing components (i.e., web services), leading to higher reusability and thus faster development and reduced costs. Access to a workflow is exposed by the execution engine through a web service interface, allowing the workflow to be accessed by clients or to be used as a basic activity in other workflows. Despite excellent tool support, current BPEL implementations do not meet all of the requirements of scientific workflows. In contrast to the majority of business processes, scientific workflows tend to be compute- and data-intensive and typically run longer than the average business process. Therefore, a scientific BPEL execution system needs to provide features such as, for example, fault tolerance, runtime adaptability and data flow aware scheduling. While the first two requirements have already been addressed in the context of BPEL, no data flow aware scheduler for BPEL seems to exist yet. We have developed an approach that extends a well-known open-source BPEL implementation (ActiveBPEL) by the dynamic scheduling of the service calls of a BPEL process based on the target hosts' load [1]. To handle peak loads, it integrates a provisioning component that dynamically launches virtual machines in Amazon's EC2 (Cloud computing) infrastructure and deploys the required middleware components (web/Grid service stack) on-the-fly. While composition languages like WS-BPEL offer fault handling mechanisms, we argue that *infrastructural failures* like network timeouts and server outages should not be handled using the language mechanisms, since this would clutter the composition logic with non-functional aspects. Consequently, we identify classes of faults that can be handled automatically and define a policy language to configure automatic recovery behavior without the need to add explicit fault handling mechanisms to the BPEL process [2]. The approach provides automatic Cloud-based redundancy of services for the substitution of defective services. The approach takes data dependencies between workflow steps and the utilization of resources at runtime into account [3]. At development time, the workflow developer annotates the workflow with data flow and execution time information. At execution time, these annotations are used to create a data flow graph that in turn serves as input for the developed heuristic algorithm performing the assignment of BPEL workflow steps on resources.

For the evaluation of our approach, a real-life workflow originating from the area of *sleep research* has been used. The workflow basically performs an ECG (electrocardiogram) analysis and, based on the obtained results, conducts *apnea* detection (see Figure 3.1). The implementation uses the Physio Toolkit, which is a common set of open source tools in biomedical sciences. Since the data format (European Data Format, EDF) of the recorded vital signs (real, anonymized patient data) differs from the format required by the Physio Toolkit (WaveForm DataBase, WFDB), a data conversion is needed (*InvokeEDF*). Afterwards, Q-S peaks are detected within the ECG signal (*InvokeWQRS*). The results are passed to the annotation reader service (*InvokeAnnotationReader*) that in turn decodes the input and passes the results to the beat detection service *InvokeBeatDetection* which detects R waves within the signal. In parallel, the output of *InvokeWQRS* is passed to the apnea detection service (*InvokeApnoe*) that analyzes the input signal and detects respiration dropouts (to diagnose the sleep apnea syndrome). The tools are mainly written in C and perform command-line based tasks. For this reason, they (more explicitly *edf2mit*, *wqrs*, *get_apdet*, *rdann*) first had to be wrapped by web service interfaces before they could be used in BPEL.

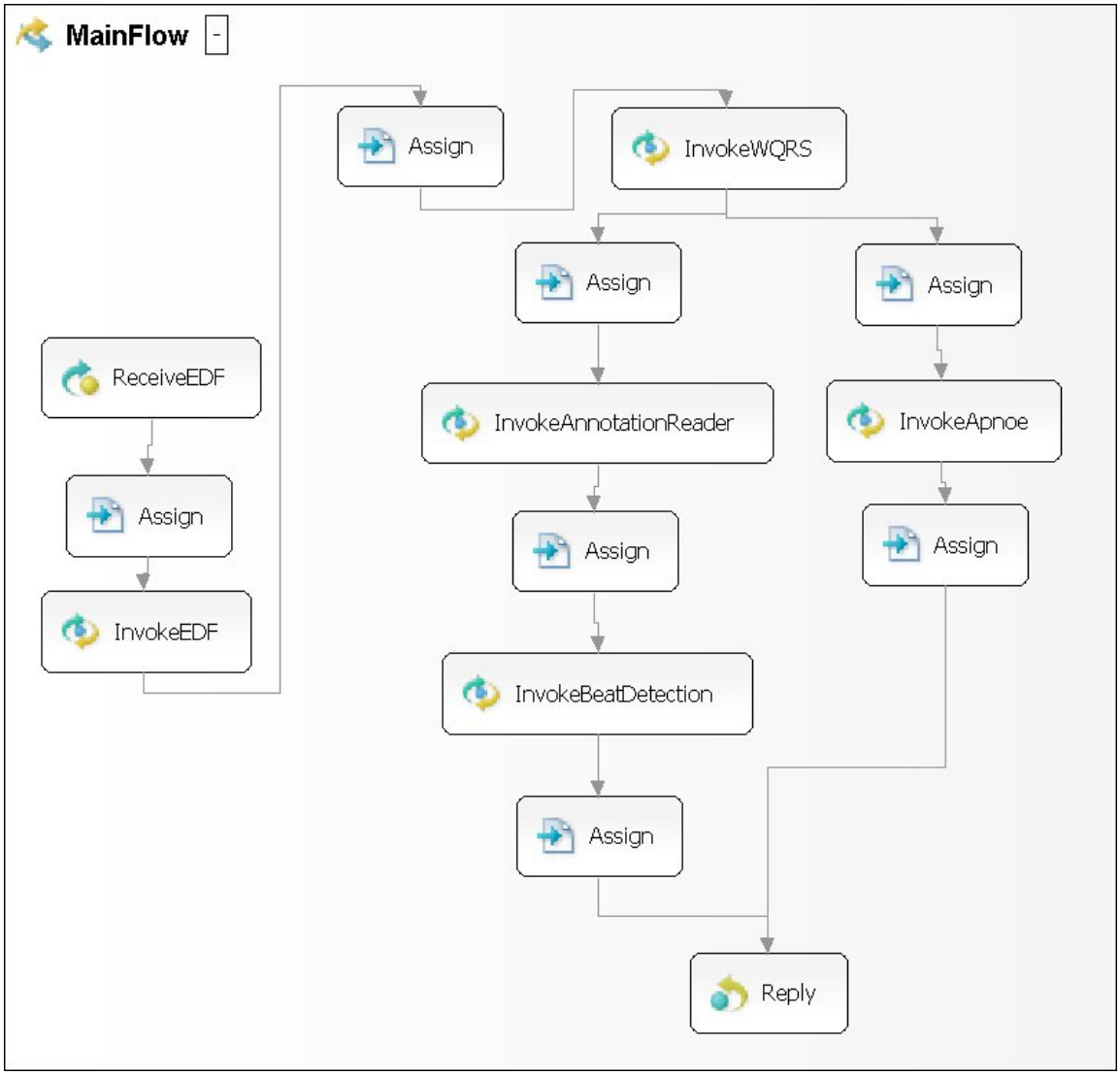

Abbildung 3.1: *The beat and apnea detection workflow*

The integration of our approaches within a cluster and Grid infrastructure will be based on the work of Schmidt et al. [4]. They present "multiorganizational resources and private, root-access compute nodes reachable by the Internet [...] (allowing) service-oriented applications direct, multi-site access to the cluster nodes". This fits perfectly into our dynamic infrastructure and thus allows a BPEL workflow to utilize the resources of one or more compute clusters.

References

1. T. Dörnemann, E. Juhnke, and B. Freisleben. On-Demand Resource Provisioning for BPEL Workflows using Amazon's Elastic Compute Cloud. In *Proceedings of the 9th IEEE International Symposium on Cluster Computing and the Grid*, page 140–147, Los Alamitos, CA, USA, 2009. IEEE Computer Society.

2. E. Juhnke, T. Dörnemann, and B. Freisleben. Fault-Tolerant BPEL Workflow Execution via Cloud-Aware Recovery Policies. In *Proceedings of 35th EUROMICRO Conference on Software Engineering and Advanced Applications (SEAA)*, pages 31–38. IEEE Computer Society, 2009.

3. T. Dörnemann, E. Juhnke, T. Noll, D. Seiler, B. Freisleben. Data Flow Driven Scheduling of BPEL Workflows in Hybrid Cloud Systems. *(submitted for publication)*.

4. M. Schmidt, N. Fallenbeck, M. Smith, B. Freisleben. Secure Service-Oriented Grid Computing with Public Virtual Worker Nodes. In *Proceedings of 35th EUROMICRO Conference on Internet Technologies, Quality of Service and Applications (ITQSA)*, pp. 555–562, IEEE Press, 2009.

4.4.4 Multimedia Computing

Ralph Ewerth, Markus Mühling, Thilo Stadelmann, Dominik Seiler, and Bernd Freisleben
Philipps-Universität Marburg, Fachbereich Mathematik und Informatik

Due to the increasing proliferation of digital data, the use of automatic multimedia analysis tools in combination with high performance computing is essential to support the management of and access to huge multimedia databases. Automatic multimedia content analysis is a demanding task with respect to the computational resources required: the amounts of data to be processed are huge (e.g., for video in the range of several hundred megabytes per hour) and the runtimes of the used machine learning and pattern recognition algorithms are vast. Using our local cluster MARC, we were able to conduct our work in several multidisciplinary, international environments:

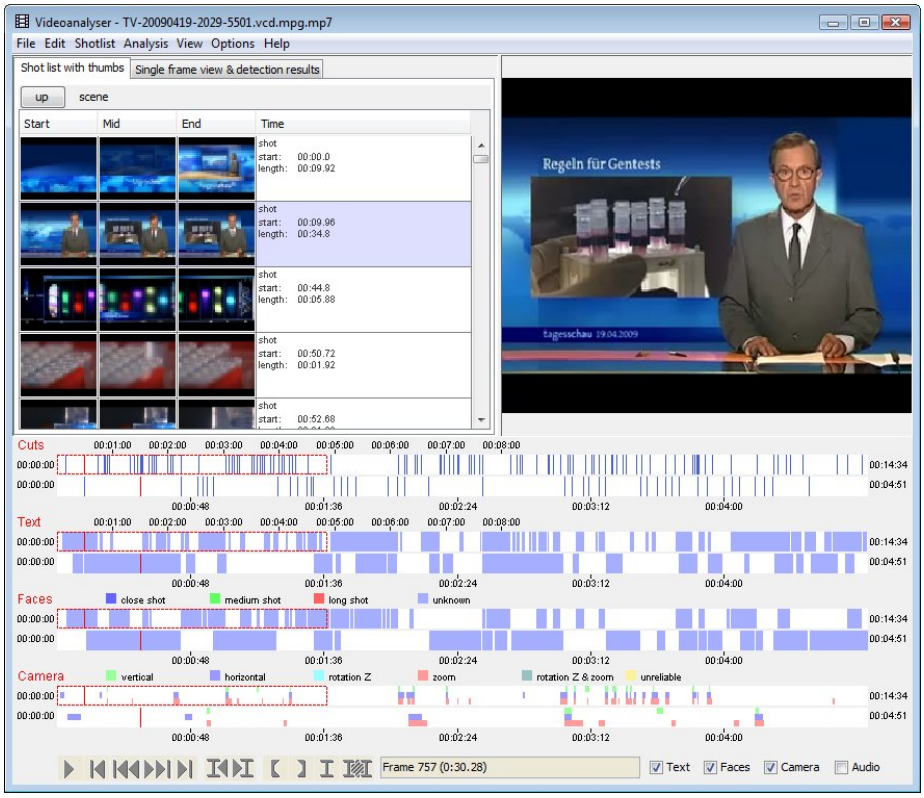

Abbildung 4.1: *Screenshot of the Videana user interface*

The project *Methods and Tools for Computer-Assisted Media Analysis*, funded by Deutsche Forschungsgemeinschaft (DFG), is conducted within the large transdisciplinary research center *Media Upheavals* (DFG-Sonderforschungsbereich SFB/FK 615). To relieve media scholars from the time-consuming task of annotating videos and films manually, our work focuses on methods for recognizing relevant objects in images and videos, understanding events and their relationships in multimedia data. For this purpose, distributed software architectures based on the service-oriented Grid computing paradigm were built for multimedia processing and retrieval. The automatic computer-assisted annotation of video sequences based on the appearance of certain objects, shapes and categories allows the objective analysis of a large number of video sequences. Our software toolkit *Videana* [1] combines the following state-of-the-art image and video analysis algorithms: shot boundary detection, camera motion estimation, text detection, segmentation and optical character recognition, face detection, person indexing, audio segmentation and speaker clustering. A screenshot of *Videana*'s user interface can be seen in Figure 4.1.

Since the beginning of the research center in 2002, the associated media scientists have collected huge amounts of dedicated video data from different domains. In several cooperations, we have supported these scientists by providing tools for automatic video content analysis. We have used the MARC cluster to analyze more than 200 video files of early movies for the project A5 (Industrialization of Perception) using shot boundary detection, text detection, text segmentation and optical character recognition. In an ongoing cooperation with the project A7 (Kulturgeographie des Medienumbruchs analog/digital) we built automatic video analysis tools to support media-scientific investigations of user navigation behavior in Google Earth. For this purpose, we provided dominant color analysis, camera motion estimation and optical character recognition, including text detection and segmentation. Furthermore, a procedure to detect Google popup windows, so called Google bubbles, has been developed; it is used to integrate additional information into Google maps and earth applications.

Associated media scientists of the project B9 (Media Narration and Media Games) are interested in certain semantic concepts or categories, such as *top view, cliffhanger, bullet time*. They benefit from our work on concept detection, although these different concepts are beyond the scope of the main research in the field of semantic video retrieval. First experiments on these challenging concepts with more than 600 video sequences have been conducted using our concept detection system, which is described in more detail below.

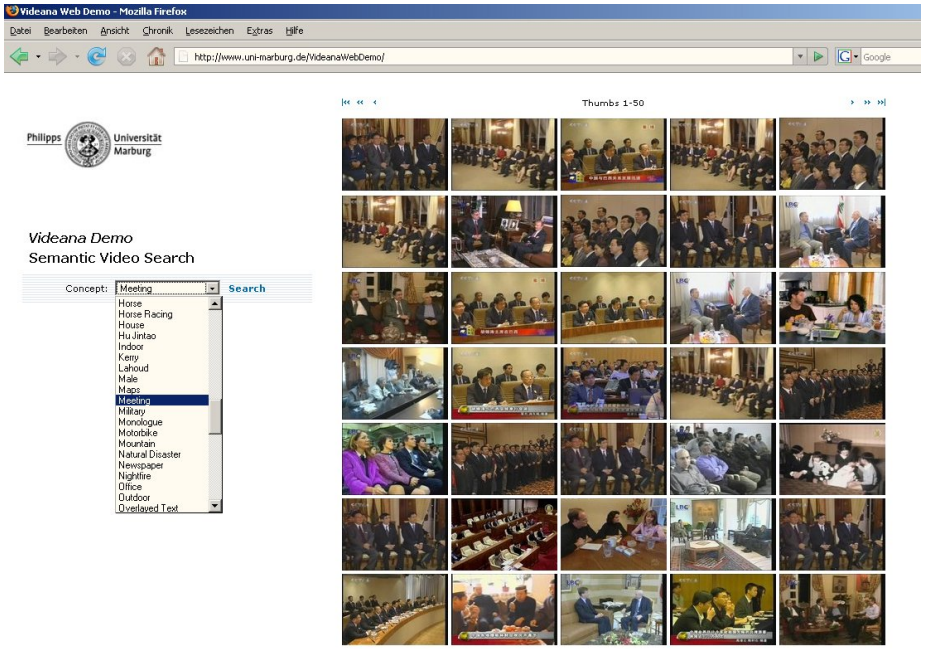

Abbildung 4.2: *Detection result of the concept* meeting

Furthermore, we participated in the high-level feature extraction task of the TRECVID (TREC Video Retrieval Evaluation; TREC: Text Retrieval Conference) series, which is the de-facto international benchmark for evaluating video analysis and retrieval algorithms. High-level feature extraction, also known as concept detection, plays a key role in semantic video retrieval, navigation and browsing. Queries-by-content are insufficient to search successfully in large-scale multimedia databases. Thus, several approaches in the field of video retrieval focus on high-level features, such as *car, outdoor, sports, meeting*, serving as intermediate descriptions to bridge the semantic gap between low-level image and video representation and human interpretation. Detection results for the concept *meeting* are shown in Figure 4.2. The indexed video shots are finally used to support different kinds of queries. The research community assumes that less than 5000 concepts, detected

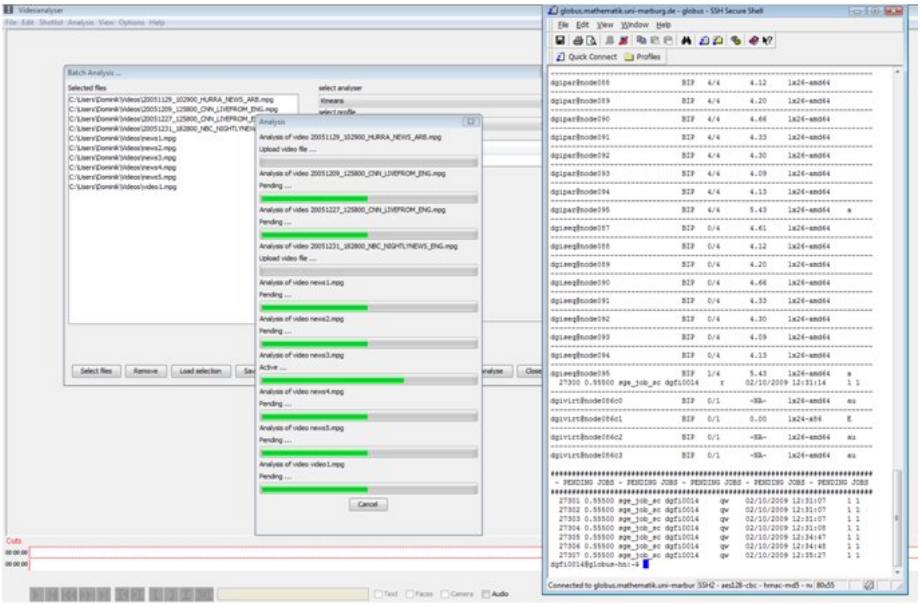

Abbildung 4.3: *Execution of a batch job via Videana's Grid connection*

with a minimum accuracy of 10% mean average precision, are sufficient to provide search results comparable to text retrieval in the World Wide Web. The video collection of the TRECVID 2009 series consists of the huge amount of 838 video files containing about 380 hours of news magazine, science news, news reports, documentaries, educational programming and archival video. Our video analysis system [5] automatically extracts several low-level as well as mid-level features, which are the result of state-of-the-art algorithms in the field of camera motion estimation [2], text detection [3], face detection, object detection and audio segmentation. Based on the observation that the use of face detection results as mid-level features in our concept detection system improved the performance of several related concepts, detection results for further object classes have been incorporated. Using object detectors trained on separate public data sets, detection results were assembled to object sequences, and a shot-based confidence score as well as several further object-based features [4] were computed. The multi-modal low-level and mid-level features are concatenated in an early fusion scheme and fed into a support vector machine to learn the final models for the semantic concepts. Due to the huge amount of video data, we generated single jobs per analysis algorithm and video file in the feature extraction phase as well as per concept during training and testing. The Sun Grid Engine was used to manage the distributed execution on MARC. In total, we submitted about 12000 jobs with up to 72 hours execution time depending on the video length and the complexity of the analysis algorithm.

Since the task of deploying computational jobs on external high performance computing resources usually requires a certain amount of background knowledge and preparation time, we have integrated a connection to Grid resources in *Videana*. This connection is based on the *Globus Toolkit 4* and designed to ease the usage of Grid resources (for non-experts) for the analysis of audio/visual data. Given a valid user certificate, the system transfers data to a special Grid service that is adapted to specific nature of an audio-visual analysis job on a Grid-enabled site. The service submits jobs with the help of the underlying *Globus Toolkit* and locally installed scheduler. The integrated client in *Videana* is continuously informed about the current execution state. During the execution, the user can continue his/her current analysis on his/her local machine. After job completion, the results are sent back to the client in an MPEG-7 file and visualized in *Videana*. Figure 4.3 shows a screenshot of an ongoing batch analysis for cut detection.

References

1. R. Ewerth, M. Mühling, T. Stadelmann, J. Gllavata, M. Grauer, B. Freisleben, Videana: A Software Tool for Scientific Film Studies, Digital Tools in Media Studies, Transcript Verlag Bielefeld, 101-116, 2008

2. R. Ewerth, M. Schwalb, P. Tessmann, B. Freisleben, Estimation of Arbitrary Camera Motion in MPEG Videos. In Proceedings of the 17th International Conference on Pattern Recognition, Vol. 1, Cambridge, UK, pp. 512-515, 2004

3. J. Gllavata, R. Ewerth, B. Freisleben, Text Detection in Images Based on Unsupervised Classification of High-Frequency Wavelet Coefficients. In Proceedings of 17th International Conference on Pattern Recognition, Vol. 1, Cambridge, UK, pp. 425-428, 2004

4. M. Mühling, R. Ewerth, B. Freisleben, Improving Semantic Video Retrieval via Object-Based Features. Proceedings of the IEEE International Conference on Semantic Computing, Berkeley, USA, pp.109-115, IEEE Press, 2009

5. M. Mühling, R. Ewerth, T. Stadelmann, B. Shi, B. Freisleben, University of Marburg at TRECVID 2009: High Level Feature Extraction. In Online Proceedings of TRECVID Conference Series 2009: `http://www-nlpir.nist.gov/projects/tvpubs/tv.pubs.org.html`

4.4.5 Turbulence Simulations on Clusters and Desktop Computers

Kay Dörnemann, Tobias Schneider, Tim Dörnemann, Bruno Eckhardt, and Bernd Freisleben
Philipps-Universität Marburg, Fachbereich Mathematik und Informatik / Fachbereich Physik

The motion of fluids is generally ordered, smooth and time-independent as long as flow velocities are low. However, at higher velocities one observes turbulent motion – the flow is complex and fluctuates wildly in space and time. Deeper understanding of the underlying transition mechanism has emerged only recently especially for flow situations where the transition is not mediated by a linear instability of the laminar flow [2]. In these linearly stable systems, which include pressure driven flow down a circular pipe and the flow between two parallel plates moving in opposite direction (plane Couette flow), laminar and turbulent dynamics coexist for the same parameter values. In this parameter regime, triggering turbulence requires to exceed a minimal flow rate *and* to apply a perturbation of sufficient strength.

Once turbulence is established, it was generally believed that it persists indefinitely. However, experiments and simulations on pipe flow have recently indicated that turbulence in this geometry is intrinsically transient for all flow speeds [4]. The observed features of the turbulence transition are compatible with the formation of a strange chaotic saddle in the state space of the hydrodynamical system. It coexists with an attracting fixed point that corresponds to the laminar flow. This saddle supports transient turbulent motion (see Figure 5.1). An important signature of the saddle is the observation of suddenly decaying turbulence without any prior indication.

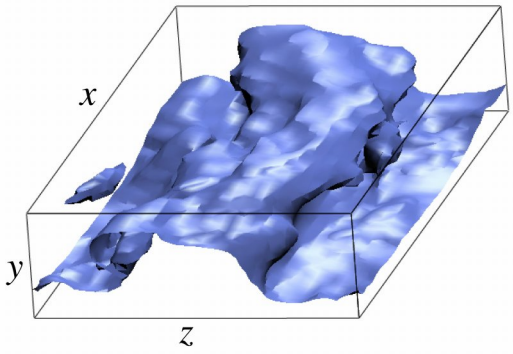

Abbildung 5.1: *Typical turbulent state on the chaotic saddle*

The problem investigated (via numerical simulations of plane Couette flow) is whether the characteristic lifetime of turbulence diverges at finite critical flow speed [5]. The characteristic lifetime of turbulent structures is a function of three parameters: the Reynolds number Re and both the length L_x and width L_z of the computational domain. Since each individual data point has to be statistically based on an ensemble of many independent simulations generating the required data, this requires an enormous amount of CPU time (typical values for a simulation run are 35 hours wall-clock time on a 2.4 GHz AMD DualCore Opteron CPU). The large computational costs are contrasted by very low memory and interconnection speed requirements. The following computational environment, consisting of dedicated clusters and a pool of desktop computers, has been used to investigate the problem discussed above.

Our local compute cluster headnode runs the Grid middleware Globus Toolkit 4 (GT4), which in turn interfaces with the local cluster scheduler to submit jobs to the cluster nodes. Several clusters are combined using the popular GridWay meta-scheduler that interfaces with GT4 installed on each of the headnodes of two additional locations (Siegen and Frankfurt). To integrate our local pool of desktop computers, we have developed a bridge between GridWay and the pool of desktop PCs. For GridWay, the pool of desktop PCs then looks like a Grid headnode, but internally the bridge interfaces with a peer-to-peer (P2P) scheduler that runs on the desktop PCs and schedules jobs among them in a P2P fashion. Our bridge is called Omnivore [3], and the P2P scheduler is called PPS, which is an extended version of our P2P scheduler PPM [1]. In contrast to PPM, PPS runs on Microsoft Windows, Linux and MacOS X desktop computers and does not require GT4 to run on each of the desktop PCs. Thus, as in a normal Grid, GridWay is the central point to submit jobs, but now a P2P pool of desktop PCs can be seamlessly integrated into the Grid setup, which contains our cluster and the other computers, as a virtual cluster.

The components of the architecture are shown in Figure 5.2. The jobs are executed on our local cluster MARC, the other clusters or with low priority on the desktop machines, allowing users to

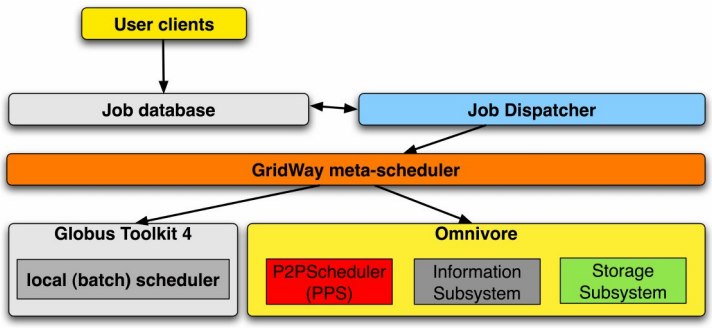

Abbildung 5.2: *Logical components of the architecture*

work with the desktop computers while spending unused resources. Currently, GridWay is configured to use our local MARC cluster as long as it has free nodes. Only if there are no free cluster nodes (in Marburg, Siegen or Frankfurt), Omnivore is used. PPS is integrated into Omnivore as its execution component. Omnivore adds information retrieval mechanisms, distributed data management and mimics a cluster from the viewpoint of GridWay.
The resulting infrastructure is shown in Figure 5.3. MARC, Omnivore, PPS and GridWay form the generic part of our infrastructure, and the figure also shows the application-specific part.

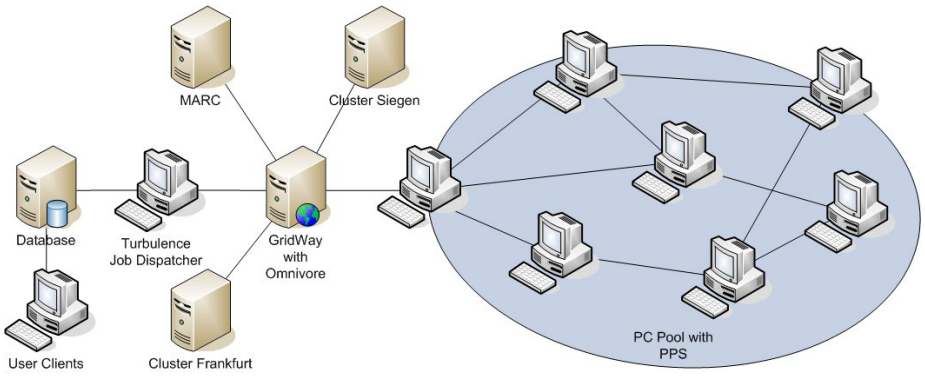

Abbildung 5.3: *Topology of the architecture.*

The application-specific components in Figure 5.3 are the user clients, a database and the turbulence job dispatcher. The user clients provide the following functionality: a command-line application for job submission, removal of jobs, gathering information, and retrieving results of finished jobs. The clients can be easily integrated into scripts, which is necessary since a series of numerical experiments consists of thousands of jobs which cannot be submitted manually. The clients only communicate with the database in which job information, the application itself and simulation data are stored. The turbulence job dispatcher periodically queries the database for new jobs and GridWay for failed and finished jobs. It controls the number of jobs scheduled coevally to GridWay. Whenever a job is finished, the dispatcher retrieves the job and its corresponding data and writes it back to the database. A field in the database represents the state of jobs (running, failed, finished, iteration required). The last state is reached if a job runs longer than a predefined runtime but has not reached the finished state. The turbulence application then saves the state of the computation and exits with the return code for iteration. Using the database and the dispatcher indirection makes the solution more flexible. For instance, it allows to exchange the Gridway meta-scheduler or to utilize more than one. Job handling is very easy, no knowledge about the meta-scheduler is required, and no Grid-related software packages must be installed on the client node. The database itself provides the possibility to store additional information like statistics and job states. Security is another reason:

no user needs access to the machine the scheduler runs on – the machine's firewall only needs to have very few ports open. Only database access is necessary, which is protected by user name and password.
During the last 12 months, the proposed approach was used to dispatch 31.742 turbulence simulation jobs to cluster and desktop resources, requiring a total of 442.382 CPU hours. Waiting times in GridWays's queue could be significantly reduced by adding desktop machines. The system has proven to be stable in case of failure, meaning that no jobs have been lost due to failures of desktop machines.

References

1. K. Dörnemann, J. Prenzer, and B. Freisleben. A Peer-to-Peer Meta-Scheduler for Service-Oriented Grid Environments. In *Proceedings of the First International Conference on Networks for Grid Applications*, pages 1 – 8, 2007.

2. Bruno Eckhardt, Tobias M. Schneider, Björn Hof, and Jerry Westerweel. Turbulence Transition in Pipe Flow. *Annual Review of Fluid Mechanics*, 39:447–468, 2007.

3. Michael Heidt, T. Dörnemann, K. Dönemann, and B. Freisleben. Omnivore: Integration of Grid Meta-Scheduling and Peer-to-Peer Technologies. In *8th IEEE International Symposium on Cluster Computing and the Grid*, pages 316-323, IEEE Press, 2008.

4. Björn Hof, Jerry Westerweel, Tobias M. Schneider, and Bruno Eckhardt. Finite Lifetime of Turbulence in Shear Flows. *Nature*, 443:60–64, 2006.

5. Tobias M. Schneider, Filippo DeLillo, Jürgen Buehrle, Bruno Eckhardt, Tim Dörnemann, Kay Dörnemann, and Bernd Freisleben. Transient Turbulence in Plane Couette Flow. *Physical Review E*, 2009 (accepted for publication).

4.4.6 Virtualized Cluster Computing

Matthias Schmidt, Niels Fallenbeck, Roland Schwarzkopf, and Bernd Freisleben
Philipps-Universität Marburg, Fachbereich Mathematik und Informatik

One of the biggest challenges for on-demand computing is the requirement that users must be able to install custom software with root privileges autonomously (and preferably without the hassle of a job based installation procedure). To satisfy this requirement, we have developed a software installation process based on virtualization technology. A user receives a private virtual environment that looks and behaves exactly like a native worker node of a compute cluster to be used. The user has root access and can install software in the same way as software is installed on a local machine. This functionality is provided by an Image Creation Station (ICS) [1] developed for this purpose.
The ICS consists of two parts: front ends and a back end. The front ends can be a website that allows the user to define some basic parameters for the virtual machine, or a Grid service interface that allows to integrate the ICS image generation and customization process into e.g. a BPEL workflow. Once the user has selected the required options, an image can be created and then booted. To create the basic image, the ICS back end uses the Xen-tools scripts.
Once the image is finished, it is booted using a dynamic IP address. Since the creation process takes some time, a notification email is sent to the virtual machine's owner containing the dynamically chosen location of the image and the login information. The ICS accepts a PGP public key with which the email can be protected. Alternatively, a SSH public key can be passed to the ICS during the image creation process, and the ICS will configure the image to accept SSH login authentication using the corresponding private key. Once the user is logged in, software can be installed with root privileges in the traditional way, which greatly eases the installation process compared to asking a local administrator to do so. A user can make any modifications to the operating system configuration and installation, any required shared libraries and third-party software. This also paves the way for more fine grained service-oriented applications, since a service hosting environment can be installed on the worker nodes without endangering other users [2].

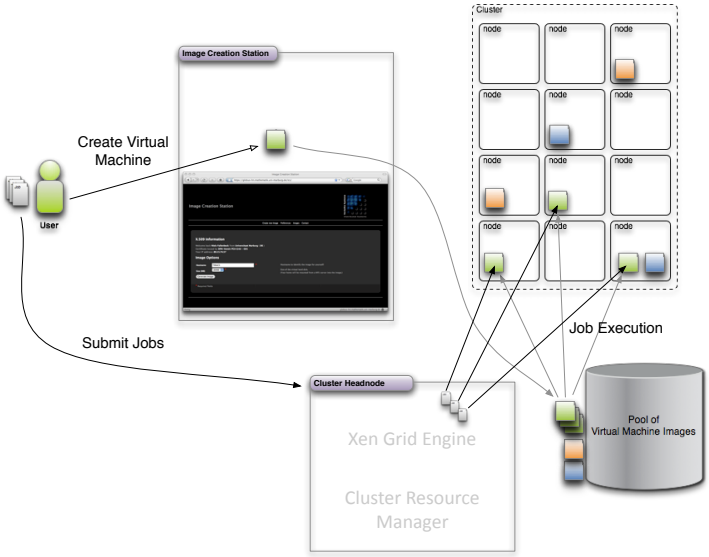

Abbildung 6.1: *Image Creation Station and Xen Grid Engine*

A user can create several (different) images giving each image a separate name. The ICS deploys the images to the cluster and provides the image-to-user-mapping that is later used by the cluster scheduler to select the correct virtual machine.
The execution of user jobs is handled by the installed batch scheduler (in our case: Torque), while

the management of the virtual machines is handled by the Xen Grid Engine II (XGE) [1] that deals with virtual machine selection, deployment and virtual machine startup. The main reason for transparently extending an existing batch scheduling environment is that existing scheduling algorithms like backfilling and advanced reservation can then be used by a Grid consisting of multiple clusters. The proposed architecture can be seen in figure 6.1.
To make the XGE extension transparent to the batch scheduler, the latter should not realize that it is operating on virtual machines, since it would then see worker nodes appearing and disappearing. This would break its ability to properly schedule jobs, since the nodes allocated to the job queues change all the time (when nodes disappear for a while, the scheduler believes the nodes have crashed and cannot be used for further jobs and thus reschedules these jobs). To prevent this from happening, our solution uses placeholder virtual machines that are registered with the scheduler's job queues. Every placeholder virtual machine has an execution daemon (here a pbs_mom) installed to let the master know about the number of compute nodes and to enable it to make scheduling decisions. When a job is scheduled, the placeholder virtual machine is transparently exchanged with the user virtual machine, so that the scheduler does not notice any change.
The following execution flow is performed when a job is submitted to the cluster scheduling system: (1) A job is submitted to Torque. (2) Based on its scheduling configuration and the given constraints (required number of CPUs, RAM, etc.), Torque decides on which hosts the job will be executed. (3) Before it notifies the execution daemons on the chosen hosts, it is interrupted and hands control over to the XGE. (4) The XGE shuts down all placeholder virtual machines on the chosen hosts and starts the users' own virtual machines. (5) Every virtual machine reports back when it has started correctly. When all virtual machines are up and running, the XGE runs the user specific firewall configuration scripts and then hands back the control to Torque. (6) Torque continues as normal and executes the job. (7) After execution, a pre-defined epilog script is called which activates the cleanup procedure of the XGE. (8) All virtual machines belonging to the job are shut down, and the XGE boots up the placeholder virtual machines.
The integration of virtual machine staging and the transparent exchange of placeholder and user virtual machine images allows us to combine the years of development implemented in cluster scheduling systems such as Torque with the security and deployment advantages of virtualization technology. Further aspects of virtual machine management, such as distribution of virtual machines and security updates in virtual machines, are discussed in recent publications [3],[4].

References

1. M. Smith, M. Schmidt, N. Fallenbeck, T. Dörnemann, C. Schridde, B. Freisleben. Secure On-Demand Grid Computing. In: *Journal of Future Generation Computer Systems*, pp. 315-325, Elsevier, 2008

2. M. Schmidt, N. Fallenbeck, M. Smith, B. Freisleben. Secure Service-Oriented Grid Computing with Public Virtual Worker Nodes. In *Proceedings of 35th EUROMICRO Conference on Internet Technologies, Quality of Service and Applications*, pp. 555–562, IEEE Press, 2009.

3. R. Schwarzkopf, M. Schmidt, N. Fallenbeck, B. Freisleben: Multi-Layered Virtual Machines for Security Updates in Grid Environments. In: *Proceedings of 35th EUROMICRO Conference on Internet Technologies, Quality of Service and Applications*, pp. 563-570, IEEE Press, 2009

4. M. Schmidt, N. Fallenbeck, M. Smith, B. Freisleben: Efficient Distribution of Virtual Machines for Cloud Computing. In: *Proceedings of the 18th Euromicro Conference on Parallel, Distributed and Network-based Processing (PDP 2010)*, IEEE Press, 2010, pp. 567-574.

4.4.7 PASTHA – Parallelizing Stencils in Haskell

Michael Lesniak
Research Group Programming Languages / Methodologies
Department of Computer Science and Electrical Engineering, University of Kassel

Stencils are building-blocks for numerical scientific applications. A stencil is a pattern to describe the calculation of matrix elements by defining the relative positions of elements required for the calculation. The values at these positions are used to update the value of the current position. Stencils are used for example in the approximation of partial differential equation systems by applying iterative numerical approximation methods such as the Jacobi or Gauß-Seidel relaxation method.
Despite the progress in both hardware and software development the demand for increasing processing power of stencil codes is still prevailing. Greater processing power leads to more detailed simulations, increases the quality of the results or reduces the time for finishing them. Therefore improving the calculation speed of stencil-based applications leads to a general improvementof numerical applications.
The current solution to this problem is no longer limited to increasing clock rates: instead parallelization of applications executed on modern shared-memory multicore architectures is favoured. Unfortunately the increase of computing power comes with a price: not only need the developers handle the single-threaded correctness of their programs but have to handle for example thread synchronization and race conditions as well at least in the traditional explicit thread-parallelism model.
One possibility to manage the complexity while still enabling parallelism is tohide it from the developer. Libraries are well known to achieve this goal: Firstly, they can handle the parallel aspects of the execution. Secondly, they can provide (semi-)automatic techniques to choose the most performant implementation depending on the specific problem. Thirdly, by allowing a declarative description of the problem calculation, details are abstracted. Developing a library to handle the parallel calculation for a class of problems like stencil calculation should fulfill some constraints. These constraints should make the library useful for real-world applications:

- The provided functions of the library should be flexible enough to be applied on different classes of problems while at the same time the learning curve for simple examples should be small.
- The library should use the resources of modern multicore hardware and provide a good speedup.
- The efficiency of the provided functions should not be significantly worse than the efficiency of existing hand-coded versions. On the other hand small decreases in computation speed for having a more convenient development environment are a common trade-off.
- Depending on the problem type it should assist – or even automatize – the choice for the most performant implementation.

Haskell[2] provides a solid basis for parallel programming due to its active research on parallel programming models and the resulting developer-friendly parallel programming techniques. Since Haskell supports parallelization using explicit, semi-implicit and data parallel techniques, it allows to explore and compare the advantages and disadvantages of the different approaches to parallel stencil calculation while using a common code basis and common abstractions. As a functional language, its support for higher level abstraction and thus declarative stencil descriptions and parallelization strategies is better than in most imperative programming languages. Our contributions are
The definition of types in Haskell that allow to declaratively express 2D stencil-based problems. Addressing both multiple data matrices and arbitrary referencing of values from past iterations is possible.

PASTHA, the prototype of a library for parallel stencil calculations. It allows us to evaluate parallel strategies for stencil-based calculations and to calculate stencil-based problems on multicore architectures. Our implementation is based on task queues and strict evaluation by which we achieve speedups for Gauß-Seidel-based stencils of 3 on four and 4 on six cores for instance (see Figure 7.1). The parallelization of the affine sequence score algorithm in the Haskell bioinformatics library *bio*[3]. Thereby we explore the advantages and disadvantages of the library's current parallelization strategies and provide some real-world benchmarks and experiences. It was of special importance to us that biolib users should be able to use the parallelization without having to change their code too much. We were able to achieve speedups of up to 55 on four cores (see Figure 7.2). This speedup is due to strict evaluation, computing in the IO monad, and partially the use of PASTHA.
Despite being a prototype implementation, PASTHA can already be used to calculate some commonly used and declaratively described stencils in parallel. For other stencils the user has to define two simple functions to describe the dependency relation between stencil elements. Due to the prototype nature of PASTHA, our design decision was aimed at perspicuity: When having the choice between a simple, clean and possibly slower implementation and a more complex one (for example, involving customized shared data structures, STM etc.) we chose the simpler one.

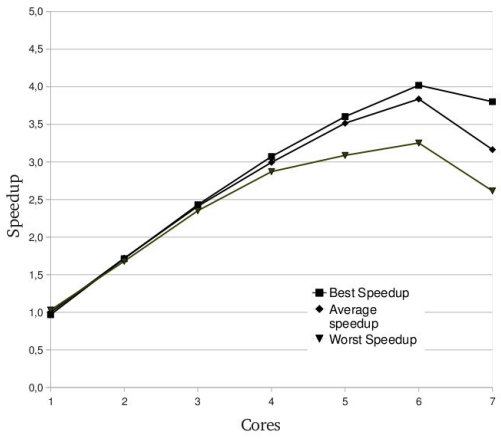

Abbildung 7.1: *Speedup for a Gauß-Seidel based stencil*

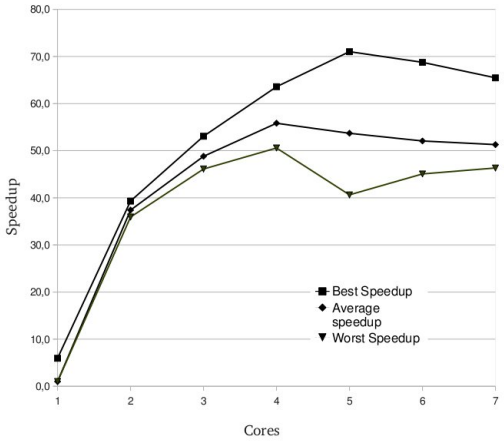

Abbildung 7.2: *Speedup for local scoring in a sequence alignment*

References

to appear in: Declarative Aspects of Multicore Programming (DAMP'10), Madrid, Spain. S. Peyton Jones, *Haskell 98 Language and Libraries: the Revised Report*, 2003.
`http://hackage.haskell.org/package/bio`

4.4.8 Erfassung großer Datenmengen auf Hochleistungsrechnern

Prof. Dr. Volker Lindenstruth und Dr. Timm Steinbeck
Fachbereich Informatik und Mathematik und Frankfurt Institute for Advanced Studies,
Goethe Universität Frankfurt

Die Schwerpunkte der Arbeiten dieser Gruppe konzentrieren sich um die Erfassung sehr großer Datenmengen und deren Verarbeitung mit Hilfe komplexer Hochleistungsrechner. Unter anderem ist Professor Lindenstruth verantwortlich für die intelligenten Datenselektionssysteme TRD Trigger und HLT Trigger des ALICE Experiments am CERN Large Hadron Collider LHC, die im Folgenden exemplarisch kurz beschrieben werden.
Der TRD Trigger implementiert 280000 custom RISC Prozessoren, die speziell für diese Aufgabe entwickelt wurden. Er verarbeitet einen Datenstrom von 17,5 Terabyte/s. Die Abbildung rechts zeigt den Blick auf eine von 108 Lagen des TRD Systems mit seinen Wasser gekühlten Multi Chip Modulen (MCM). Insgesamt befinden sich 70000 MCMs auf 700 m² des Detektors. Diese 70000 MCMs werden mit 1080 Glasfasern bei 2,5 GBits/sec ausgelesen.

Der High Level Trigger verarbeitet die Ereignisse, die vom TRD Trigger selektiert wurden, weiter. Hierbei fällt ein Datenstrom von etwa 30 Gigabyte/s an. Um eine endgültige Entscheidung über die Aufzeichnung eines Ereignisses zu fällen, muss das Ereignis vollständig rekonstruiert werden, was den Einsatz von Clusterdekonvolutionsalgorithmen, zellularen Automaten, Kalman-Filtern, etc. erfordert. Die zu verarbeitende Ereignisrate liegt zwischen 200 Hz und 2 kHz. Der High Level Trigger ist ein Hochleistungscluster mit Ethernet- und Infiniband Backbone, der in 54 Racks aufgebaut ist. Diese Triggersysteme entsprechen quasi dem Fokus eines Mikroskops, der aber intelligent und dynamisch auf sich ergebende spezielle Bedingungen reagieren kann. Ohne Trigger zeichnet das Experiment nur wenig relevante Daten auf. Dies ist unter dem Gesichtspunkt der Betriebskosten von mehr als 20.000 EUR pro Stunde zu sehen, was besondere Anforderungen an die Betriebssicherheit und Robustheit der Systeme stellt.
Die ALICE Kollaboration ist mit mehr als 1000 Wissenschaftlern eine sehr große, internationale Nutzergemeinschaft, die alle von der korrekten Funktion dieser Triggersysteme abhängig sind. Die Triggeralgorithmen der genannten Systeme werden von den verschiedenen Kollegen beigesteuert und werden in die bestehenden Systeme integriert. Diese Systeme wurden vom korrespondierenden Antragssteller konzipiert und gebaut. Die Nutzung der Triggersysteme im Experiment und vor Allem die Auswahl der spezifischen Triggeralgorithmen werden von einem Komitee des Experiments durchgeführt. Für den reibungslosen Betrieb der Trigger HPC Systeme ist der Antragssteller für die geplante Laufzeit des Experiments von mehr als 15 Jahren verantwortlich.
Ein wesentlicher Aspekt der Entwicklung von Trigger Systemen ist die Entwicklung schneller Algorithmen zur Ereignisrekonstruktion. Der Lehrstuhl hat von Anfang an die Ereignisrekonstruktionssoftware auf moderne Rechenarchitekturen getrimmt. Hierbei wurde besonderes Augenmerk auf intrinsische Parallelität, Speicherbedarf und Cache Nutzung wie Einsatz von Vektorisierung, bzw SIMD Befehlen [3] gelegt. In diesem Zusammenhang wurde für den Kalman Filter basierten CBM Tracker eine Geschwindigkeitssteigerung von 120000 auf einem CELL Prozessor erreicht. Diese Arbeiten sind mittlerweile die Grundlage verschiedener Entwicklungen am CERN, bei FAIR und auch

in der Industrie. Die ALICE on-line Spurrekonstruktion hat mittlerweile eine Stufe erreicht, dass sie alle anderen Algorithmen, einschließlich der off-line Algorithmen in ihrer Qualität übersteigt bei wesentlichen Geschwindigkeitssteigerungen. Der Einsatz dieser Algorithmen auf GPGPUs gibt weiteres Leistungssteigerungspotential. Dazu dient die aktuelle Portierung der Programme auf den SCOUT GPGPU-Cluster des Center for Scientific Computing in Frankfurt, die als erster Schritt zu einer erheblichen Leistungssteigerung der Analysen führen wird.

Publikationen

1. The ALICE Collaboration: THE ALICE EXPERIMENT AT THE CERN LHC, JINST 3: S08002, 2008 259pp
2. S. R. Bablok et al: HIGH LEVEL TRIGGER ONLINE CALIBRATION FRAMEWORK IN ALICE, J. Phys.: Conf. Ser. 119 022007 (9pp)
3. S. Gorbunov, U. Kebschull, I. Kisel, V. Lindenstruth, W.F.J. Müller: FAST SIMDIZED KALMAN FILTER BASED TRACK FIT, Computer Physics Communication (2007), DOI:`http://dx.doi.org/10.1016/j.cpc.2007.10.001`
4. V. Lindenstruth for the ALICE TRD collaboration: AN EXTREME PROCESSOR FOR AN EXTREME EXPERIMENT, IEEE Micro, March/April 2006, P 48-57
5. T. Alt et al.: BENCHMARKS AND IMPLEMENTATION OF THE ALICE HIGH LEVEL TRIGGER, IEEE Transactions on nuclear science vol. 53:854-858,2006

4.4.9 On Whitehead's asphericity conjecture

Stephan Rosebrock
Frankfurt

A 2-complex K is called *aspherical* if its second homotopy group is trivial ($\pi_2(K) = 0$). This means, every continuous map $f\colon S^2 \to K$ is homotopy equivalent to the trivial map where the 2-sphere S^2 is mapped to a single point.
The Whitehead-conjecture states that any subcomplex of an aspherical complex is itself aspherical. Whitehead posed this 1941 as a question and it is still open although for many classes of 2-complexes it is known to be true.
Let $P = < x_1, \ldots, x_n \mid R_1, \ldots, R_m >$ be a finite presentation where each relator is of the form $x_i x_j = x_j x_k$, i.e. is a Wirtinger relation. Such a presentation is called a *labelled oriented graph presentation*, or short, *LOG-presentation* because it is represented by a *labelled oriented graph* T_P in the following way: For each generator x_i of P, T_P has a vertex labelled x_i and for each relator $x_i x_j = x_j x_k$ (or, equivalently, $x_i = x_j x_k x_j^{-1}$), T_P has an oriented edge from the vertex x_i to the vertex x_k labelled by x_j. If T_P is a tree we call it a *labelled oriented tree* or *LOT* and P a *LOT-presentation*. The 2-complex modeled on P will be called a LOG (or LOT)-complex. LOTs are important for the Whitehead-question because of the following Theorem:

Theorem (Howie 1983): *Let L be a finite 2-complex and $e \subset L$ a 2-cell. If L 3-deforms to a single vertex then $L - e$ 3-deforms to K and K is a LOT complex.*

This implies that LOT-complexes are good testcases for the Whitehead-conjecture.
For a given 2-complex it cannot be decided whether it is aspherical or not. Nevertheless we developed a computer program which runs parallel on up to 300 computers for over a year now which constructs reduced surface diagrams over LOTs. The program has checked roughly estimated about 40 billion LOTs, only checking those LOTs which are not known to be aspherical by other methods. Certainly none of the LOTs is thereby proved to be aspherical but the program found reduced spherical diagrams over about 40 different LOTs which have a certain, more general, structure than spherical diagrams which were known before.
A publication is in preperation (see [3]). The program is still running and may hopefully find a Whitehead-counterexample in the future.

Verweise

1. J.H.C. Whitehead. *On adding relations to homotopy groups*, Ann. of Math. 2 42, (1941).
2. S. Rosebrock. *The Whitehead-Conjecture – an Overview*, Siberian Electronic Mathematical Reports 4; (2007); S. 440 – 449.
3. J. Harlander and S. Rosebrock. *On the asphericity of LOTs containing sub-LOTs*, preprint (2009).

4.5 Biologie & Medizin

4.5.1 Entwicklung von Methoden und Algorithmen für genomweite Assoziationsstudien

Helmut Schäfer, Roman Pahl, Thuy Trang Nguyen
Institut für Medizinische Biometrie und Epidemiologie,
Philipps-Universität Marburg

Genomweite Assoziationsstudien dienen der Identifikation von genetischen Varianten, die an der Entstehung komplexer Erkrankungen beteiligt sind. Die untersuchten Kollektive umfassen bis zu mehreren 1000 von betroffenen Patienten (Fälle) und Kontrollen im sogenannten Fall-Kontroll-Design, die anhand von sehr dichten genetischen Markernetzen genotypisiert werden. Heutige kommerzielle Chips erlauben die Bestimmung von bis zu 1 Mio. sogenannter SNP-Marker (SNP = Single Nucleotide Polymorphism) bei jeder Einzelperson, sodass sich insgesamt außerordentlich umfangreiche Datenstrukturen ergeben.

Ein Ziel unserer Arbeiten ist die *Entwicklung effizienter Algorithmen für sogenannte Permutationstests*. Permutationstests erlauben es, eine Adjustierung der statistischen Fehlerrisiken 1. Art vorzunehmen unter Berücksichtigung des sogenannten Kopplungsungleichgewichts der Marker, d.h. statistisch unter Berücksichtigung der stochastischen Abhängigkeiten der markerweisen Teststatistiken. Da diese Verfahren auf der Erzeugung von Permutationen beruhen, die von exponentieller algorithmischer Komplexität ist, und die Fallzahlen solcher Studien inzwischen bis in die Tausende gehen, bedarf es hocheffizienter Algorithmen, um diese Verfahren praktikabel zu machen. Wir arbeiten daran, mit Hilfe von Binärvektor-Arithmetik und Parallelisierung des Permutationsalgorithmus beschleunigte Algorithmen für Permutationstests bei solchen hochdimensionalen Datenvektoren zu entwickeln. Erste Laufzeittests ergeben eine Laufzeitverkürzung um den Faktor 18 bereits ohne Parallelisierung im Vergleich zur Implementation von Permutationstests in vorhandenen Softwarepaketen zur statistischen Genetik (z.B. PLINK). Wir haben in 2009 erfolgreiche Vorversuche durchgeführt und einen Antrag an die von Behring-Röntgen-Stiftung gestellt, der inzwischen bewilligt wurde.

Ein zweites Teilvorhaben beschäftigt sich mit der *Entwicklung optimaler Designs für genomweite Assoziationsstudien*, wobei die Idee eines zweistufigen Vorgehens zugrunde liegt, bei dem das volle Markernetz nur in einer Teilstichprobe genotypisiert wird und anhand einer Zwischenauswertung nur die vielversprechenden Marker für die weitere Genotypisierung in der Reststichprobe ausgewählt werden. Auf diese Weise soll die Zahl der benötigten DNA-Chips reduziert und die Genotypisierungskosten für eine solche Studie gesenkt werden. Die statistischen Eigenschaften wie Fehlerrisiken 1. und 2. Art und Studienkosten können nur numerisch bestimmt werden (numerische Integration), sodass die Optimierung solcher Designs, d.h. die Bestimmung optimaler Design-Parameter wie Größe der Teilstichprobe und Anteil der weiterzuführenden Marker, unter Nebenbedingungen der Einhaltung von Fehlerrisiken 1. und 2. Art, numerisch sehr aufwändig ist und hohe Rechnerleistung erfordert.

Diese beiden Projekte sind möglich geworden durch die Nutzung des MaRC-Clusters am HRZ Marburg.

Jüngere Ergebnisse des zweiten Teilprojekts (Optimierung von Designs, vor allem von robusten Designs) finden sich in der Arbeit Nguyen TT, Pahl R, Schäfer H (2009) Optimal robust two-stage designs for genome-wide association studies. *Annals of Human Genetics* 73:638-651. Ferner wird im Rahmen dieses Projekts eine Dissertationsschrift von Frau Dipl.-Math. oec. T.T. Nguyen bearbeitet.

4.5.2 Weiterentwicklung und Implementation von Methoden der Kopplungsanalyse für die genetische Kartierung komplexer Krankheiten

Prof. Dr. Konstantin Strauch, Markus Brugger, Dr. Antònia Flaquer, Dipl.-Math. Thomas Künzel
Institut für Medizinische Biometrie und Epidemiologie, Philipps-Universität Marburg

Die Genetische Epidemiologie befaßt sich mit der Identifizierung und Charakterisierung von Genen, die ursächlich an der Entstehung von Krankheiten beim Menschen beteiligt sind. Der erste Schritt dazu ist die Lokalisierung oder Kartierung der Gene. Mittels der Kopplungsanalyse läßt sich untersuchen, ob bestimmte Markerausprägungen und Krankheitsphänotypen in Familien überproportional häufig gemeinsam vererbt werden. Ist dies der Fall, so spricht dies für die Existenz eines krankheits(mit)verursachenden Gens in der chromosomalen Region. Die genetische Kartierung ist vor allem bei komplexen Krankheiten schwierig, da diese meist durch mehrere Gene und Umweltfaktoren hervorgerufen werden. Deshalb ist es wichtig, statistische Analyseverfahren zu entwickeln, welche diese komplexen Erbgänge adäquat modellieren. Ein solches Verfahren ist die MOD-Score-Analyse, bei dem die Krankheitsmodellparameter (Erkrankungswahrscheinlichkeiten bei den verschiedenen genetischen Konstellationen, Häufigkeit des Mutationsallels in der Population) durch Optimierung an eine Familienstichprobe mit genetischen Markerdaten und Krankheitsinformationen angepaßt wird. Hierdurch erhöht sich nicht nur die Power, krankheitsverursachende Gene zu finden, sondern es werden auch Informationen über den Erbgang der Krankheit bzw. Wirkungsweise eines Gens gewonnen. Unsere Arbeitsgruppe hat das MOD-Score-Verfahren für dichotome Phänotypen in frei verfügbare Software implementiert (GENEHUNTER-MODSCORE) und auf verschiedene komplexe Krankheiten wie Diabetes, Allergie/Asthma und neuropsychiatrische Krankheiten angewendet.
Im Rahmen dieses Projektes führen wir umfangreiche Simulationen zum Vergleich der Power der MOD-Score-Methode mit jener anderer Kopplungsanalyse-Verfahren durch. Dabei werden verschiedene Simulationsszenarien mit unterschiedlichen Familienstrukturen und Erbgängen betrachtet. Es müssen eine Vielzahl simulierter Datensätze erzeugt und analysiert werden, um hinreichend genaue Aussagen über die Eigenschaften der miteinander verglichenen Methoden treffen zu können. Darüberhinaus entwickeln wir ein MOD-Score-Verfahren für quantitative Phänotypen; diese Methode wird in Software implementiert und ebenfalls durch Simulationen bezüglich ihrer Power mit anderen Verfahren verglichen. Der MOD-Score-Ansatz stellt sowohl bei dichotomen als auch bei quantitativen Phänotypen hohe Anforderungen an die Rechenkapazitäten, da der Score zur Bewertung der Kopplung für viele verschiedene Parameterkombinationen berechnet werden muß.
Ein weiterer Projektteil befaßt sich mit der adäquaten Modellierung des genomischen Imprintings. Bei diesem epigenetischen Effekt hängt die Erkrankungswahrscheinlichkeit davon ab, ob das Krankheitsallel vom Vater oder von der Mutter geerbt wurde. Es besteht ein sogenanntes Confounding zwischen Imprinting und Geschlechtsunterschieden in den Rekombinationsfrequenzen, so daß z.B. eine größere Crossover- und damit Rekombinationshäufigkeit bei Frauen als bei Männern (was in weiten Teilen des menschlichen Genoms auftritt) als maternales Imprinting fehlinterpretiert werden kann. Den Ausmaß dieses Confoundings zu quantifizieren war Gegenstand einer umfangreichen Simulationsstudie unter Annahme von Markeranordnungen mit unterschiedlichen Abständen und Verhältnissen zwischen den männlichen und weiblichen Rekombinationsfrequenzen.
Die Berechnungen sind mit sehr hohem Rechenzeit- und Speicherbedarf verbunden, so daß sie in angemessener Zeit nur auf großen Rechenclustern durchführbar sind. Die erfolgreiche Bearbeitung dieses Projekts hängt daher entscheidend von der Verfügbarkeit des Marburger Rechenclusters (MaRC) am Marburger Hochschulrechenzentrum ab, auf dem ein Großteil der erforderlichen Berechnungen durchgeführt wird.
Im Rahmen dieses Projektes findet die Promotionsarbeit von T. Künzel statt; außerdem ist daraus die Diplomarbeit von M. Brugger entstanden, die vor kurzem abgeschlossen wurde.

4.5.3 Simulationen mit SAS

Dr. R.-H. Bödeker
Institut für Medizinische Informatik, Gießen

Im Rahmen einer Studienarbeit mussten mit Hilfe des Statisik-Programmpakets SAS aufwendige Simulationen durchgeführt werden. Daher sollte in diesem Zusammenhang überprüft werden, ob das Programmpaket auf dem HLR implementiert werden kann und durch die Anwendung der vorhandenen „parallel processing Routinen“ der Zeitaufwand deutlich verringert werden kann.

4.5.4 Biophysical Annotation of Molecular Evolution

K. Hamacher, F. Hoffgaard, P. Weil
Technische Universität Darmstadt

The understanding of molecular evolution requires a detailed understanding of the biophysical rammifications of the effects of mutations within the molecular phenotype. To this end we set up a pipeline of biophysical methods for *functional* and *structural* annotation of the effects mutations induce.
To correlate the physical and chemical effects with the sequence space in which the mutation operator acts, we also investigates the applicability of informational theoretical measures.

Information Theory

The mutual information is a particular useful measure of correlation for discrete data sets. In particular it allows the quantification of *co*-evolution within a molecule and thus the direct investigation of selective pressures induced by requirements on the function and structure of the molecule itself. We have investigated the effects of finite sized sample data on the mutual information (1). Our findings indicate that in a typical study with some 10^2 sequences the mutual information computed in a naive fashion is insignificant with respect to a null model of neutral evolution (see figure 4.1). This finding prompts for normalization procedures to account for such finite-size effects. We currently develop such normalization procedures.

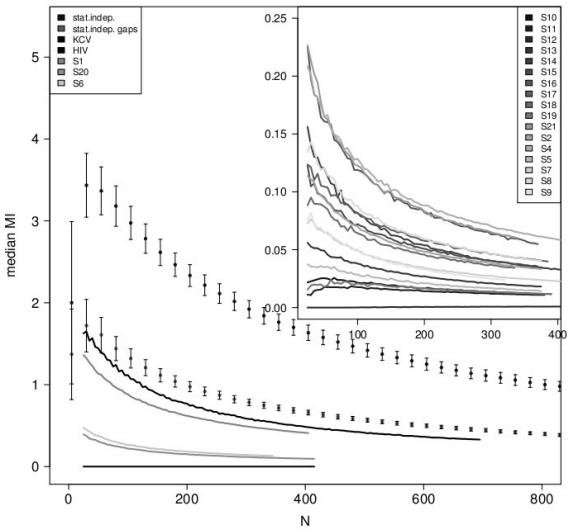

Abbildung 4.1: *Number of sequences (N) used to compute the median of the mutual information (MI) after shuffling of an original alignment (null model). The dots with error bars are the statistically independent generated amino acid pairs. The median for each N is plotted. The error bars indicate the standard deviation over the sample of 1,000 sequences.* Inset: *as in the main plot the MI for each alignment was computed by shuffling the original alignment column-wise and picking the first N rows of the alignment to compute the MI. The median of the so obtained MI was plotted against the number of sequences used N.*

Biophysical Models

We developed several protocols to investigate the molecular mechanics of proteins in an efficient fashion. This allowed us to look at a large number of mutants and/or thought experiments. In this set-up we were able to understand in more detail the evolution of several important, disease-realted molecules: 1) the HIV1 protease, 2) the HIV1 reverse transcriptase, and 3) the acetylcholinesterase. In particular we were able to correlate high co-evolution to the stability of the HIV1 protease dimer (see figure 4.2a and ref. (2)) the temperature dependence of fluctuation in the same molecule (see figure 4.2b and ref. (3)), and finally we have submitted a paper that shows an interesting correlation between the sequence evolution and the "tunnel" in acetylcholinesterase. This "tunnel" is the route of substrate intake and therefore a prime drug target, e.g. for neurotoxins and drugs for Alzheimer's disease.

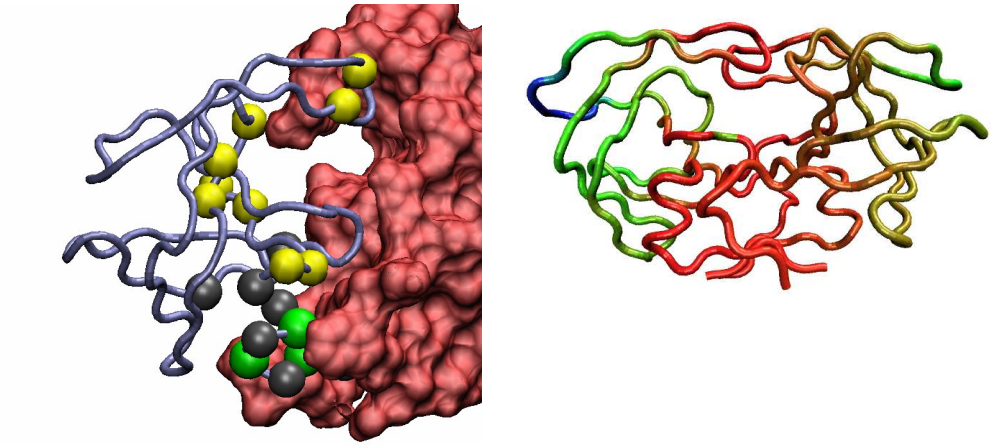

Abbildung 4.2: *left: The HIV1 protease dimer (chains depicted in red & blue) and the most relevant interactions with low MI/large mechanical change upon mutation* inside a monomer *Yellow are the residues responsible for slow, functional modes; gray are the ones for fast, stabilizing ones; and marked in green are the amino acids that belong to both categories. right: The lowest energy mode at the folding temperature T_f of the HIV1 protease. Red indicates small, blue & green large fluctuations.*

References

1. P. Weil, F. Hoffgaard, K. Hamacher. Estimating Sufficient Statistics in Co-Evolutionary Analysis by Mutual Information, Computational Biology and Chemistry 33(6), 440-444, 2009.

2. K. Hamacher. Relating Sequence Evolution of HIV1-Protease to Its Underlying Molecular Mechanics , Gene, 422, 30-36, 2008.

3. K. Hamacher. Temperature dependence of fluctuations in HIV1-Protease Eur. Biophys. J., 2009, in press

4.5.5 Molecular Structure of Gas Vesicle Forming Proteins – work in progress

K. Hamacher, F. Pfeifer, W.Wenzel, F. Hoffgaard
Technische Universität Darmstadt

Gas Vesicles are important compartments within single-cellular organisms. They allow for "locomotion" of single-cellular organisms in fluids by modifying lift forces with respect to the fluid the organism is immersed in.
The structure of proteins that built gas vesicles is important for two reasons: 1) one can better understand evolution and specialization of particular branches (e.g. halophilic vs. thermophilic organisms) and 2) the vesicles themselves are very robust, thus interesting in material research.
We set out to model such a protein. The modeling was done in collaboration with the Research Center Karlsruhe and their force-field for protein structure prediction (1) and our global optimization protocols (2,3). In Darmstadt we then performed two additional steps:
a) we convinced ourselves about the stability of the predicted structure by sufficiently long molecular dynamics simulations using GROMACS (4) and NAMD (5)
b) we investigated the assembly process by analyzing the binding dynamics of the predicted proteins into dimer, trimers, ... using distributed version of the Rosetta package (6).

References

1. A. Verma and W. Wenzel. De-novo all-atom folding of a HIV-V3 hairpin loop in an improved free energy forcefield. J. Chem. Phys. 128, 105103, 2008.
(2) K. Hamacher. Adaptation in Stochastic Tunneling Global Optimization of Complex Potential Energy Landscapes, Europhys.Lett. 74(6):944, 2006.

2. W. Wenzel and K. Hamacher. A Stochastic tunneling approach for global minimization. Phys. Rev. Lett., 82(15):3003-3007, 1999.
(4) Hess, et al., GROMACS 4: Algorithms for Highly Efficient, Load-Balanced, and Scalable Molecular Simulation, J. Chem. Theory Comput. 4: 435-447, 2008

3. Philips et al., Scalable Molecular Dynamics with NAMD, J. Comp Chem. 26:1781-1802, 2005.

4. Gray, J.J., S.E. Moughan, C. Wang, O. Schueler-Furman, B. Kuhlman, C.A. Rohl, D. Baker. Protein-Protein Docking with Simultaneous Optimization of Rigid-Body Displacement and Side-Chain Conformations, J. Mol. Biol. 331: 281-299, 2003.

4.5.6 Surface reconstruction using Delaunay triangulations for application in life sciences

Graziela Grise and Michael Meyer-Hermann
Frankfurt am Main

The interacting sub-particles of a cell can assume specific roles – i.e., membrane sub-particle, internal sub-particle, organelles, etc –, distinguished by specific interaction potentials and, eventually, also by the use of modified interaction criteria. The use of Delaunay triangulations to define neighborhood relations is established for multi-particle systems – in particular in Biology. However, the extension of Delaunay triangulations to a sub-cellular level that considers the membrane and the inner structure of cells is not straight forward.

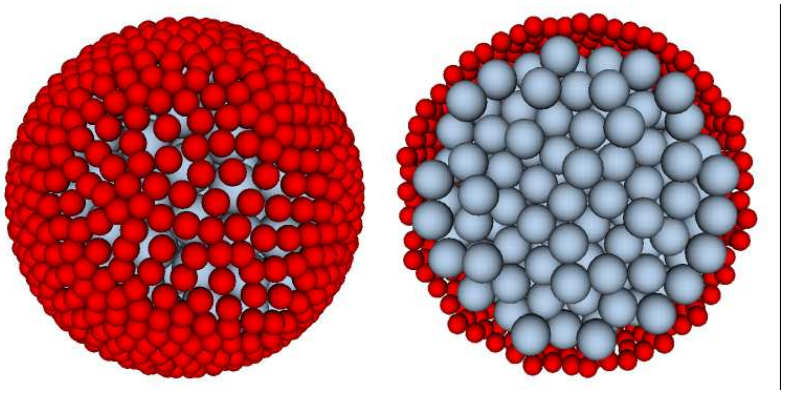

Abbildung 6.1: *Thermalized configuration with membrane particles (red) and internal particles (grey). In the right side, the cell is shown sliced in half. Notice that in this example the radius of the internal particles is twice as big as the radius of the membrane particles. The size of the particles is related to the strength of the potential as well as with the resolution used to describe the cell.*

An essential problem of this objective is the conservation of the number of particles belonging to the surface. This excludes established surface reconstruction algorithms. We developed an algorithm that allows the definition of a triangulation within a subset of particles attributed to a surface without the deletion of particles. A particular challenge is the deletion of connections that infer three-dimensional structures in the surface. The method is not fail safe but suitable for many configurations. Figure 6.2 shows the neighborhood relations on a piece of the cell membrane. On the left side, the connections existent before the re-triangulation algorithm is applied are shown. On the right side, only the connections kept after the re-triangulation are shown.

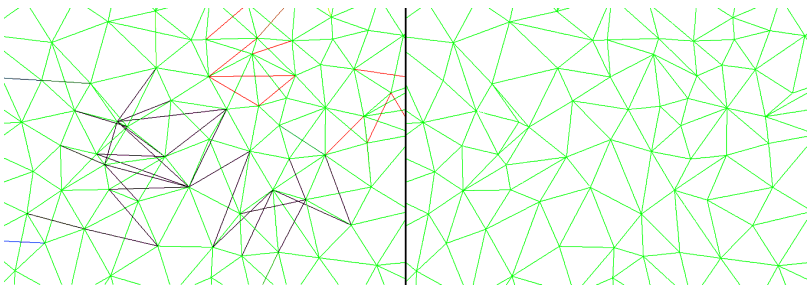

Abbildung 6.2: *Zoom of the cell membrane. Shown are the connections between membrane particles. On the left side, the configuration is shown before the re-triangulation is done. On the right side, the configuration after the re-triangulation (only with the kept connections) is shown.*

The developed algorithm for the reconstruction of connections in a surface is suitable to be used for simulations of biological cells because of the inherent conservation of the number of particles attributed to the membrane. However, some limitations of the method have still to be overcome in order to make it a realistic framework for simulations of cell systems in Biology. The model has the potential to be used not only to study cell shape and movement, but also to investigate the coupling between internal space-resolved movement of molecules and determined cell behaviors.

Verweise

1. G. Grise and M. Meyer-Hermann. *Surface reconstruction using Delaunay Triangulation for applications in life sciences*. Submitted (2009).

2. G. Grise and M. Meyer-Hermann. *Towards sub-cellular modeling with Delaunay triangulation*. Math. Model. Nat. Phenom. Accepted (2009).

4.6 Sonstige

4.6.1 Calculating NMR Order Parameters from MD Simulations

Alrun N. Koller and Holger Gohlke
Department of Biological Sciences, Goethe-University, Frankfurt am Main, Germany

Molecular dynamics (MD) simulations and NMR spin relaxation spectroscopy are complementary tools to investigate the dynamics of biomolecules. Comparing experimental NMR spin relaxation data to those calculated from MD trajectories also allows assessing whether MD simulations accurately reproduce structural and dynamical properties of the system. A comparison of experimental and MD-derived N-H S^2 order parameters is increasingly used to judge force-field quality in this regard. Aside from simulation conditions and the approach used to extract S^2 parameters, an influence of the MD starting structure on the computed S^2 parameters ought to be expected too, considering that system dynamics and (local) structure are intimately related. This influence should become particularly pronounced in flexible parts of the molecule, where conformational variability in experimental structures is most likely to occur. In our study, we demonstrate for the well-investigated model system hen egg white lysozyme (HEWL) that different starting structures can lead to differences in MD-derived S^2 parameters that can be even larger than deviations due to different force fields [1]. For four different representative HEWL structures we performed MD simulations in explicit solvent for a minimum of 30 ns with AMBER9 and ff99 and ff99SB force field, respectively. The MD simulations for one starting structure were extended to 100 ns to characterize the influence of the simulation time onto the calculated S^2 parameters. S^2 parameters were calculated for backbone N-H bonds according to the isotropic reorientational eigenmode dynamics approach.

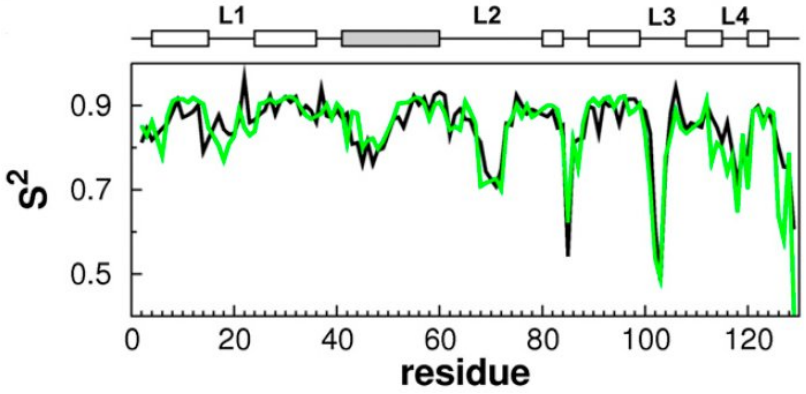

Abbildung 1.1: *Experimental S^2 values (black) are compared to calculated values (green) from the 30 ns simulation of 1IEE with ff99SB. RMSD between experimental and calculated S^2 values: 0.042. Secondary structure elements are indicated by boxes (white: α-helix; gray: β-sheet).*

Our results demonstrate that caution should be taken in general when simulated S^2 parameters are compared to experimental data with the aim of judging force-field quality. To assess the consistency of computed S^2 parameters, trajectories started from conformationally varying structures should be evaluated in parallel whenever possible. Adequately sampling flexible regions (˜100 ns) with the aim to obtain an accurate representation of the structure and dynamics and only calculating S^2 parameters over short time windows (˜1 ns) furthermore proved necessary to obtain consistent and accurate results irrespective of the starting coordinates. With this strategy we were able to calculate the most accurate S^2 values for HEWL compared to experiment (Figure 1.1).

Verweise

1. A.N. Koller, H. Schwalbe, H. Gohlke, *Biophys. J.* **95**, L4-L6 (2008).

4.6.2 Ursachen der unerwarteten Stabilität von RNA-Fluorbasen

Hannes Kopitz, Aleksandra Živković, Joachim W. Engels, Holger Gohlke
Institut für pharmazeutische und medizinische Chemie, Heine-Universität, Düsseldorf
Fachbereich Biochemie, Chemie und Pharmazie, Goethe-Universität, Frankfurt am Main

Der Austausch von Wasserstoff durch Fluor wird in der medizinischen Chemie häufig angewendet, weil er zu (1) metabolischer Stabilisierung, (2) pK_S-Verschiebung benachbarter Gruppen und/oder (3) Erhöhung der Hydrophobizität ohne Störung der lokalen Stereochemie führt.[1]
Mit Hilfe von „Freie Energie"-Rechnungen untersuchten wir den experimentell gemessenen Stabilitätsanstieg eines doppelsträngigen RNA-Fragments, das ein zentrales Fluorbenzol-Selbstpaar (d. h. Fluor-benzol mit Fluorbenzol gepaart) enthält, in Abhängigkeit zunehmender Fluorsubstitution.[2] Dazu berechneten wir die relativen Freie Bindungsenergien der Doppelstränge mit der Methode der Thermodynamischen Integration (TI). Um strukturelle Ursachen der Stabilitätsunterschiede aufklären zu können, implementierten wir eine Zerlegung der freien Energie in Beiträge einzelner Substrukturen, wie z. B. Einzelbeiträge des Lösungsmittels und des Soluts, in die verwendete Software Sander des Programmpakets Amber 8.

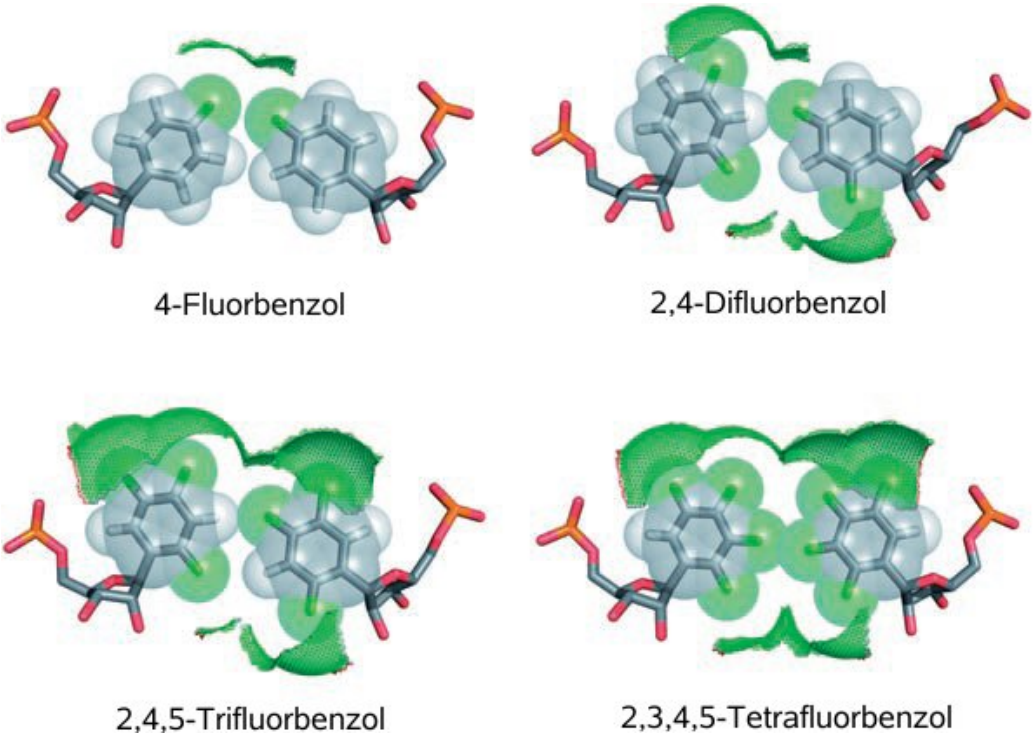

Abbildung 2.1: *Gemittelte Struktur einer MD-Trajektorie von selbstgepaarten Fluorbenzene-Nucleotiden. Die Lösemittel-zugämgliche Oberfläche der Fluoratome ist als grünes Gitter dargestellt.*

Diese strukturelle Zerlegung ergab fundamental unterschiedliche Ursachen der erhaltenen Stabilitätsunterschiede. Experimentell bestimmte $\log P$-Werte der Fluorobenzol-Nukleoside deuten auf eine steigende Hydrophobizität als Ursache der ansteigenden Stabilität hin. Jedoch zeigen die berechneten $\Delta\Delta G_{\mathrm{Solv}}$-Werte, dass nur im Fall der Benzol→4-Fluorbenzol- und 2,4,5-Trifluorbenzol→2,3,4,5-Tetrafluorbenzol-Vergleiche der Lösungsmitteleinfluss der bestimmende Faktor für die Stabilitätsanstiege ist.
Die relative freie Bindungsenergie von 4-Fluorbenzol→2,4-Difluorbenzol zeigt eine ähnlich hohe Stabilitätserhöhung wie Benzol→4-Fluorbenzol, jedoch aufgrund völlig anderer Ursachen. Hier konnten

wir mit Hilfe von Molekulardynamik-Simulationen zeigen, dass unterschiedlich ausgeprägte dipolare C-H···F-C Wechselwirkungen die Ursache sind.
Die Rechnungen wurden auf dem CSC-Cluster „quad“ durchgeführt und benötigten insgesamt einen Bedarf an CPU-Zeit von ca. 6800 h.
Die Arbeiten führten zu einer Publikation in der Zeitschrift ChemBioChem.

Verweise

1. H.-J. Böhm, D. Banner, S. Bendels, M. Kansy, B. Kuhn, K. Müller, U. Obst-Sander, M. Stahl, *ChemBioChem* **5**, 637 – 643 (2004).

2. H. Kopitz, A. Živković, J. W. Engels, H. Gohlke, *ChemBioChem* **9**, 2619 – 2622 (2008).

4.6.3 Global water resources in a changing world

Petra Döll
AG Hydrologie, Institut für Physische Geographie, Goethe-Universität Frankfurt

To achieve a sustainable development of the planet Earth, water resources need to be managed well. This requires an assessment of the current water situation, an understanding of historic developments and the generation of scenarios of the future. A global-scale freshwater assessment helps to understand the global water system and how it is impacted by humans, as in a globalized world, freshwater assessments can no longer be restricted to the river basin scale.
To support these tasks, we have developed the global-scale water model WaterGAP that computes both water resources and water use with a spatial resolution of 0.5°x 0.5°(55 km at the equator). WaterGAP has recently been improved with respect to lateral flow velocities and the storage dynamics of man-made reservoirs. Together with new data sets, including data on the Earth's dynamic gravity field, precipitation, reservoirs and land use, new analyses regarding certain aspects of the global water system have been performed. These include the alteration of natural river flow regimes by human water withdrawals and reservoir construction, with its impacts on aquatic ecosystems. The figure below shows to what extent WaterGAP is able to simulate the impact of reservoirs on the seasonality of river discharge (Döll et al., 2009). Six ecologically relevant flow indicators were quantified using an improved version of the global water model WaterGAP.

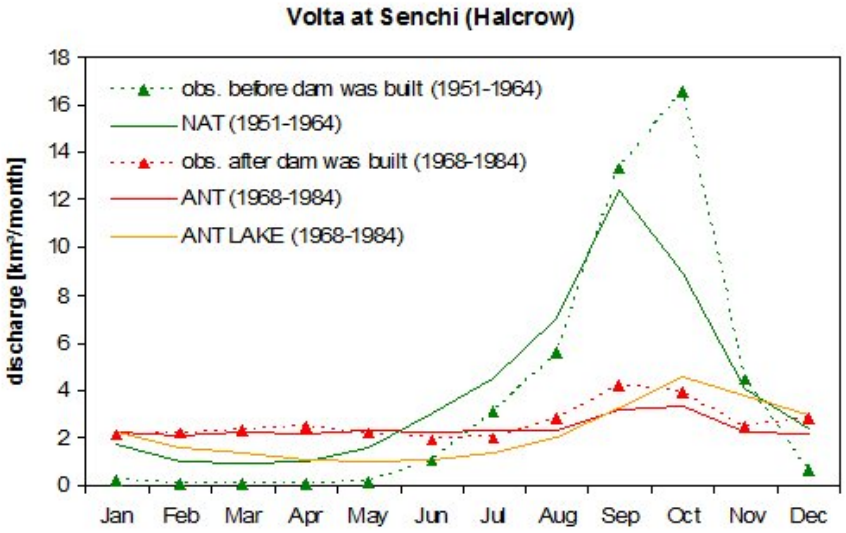

Abbildung 3.1: *River discharge of the Volta at Senchi (West Africa). Comparison of simulated and observed values.*

WaterGAP simulated, with a spatial resolution of 0.5 degree, river discharge as affected by human water withdrawals and dams, as well as naturalized discharge without this type of human interference. Mainly due to irrigation, long-term average river discharge and statistical low flow Q90 (monthly river discharge that is exceeded in 9 out of 10 months) have decreased by more than 10% on one sixth and one quarter of the global 15 land area (excluding Antarctica and Greenland), respectively. Q90 has increased significantly on only 5% of the land area, downstream of reservoirs. Due to both water withdrawals and dams, seasonal flow amplitude has decreased significantly on one sixth of the land area, while interannual variability has increased on one quarter of the land area mainly due to irrigation. It has decreased on only 8% of the land area, in areas with little consumptive water use that are downstream of dams.

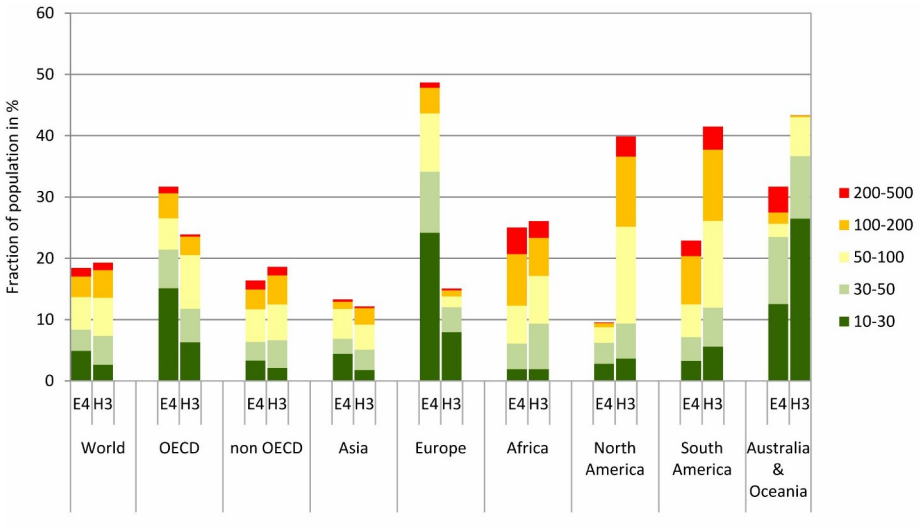

Abbildung 3.2: *Percentage of population in different world regions that will suffer from vulnerability to climate change induced decrease of GWR. Colours indicate degree of vulnerability as described by VI for climate change scenarios ECHAM4 A2 (E4) and HadCM3 A2 (H3). Central America is part of North America.*

Another focus is the assessment of the impact of climate change on water resources. A study on human vulnerability to climate-change induced reductions of renewable groundwater resources by the year 2050 was performed (Döll, 2009). In the A2 (B2) emissions scenario, 18.4–19.3% (16.1–18.1%) of the global population of 10.7 (9.1) billion would be affected by groundwater recharge decreases of at least 10%, and 4.8–5.7% (3.8–3.8%) of the global population would be in the two highest vulnerability classes. The highest vulnerabilities are found at the North African rim of the Mediterranean Sea, in southwestern Africa, in northeastern Brazil and in the central Andes, which are areas of moderate to high sensitivity. For most of the areas with high population density and high sensitivity, model results indicate that groundwater recharge is unlikely to decrease by more than 10% until the 2050s. However, a fifth to a third of the population may be affected by a groundwater recharge increase of more than 10%, with negative impacts in the case of shallow water tables. The spatial distribution of vulnerability, even at the continental scale, differs more strongly between the two climate models than between the two emissions scenarios. Continental averages of vulnerabilities are shown in Fig. 3.2.

References

1. Döll, P. (2009): Vulnerability to the impact of climate change on renewable groundwater resources: a global-scale assessment. Environ. Res. Lett., 4, 036006 (12pp). doi: `http://dx.doi.org/10.1088/1748-9326/4/3/03500610.1088/1748-9326/4/3/035006`.

2. Döll, P., Fiedler, K., Zhang, J. (2009): Global-scale analysis of river flow alterations due to water withdrawals and reservoirs, Hydrol. Earth Syst. Sci. Diss., 6, 4773-4812.

4.6.4 WaterGAP: *Water* - *G*lobal *A*ssessment and *P*rognosis

Frank Voß, Ellen Teichert
Center for Environmental Systems Research (CESR), University of Kassel
D-34109 Kassel

Changes in the hydrological cycle induced by global warming may affect society more than any other changes, e.g. with regard to flood and drought risks, changing water availability and water quality. Levels of water use are already today unsustainable in many countries worldwide. Water availability and water demands are heavily outbalanced as a result of natural and socio-economic alterations. But there are many uncertainties in our understanding of the current water cycle and how it will develop in the future. A number of studies have sought to assess the global-scale implications of climate change on water resources, their availability and water resources stresses. One of the models to calculate water availability globally is WaterGAP. It is used to study the state of current and future global water resources and is calibrated and validated against measured discharge data. By means of this hydrological modelling tool the impacts of climate change and socio-economic driving forces can be studied.
The WaterGAP-model (Water - Global Assessment and Prognosis) has been developed to simulate the distribution and availability of water on global scale (Alcamo et al. 2003, Döll et al. 2003). Since then the model has been further developed and its spatial resolution increased from 30 (0.5°in WaterGAP2) to 5 arc-minutes (1/12°) globally in the version WaterGAP3. WaterGAP3 consists of three main components (Figure 1): 1) a hydrology model to simulate the continental water cycle, 2) a water use model to estimate water withdrawals and water consumption for agriculture, manufacturing (divided into industry water use and uses for electricity production) and domestic water use, and 3) a water quality module which is currently being developed to calculate changes in the quality of surface water resources. All three sub-models provide output at a spatial resolution of 5 arc-minutes with a temporal resolution varying from daily to annual and having a consistent land-sea mask. This allows an easy soft-linking of the models (as shown in Figure 4.1) to address the following research questions:
What is the status of water resources in the 20^{th} and how will they be in 21^{st} century?
How will the occurrence of future floods and related flood risks change?
How can 'natural flow' and 'ecosystem services' be defined (environmental flow concept)?
How will water quality deteriorate water resources?
The increased spatial resolution of WaterGAP3 consequently produces more detailed model output. This is crucial for the application in present EU funded projects like SCENES [1] and WATCH [2], but it also implies that mass storage increases enormously.
From a computational point of view, the vertical simulation in WaterGAP gives rise to data parallelism, as grid cells are computed independently (Leopold et al 2006). The parallel program runs on a heterogeneous SMP cluster and combines different parallel programming paradigms: First, at its outer level, it uses master/slave communication implemented with MPI. Second, within the slave processes, multiple threads are spawned by OpenMP directives to exploit data parallelism.
To ensure a proper work flow within the working group at CESR, computational resources at the computing centre of the University of Kassel have to be guaranteed.

Literatur

1. ALCAMO, J., P. DÖLL, T. HENRICHS, F. KASPAR, B. LEHNER, T. RÖSCH & S. SIEBERT (2003): Development and testing of the WaterGAP2 global model of water use and availability. Hydrological Sciences Journal 48: 317-337.

2. DÖLL, P., F. KASPAR & B. LEHNER, B. (2003): A global hydrological model for deriving water availability indicators: model tuning and validation. Journal of Hydrology 270: 105 – 134.

[1] `http://www.environment.fi/default.asp?contentid=342422\&lan=EN`
[2] `http://www.eu-watch.org/http://www.eu-watch.org/`

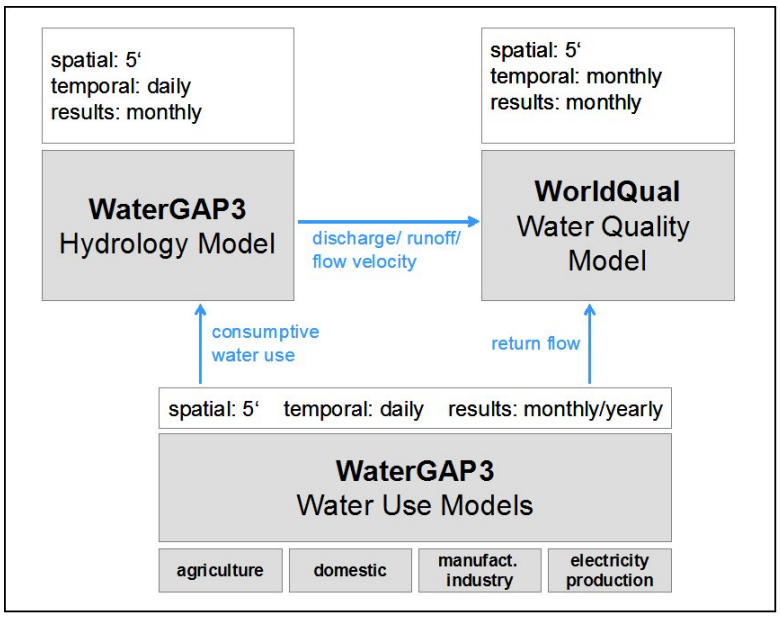

Abbildung 4.1: *Model suite developed at CESR and schematic overview for offline coupling of model components (VOß et al. 2009).*

3. VOß, F., A. VOß, I. BÄRLUND & J. ALCAMO (2009): Preliminary water quality module: state of development and plan for linkage to the overall modelling framework. WATCH project deliverable 6.1.4.

4. LEOPOLD C., SÜß M. & BREITBART J. (2006): Programming for Malleability with Hybrid MPI-2 and OpenMP: Experiences with a Simulation Program for Global Water Prognosis. European Conference on Modelling and Simulation (pp.665 - 670). Bonn.

4.6.5 Regional climate simulations over South Asia

Shakeel Asharaf, Andreas Dobler, Bodo Ahrens
Institute for Atmospheric and Environmental Sciences, Goethe–University Frankfurt/Main

South Asia, particularly the Indian subcontinent, experiences a summer monsoon season from June to September (JJAS) in every year (it signifies the winds of Southern Asia with a complete reversal of wind direction between winter and summer). The summer monsoon is accompanied by heavy precipitation with convective storms. However, the nature of this convective system varies from region to region, and many scientists argued these phenomenon as the results of complex land-atmosphere interaction. For example, the heavy rainfall along the North-East part of India is due to orographic lifting, which triggers deep convection in this region. From the Western to the Eastern foothills of the Himalayan region, the convective systems vary dramatically due to region-specific orographically modified flows and land surface fluxes feedbacks (Medina et al., 2008). Thus, the surface fluxes of heat and the orography play important roles in triggering and maintaining convection in the tropics and the formation of South Asian monsoon climate.

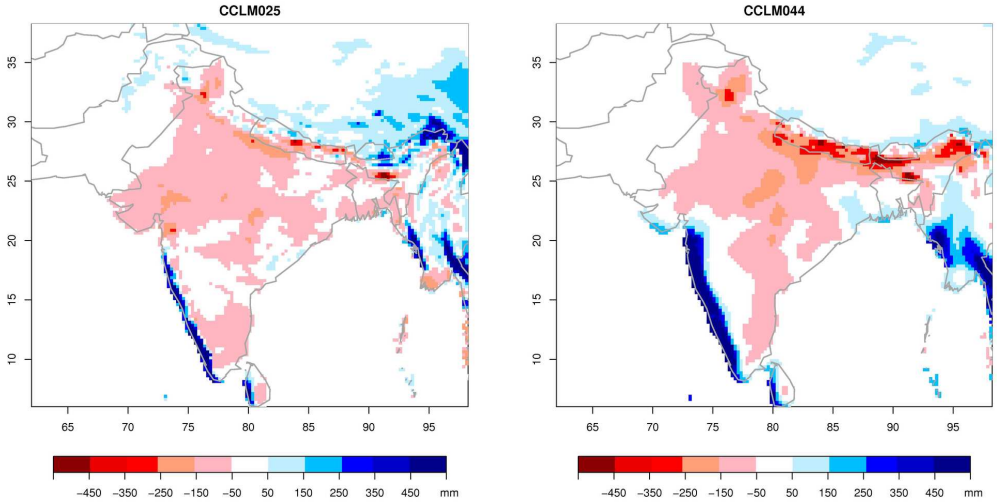

Abbildung 5.1: *CCLM precipitation bias with respect to the APHRODITE (Xie et al., 2007) gridded observed precipitation data-set (JJAS, from 1989 to 2000)*

Nowadays, with development of vastly more powerful computing resources and sophisticated modeling techniques allow us to run the climate model in a high resolution mode. High resolution models demonstrate considerable skill in predicting local circulation driven by local topography and land surface variations, which were often missed or not resolved by coarse resolution operational models. The computational resources available at CSC (Center for Scientific Computing), Frankfurt, fulfilled all the necessary requirements for high amount of computational resources. Here, dynamical downscaling of global coarse–grid ERA-Interim re-analysis data (as ideal place–holder for global climate model data) to 0.25° horizontal grid resolution has been carried out using the state of the art non-hydrostatic regional climate model CCLM (consortium for small scale modeling in climate mode, www.clm-community.eu) with 32 layers in vertical column. The simulated results clearly added valuable informations. Figure 5.1 depicts the monthly mean precipitation biases with respect to an East Asia gridded rainfall observational data-set during summer (JJAS) monsoon period. In comparison with previous simulations (Dobler and Ahrens, 2008; 2009) with 0.44° horizontal grid spacing including 20 layers in vertical column, it can be seen that both the simulations have still difficulties to capturing monsoon precipitation, especially an overestimation at Indian west coast and an underestimation at the Himalayan foothills regions. However, the CCLM simulation at 0.25°

grid spacing provides significantly improved precipitation. Recently, extensive simulation studies of Kothe et al (2009) discussed the sensitivity of simulations to the number of vertical layers. In this 32 vertical layers simulated results are closer to observation than 20 layers experiment especially in surface radiation budget components. Although, improvement was relatively small in terms of long wave and short wave radiation. More vertical layers consisting higher resolution in the troposphere, which could adequately resolved the smaller eddies than less layers experiment. In fact, observations in atmosphere and surface are disproportionately sparse, both temporally and geographically. This uncertainty in observations is likely one of the largest limiting factors in climate modeling.
The present simulation study suggests that both horizontal and vertical resolutions have significant impact in the South Asia monsoon simulations. In the next step, towards the goal of improving simulations and to understand the role of land-surface processes in the South Asia (particularly, Indian subcontinent) monsoon system, a number of sensitivity test simulations of land surface processes for present climate condition will be performed with respect to initial and boundary conditions. Indeed, at the end of the experiments, we expect a new and more complete description of land surface processes, and the ability to explain the relative importance of the various factors affecting the monsoon system.

References

Dobler, A., and Ahrens, B (2009): Analysis of the Indian summer Monsoon system in the regional climate model COSMO CLM. J.G.R.(submitted).

Dobler, A., and Ahrens, B (2008): Precipitation by a regional climate model and bias correction in Europe and South Asia. Meteorologische Zeitschrift, 17 (4), 499-509.

Kothe S, Dobler A, Beck A, Ahrens B (2009): The radiation budget in a regional climate model. Climate Dynamics (cond. accepted).

Medina, S., Houze, R. A., Kumar, A., and Niyogi, D (2008): Summer monsoon convection in the Himalayan region: terrain and land cover effects. Q.J.R. Meteorol. Soc. (revised).

Xie et al. (2007): A gauge-based analysis of daily precipitation over East Asia. J. Hydrometeor., 8,607-627.